THE UNIVERSITY OF
SYDNEY

Geometric Singular Perturbation Analysis of Mixed-Mode Dynamics in Pituitary Cells

Theodore Minh Tam Vo

A thesis submitted in fulfillment of
the requirements for the degree of
Doctor of Philosophy

Applied Mathematics
Faculty of Science
University of Sydney

THE UNIVERSITY OF SYDNEY

September 2014

Acknowledgements

This thesis is the culmination of four years worth of work. It started as an extracurricular undergraduate project and eventually evolved into my doctoral research. The road has been long (and sometimes chaotic), but deeply fulfilling. That I have made it this far has been due in no small part to the generous contributions of the following people, to whom I express my sincerest gratitude.

Warren Weckesser: for getting me started with AUTO, especially since there was no 'local' AUTO support when I was starting out.

Hinke Osinga and Bernd Krauskopf: for inspiring me to learn how to compute invariant slow manifolds and canards using AUTO. In fact, every time I attend one of your talks, I feel inspired to go out and learn something new.

Vivien Kirk: for supporting my visit to the University of Auckland in November, 2011. The work I did during my visit inspired the contents of Chapter 4 of this thesis.

Robby Marangell: for your sagely advice on matters both academic and non-academic.

Joël Tabak: for giving me a place to stay during my visit to Tallahassee, for teaching me the dynamic clamp technique, for staying with me in the lab till the wee hours of the morning, and for showing me the Tallahassian sights.

Richard Bertram: for reading and providing feedback on countless drafts, for being my unofficial associate supervisor and for supporting my visit to your lab at Florida State University during the latter half of 2012. My thesis topic was born out of the work done by your lab. I have thoroughly enjoyed our collaboration and look forward to working with you in future.

John Mitry and Kerry-Lyn Roberts: for your moral support, your wisdom, your humour, and more importantly, your friendship. I've treasured every moment spent in your company and I can only hope to have made as much of an impact on you as you have on me.

My family: for your unwavering love and support. You have always managed to keep my head in the clouds and my feet on the ground. Without you behind me, I could never have achieved any of my goals.

Above all, I would like to thank my doctoral advisor A/Prof. **Martin Wechselberger**, without whom, none of this would have been possible. You took me under your wing and saw me through to the end of a significant milestone of my life: the PhD. You have always had time for me and your good judgement has never led me astray. Thank you for your ceaseless encouragement, your assiduous guidance and your infinite reserves of patience. I am forever in your debt.

Nothing in the world can take the place of persistence.
Talent will not; nothing is more common than
unsuccessful men with talent.
Genius will not; unrewarded genius is almost a proverb.
Education will not; the world is full of educated derelicts.
Persistence and determination alone are omnipotent.

John Calvin Coolidge, Jr.

Abstract

Pseudo-plateau bursting is a type of oscillatory waveform associated with mixed mode dynamics in slow/fast systems and commonly found in neural bursting models. In a recent model for the electrical activity in a pituitary lactotroph, two types of pseudo-plateau bursts were discovered: one in which the calcium drives the bursts and another in which the calcium simply follows them. Multiple methods from dynamical systems theory have been used to understand the bursting. The classic 2-timescale approach treats the calcium concentration as a slowly varying parameter and considers a parametrized family of fast subsystems. A more novel and successful 2-timescale approach divides the system so that there is only one fast variable and shows that the bursting arises from canard dynamics. Both methods can be effective analytic tools but there has been little justification for one approach over the other. In the first part of this thesis, we demonstrate that the two analysis techniques are different unfoldings of a 3-timescale system. We show that elementary applications of geometric singular perturbation theory and bifurcation theory in the 2-timescale and 3-timescale methods provides us with substantial predictive power. We use that predictive power to explain the transient and long-term dynamics of the pituitary lactotroph model.

The canard phenomenon occurs generically in singular perturbation problems with at least two slow variables. Canards are closely associated with folded singularities and in the case of folded nodes, lead to a local twisting of invariant manifolds. Folded node canards and folded saddle canards (and their bifurcations) have been studied extensively in $\mathbb{R}^3$. The folded saddle-node (FSN) is the codimension-1 bifurcation that gives rise to folded nodes and folded saddles. There are two types of FSN. In the FSN type I, the center manifold of the FSN is tangent to the curve of fold bifurcations of the fast subsystem. In the FSN II, the center manifold of the FSN is transverse to the curve of fold bifurcations of the fast subsystem. Both types of FSN bifurcation are ubiquitous in applications and are typically the organizing centers for delay phenomena. In particular, the FSN I and FSN II demarcate the bursting regions in parameter space. Their dynamics however, are not completely understood. Recent studies have unravelled the local dynamics of the FSN II. In the second part of this thesis, we extend canard theory into the FSN I regime by combining methods from geometric singular perturbation theory (blow-up), and the theory of dynamic bifurcations (analytic continuation into the plane of complex time). We prove the existence of canards and faux canards near the FSN I, and study the associated delayed loss of stability.

CONTENTS

CHAPTER 1

Introduction

The neuroendocrine system is the remarkably complex network of cells, glands and tissues that maintain homeostasis and regulate reproduction, metabolism, energy utilisation, osmolarity, and blood pressure within the human body. The neuroendocrine system is made up of the nervous system and the endocrine system (Figure 1.1) and together, these work to keep the body functioning regularly. The nervous system coordinates voluntary and involuntary actions, and transmits signals between different parts of the body. At the cellular level, the nervous system is defined by the presence of a special type of cell, called the neuron (or nerve cell), which provides a long-range signalling mechanism to coordinate the behaviour of cells in remote parts of the body [**1**]. Neurons typically extend long branching processes (axons) that terminate at specialized sites of signal transmission known as chemical synapses. The axons enable neurons to contact target cells that are far away. When activated by stimuli from the environment or from other nerve cells, the neuron sends electrical impulses (action potentials) rapidly along its axon, triggering neurotransmitter release at the synapse. Neurotransmitters in turn communicate information throughout the brain and body by relaying signals between neurons. The brain essentially uses neurotransmitters to tell the heart to beat, the lungs to breathe and the stomach to digest.

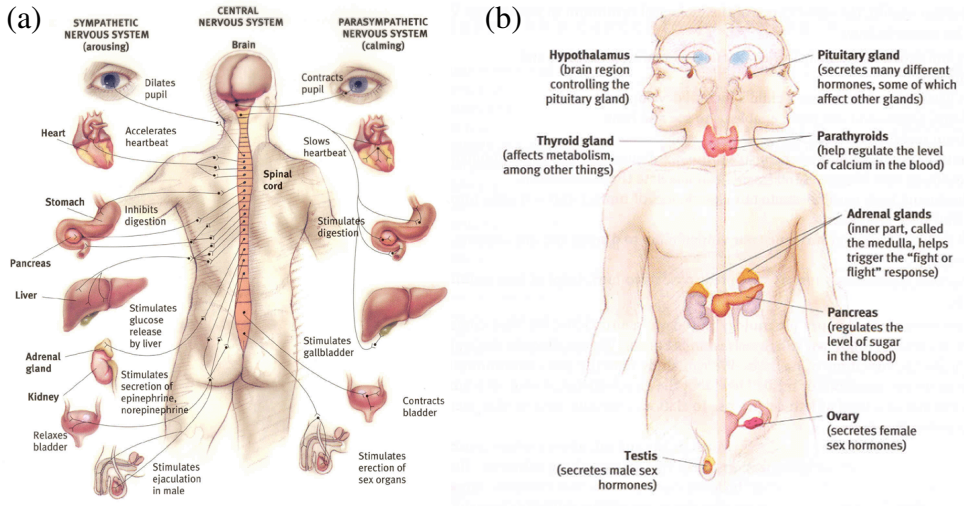

Figure 1.1. The neuroendocrine system is composed of the (a) nervous and (b) endocrine system. Adapted from `http://members.shaw.ca/renaissanceservices/health/stress/stress.htm`.

The endocrine system consists of the pituitary, pineal, thyroid, parathyroid and adrenal glands, pancreatic islet cells, and the ovaries or testicles. It controls physiological and behavioural activities via the secretion of hormones directly into the bloodstream, which carries the hormones far and wide, allowing them to act on target cells that may lie anywhere in the body [**1**]. Hormones regulate various human functions such as metabolism, growth and development, tissue function, sleep, and mood. The endocrine system's effects are slow to initiate, and prolonged in their response, since it relies on diffusion and blood flow. This is

in contrast to the synaptic signalling of the nervous system, which is much faster (and more precise) with short lived responses.

The control centre of the endocrine system is the hypothalamus, a small area located in the middle of the base of the brain (behind and between the eyes). Typically weighing about 4 grams out of the 1400 gram brain mass of an adult human [**108**], the hypothalamus stimulates cellular activity in various parts of the body by directing the release of hormones from the pituitary gland. By controlling the secretory functions of the pituitary gland, the hypothalamus exerts control over most of the vegetative and endocrine functions of the body as well as many aspects of emotional behaviour [**56**]. Damage to the hypothalamus can result in severe imbalances in the internal environment.

The pituitary gland is the pea-sized organ that lies immediately beneath the hypothalamus. It is considered the 'master gland' of the body as it secretes a battery of hormones that collectively influence all cells and affect virtually all physiological processes (Figure 1.2). The pituitary gland is connected to the hypothalamus via the hypophyseal stalk. This stalk contains neuronal processes and blood vessels that collect neurotransmitters released by neurons in the hypothalamus. In this way, the endocrine system is connected to and controlled by the nervous system [**56**].

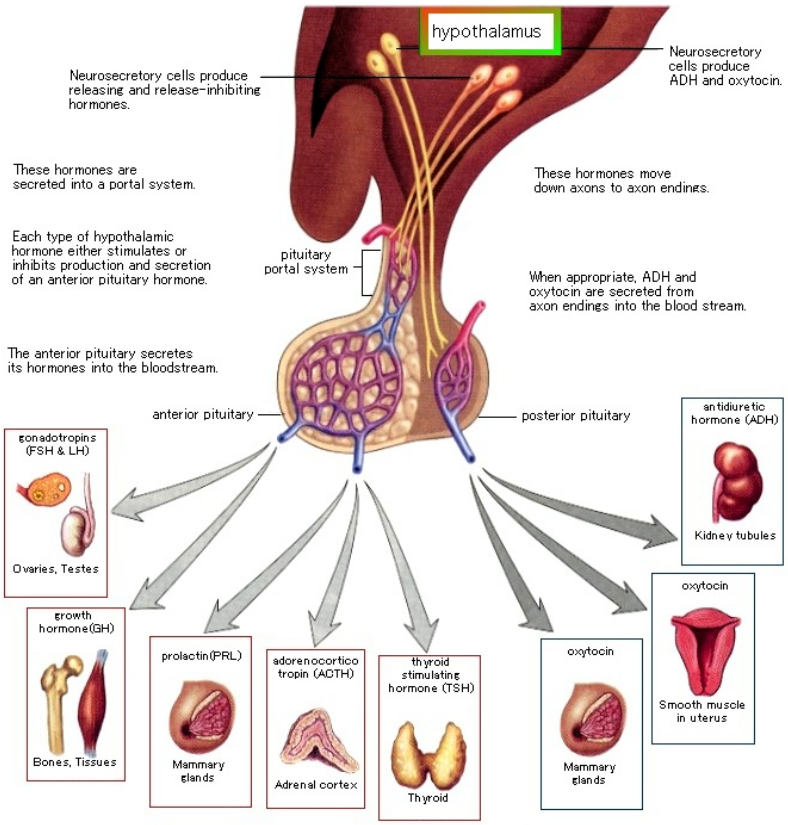

Figure 1.2. The hypothalamus, pituitary gland, and the array of hormones released from the anterior and posterior pituitary lobes. Adapted from [**9**].

Physiologically, the pituitary gland is split into two distinct regions: the posterior and anterior lobes. The posterior lobe of the pituitary gland is an extension of the hypothalamus and is composed largely of axons of hypothalamic neurons, which extend downward as a large bundle that terminate behind the anterior pituitary. The posterior pituitary is where the hormones oxytocin (which affects uterine contractions and lactation) and vasopressin (which affects water retention and blood pressure) are stored and released. Secretion from

the posterior pituitary is controlled by nerve signals that originate in the hypothalamus and terminate in the posterior pituitary [**56**]. The anterior lobe of the pituitary gland is responsible for the synthesis and release of most pituitary hormones. The anterior pituitary does not receive direct neural input from the brain, but is instead connected to the hypothalamus through a vascular network called the hypophyseal portal system. The primary function of the hypophyseal portal system is the transport and exchange of hormones to allow rapid communication between the hypothalamus and the pituitary gland. More specifically, hypothalamic releasing and hypothalamic inhibitory hormones secreted within the hypothalamus are conducted (via the hypophyseal portal system) to the anterior pituitary, where they act on the glandular cells to control hormone secretion [**40**].

The anterior region of the pituitary gland contains five types of trophic endocrine cells that secrete a variety of hormones into the blood, which affect the growth of their target tissues [**9, 40, 56, 83**]:

(i) *Corticotrophs* secrete adrenocorticotropic hormone, which stimulates the synthesis and release of glucocorticoids (GCs) from the adrenal cortex. GCs regulate the metabolism of glucose and are part of the immune system's feedback mechanism to turn down immune activity (i.e. inflammation).

(ii) *Somatotrophs* secrete growth hormone, which promotes the growth of most cells in the body. Excess secretion of growth hormone can lead to gigantism (before puberty) or acromegaly (after puberty). Growth hormone deficiency can lead to pituitary dwarfism, which can result in a number of physical and psychological symptoms. Unlike the other major anterior pituitary hormones, growth hormone does not function by stimulating a target gland but exerts its effects directly on all or almost all tissues of the body.

(iii) *Lactotrophs* target the mammary glands by secreting prolactin, which initiates milk synthesis and has many other roles related to reproduction and parental behaviour. Unlike the other anterior pituitary hormones, the hypothalamus mainly inhibits prolactin production, rather than promoting it. Dopamine is the primary neuroendocrine inhibitor of the secretion of prolactin from the anterior pituitary.

(iv) *Gonadotrophs* secrete luteinizing hormone (LH) and follicle stimulating hormone (FSH), which target cells in the gonads. In females, LH stimulates ovulation and the formation of corpora lutea in the ovary. In males, LH stimulates the Leydig cells to secrete androgens such as testosterone. FSH promotes the development of gametes and the secretion of gonadal hormones in males and females.

(v) *Thyrotrophs* target the thyroid gland by secreting thyroid stimulating hormone, which stimulates the synthesis and release of thyroxine and triiodothyronine from the thyroid gland.

These pituitary hormones are transported by the vasculature to other regions of the body where they act on other endocrine glands, which in turn secrete their hormones into the blood, and on other tissue including the brain.

Like neurons and muscle cells, endocrine pituitary cells are electrically excitable. They generate brief electrical impulses (called action potentials or spikes) that bring calcium ions into the cell, which can in turn evoke the exocytosis of hormone-containing granules. In this way, the hormone secretion from pituitary cells is, to a large extent, controlled by the electrical activity of the cells. There are many types of ion channels expressed in pituitary cells, and the ionic currents mediated by these channels determine the electrical activity exhibited by the cells [**118**]. In a physiological setting, this spontaneous activity is subject to continuous adjustment by hypothalamic neuropeptides, by hormones from other glands such as the testes or ovaries, and by other pituitary hormones [**42, 118**].

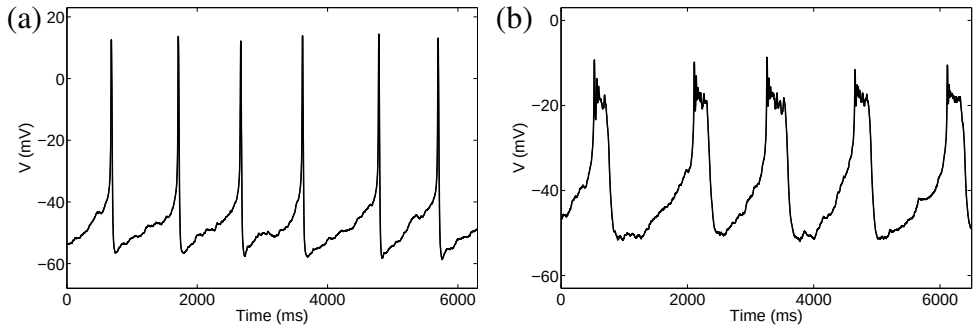

Figure 1.3. Electrical activity recorded in GH4C1 lacto-somatotroph cell lines. The cells are able to exhibit (a) spiking and (b) bursting behaviour.

One typical pattern of electrical activity commonly seen in nerve and endocrine cells is bursting [**84, 38, 100, 74, 101, 104**] (Figure 1.3(b)). Characterized by alternating periods of fast spiking in the active (depolarized) phase and quiescence during which the cell is repolarized, bursts are typically more efficient than spikes in evoking hormone and neurotransmitter release [**82, 117**]. Such bursting oscillations have been observed in the spontaneous activity of prolactin-secreting lactotrophs, growth hormone-secreting somatotrophs, and ACTH-secreting corticotrophs [**132, 133, 78, 128**], as well as GH4C1 lacto-somatotroph tumor cells [**122**]. Characteristics of the burst pattern such as frequency and duration determine how much calcium enters the cell, which in turn determines the level of hormone secretion [**133**]. More specifically, the bursting elevates the Ca^{2+} concentration in the cytosol of the cell and thus generates higher levels of hormone secretion than tonic spiking patterns.

In this introductory chapter, we provide a brief overview of the bursting phenomenon that motivates this thesis. In Section 1.1, we review the bursting phenomenon from a mathematical viewpoint with particular emphasis on plateau and pseudo-plateau bursting. The underlying mathematical structure we introduce is the singular perturbation problem, which lies at the heart of bursting phenomena. In Section 1.2, we introduce the pituitary cell model of interest that generates pseudo-plateau bursting and formally show that it is singularly perturbed. We then outline the aims, scope and main contributions of the thesis in Section 1.3.

1.1. Slow/Fast Analysis of Plateau and Pseudo-Plateau Bursting

Bursting has been observed in various excitable systems, such as neurons [**74, 84**], cardiac and muscle cells [**109, 127**], and endocrine cells [**38, 65**]. Given the ubiquity and complexity of the bursting pattern, there has been a great deal of attention from the modelling community. The earliest models of bursting neurons were developed in the 1970s and bursting models have been published regularly ever since. Several books describe these models and the techniques to analyze them [**19, 66, 70**]. The key observation is that the dynamics operate on multiple timescales and are described by singularly perturbed systems of the form

$$\begin{aligned} \dot{y} &= g(y,z), \\ \dot{z} &= \delta\, h(y,z), \end{aligned} \tag{1.1}$$

where $y \in \mathbb{R}^n$ is fast, $z \in \mathbb{R}^k$ is slow, $0 < \delta \ll 1$ is a small parameter and the overdot denotes a time derivative. Such slow/fast systems are amenable to singular perturbation methods and one technique that has been used with great success is geometric singular perturbation theory (GSPT) [**41, 68**].

Remark 1.1. Many biological systems evolve on more than 2 timescales and the canonical form (1.1) is achieved through either model reductions or by a convenient grouping of the variables into slow and fast categories.

The traditional implementation of GSPT in bursting problems (as pioneered in [**98**]) groups the variables so that there is only 1 slow variable, and takes the singular limit $\delta \to 0$ and analyzes the dynamics of the resulting fast subsystem

$$\begin{aligned} \dot{y} &= g(y, z), \\ \dot{z} &= 0, \end{aligned} \tag{1.2}$$

where $z \in \mathbb{R}$ is now a parameter. The dynamics of the fully perturbed problem (1.1) are then understood as a slow drift through the dynamic regimes of (1.2). Such a geometric singular perturbation analysis is also referred to as a 'slow/fast' analysis. Bursts are classified according to the fast y-subsystem bifurcations (with respect to z) involved in the initiation/termination of the active (depolarized) phase [**99, 65**]. More precisely, the topological classification of bursting is based on two important bifurcations of the fast subsystem (1.2):

(i) Initiation – bifurcation of equilibria of (1.2) resulting in a transition to limit cycles.
(ii) Termination – bifurcation of limit cycles resulting in a transition to equilibria.

Based on this classification scheme, there are 16 possible types of bursting when the fast subsystem (1.2) is 2D and there are 120 types when the dimension of (1.2) is higher. We refer to [**65**] for a complete listing of these bursters.

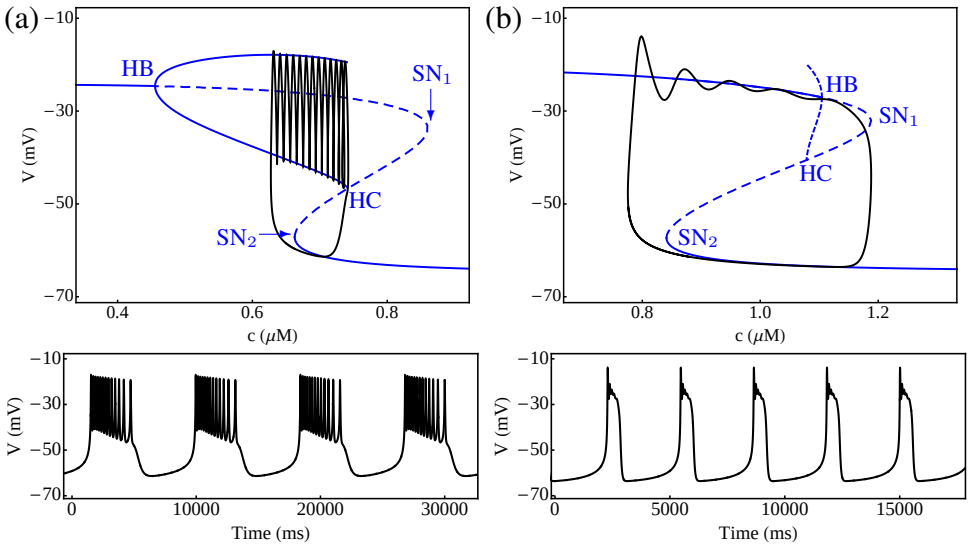

Figure 1.4. Typical slow/fast analysis (with c slow and V fast) for (a) plateau and (b) pseudo-plateau bursting. The fast subsystem equilibria (blue) undergo a (a) supercritical and (b) subcritical Hopf bifurcation (HB). The plateau bursting closely follows stable limit cycles of (1.2) until the homoclinic (HC). The pseudo-plateau bursting is not as well understood in this formulation. In both cases, the active phase initiates at the lower fold (SN_2).

One particular type of bursting that has been the focus of recent modelling efforts is pseudo-plateau bursting, which features small amplitude oscillations or spikes in the active phase superimposed on large amplitude relaxation type oscillations [**121, 116**]. Pseudo-plateau bursting is usually associated with higher levels of hormone or neurotransmitter secretion in nerve and endocrine cells and there is evidence it may have important roles in neuronal signalling [**82, 117**]. Pseudo-plateau bursts are distinguished from plateau bursts, which feature large amplitude fast spiking in the active phase [**98, 6, 81, 128**]. In terms of (1.2), plateau and pseudo-plateau bursting feature a Hopf bifurcation of the fast subsystem in the active phase, the criticality of which distinguishes the two bursting types [**95, 129**]. In the plateau case, the Hopf is supercritical and the large amplitude active phase spikes are related

to stable periodic orbits of the fast subsystem. The spiking activity in the active phase terminates at a saddle homoclinic orbit. In the pseudo-plateau case, the small amplitude spikes are transient oscillations that pass through a neighbourhood of the subcritical Hopf [**116**] (see Figure 1.4). The small amplitude active phase spiking can persist even when there is no stable solution of (1.2). Note that plateau and pseudo-plateau bursting can be converted into one another via parameter changes that alter the criticality of the fast subsystem Hopf [**95, 124**]. In both plateau and pseudo-plateau bursting, the initiation of the active phase occurs via a fold bifurcation of the fast subsystem.

The slow/fast analysis outlined above has been very successful in understanding the plateau bursting that occurs in pancreatic islets [**7**], pre-Bötzinger neurons of the brain stem [**16**], trigeminal motoneurons [**21**] and neonatal CA3 hippocampal principal neurons [**105**]. It has also been useful in understanding aspects of pseudo-plateau bursting such as resetting properties [**116**], how fast subsystem manifolds affect burst termination [**94**], and how parameter changes convert the system from plateau to pseudo-plateau bursting [**124**]. There are features of the pseudo-plateau bursting however that are not well described by the standard slow/fast analysis. Most notably, the transition from spiking to bursting cannot be predicted. In fact, periodic spiking trajectories of the full system (1.1) can occur over a range of the fast subsystem bifurcation diagram that only contains stable equilibria (see [**123**] for example). As noted in Remark 1.1, most bursting models usually evolve on more than 2 timescales and it may be more instructive to decompose the system so that there is more than 1 slow variable. This thesis is concerned with breaking partially from the traditional approach by using alternative slow/fast analyses where there is more than 1 slow variable.

1.2. The Pituitary Lactotroph Cell Model

Many hormone-secreting cells in the anterior pituitary gland, such as lactotrophs, somatotrophs and corticotrophs exhibit fast bursting with small spikes arising from an elevated or depolarized voltage [**78, 133**] – see Figure 1.3(b). Many mathematical models have been developed for the pseudo-plateau bursting in lactotrophs [**121, 130**], somatotrophs [**128**], corticotrophs [**81, 114**] and single β-cells [**146**]. In this thesis, we consider a conductance-based model for the electrical activity and calcium signalling in a pituitary lactotroph [**121**]. Conductance-based models are derived from equivalent circuit representations of a cell membrane [**64**]. The model variables are the membrane potential V of the cell, the fraction n of activated K^+ channels of the delayed rectifier type, the fraction e of A-type K^+ channels that are not inactivated and the cytosolic free Ca^{2+} concentration c. The equations are

$$\begin{aligned} C_m\frac{dV}{dt} &= -\left(I_{Ca}+I_K+I_{BK}+I_{SK}+I_A\right), \\ \frac{dn}{dt} &= \frac{\lambda}{\tau_n}(n_\infty(V)-n), \\ \frac{de}{dt} &= \frac{1}{\tau_e}(e_\infty(V)-e), \\ \frac{dc}{dt} &= -f_c\left(\alpha I_{Ca}+k_c c\right), \end{aligned} \tag{1.3}$$

where I_{Ca} is an inward Ca^{2+} current responsible for the upstroke of an action potential. The outward current I_K is a delayed rectifying current largely responsible for the downstroke of a spike whilst I_{BK} is a fast-activating large-conductance BK-type K^+ current that limits the upstroke and contributes to the downstroke of an action potential [**112**]. The small Ca^{2+}-activated K^+ current I_{SK} contributes to the patterning of spikes, rather than the actual spike dynamics and I_A is an A-type K^+ current that hyperpolarizes the membrane. The currents

are defined, via Ohm's law, by

$$\begin{aligned} I_{Ca} &= g_{Ca} m_\infty(V)(V - V_{Ca}), \\ I_K &= g_K n(V - V_K), \\ I_{BK} &= g_{BK} f_\infty(V)(V - V_K), \\ I_{SK} &= g_{SK} s_\infty(c)(V - V_K), \\ I_A &= g_A a_\infty(V) e(V - V_K). \end{aligned}$$

The steady state functions are given by

$$\begin{aligned} x_\infty(V) &= \left[1 + \exp\left(\frac{V_x - V}{s_x}\right)\right]^{-1}, \\ e_\infty(V) &= \left[1 + \exp\left(\frac{V - V_e}{s_x}\right)\right]^{-1}, \\ s_\infty(c) &= \frac{c^2}{c^2 + k_s^2}, \end{aligned}$$

where $x \in \{m, n, f, a\}$. The parameters V_x and s_x set the half-maximum location and the slope of the Boltzmann curve, respectively. Details of the parameters are listed in Table 1.1.

Table 1.1. System parameters for the pituitary lactotroph model (1.3)

Parameter	Value	Definition
C_m	$0 - 10$ pF	Membrane capacitance
g_{Ca}	2 nS	Maximal conductance of Ca^{2+} channels
V_{Ca}	50 mV	Reversal potential for Ca^{2+}
V_m	-20 mV	Voltage value at midpoint of m_∞
s_m	12 mV	Slope parameter of m_∞
g_K	$0 - 10$ nS	Maximal conductance of delayed rectifier K^+ channels
V_K	-75 mV	Reversal potential for K^+
V_n	-5 mV	Voltage value at midpoint of n_∞
s_n	10 mV	Slope parameter of n_∞
τ_n	30 ms	Time constant for n
λ	0.7	Parameter used to control spiking pattern
g_{BK}	$0 - 0.7$ nS	Maximum conductance of BK-type K^+ channels
V_f	-20 mV	Voltage value at midpoint of f_∞
s_f	5.6 mV	Slope parameter of f_∞
g_{SK}	1.7 nS	Maximum conductance of SK channels
k_s	0.5 μM	c at midpoint of s_∞
g_A	$0 - 25$ nS	Maximal conductance of A-type K^+ channels
V_a	-20 mV	Voltage value at midpoint of a_∞
s_a	10 mV	Slope parameter of a_∞
V_e	-60 mV	Voltage value at midpoint of e_∞
s_e	10 mV	Slope parameter of e_∞
τ_e	20 ms	Time constant of e
f_c	0.01	Fraction of free Ca^{2+} ions in cytoplasm
α	0.0015 μMfC^{-1}	Conversion from charge to concentration
k_c	0.16 ms^{-1}	Rate of Ca^{2+} extrusion

The model (1.3) represents a minimal biophysical interpretation for a pituitary lactotroph cell in which current flow across the membrane is due to charging of the membrane capacitance and movement of ions across ion channels. The main parameters of interest (i.e. that can be tuned experimentally) are the maximal conductance of delayed rectifier K^+ channels g_K, the maximum conductance of BK-type K^+ channels g_{BK} and the maximal conductance

of A-type K^+ channels g_A. System (1.3) can also be thought of as a model for the pituitary somatotroph, since lactotrophs and somatotrophs exhibit similar behaviours and the level of detail in the model is insufficient to distinguish the two.

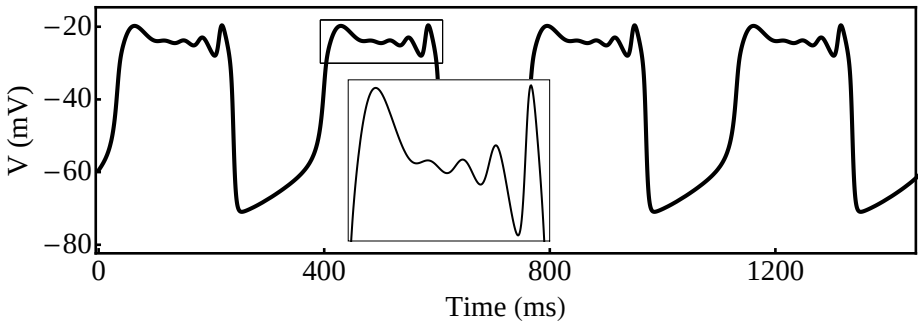

Figure 1.5. A typical pseudo-plateau burst or 1^4 MMO generated by system (1.3).

A typical (pseudo-plateau) burst generated by system (1.3) is shown in Figure 1.5. Such bursts are also known as mixed mode oscillations (MMOs). MMOs are oscillatory trajectories in which there is an alternation between large amplitude and small amplitude spiking. A prototypical MMO is composed of L large amplitude oscillations followed by s small amplitude oscillations. This is denoted L^s and called the MMO signature. A general MMO pattern then is just a concatenation of these MMO units resulting in a signature $L_1^{s_1} L_2^{s_2} \dots L_n^{s_n}$.

The pituitary lactotroph model (1.3) is capable of generating pseudo-plateau bursting (MMOs) over a range of parameter values. In most endocrine cell bursting models, the bursting oscillations are driven by the slow, systematic variation in the calcium concentration [**81, 121, 128, 146**]. Changes in the intracellular calcium concentration play a crucial role in the functioning of almost every cell type [**70**]. When the intracellular calcium concentration is fixed, the bursting ceases (Figure 1.6(a)). This is referred to in [**130**] as classic bursting. Unexpectedly, there are instances where the pseudo-plateau bursting persists almost unaltered when the calcium concentration is fixed [**130**] (Figure 1.6(b)). This is unusual since the slow variation of the intracellular calcium concentration is typically responsible for clustering impulses into episodes of electrical activity. We dub bursts driven by the calcium fluctuations *dynamic* bursts. We call those bursts that do not require the calcium fluctuations *calcium-conducting* bursts. Here, we use 'conducting' in the sense that the calcium oscillations follow the bursts rather than drive them.

We would like to understand the dynamic mechanisms that underlie the bursting, and how and why the bursts switch between dynamic and calcium-conducting MMOs. To facilitate our analysis, we first perform a 'dimensional analysis' of (1.3) to identify the time scales of the problem. The variables (V, n, e, c) vary on different time scales. To see this, we introduce a dimensionless time scale $t_I = t/k_t$ with reference time scale $k_t = \tau_e$, transforming (1.3) to

$$\begin{aligned}
\frac{C_m}{k_t\, g_{\max}} \frac{dV}{dt_I} \equiv \varepsilon \frac{dV}{dt_I} &= f(V, n, e, c), \\
\frac{dn}{dt_I} &= \frac{\lambda k_t}{\tau_n}(n_\infty(V) - n) \equiv g_1(V, n), \\
\frac{de}{dt_I} &= \frac{k_t}{\tau_e}(e_\infty(V) - e) \equiv g_2(V, e), \\
\frac{dc}{dt_I} &= -\frac{k_t}{(f_c k_c)^{-1}} \left(\frac{\alpha}{k_c} I_{Ca} + c \right) \equiv \delta\, h(V, c),
\end{aligned} \tag{1.4}$$

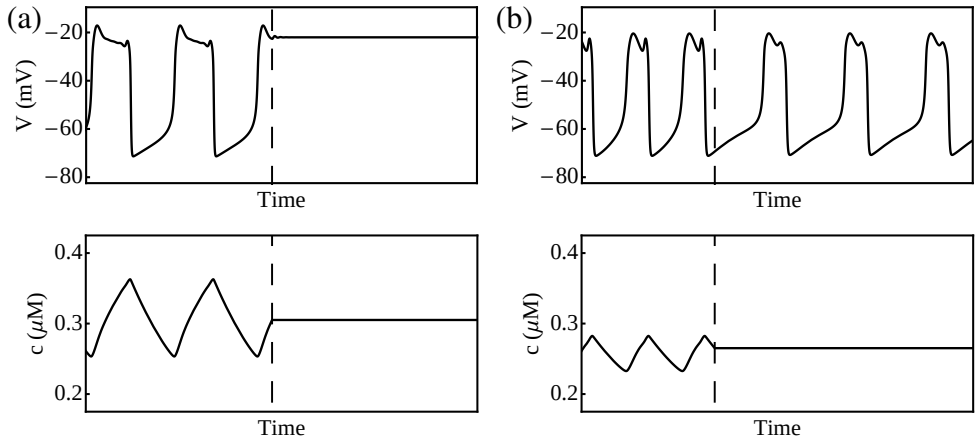

Figure 1.6. Time traces of the electrical activity and calcium concentration in (1.3) for (a) classic bursting, in which the slow changes in the calcium concentration drives the bursts and (b) 'novel' bursting, in which the calcium concentration is not driving the bursts but simply follows them. The parameters were set at $C_m = 2$ pF, $f_c = 0.01$, $g_{BK} = 0.4$ nS, $g_A = 10$ nS and (a) $g_K = 4$ nS or (b) $g_K = 6$ nS. The vertical dashed line marks the instant at which the calcium is fixed.

where $g_{\max} = 10$ nS is a typical conductance scale and

$$f(V, n, e, c) = -\frac{1}{g_{\max}} \left(I_{Ca} + I_K + I_{BK} + I_{SK} + I_A \right)$$

is a rescaled version of the right hand side of the V-equation of (1.3).

Remark 1.2. We avoid complete nondimensionalization as the V and c scalings have no influence on the timescales. This also allows easy comparison with experimental data.

The membrane potential V evolves on a fast timescale (given by $C_m/g_{\max} < 1$ ms to leading order) whilst (n, e) evolve on an intermediate timescale ($\tau_e = 20$ ms and $\tau_n/\lambda \approx 43$ ms). The calcium concentration evolves on a slow timescale ($\frac{1}{f_c k_c} = 625$ ms). In particular, decreasing C_m increases the timescale separation between V and (n, e, c), which is reflected in the small parameter $\varepsilon = \frac{C_m}{k_t g_{\max}} \ll 1$. Similarly, decreasing f_c increases the timescale separation between (V, n, e) and c, which is reflected in the small parameter $\delta = k_t f_c k_c \ll 1$, which is independent of ε. We will use (ε, δ) and (C_m, f_c) interchangeably since (ε, δ) have simple linear dependences on the biophysical parameters (C_m, f_c). Thus, system (1.4) is a singularly perturbed problem with fast variable V, intermediate variables (n, e), slow variable c and small, independent perturbation parameters (ε, δ).

1.3. Aims & Outline

In this thesis, we focus on MMOs in 3-timescale systems of the form

$$\begin{aligned} \varepsilon \, \dot{x} &= f(x, y, z), \\ \dot{y} &= g(x, y, z), \\ \dot{z} &= \delta \, h(x, y, z), \end{aligned} \tag{1.5}$$

where $0 < \varepsilon, \delta \ll 1$ are small, independent parameters, and f, g and h are sufficiently smooth functions. The variables (x, y, z) vary over different timescales with $x \in \mathbb{R}^m$ classified as fast, $y \in \mathbb{R}^n$ classified as intermediate and $z \in \mathbb{R}^k$ classified as slow. Such 3-timescale systems have received little attention [**67, 74, 75**] and are typically treated as 2-timescale problems, which is the natural setting for GSPT [**41, 68**]. However, the presence of two

perturbation parameters means that there are various ways in which the theory can be implemented (see Figure 1.7). One implementation uses ε as the singular perturbation parameter whilst keeping δ fixed. System (1.5) is then partitioned into a fast subsystem described by the x dynamics and a slow subsystem described by the (y, z) dynamics (1-fast/3-slow pathway of Figure 1.7). The more traditional viewpoint of (1.5), as outlined in Section 1.1, utilizes δ as the singular perturbation parameter with ε fixed, creating a family of fast (x, y) subsystems parametrized by the slow variable z (3-fast/1-slow pathway of Figure 1.7).

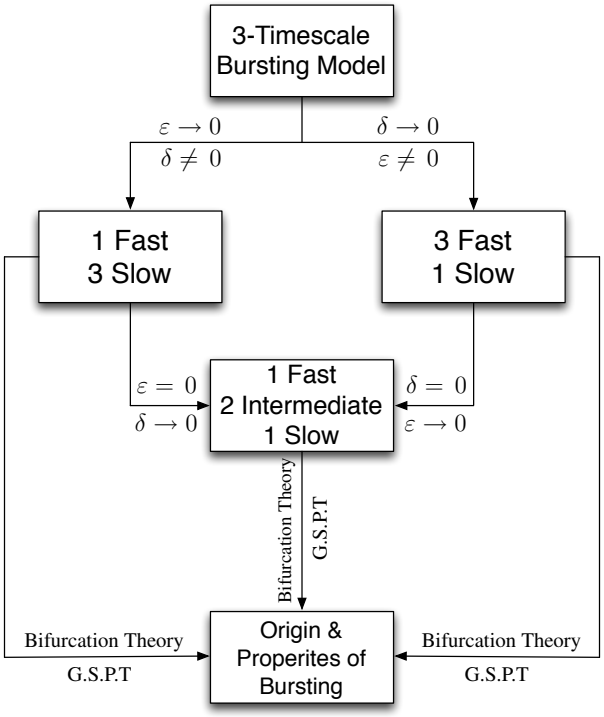

Figure 1.7. Schematic of the multiple geometric approaches to bursting in the context of the 4D, 3-timescale system (1.4), where $x = V \in \mathbb{R}$, $y = (n, e) \in \mathbb{R}^2$ and $z = c \in \mathbb{R}$.

There are multiple goals to this work. First and foremost, we wish to broaden the scope of GSPT by showing that elementary applications of the theory can be a powerful analytical tool in understanding 3-timescale problems. We compare the familiar 2-timescale methods with a 3-timescale analysis (1-fast/2-intermediate/1-slow pathway of Figure 1.7) and demonstrate the efficacy of each technique. In conjunction with this, we illustrate our assertions by analyzing the 3-timescale, 4D pituitary lactotroph model (1.4) [**121, 130**] and show that our multiple geometric viewpoints provide a fairly complete view of the dynamics. Physiologically, we are motivated by a desire to understand a complex neuroendocrine cell model. Mathematically, we are interested in the relationship between multiple analytical techniques.

The main contributions of this thesis are as follows. Firstly, we show that the pseudo-plateau bursting is a canard-induced MMO [**123, 134**]. Mixed mode oscillations have been described previously for neural models and data [**15, 33, 38, 39, 47, 74, 101, 103, 140**], but this is the first example where they form pseudo-plateau bursting oscillations. We then study the bifurcation sequences of canard-induced MMOs via return maps [**135**] in order to understand the dynamics of spike-adding in pseudo-plateau bursting. Our next major result is the extension of GSPT to 3-timescale problems of the form (1.5). In particular, we reconcile the different timescale decompositions (3-fast/1-slow and 1-fast/3-slow) in the 3-timescale context [**136**].

The key mathematical objects at the heart of our results are canards, which are special solutions of slow/fast systems that typically act as separatrices for the flow and organize the dynamics in phase space. Closely associated with folded singularities (degenerate fold bifurcations of the fast subsystem), canards of folded node type and folded saddle type have been studied extensively in $\mathbb{R}^3$ [**5, 49, 119, 140**]. The codimension-1 bifurcation that generates folded nodes and folded saddles is called folded saddle-node (FSN) and has been observed in various applications (including ours). There are two types of FSN and in either case, the local dynamics of the FSN are not well understood. Recent studies of the FSN type II have begun to unravel its dynamics [**20, 51, 76**], however, there are currently no results for the FSN type I. The main mathematical contribution of this thesis then is the extension of canard theory into the FSN type I regime. In particular, we prove the existence of canard (and faux canard) solutions, and study the delayed loss of stability near the FSN type I limit [**138**].

The outline of the thesis is as follows: In Chapter 2, we introduce the theoretical framework of GSPT with particular emphasis on canard theory. We describe the canard phenomenon, state the main results of canard theory and show how it can lead to MMOs. In Chapter 3, we examine the dynamics underlying the calcium-conducting bursts by taking the limit $\delta \to 0$ in (1.4) and studying the resulting singularly perturbed subproblem. We provide a detailed bifurcation analysis of the pseudo-plateau bursting in this subproblem and show that it is a canard-induced MMO. We then examine the bifurcation sequences of these MMOs by constructing a global return map. The canards act as separatrices in the return map, organizing the dynamics along the Poincaré section. Using the return map formulation, we study the bifurcation sequences involved in the creation and crossing of folded node type canards, which informs our geometric intuition of the bursting phenomenon.

In Chapter 4, we extend the results of Chapter 3 to $0 < \delta \ll 1$, explaining the difference between dynamic and calcium-conducting MMOs in the process. In particular, we use the lactotroph model (1.4) to demonstrate that the classic 3-fast/1-slow and novel 1-fast/3-slow analyses are different unfoldings of a 3-timescale system. We show that elementary applications of GSPT in the 2-timescale and 3-timescale methods provide us with substantial predictive power. We use that predictive power to explain the transient and long-term dynamics of (1.4). The analysis in Chapter 4 reveals that the FSN bifurcations (types I and II) are crucial and persistent features of bursting models. In Chapter 5, we analyze the local dynamics near the FSN type I, which is typically the organizing center for delay phenomena. By combining methods from GSPT (blow-up), and the theory of dynamic bifurcations (analytic continuation into the plane of complex time), we extend canard theory into the FSN I regime. We obtain results on the existence of canards in the FSN I limit and results on the associated delay effects. We conclude in Chapter 6 with a summary and discussion of the main results of the thesis, their implications and open questions.

CHAPTER 2

Geometric Singular Perturbation Theory & Canard Theory

The dynamics of bursting occurs over multiple timescales, alternating between periods of rapid oscillation and slow silent phases where the cell is hyperpolarized. The mathematical models that describe such burst phenomena are often singularly perturbed. Various analytic methods exist for dealing with such problems and one approach that has been used with great success is GSPT, which combines the power of asymptotic theory with dynamical systems techniques. In this chapter, we review the theoretical framework of the geometric singular perturbations approach with particular emphasis on canard theory. The theoretical foundation established here forms the basis of our results in subsequent chapters.

In Section 2.1, we state Fenichel's theorems, which are fundamental in the analysis of slow/fast systems. Fenichel theory is limited to normally hyperbolic manifolds. Normal hyperbolicity breaks down on folded critical manifolds and in Section 2.2, we examine features of such problems. The blow-up technique, which we outline in Section 2.3, is a desingularization procedure that extends Fenichel theory to nonhyperbolic problems. One of the great successes of the combined power of the blow-up technique and GSPT is the analysis of folds and canards. In Section 2.4, we give the results of a blow-up analysis of regular folds. We follow in Section 2.5 with the results of a blow-up analysis of canards, which is collectively known as canard theory. We take our local results and show in Section 2.6 how they can be used to construct global solutions (relaxation oscillations and MMOs). We follow in Section 2.7 with an outline of the numerical methods involved in the computation and continuation of invariant slow manifolds and canards.

2.1. Fenichel Theory

Many natural phenomena that vary over multiple timescales are described by singular perturbation problems of the form

$$\begin{aligned} \dot{x} &= g(x, z, \varepsilon), \\ \varepsilon\, \dot{z} &= f(x, z, \varepsilon), \end{aligned} \tag{2.1}$$

where $x \in \mathbb{R}^n$ is slow, $z \in \mathbb{R}^m$ is fast, t is the slow time, the overdot denotes derivatives with respect to t, $0 < \varepsilon \ll 1$ is a small perturbation parameter that measures the timescale separation (between x and z), and $f : \mathbb{R}^n \times \mathbb{R}^m \times \mathbb{R} \to \mathbb{R}^m$ and $g : \mathbb{R}^n \times \mathbb{R}^m \times \mathbb{R} \to \mathbb{R}^n$ are sufficiently smooth functions. A time rescaling $t = \varepsilon\, \tau$ gives an equivalent description of the dynamics

$$\begin{aligned} x' &= \varepsilon\, g(x, z, \varepsilon), \\ z' &= f(x, z, \varepsilon), \end{aligned} \tag{2.2}$$

where τ is the fast time, the prime denotes derivatives with respect to τ, and the trajectories of (2.1) trace out the same paths in phase space as those of (2.2) but at different speeds. The idea of GSPT is that, dynamically, the equations can be partitioned into slow and fast subsystems by taking the singular limit $\varepsilon \to 0$ on the slow and fast timescales, respectively. Taking the singular limit $\varepsilon \to 0$ in (2.1) gives the n-dimensional differential-algebraic system

called the *reduced system* (or *slow subsystem*)

$$\begin{aligned} \dot{x} &= g(x,z,0), \\ 0 &= f(x,z,0), \end{aligned} \tag{2.3}$$

which is an approximation of (2.1) wherein the fast variables move so rapidly they immediately settle to their equilibrium state defined by $f = 0$ (assuming it exists and is attracting). The singular limit $\varepsilon \to 0$ in (2.2) gives the m-dimensional *layer problem* (or *fast subsystem*)

$$\begin{aligned} x' &= 0, \\ z' &= f(x,z,0), \end{aligned} \tag{2.4}$$

which is an approximation of (2.2) wherein the slow variables move so slowly they are essentially fixed. GSPT uses the lower dimensional subproblems (2.3) and (2.4) to predict the dynamics of the full $(n+m)$-dimensional system (2.1) for $0 < \varepsilon \ll 1$. For an overview of GSPT, we refer to the reviews in [**60, 69**].

Any slow/fast analysis starts with a bifurcation analysis of the layer problem (2.4).

Definition 2.1. The *critical manifold* is the set of equilibria of the layer problem

$$S := \{(x,z) \in \mathbb{R}^n \times \mathbb{R}^m : f(x,z,0) = 0\}. \tag{2.5}$$

In general, S defines an n-dimensional manifold, i.e. the Jacobian $D_{(x,z)}f\big|_S$ has full rank. The critical manifold is arguably the most important object in the geometric singular perturbations approach and the classification of singularly perturbed systems is based on the properties of S as equilibria of the layer problem (2.4).

Definition 2.2. A subset S_0 of S is *normally hyperbolic* if all $(x,z) \in S_0$ are hyperbolic equilibria of the layer problem, i.e. the eigenvalues of the Jacobian $D_z f|_{S_0}$ are uniformly bounded away from the imaginary axis. A normally hyperbolic subset

(i) $S_a \subset S$ is *attracting* if all eigenvalues of $D_z f$ have negative real part for $(x,z) \in S_a$,
(ii) $S_r \subset S$ is *repelling* if all eigenvalues of $D_z f$ have positive real part for $(x,z) \in S_r$,
(iii) $S_s \subset S$ is of *saddle type* if it is neither attracting nor repelling.

Remark 2.1. A manifold is hyperbolic if the local linearization is structurally stable (i.e. the eigenvalues have non-zero real part), and it is normally hyperbolic if in addition, the expansion/contraction near the manifold in the transverse direction is stronger than in the tangential direction, as may be quantified using Lyapunov type measures [**63, 145**] for instance.

For normally hyperbolic critical manifolds $S_0 \subset S$, we have a uniform splitting of the eigenvalues of $D_z f$ along S_0 into two groups. That is, for each $p \in S_0$, the Jacobian $D_z f$ has m_u (m_s) eigenvalues with positive (negative) real part, where $m_u + m_s = m$. This leads to the following definition of local stable and unstable manifolds of the critical manifold S_0:

Definition 2.3. The *local stable and unstable manifolds of the critical manifold* S_0 denoted by $W^s_{\text{loc}}(S_0)$ and $W^u_{\text{loc}}(S_0)$, respectively, are the unions

$$W^s_{\text{loc}}(S_0) = \bigcup_{p \in S_0} W^s_{\text{loc}}(p), \qquad W^u_{\text{loc}}(S_0) = \bigcup_{p \in S_0} W^u_{\text{loc}}(p).$$

The manifolds $W^s_{\text{loc}}(p)$ and $W^u_{\text{loc}}(p)$ form a family of *fast fibers* (called a *fast fibration* or *foliation*) for $W^s_{\text{loc}}(S_0)$ and $W^u_{\text{loc}}(S_0)$, respectively, with *base points* $p \in S_0$. The dimension of $W^s_{\text{loc}}(S_0)$ is $n + m_s$ and the dimension of $W^u_{\text{loc}}(S_0)$ is $n + m_u$.

The geometric theory of slow/fast systems with normally hyperbolic critical manifolds is referred to as *Fenichel theory* [**41, 68**]. It is one of the fundamental tools in the analysis of singularly perturbed problems. Fenichel's theorems guarantee the persistence of a normally

hyperbolic manifold that is a small perturbation of S_0, and corresponding local stable and unstable manifolds close to $W^s_{\text{loc}}(S_0)$ and $W^u_{\text{loc}}(S_0)$ as follows:

Theorem 2.1 (Fenichel's Theorem 1 [41, 68]). *Consider system* (2.1) *with* $f, g \in C^\infty$. *Suppose* S_0 *is a compact normally hyperbolic manifold, possibly with boundary. Then for* $\varepsilon > 0$ *and sufficiently small, the following holds:*

(i) For any $r < \infty$, *there exists a* C^r*-smooth slow manifold* S^ε, *locally invariant under the flow of* (2.1), *that is* C^r $\mathcal{O}(\varepsilon)$ *close to* S_0.

(ii) For any $r < \infty$, *there exist* C^r*-smooth, locally invariant, stable and unstable manifolds*

$$W^s_{loc}(S^\varepsilon) = \bigcup_{p^\varepsilon \in S^\varepsilon} W^s_{loc}(p^\varepsilon), \qquad W^u_{loc}(S^\varepsilon) = \bigcup_{p^\varepsilon \in S^\varepsilon} W^u_{loc}(p^\varepsilon),$$

that are C^r $\mathcal{O}(\varepsilon)$ *close to* $W^s_{loc}(S_0)$ *and* $W^u_{loc}(S_0)$, *respectively.*

Remark 2.2. The slow manifold S^ε is generally non-unique, but all representations of S^ε lie $\mathcal{O}(e^{-K/\varepsilon})$ close to each other for some $K > 0$. That is, all r-jets are uniquely determined.

The price we pay for the approximation (2.4) is that the dynamics on S are trivial. To obtain a non-trivial flow, we turn to the reduced flow (2.3), which describes the slow motions along S. That is, S interfaces between the reduced and layer problems. The price we pay for the approximation (2.3) is that the flow is not defined off S. For normally hyperbolic critical manifolds S_0 (i.e. $D_z f|_{S_0}$ has full rank), the implicit function theorem implies that S_0 has local graph representation $z = h(x)$. That is, S_0 can be represented over a single coordinate chart given by the slow variable base $x \in \mathbb{R}^n$. The reduced flow (2.3) on S_0 then, is

$$\dot{x} = g(x, h(x), 0). \tag{2.6}$$

Fenichel theory guarantees the persistence of a slow flow on the slow manifold S^ε close to the reduced flow on S in the following way:

Theorem 2.2 (Fenichel's Theorem 2 [41, 68]). *Consider system* (2.1) *with* $f, g \in C^\infty$. *Suppose* S_0 *is a compact normally hyperbolic manifold, possibly with boundary. Then for* $\varepsilon > 0$ *and sufficiently small, Theorem 2.1(i) holds, and*

(iii) The slow flow on S^ε *converges to the reduced flow on* S_0 *as* $\varepsilon \to 0$.

Since S_0 is a graph $z = h(x)$, it follows that S^ε also has a graph representation $z^\varepsilon = h(x, \varepsilon)$ for $0 < \varepsilon \ll 1$. Thus, the slow flow on S^ε satisfies

$$\dot{x} = g(x, h(x, \varepsilon), \varepsilon), \tag{2.7}$$

and we are now dealing with a regular perturbation problem on S^ε, which is a remarkable result. Consequently, we have

Corollary 2.1. *Hyperbolic equilibria of the reduced problem* (2.6) *persist as hyperbolic equilibria of the full system* (2.1) *for sufficiently small* ε.

For $\varepsilon > 0$, the base points $p^\varepsilon \in S^\varepsilon$ of the fast fibers $W^s_{\text{loc}}(p^\varepsilon)$ and $W^u_{\text{loc}}(p^\varepsilon)$ evolve according to (2.7). Hence, the individual fast fibers $W^s_{\text{loc}}(p^\varepsilon)$ and $W^u_{\text{loc}}(p^\varepsilon)$ are not invariant, but the families of fibers $W^s_{\text{loc}}(S^\varepsilon)$ and $W^u_{\text{loc}}(S^\varepsilon)$ are invariant in the following sense:

Theorem 2.3 (Fenichel's Theorem 3 [41, 68]). *Consider system* (2.1) *with* $f, g \in C^\infty$. *Suppose* S_0 *is a compact normally hyperbolic manifold, possibly with boundary. Then for* $\varepsilon > 0$ *and sufficiently small, Theorem 2.1(ii) holds, and*

(iv) The foliation $\{W^s_{loc}(p^\varepsilon) : p^\varepsilon \in S^\varepsilon\}$ *is (positively) invariant, i.e.*

$$W^s_{loc}(p^\varepsilon) \cdot t \subset W^s_{loc}(p^\varepsilon \cdot t),$$

for all $t \geq 0$ *such that* $p^\varepsilon \cdot t \in S^\varepsilon$, *where* $\cdot t$ *denotes the solution operator of* (2.1).

(v) The foliation $\{W^u_{loc}(p^\varepsilon) : p^\varepsilon \in S^\varepsilon\}$ *is (negatively) invariant, i.e.*

$$W^u_{loc}(p^\varepsilon) \cdot t \subset W^u_{loc}(p^\varepsilon \cdot t),$$

for all $t \leq 0$ *such that* $p^\varepsilon \cdot t \in S^\varepsilon$*, where* $\cdot t$ *denotes the solution operator of* (2.1).

Theorem 2.3 implies that the exponential decay of a trajectory in the stable manifold $W^s(S^\varepsilon)$ towards its base point $p^\varepsilon \in S^\varepsilon$ is inherited from the unperturbed case. Similarly for a trajectory in the unstable manifold $W^u(S^\varepsilon)$, but in backward time. Formally:

Theorem 2.4 (Fenichel's Theorem 4 [41, 68]). *Let* $\alpha_s < 0$ *be an upper bound for the real part of the stable eigenvalues of the critical manifold* S_0*. There exists a constant* $\kappa_s > 0$*, so that if* $p^\varepsilon \in S^\varepsilon$ *and* $q^\varepsilon \in W^s_{loc}(p^\varepsilon)$*, then*

$$\|q^\varepsilon \cdot t - p^\varepsilon \cdot t\| \leq \kappa_s \exp(\alpha_s t),$$

for all $t \geq 0$*, such that* $p^\varepsilon \cdot t \in S^\varepsilon$*.*

Similarly, let $\alpha_u > 0$ *be a lower bound for the real part of the unstable eigenvalues of the critical manifold* S_0*. There exists a constant* $\kappa_u > 0$*, so that if* $p^\varepsilon \in S^\varepsilon$ *and* $q^\varepsilon \in W^u_{loc}(p^\varepsilon)$*, then*

$$\|q^\varepsilon \cdot t - p^\varepsilon \cdot t\| \leq \kappa_u \exp(\alpha_u t),$$

for all $t \leq 0$*, such that* $p^\varepsilon \cdot t \in S^\varepsilon$*.*

Remark 2.3. If we assume that $S_0 = S_a$ is an attracting normally hyperbolic manifold, then Fenichel theory implies that the dynamics of (2.1) are completely described (after some initial transient time) by the dynamics on the n-dimensional slow manifold S^ε, which to leading order, can be completely determined by the reduced flow on S_a.

In summary: Fenichel theory [**41, 68**] guarantees that normally hyperbolic invariant manifolds of equilibria of the layer flow (2.4) persist as locally invariant slow manifolds S^ε of the full system (2.1) for sufficiently small ε. Moreover, the restriction of the flow (2.1) to S^ε is an $\mathcal{O}(\varepsilon)$ smooth perturbation of the slow flow along S described by the reduced flow (2.3).

2.2. Folded Critical Manifolds

For normally hyperbolic critical manifolds, the geometric theory is fairly complete. However, Fenichel theory breaks down at points on the critical manifold where normal hyperbolicity is lost. The most common causes of loss of normal hyperbolicity are fold [**119**] and Hopf bifurcations [**91, 92, 113**] of (2.4), and points of self-intersection of S [**72**]. Often, these non-hyperbolic regions are of interest since they tend to generate complex dynamics.

Definition 2.4. The n-dimensional critical manifold S is *(locally) folded* if there exists a set L that forms an $(n-1)$-dimensional manifold in S, where

$$\begin{aligned} L := \{\, (x,z) \in S : \operatorname{rank}(D_z f)(x,z,0) = m-1, \\ v \cdot [(D^2_{zz} f)(x,z,0)(w,w)] \neq 0, v \cdot [(D_x f)(x,z,0)] \neq 0 \,\}, \end{aligned}$$

and v and w denote the left and right nullvectors of $D_z f$, respectively. The set L is the set of *fold points* of the critical manifold.

Folded critical manifolds are particularly common in applications and the dynamics around them have been carefully studied in the plane [**71, 73**] and in $\mathbb{R}^3$ [**119, 120, 140**]. For problems with $m > 1$ fast variables, the $(m-1)$ fast hyperbolic eigendirections do not alter the local dynamics significantly and the system can be reduced (via center manifold reduction) to an $(n+1)$-dimensional system [**14**]:

Theorem 2.5 (**Reduction Theorem [14, 143]**). *Consider system* (2.1) *with critical manifold* S. *Suppose* $(x_0, z_0) \in S$ *is such that* $D_z f(x_0, z_0, 0)$ *has a zero eigenvalue with algebraic multiplicity 1, and all other eigenvalues have negative real part. Then there exists an* $(n+1)$*-dimensional center manifold* W^C *with the following properties:*

(i) W^C *is tangent to the* $(n+1)$*-dimensional space spanned by the slow directions and the nullvector of* $D_z f(x_0, z_0)$.
(ii) W^C *is exponentially attracting.*
(iii) The vector field (2.1) *reduced to* W^C *has the form*

$$\begin{aligned} \dot{x} &= \tilde{g}(x, \tilde{z}, \varepsilon), \\ \varepsilon\, \dot{\tilde{z}} &= x_1(1 + \mathcal{O}(x, \tilde{z})) + \tilde{z}^2(1 + \mathcal{O}(x, \tilde{z})) + \varepsilon\, \mathcal{O}(x, \tilde{z}, \varepsilon) =: \tilde{f}(x, \tilde{z}, \varepsilon), \end{aligned} \tag{2.8}$$

where $x \in \mathbb{R}^n$ *and* $\tilde{z} \in \mathbb{R}$.

Remark 2.4. Theorem 2.5(iii) states that the point (x_0, z_0) corresponds to a saddle-node bifurcation of the layer problem of (2.8).

Thus, we restrict attention to $z \in \mathbb{R}$ and drop the tildes, in which case the fold points are

$$L = \{(x, z) \in S : f_z(x, z, 0) = 0, f_{zz}(x, z, 0) \neq 0, D_x f(x, z, 0) \neq 0\}, \tag{2.9}$$

where f is the right hand side of the z-equation in (2.8). The fold L divides the critical manifold into attracting sheets S_a (where $f_z < 0$) and repelling sheets S_r (where $f_z > 0$). Solutions of (2.4) flow along the 1D fast fibers $\{x \text{ constant}\}$ towards an attracting sheet S_a or away from a repelling sheet S_r. As before, the slow flow on S is described by the reduced vector field (2.3), which is (by definition) in the tangent bundle TS of S. The total time derivative of the algebraic constraint $f(x, z, 0) = 0$ gives

$$D_x f \cdot \dot{x} + f_z \dot{z} = 0,$$

which provides the definition for a tangent vector $(\dot{x}, \dot{z})$ of an integral curve $(x(t), z(t))$ to be constrained to the tangent bundle TS. This leads to the following representation of (2.3):

$$\begin{aligned} \dot{x} &= g(x, z, 0), \\ -f_z \dot{z} &= D_x f \cdot g(x, z, 0), \end{aligned} \tag{2.10}$$

where (2.10) is evaluated along (2.5). In many applications, S is a smooth manifold with an atlas containing overlapping charts, where each chart describes the local structure of the manifold. System (2.10) provides a representation of the original reduced problem (2.3) in any (local) coordinate chart on the manifold S.

For a folded critical manifold S, a (local) graph representation can be used to analyse the n-dimensional reduced problem (2.10). The difference from the normally hyperbolic case is that the slow variable base $x \in \mathbb{R}^n$ has to be replaced by a slow/fast variable base (see **[144]** for further details). The fold condition (2.9) together with the implicit function theorem imply that S has a local graph representation, say $x_1 = h(x_2, \ldots, x_n, z)$, which leads to the projection of the reduced problem (2.10) onto the coordinate chart $(x_2, \ldots, x_n, z) \in \mathbb{R}^n$:

$$\begin{aligned} \dot{x}_i &= g_i(x, z, 0), \qquad\qquad i = 2, \ldots, n, \\ -f_z \dot{z} &= D_x f \cdot g(x, z, 0). \end{aligned} \tag{2.11}$$

We observe that the reduced problem (2.11) is singular along the fold L, where $f_z = 0$.

Definition 2.5. *Regular fold points* $p \in L$ of the reduced flow (2.11) satisfy the *transversality condition* (or *normal switching condition*)

$$D_x f \cdot g\,|_{p \in L} \neq 0. \tag{2.12}$$

Geometrically, the condition $D_x f \cdot g = 0$ is a violation of transversality: the reduced flow on S projected onto the slow subspace is tangent to the fold. The non-degeneracy condition $f_{zz} \neq 0$ along L implies that f_z changes sign at the fold. Thus, in the neighbourhood of regular fold points, the flow is directed either towards or away from L. Solutions of (2.11) reach the fold L in finite (forward or backward) time where they cease to exist.

Desingularization (i.e. a time rescaling $dt = -f_z ds$) removes the singular term at the fold and gives the *desingularized system*

$$\begin{aligned} \dot{x}_i &= -f_z\, g_i(x, z, 0), \qquad i = 2, \ldots, n, \\ \dot{z} &= D_x f \cdot g(x, z, 0), \end{aligned} \tag{2.13}$$

where the overdot denotes differentiation with respect to s. System (2.13) is topologically equivalent (2.11) on S_a but has opposite orientation to (2.11) on S_r due to the time rescaling. Obviously, the desingularized system (2.13) is simpler to analyse than the reduced problem (2.11). The aim is to understand properties of (2.11) based on properties of (2.13).

Definition 2.6. *Ordinary singularities* of the desingularized problem (2.13) are defined by

$$E := \{(x, z) \in S : g(x, z, 0) = 0\}.$$

Folded singularities of the desingularized problem (2.13) are points along the fold L where the transversality condition (2.12) is violated:

$$M := \{(x, z) \in L : D_x f \cdot g(x, z, 0) = 0\}.$$

Remark 2.5. Generically (i.e. for $f_z \neq 0$), the ordinary singularities are equilibria of (2.11). By Corollary 2.1, the points of E are $\mathcal{O}(\varepsilon)$ close to hyperbolic equilibria of the full system.

Considered as equilibria of (2.13), folded singularities are classified according to their linearization. Note that for $n \geq 2$ slow variables, the linearization of (2.13) always has $n-2$ zero eigenvalues, the eigenvectors of which are tangent to the set M. The classification of folded singularities is based on the two remaining eigenvalues.

Definition 2.7. The linearization of (2.13) about a folded singularity has $n-2$ zero eigenvalues. Let λ_1, λ_2 denote the remaining eigenvalues. The folded singularity is a

- *Folded saddle* if $\lambda_1, \lambda_2 \in \mathbb{R}$ and $\lambda_1 \lambda_2 < 0$.
- *Folded saddle-node* if $\lambda_1, \lambda_2 \in \mathbb{R}$ and $\lambda_1 \lambda_2 = 0$.
- *Folded node* if $\lambda_1, \lambda_2 \in \mathbb{R}$ and $\lambda_1 \lambda_2 > 0$.
- *Degenerate folded node* if $\lambda_1, \lambda_2 \in \mathbb{R}$ and $\lambda_1 = \lambda_2$.
- *Folded focus* if $\lambda_1, \lambda_2 \in \mathbb{C}$.

Remark 2.6. Folded saddles, folded nodes and folded foci are generic singularities of M. Their reduced flows are locally topologically equivalent to those shown in Figure 2.1. The sets of folded saddle-nodes and degenerate folded nodes are codimension-1 subsets of M. Folded saddles, folded saddle-nodes and folded nodes are also known as canard points [**119**].

Folded singularities are not equilibria of the reduced system (2.11) but are points where the right hand side of the z-equation vanishes. That is, they are points of (2.11) where there is potentially a cancellation of a simple zero and trajectories of the reduced flow may pass through the folded singularity with finite speed. This allows solutions to cross the fold L in finite time and move from one sheet of the critical manifold to another (of opposite stability), leading to the notion of canards [**119, 140, 143**]:

Definition 2.8. Solutions of the reduced problem (2.11) passing through a canard point from an attracting manifold S_a to a repelling manifold S_r are called *singular canards*. Solutions of the reduced problem (2.11) passing through a canard point from a repelling manifold S_r to an attracting manifold S_a are called *singular faux canards*.

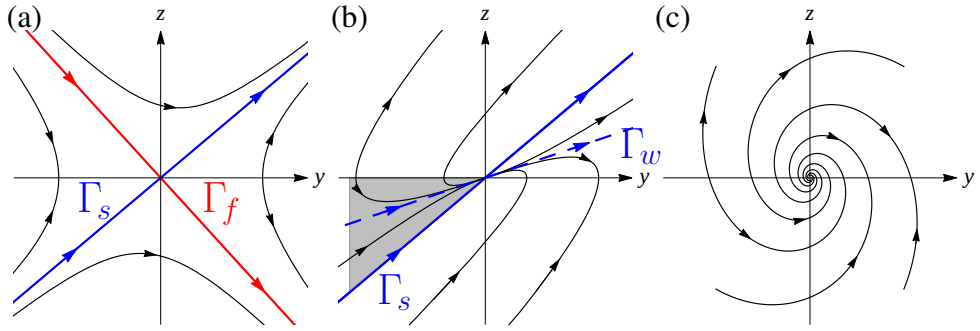

Figure 2.1. Reduced flow with (a) folded saddle, (b) folded node, and (c) folded focus at the origin projected onto a slow/fast variable base (y, z). The fold L is the (slow) y-axis. S is attracting for $z < 0$ and repelling for $z > 0$. The folded saddle has singular canard Γ_s and singular faux canard Γ_f. The folded node has a sector (shaded) of singular canards enclosed by the singular strong canard Γ_s and the fold. The singular canards pass through the folded node tangent to the singular weak canard Γ_w. The folded focus has no singular canards.

The folded saddle has a singular canard and a singular faux canard, corresponding to the stable and unstable eigendirections of the folded saddle, respectively. The folded node has strong and weak eigendirections. The unique trajectory tangent to the strong eigendirection is called the strong canard. Every trajectory that starts inside the trapping region enclosed by the strong canard and by the fold is filtered into the folded node, and is a singular canard.

Definition 2.9. The strong canard together with the $(n-1)$-dimensional set of fold points L bounds a sector in S_a, called the *singular funnel*. Every trajectory starting in the singular funnel reaches the set of folded nodes in finite time and subsequently crosses L transverse to S_r in the direction tangent to the weak stable eigenvector of the corresponding folded node.

Remark 2.7. Trajectories that start on the strong canard in S_a reach the folded node in finite time but cross it tangent to the strong stable eigenvector of the folded node.

Lemma 2.1. *All folded singularities, except the folded focus, possess singular canards or singular faux canards.*

Singular canards and their persistence under small perturbations are the subject of canard theory (see Section 2.5). Canards have been studied extensively using various methods such as nonstandard analysis [**5, 29**], matched asymptotic expansions [**37, 87**] and geometric desingularization, i.e. blow-up [**73, 119, 140, 143**]. In planar slow/fast systems, canards are degenerate and only occur in an exponentially small parameter window [**30, 36, 73**]. The addition of a second slow variable makes the canards generic and robust and these have been classified and analyzed in [**119, 139, 140**]. The remarkable insight of [**143**] is that (to leading order) the dynamics near generic canards for $n > 2$ slow variables is precisely described by the canard theory for two slow variables:

Theorem 2.6. *Suppose* (2.8) *possesses folded singularities p of either saddle or node type. Then there exists a smooth change of coordinates that brings* (2.8) *to the canonical form*

$$\begin{aligned}
\dot{x_1} &= \frac{1}{2}\mu(x_3,\ldots,x_n)x_2 - (1+\mu(x_3,\ldots,x_n))\,z + \mathcal{O}\left(x_1,\varepsilon,(x_2+z)^2\right),\\
\dot{x_2} &= 1+\mathcal{O}(x_1,x_2,z,\varepsilon),\\
\dot{x_j} &= a_j + g_{j,1}(x_3,\ldots,x_n) + \mathcal{O}(x_1,x_2,z,\varepsilon), \qquad j=3,\ldots,n,\\
\varepsilon\,\dot{z} &= x_1(1+z\mathcal{O}(x_2,\ldots,x_n)) + z^2(1+\mathcal{O}(x_1,z)) + \varepsilon\,\mathcal{O}(x_1,x_2,z,\varepsilon),
\end{aligned} \tag{2.14}$$

where the a_j are constants, $g_{j,1}(0,\ldots,0)=0$ and $\mu(x_3,\ldots,x_n)$ denotes the eigenvalue ratio of the folded singularity p, regarded as an equilibrium of the desingularized system.

Corollary 2.2. *The local $(n+1)$-dimensional flow past the set of folded singularities M is described to leading order by the 3D system*

$$\begin{aligned} \dot{x_1} &= \frac{1}{2}\mu(x_3,\ldots,x_n)x_2 - (1+\mu(x_3,\ldots,x_n))\,z, \\ \dot{x_2} &= 1, \\ \dot{z} &= x_1 + z^2, \end{aligned} \tag{2.15}$$

where $(x_3,\ldots,x_n)$ and hence $\mu = \mu(x_3,\ldots,x_n)$ are parameters.

Remark 2.8. Corollary 2.2 is obtained by rescaling system (2.14) by (and dropping the bars)

$$x_1 = \varepsilon\,\overline{x}_1, \quad x_2 = \sqrt{\varepsilon}\overline{x}_2, \quad z = \sqrt{\varepsilon}\overline{z}, \quad t = \sqrt{\varepsilon}\,\overline{t}. \tag{2.16}$$

This represents an $\mathcal{O}(\sqrt{\varepsilon})$ zoom of (2.14) in the (x_1,x_2,z)-space transverse to M. The rescaling converts the singular perturbation problem (2.14) into a regular perturbation problem, which is governed to leading order by the limiting system (2.15).

System (2.15) is the canonical form for folded saddles/nodes of singular perturbation problems with $n=2$ in an $\mathcal{O}(\sqrt{\varepsilon})$ neighbourhood of the folded singularity [**5, 14, 140**]. Thus, for systems with $n>2$ slow variables, a model reduction to two slow variables is (in principle) not necessary to identify canard-induced phenomena. Consequently, to describe the canard phenomenon, we invoke Theorem 2.5, Theorem 2.6 and Corollary 2.2 to restrict our treatment to slow/fast systems in $\mathbb{R}^3$. That is, to study the local dynamics near a folded singularity of node or saddle type, it suffices to consider (cf. system (2.14)):

Proposition 2.1 (**Folded Node/Folded Saddle Normal Form [5, 14, 140]**). *Suppose* (2.8) *with $n=2$ has a folded node/folded saddle at the origin, and that the other fold points are regular. Then there exists a smooth change of coordinates, which brings* (2.8) *to the form*

$$\begin{aligned} \dot{x} &= \frac{1}{2}\mu y - (\mu+1)z + \mathcal{O}(x,\varepsilon,(y+z)^2), \\ \dot{y} &= 1 + \mathcal{O}(x,y,z,\varepsilon), \\ \varepsilon\,\dot{z} &= x + z^2 + \mathcal{O}(z^3, xz^2, xyz, \varepsilon(x+y+z), \varepsilon^2), \end{aligned} \tag{2.17}$$

in a neighbourhood of the origin, where $\lambda_1 = -\mu \in \mathbb{R}$ and $\lambda_2 = -1$ correspond to the eigenvalues of the linearization of the desingularized flow of (2.17).

Remark 2.9. The folded singularity at the origin is saddle type for $\mu<0$ (Figure 2.2(a)) and node type for $\mu>0$ (Figure 2.2(b)). For general slow/fast systems (2.1), μ is the eigenvalue ratio of the folded singularity. A description of the dynamics around the folded saddle-node ($\mu=0$) requires consideration of higher order terms in (2.17) (see Section 2.5).

Note that (2.16) is related to the blow-up transformation. The blow-up technique facilitates the analysis of slow/fast systems in regions where normal hyperbolicity fails. Given its importance, we devote the next section to a description of the procedure.

2.3. The Blow-Up Technique

Fenichel theory [**41, 68**] breaks down when normal hyperbolicity is lost, which occurs frequently in applications (regular fold and canard points being prime examples). The key insight of [**36**] is that the blow-up technique [**35, 102**] is the right tool to desingularize and hence analyze folds in S. In this section, we outline the blow-up technique in the context of (2.17). For a rigorous formulation in a general setting, we refer to [**22, 35, 102**]. The blow-up technique is a procedure that takes a nilpotent equilibrium and restores enough hyperbolicity

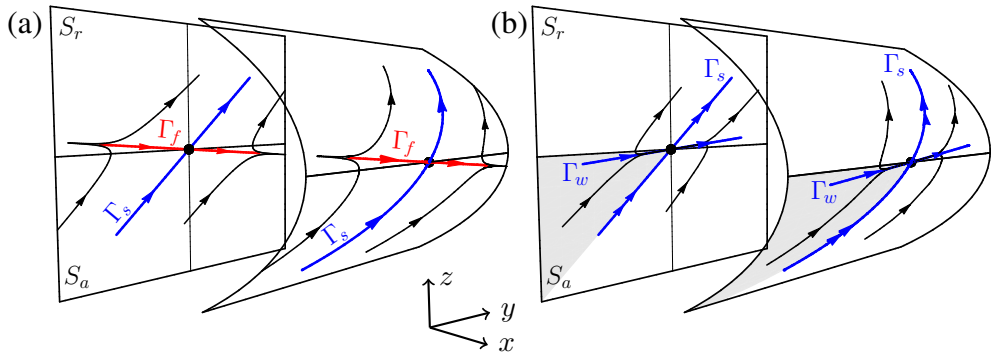

Figure 2.2. Reduced flow of (2.17) on the critical manifold S along with its projection into the (y, z)-plane for the (a) folded saddle and (b) folded node. The fold curve is given by the y-axis. All trajectories in the funnel (shaded) of the folded node are singular canards.

that a complete analysis can be done via standard dynamical systems techniques [**46, 34**]. We rewrite (2.17) on the fast timescale ($\tau = t/\varepsilon$) as the extended system in $\mathbb{R}^4$

$$\{(2.17), \varepsilon' = 0\}, \tag{2.18}$$

i.e. we include the trivial equation for ε. In this extended phase space, the set $S \times \{0\}$ is a manifold of equilibria. Away from the fold curve L, the linearization of (2.18) along $S_a \times \{0\}$ has a triple zero eigenvalue and one negative eigenvalue.

Remark 2.10. The slow manifolds $S_a^\varepsilon, S_r^\varepsilon$ are obtained as sections $\varepsilon =$ constant of 3D, locally invariant, center-like manifolds M_a, M_r of the extended system (2.18).

The linearization of (2.18) along L has a quadruple zero eigenvalue, i.e. the fold curve is a set of degenerate equilibria of (2.18). Let X denote the vector field (2.18), and suppose that $X(0) = 0$ and $f_z(0, 0, 0, 0) = 0$ so that the origin is a nilpotent equilibrium where f denotes the right hand side of the z equation in (2.17). We define two kinds of blow-up transformation: one for regular folds and one for folded singularities.

Definition 2.10. The *cylindrical blow-up* $\Phi_L : B_{L,0} \subset B_L \to \mathbb{R}^4$ is the mapping

$$\Phi_L(\overline{x}, \overline{y}, \overline{z}, \overline{\varepsilon}, \overline{r}) = (\overline{r}^{\alpha_1}\overline{x}, \overline{y}, \overline{r}^{\alpha_3}\overline{z}, \overline{r}^{\alpha_4}\overline{\varepsilon}),$$

where $B_L = \mathbb{S}^2 \times \mathbb{R} \times \mathbb{R}$, $B_{L,0} = \mathbb{S}^2 \times \mathbb{R} \times [-r_0, r_0]$, $r_0 > 0$ with weights $(\alpha_1, \alpha_3, \alpha_4) \in \mathbb{N}^3$. That is, the y-axis is blown-up by Φ_L to a cylinder with

$$\overline{x}^2 + \overline{z}^2 + \overline{\varepsilon}^2 = 1.$$

The *spherical blow-up* $\Phi_M : B_{M,0} \subset B_M \to \mathbb{R}^4$ is the mapping

$$\Phi_M(\overline{x}, \overline{y}, \overline{z}, \overline{\varepsilon}, \overline{r}) = (\overline{r}^{\alpha_1}\overline{x}, \overline{r}^{\alpha_2}\overline{y}, \overline{r}^{\alpha_3}\overline{z}, \overline{r}^{\alpha_4}\overline{\varepsilon}),$$

where $B_M = \mathbb{S}^3 \times \mathbb{R}$, $B_{M,0} = \mathbb{S}^3 \times [-r_0, r_0]$, $r_0 > 0$ with weights $(\alpha_1, \alpha_2, \alpha_3, \alpha_4) \in \mathbb{N}^4$. That is, the origin is blown-up by Φ_M to a 3-sphere with

$$\overline{x}^2 + \overline{y}^2 + \overline{z}^2 + \overline{\varepsilon}^2 = 1.$$

Remark 2.11. The spherical blow-up 'inflates' a nilpotent equilibrium to a 3-sphere and is used for the analysis of folded singularities. For regular folds, there is no distinguished point on L and all points on L have to be treated simultaneously to obtain uniform results, hence why there is no rescaling of y in the cylindrical blow-up.

The map Φ_M is surjective and proper since it maps the 3-sphere $Z_M = \mathbb{S}^3 \times \{0\}$ to the origin. The map Φ_L is surjective and proper since it maps the cylinder $Z_L = \mathbb{S}^2 \times \mathbb{R} \times \{0\}$ to the y-axis. Let Φ denote the cylindrical or spherical blow-up. The restriction $\Phi|_{B \setminus Z}$ is

a diffeomorphism from $B\backslash Z$ to $\mathbb{R}^4\backslash\{0\}$ (spherical blow-up) or to $\mathbb{R}^3\backslash\{0\}\times\mathbb{R}$ (cylindrical blow-up). The map Φ defines the induced map $\Phi_* : TB \to T\mathbb{R}^4$ between the associated tangent bundles.

The map Φ induces a vector field $\overline{X}$ on B such that $\Phi_*\overline{X} = X$. It suffices to study $\overline{X}$ on B_0 since $\Phi(B_0)$ is a full neighbourhood of the origin. For the analysis of $\overline{X}$ on B_0, we make use of coordinate charts (to make the calculations as simple as possible), leading to the notion of directional blow-ups.

Definition 2.11. *Directional blow-ups* $\Phi_i, i = 1, 2, \ldots, 2m$ are obtained by setting one blown-up variable on $\mathbb{S}^{m-1}$ to ± 1 in the definition of Φ ($m = 4$ for spherical and $m = 3$ for cylindrical). The *directional charts* $\kappa_i : B_i \to \mathbb{R}^4$ are homeomorphic maps such that $B = \bigcup_i B_i$. In chart κ_i the blown-up vector field $\overline{X}$ is described by a vector field X_i.

Remark 2.12. The directional charts κ_i cover the 3-sphere (cylinder) by planes perpendicular to the axes. In practice, not all directional charts are needed for a complete analysis.

In singular perturbation problems, the most important chart is the *classical* or *rescaling* chart κ_2, corresponding to $\overline{\varepsilon} = 1$ in the blow-up. The associated directional blow-up is an ε-dependent rescaling of the variables since $\overline{r} = \varepsilon^{-\alpha_4}$.

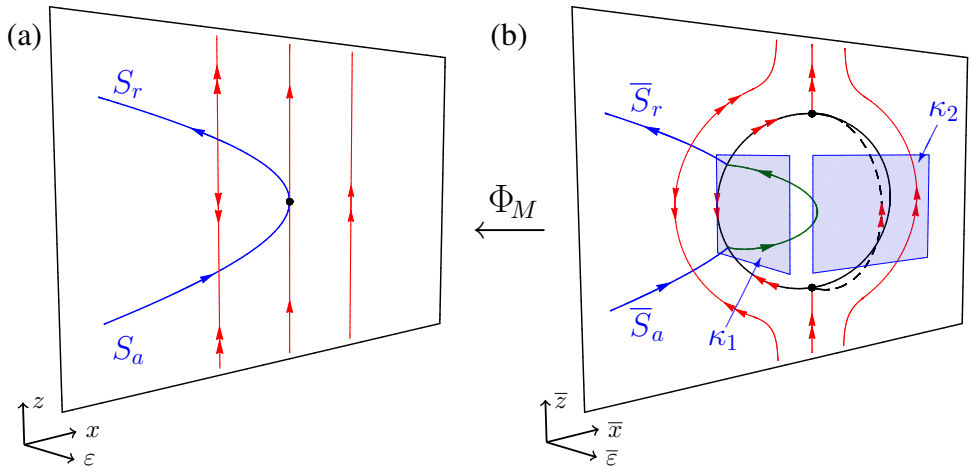

Figure 2.3. The spherical blow-up transformation Φ_M for a folded singularity (node or saddle) projected onto $y = 0$. (a) Fast fibers of the layer problem are indicated by the red lines (double arrow), and the folded singularity (black dot) is at the origin. (b) The folded singularity is blown up to a sphere. Chart κ_1 covers the incoming and outgoing flow on the blown-up sphere. The rescaling chart κ_2 covers the flow on the blown-up sphere.

Definition 2.12. A *local vector field* X is defined on a compact smooth manifold B by a finite open covering $\{B_i\}$ of B with some smooth vector field X_i on each B_i, such that for each pair of indices $i, j \in I$ with $B_i \cap B_j \neq \emptyset$, there exists a strictly positive, smooth function g_{ij} defined in $B_i \cap B_j$ such that $X_i = g_{ij}X_j$ on $B_i \cap B_j$.

Definition 2.13. Let $\{B_i\}$ be a finite open covering of B, on which local vector fields X and $\tilde{X}$ are given by X_i and $\tilde{X}_i$. Then $\tilde{X}$ is the result of *local division* of X if there exist smooth functions $f_i : B_i \to \mathbb{R}$ such that $X_i = f_i\tilde{X}_i$ in B_i.

Remark 2.13. The functions f_i tend to be polynomials in r_i, which vanish on the 3-sphere $\mathbb{S}^3 \times \{0\}$ or the cylinder $\mathbb{S}^2 \times \mathbb{R} \times \{0\}$ (where the blow-up fails to be a diffeomorphism). In that regard, local division consists of dividing out powers of r_i, leading to vector fields $\tilde{X}_i$ and X_i with the same phase portraits for $r_i > 0$. However, on $r_i = 0$, $\tilde{X}_i$ may show nontrivial dynamics that were hidden in X_i, thus validating the blow-up procedure.

The choice of weights, which is problem dependent, is guided by the requirements:

(i) Local division is possible to obtain the vector fields $\tilde{X}_i$.
(ii) The vector fields $\tilde{X}_i$ only have hyperbolic or semi-hyperbolic equilibria.
(iii) The dynamics in the planes $r_i = 0$ can be analysed.
(iv) Perturbation methods can be used to obtain the dynamics for $r_i > 0$.

We summarize the blow-up technique in the following:

Definition 2.14. A *desingularization* of vector field X in $\mathbb{R}^4$ with nilpotent equilibrium $X(0) = 0$ is a blow-up transformation $\Phi : B \to \mathbb{R}^4$ with suitable weights $(\alpha_1, \alpha_2, \alpha_3, \alpha_4)$ such that for all local vector fields X_i induced by Φ and any point $p \in Z_i$ with $\tilde{X}_i(p) = 0$, where $\tilde{X}_i$ is a result of local division of X_i, p is a hyperbolic or semi-hyperbolic singularity of $\tilde{X}_i$.

Remark 2.14. The blow-up technique is an iterative process, so that if any nilpotent equilibria remain after one blow-up, additional blow-ups can be used to desingularize these points. Moreover, if X satisfies a Lojasiewicz inequality, then only a finite sequence of blow-ups is needed to make all singularities either hyperbolic or semi-hyperbolic [**35**].

It is important to be able to connect the dynamics in different coordinate charts. To this end, we require coordinate changes that move between charts.

Definition 2.15. The change of coordinates between two charts κ_i and κ_j is defined as

$$\kappa_{ji} := \kappa_j \circ \kappa_i^{-1}.$$

2.4. The Regular Fold

We now state the results of a blow-up of regular folds [**71, 120**]. Consider (2.17) with $\mu < 0$ so that the reduced flow is directed towards L for $y < 0$ and away from L for $y > 0$ (Figure 2.2(a)). We restrict attention to a neighbourhood of L for $y < 0$ where all fold points are regular and orbits on S reach L in finite time. The only possibility to continue from there (in the singular limit) is along the weakly unstable fiber of the layer flow. The goal is to track S_a^ε and S_r^ε as they pass close to L. Note that results for $y > 0$ are obtained by time reversal.

We blow-up (a segment of) the fold curve to a cylinder $\mathbb{S}^2 \times I \times \mathbb{R}$, with $(\overline{x}, \overline{z}, \overline{\varepsilon}) \in \mathbb{S}^2$, $\overline{y} \in I$ and $\overline{r} \in \mathbb{R}$. The cylindrical blow-up transformation Φ_L in this case is

$$x = \overline{r}^2\overline{x}, \quad y = \overline{y}, \quad z = \overline{r}\overline{z}, \quad \varepsilon = \overline{r}^3\overline{\varepsilon}.$$

The only directional charts needed in the analysis of the blown-up vector field are the entry chart κ_1 defined by $\overline{x} = -1$ for the incoming flow, the classical chart κ_2 for the flow on the cylinder, and the exit chart κ_3 defined by $\overline{z} = 1$ for the outgoing flow.

Remark 2.15. The blow-up converts the singular perturbation problem to a regular perturbation problem. In chart κ_2, the unperturbed system boils down to the Riccati equation

$$z_2'' - 2z_2z_2' = \frac{1}{2}\mu y_2,$$

where $y_2 < 0$ is a parameter, which is a local canonical form for regular folds [**71, 87, 120**].

For small positive ρ and suitable rectangles $J_1, J_2 \in \mathbb{R}^2$, let

$$\Sigma_{\text{in}} := \left\{(-\rho^2, y, z) : (y, z) \in J_1\right\}, \quad \Sigma_{\text{out}} := \left\{(x, y, \rho) : (x, y) \in J_2\right\},$$

be sections transverse to S_a and the fast fibers, respectively. Let $\Pi_L : \Sigma_{\text{in}} \to \Sigma_{\text{out}}$ be the transition map for the flow of (2.17).

Theorem 2.7 (Flow past 2D regular fold [120]). *For the regular fold, there exist $\rho > 0$ and $\varepsilon_0 > 0$ such that for $\varepsilon \in (0, \varepsilon]$:*

(i) There exists an interval I_{out} such that for $y \in I_{out}$, the slow manifold S_a^ε intersects Σ_{out} in a smooth curve, which is a graph, i.e. $x_{out} = h_{out}(y_{out}, \varepsilon)$.

(ii) The section Σ_{in} is mapped to an exponentially thin strip around $S_a^\varepsilon \cap \Sigma_{out}$, i.e. its width in the x-direction is $\mathcal{O}(\exp(-c/\varepsilon))$, where c is a positive constant.

(iii) The map $\Pi_L : \Sigma_{in} \to \Sigma_{out}$ has the form

$$\Pi_L \begin{pmatrix} y \\ z \end{pmatrix} = \begin{pmatrix} h_{out}(G_L(y, z, \varepsilon), \varepsilon) + \mathcal{O}(\exp(-c/\varepsilon)) \\ G_L(y, z, \varepsilon) \end{pmatrix},$$

where $h_{out}(G_L(y, z, \varepsilon), \varepsilon) = \mathcal{O}(\varepsilon^{2/3})$ and $G_L(y, z, \varepsilon) = G_{L,0}(y) + \mathcal{O}(\varepsilon \ln \varepsilon)$. The function $G_{L,0}(y) = y + \mathcal{O}(\rho^3)$ is induced by the reduced flow on S_a from Σ_{in} to L.

Remark 2.16. Theorem 2.7 shows that solutions leave a neighbourhood of the regular fold via fast directions $\mathcal{O}(\varepsilon^{2/3})$ close to the corresponding weakly unstable fiber of the layer problem. As such, regular fold points are also known as jump points.

2.5. Canard Theory

We consider (2.17) once again, this time blowing-up the folded singularity at the origin in order to prove the persistence of singular canards under small perturbations and study their properties. The spherical blow-up transformation Φ_M for folded nodes/saddles is [**119, 140**]

$$x = \overline{r}^2 \overline{x}, \quad y = \overline{r}\overline{y}, \quad z = \overline{r}\overline{z}, \quad \varepsilon = \overline{r}^2 \overline{\varepsilon},$$

with $(\overline{x}, \overline{y}, \overline{z}, \overline{\varepsilon}) \in \mathbb{S}^3$. It suffices to consider the directional chart κ_1 (given by $\overline{x} = -1$) and the classical chart κ_2 (see Figure 2.3(b)). In the rescaling chart κ_2, the singular perturbation problem is transformed into a regular perturbation problem with leading order dynamics ($r_2 = 0$) governed precisely by system (2.15), with $(x_1, x_2, z, \mu(x_3, \ldots, x_n))$ of (2.15) replaced by (x_2, y_2, z_2, μ). The following observation [**5**] is crucial:

Lemma 2.2. *System* (2.15) *has, for $\mu \neq 0$, two explicit algebraic solutions:*

$$\gamma_1 = \left(-\frac{\mu^2}{4}t^2 + \frac{\mu}{2}, t, \frac{\mu}{2}t \right), \quad \gamma_2 = \left(-\frac{1}{4}t^2 + \frac{1}{2}, t, \frac{1}{2}t \right),$$

where γ_1 and γ_2 correspond to the eigenvalues $\lambda_1 = -\mu$ and $\lambda_2 = -1$, respectively.

Remark 2.17. The projections of the special solutions (γ_1, γ_2) into the (y_2, z_2) plane coincides with the eigendirections at the origin of the singular canards. Note that (2.15) can be rewritten as a second-order inhomogeneous differential equation

$$z_2'' - 2z_2 z_2' + (1 + \mu)z_2 = \frac{1}{2}\mu t, \tag{2.19}$$

which serves as a local normal form for generic canard problems in slow/fast systems [**143**].

The importance of the special solutions (γ_1, γ_2) is that they connect the attracting slow manifold across the 'upper half' ($\overline{\varepsilon} > 0$) of $\mathbb{S}^3$ to the repelling slow manifold or vice versa. Thus, (γ_1, γ_2) are viewed as extensions of the singular canards. The chart κ_1 is used to connect the unbounded branches of (γ_1, γ_2) with the singular canards of the reduced problem.

We are now in a position to state the existence and bifurcation theorems that form the theoretical framework of canard theory. We begin by defining canard solutions away from the singular limit. Recall that the slow manifolds are non-unique (but exponentially close).

Definition 2.16. For a fixed choice of slow manifolds, a *maximal canard* is a solution of (2.17) that corresponds to the intersection of S_a^ε and S_r^ε, extended by the flow of (2.17) into the neighbourhood of the folded singularity.

Remark 2.18. A maximal canard defines a family of canards nearby which are exponentially close to the maximal canard (which reflects the non-uniqueness of S_a^ε and S_r^ε). In the singular limit, such a family of canards is represented by a unique singular canard.

2.5.1. Folded Node Canards. Consider (2.17) in the folded node case with real, negative eigenvalues $\lambda_s < \lambda_w < 0$. In our formulation, we take $\mu = \lambda_w/\lambda_s$ so that $0 < \mu < 1$ for folded nodes. There are two kinds of results concerning folded node type canards: existence of maximal canards and rotational properties.

Theorem 2.8 (**Existence of Maximal Canards** [**14, 119, 140, 143**])**.** *Suppose system* (2.17) *has a folded node with* $0 < \mu < 1$*. Then for* $0 < \varepsilon \ll 1$ *and* μ *bounded away from zero:*

(i) The singular strong canard perturbs to a maximal canard γ_0*, called the* primary strong canard*.*
(ii) If $\mu^{-1} \notin \mathbb{N}$*, the singular weak canard perturbs to a maximal canard* γ_w*, called the* primary weak canard*.*
(iii) If $2k+1 < \mu^{-1} < 2k+3, k \in \mathbb{N}$ *and* $\mu^{-1} \neq 2k+2$*, then there exist* k *additional maximal canards* $\gamma_j, j = 1, 2, \ldots, k$*, positioned between* γ_0 *and* γ_w *called* secondary canards*, which are* $\mathcal{O}(\varepsilon^{(1-\mu)/2})$ *close to* γ_0 *at* $\mathcal{O}(1)$ *distances from the fold curve* L*.*
(iv) The secondary canards bifurcate from the primary weak canard in a transcritical bifurcation for odd $\mu^{-1} \in \mathbb{N}$*.*

Remark 2.19. Theorem 2.8(i)–(ii) follows by extending the slow manifolds along the special solutions (γ_1, γ_2). For $\mu^{-1} \notin \mathbb{N}$, the manifolds intersect transversally, so their intersection persists under small perturbations [**119**]. Theorem 2.8(iii)–(iv) follows from applications of Melnikov theory [**140**].

When the non-resonance condition $\mu^{-1} \notin \mathbb{N}$ is violated, secondary canards bifurcate from the weak canard leading to additional rotational sectors [**140**] (see Theorem 2.8 and [**52, 135**] for numerical examples). More precisely, there is a pitchfork bifurcation of canards for even μ^{-1} and there is a transcritical bifurcation of canards for odd μ^{-1}. One branch of the transcritical bifurcation and the two branches of the pitchfork bifurcation only exist in a very small neighbourhood of $\mu^{-1} \in \mathbb{N}$. The only persistent branch of secondary canards away from the resonances bifurcates from the transcritical bifurcation for odd integer μ^{-1} (i.e. at changes in $s_{\max}$).

By studying the variational equation of (2.17) along the special solution γ_1 corresponding to the weak eigendirection, we obtain the following:

Theorem 2.9 (**Rotational Properties** [**14, 119, 140, 143**])**.** *Suppose system* (2.17) *has a folded node with* $0 < \mu < 1$*. Then for* $0 < \varepsilon \ll 1$ *and* μ *bounded away from zero with* $2k+1 < \mu^{-1} < 2k+3, k \in \mathbb{N}$ *and* $\mu^{-1} \neq 2k+2$*:*

(i) the primary strong canard twists once around the primary weak canard in an $\mathcal{O}(\sqrt{\varepsilon})$ *neighbourhood of the folded node,*
(ii) the j*-th secondary canard,* $1 \leq j \leq k$*, twists* $2j+1$ *times around the primary weak canard in an* $\mathcal{O}(\sqrt{\varepsilon})$ *neighbourhood of the folded node,*

where a twist corresponds to a rotation of $180°$*.*

Thus, from Theorem 2.9, folded node type canards are known to oscillate in an $\mathcal{O}(\sqrt{\varepsilon})$ neighbourhood of the folded node. A combination of GSPT, blow-up and Melnikov arguments show that (in addition to the two primary canards) there are $\lfloor \frac{1-\mu}{2\mu} \rfloor$ secondary canards

away from the resonances $\mu^{-1} \in \mathbb{N}$, where $\lfloor \cdot \rfloor$ is the floor function [**140**]. With this information, the number of oscillations s in a neighbourhood of the folded node can be bounded:

$$0 \leq s \leq s_{\max} := \lfloor \frac{\mu + 1}{2\mu} \rfloor. \tag{2.20}$$

Corollary 2.3. *Under the conditions of Theorem 2.9, there exist* $s_{\max} - 1$ *secondary canards. The* k^{th} *secondary canard* γ_k*,* $k = 1, \ldots, s_{\max} - 1$*, makes* k *full rotations about* γ_w*.*

In geometric terms, the primary weak canard γ_w is the axis of rotation for the invariant manifolds S_a^ε and S_r^ε, and the other maximal canards. The strong canard γ_0 is the separatrix that divides the flow between those trajectories that oscillate and those that do not. The secondary canards partition the funnel into $s_{\max}$ subsectors $I_k, k \in [1, \ldots, s_{\max}]$ each with distinct rotational properties. In the singular limit, all secondary canards collapse onto γ_0 and only the maximal rotation sector persists (as the singular funnel). Initial conditions in sector I_k make $(2k + 1)$ twists about γ_w. In this way, folded node type canards organize the dynamics in phase space (Figure 2.4(b)). In practice, all solutions in the funnel experience some kind of delay before repulsion.

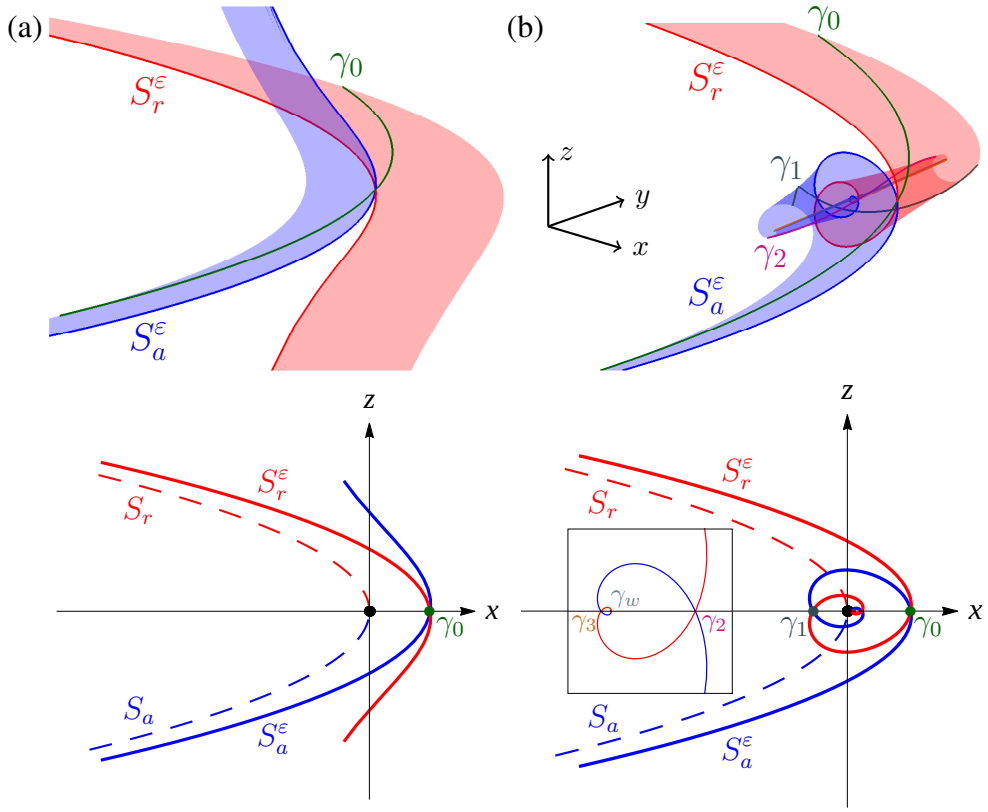

Figure 2.4. Invariant slow manifolds S_a^ε and S_r^ε ($\varepsilon = 0.005$) calculated up to the plane $y = 0$ for (a) folded saddles ($\mu = -0.1$) and (b) folded nodes ($\mu = 0.1$). In each case, the folded singularity is located at the origin. The bottom row shows the slow manifolds (solid) and their singular counterparts (dashed) in the cross-section $y = 0$. Maximal canards are identified as intersections between S_a^ε and S_r^ε.

2.5.2. Folded Saddle Canards. Consider system (2.17) in the folded saddle case with real eigenvalues of opposite sign $\lambda_s < 0 < \lambda_f$. That is, $\mu < 0$ for folded saddles. We split the results concerning folded saddles into two categories: those concerning canards and those concerning faux canards. We start with the canard result (see Figure 2.4(a)):

Theorem 2.10 (**Existence of Maximal Strong Canard [119]**). *Consider* (2.17) *with* $\mu < 0$. *Then for* $0 < \varepsilon \ll 1$ *and* μ *bounded away from zero, the singular strong canard perturbs to a maximal canard* γ_0*, called the* primary strong canard.

Studies of faux canards around the folded saddle have been much less extensive than their folded node canard counterparts. We have the following results concerning existence and rotational properties of faux canards:

Theorem 2.11 (**Existence of Faux Canards [119]**). *Consider* (2.17) *with* $\mu < 0$. *A singular faux canard implies the existence of a 2-parameter family of faux canards for* $0 < \varepsilon \ll 1$.

Proposition 2.2 (**Rotational Properties of Faux Canards [89]**). *Consider* (2.17) *with* $\mu < 0$. *Let* s *denote the number of rotations a faux canard solution makes about the folded saddle faux canard in an* $\mathcal{O}(\sqrt{\varepsilon})$ *neighbourhood of the folded saddle. Then*

$$0 \leq s \leq \lfloor \frac{1-\mu}{-2\mu} \rfloor.$$

for $-\mu^{-1} \notin \mathbb{N}$.

Remark 2.20. The folded saddle faux canard is the axis of rotation for the faux canards (cf. the primary weak canard for folded nodes). Proposition 2.2 states that faux canards only have rotational behaviour for $\mu \in (-1, 0)$. Otherwise, for $\mu < -1$, there are no rotations.

2.5.3. Folded Saddle-Node Canards. To complete our overview of canard theory, consider once again the normal form (2.17) for the dynamics near a folded node or folded saddle. For $\mu \neq 0$, an equivalent normal form is

$$\begin{aligned} \dot{x} &= y - (\mu+1)z + \mathcal{O}(x, \varepsilon, (y+z)^2), \\ \dot{y} &= \frac{1}{2}\mu + \mathcal{O}(x, y, z, \varepsilon), \\ \varepsilon\, \dot{z} &= x + z^2 + \mathcal{O}(z^3, xz^2, xyz, \varepsilon(x+y+z), \varepsilon^2). \end{aligned} \tag{2.21}$$

In both (2.17) and (2.21), the higher order terms do not alter the local dynamics and are sufficient to understand the folded node and folded saddle problems. The boundary between folded node and folded saddle is called folded saddle-node (FSN) and there are two types. The FSN type I, given by $\mu \to 0$ in (2.17), refers to a saddle-node bifurcation of a folded node and a folded saddle. The center manifold of the FSN I is tangent to the fold curve L and there are no ordinary singularities involved in the bifurcation (Figure 2.5(a) and (b)). The FSN type II, given by $\mu \to 0$ in (2.21), has center manifold transverse to L and corresponds to a transcritical bifurcation of ordinary and folded singularities (Figure 2.5(c)). Both types of FSN are common in applications, but their dynamics are not well understood.

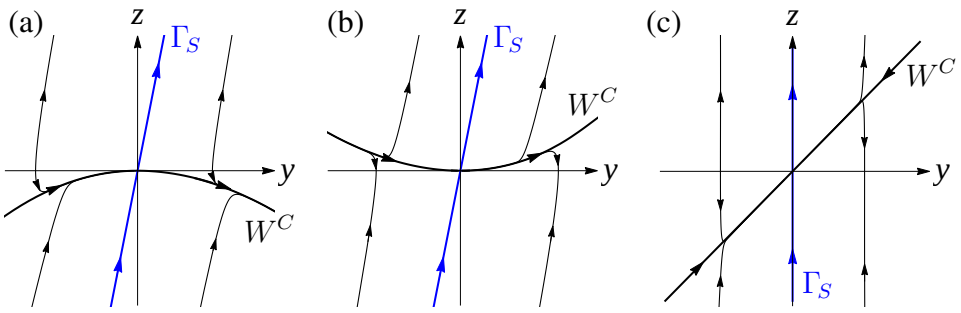

Figure 2.5. Reduced flow near a FSN (a) type I with center manifold W^C on S_a, (b) type I with W^C on S_r, and (c) type II with W^C transverse to the fold.

Both FSN singularities are known to possess canards for $0 < \varepsilon \ll 1$ [**119, 139**], however, not much can be said about their properties. Recent studies have unravelled the dynamics of the FSN II [**20, 51, 76**]. In the FSN II case, there is a nearby full system Hopf bifurcation and the periodic orbits that emanate from it can significantly impact the local dynamics. In [**51**], the small Hopf-like limit cycles near the FSN II and their bifurcations were studied in the $\mu = \mathcal{O}(\varepsilon)$ regime. The results in [**76**] complement this by considering the FSN II regime with $\mu = \mathcal{O}(\sqrt{\varepsilon})$. In this case, the onset of small Hopf-like limit cycles and their bifurcations can be ignored. The transition between the $\mu = \mathcal{O}(\varepsilon)$ and $\mu = \mathcal{O}(\sqrt{\varepsilon})$ settings was then studied extensively in [**20, 27**].

To study the dynamics near the FSN II, additional terms to explicitly describe the transcritical bifurcation of the ordinary and folded singularities are required [**76**]:

$$\begin{aligned} \dot{x} &= y - (\mu+1)z + \mathcal{O}(x, \varepsilon, (y+z)^2), \\ \dot{y} &= \frac{1}{2}\mu + a_1 y + a_2 z + \mathcal{O}(x, \varepsilon, (y+z)^2), \\ \varepsilon\, \dot{z} &= x + z^2 + \mathcal{O}(z^3, xz^2, xyz, \varepsilon(x+y+z), \varepsilon^2), \end{aligned} \tag{2.22}$$

where $(a_1 + a_2) < 0$, which guarantees that the ordinary singularity is on S_a for $\mu < 0$ and is on S_r for $\mu > 0$. The directional blow-up (to the rescaling chart κ_2)

$$x = \varepsilon\, x_2, y = \sqrt{\varepsilon} y_2, z = \sqrt{\varepsilon} z_2, \mu = \sqrt{\varepsilon}\mu_2, t = \sqrt{\varepsilon} t_2,$$

transforms the 1-fast/2-slow system (2.22) into the 2-fast/1-slow system

$$\begin{aligned} \dot{x_2} &= y_2 - z_2 + \mathcal{O}(\sqrt{\varepsilon}), \\ \dot{y_2} &= \sqrt{\varepsilon}\left(\frac{1}{2}\mu_2 + a_1 y_2 + a_2 z_2 + \mathcal{O}(\sqrt{\varepsilon})\right), \\ \dot{z_2} &= x_2 + z_2^2 + \mathcal{O}(\sqrt{\varepsilon}). \end{aligned} \tag{2.23}$$

The layer problem of (2.23) has a 1D critical manifold

$$CM := \left\{(-y_2^2, y_2, y_2) : y_2 \in \mathbb{R}\right\},$$

and the reduced flow of (2.23) simply moves trajectories along CM. Away from CM, an explicit algebraic solution is known for the layer problem of (2.23)

$$\gamma_1(t_2) = \left(-\frac{1}{4}t_2^2 + \frac{1}{2}, 0, \frac{1}{2}t_2\right),$$

where γ_1 corresponds to the eigenvalue $\lambda = -1$ of the deingularized flow.

Theorem 2.12 (**Existence of Maximal Strong Canard for the FSN II** [**76**])**.** *The singular strong canard γ_1 always perturbs to a maximal strong canard for ε sufficiently small.*

The maximal strong canard connects the attracting and repelling slow manifolds. Solutions exponentially close to the maximal strong canard cross the fold and follow the repelling manifold for $\mathcal{O}(1)$ times on the slow timescale before being repelled. All other trajectories within the funnel (and not exponentially close to the strong canard) are quickly attracted to CM, which can be viewed as the orbital limit of the primary weak canard in the folded node case. The following summarizes the main results of [**76**]:

Theorem 2.13 (**Existence of Primary Weak and Secondary Canards for the FSN II** [**76**])**.** *Consider system* (2.22) *with $\mu = \mathcal{O}(\sqrt{\varepsilon})$. There exist $\mathcal{O}(\frac{1}{\sqrt{\varepsilon}})$ maximal canards, which are $\mathcal{O}(\sqrt{\varepsilon})$ close to CM in $\mathcal{O}(\sqrt{\varepsilon})$ neighbourhoods of the FSN II singularity.*

Remark 2.21. Theorem 2.13 extends the folded node theory, $\mu > 0$ in (2.22), into the FSN II case $\mu = \mathcal{O}(\sqrt{\varepsilon})$. There are also estimates of bifurcation delay for the FSN II [**76**]. The gist of the result is that all trajectories (canard or otherwise) must leave the vicinity of CM before the ordinary singularity on S_r can be reached.

For the FSN I case, an extension of Melnikov theory to invariant manifolds on non-compact domains establishes the existence of maximal canards [**139**]. However, not much else is known about the FSN I canards. We will derive FSN I analogues of the FSN II theorems [**76**] in Chapter 5.

2.6. Global Results: Relaxation & Mixed Mode Oscillations

In Sections 2.4 and 2.5, we studied the local properties of singularly perturbed problems in neighbourhoods of a folded critical manifold. We now examine how these local results can influence the global behaviour of solutions. We consider slow/fast systems in $\mathbb{R}^3$:

$$\begin{aligned} \dot{x} &= g_1(x, y, z, \varepsilon), \\ \dot{y} &= g_2(x, y, z, \varepsilon), \\ \varepsilon\, \dot{z} &= f(x, y, z, \varepsilon). \end{aligned} \tag{2.24}$$

2.6.1. Relaxation Oscillations. We make the following assumptions on the geometry of the system [**120**]:

Assumption 2.1. The critical manifold is 'S-shaped', with attracting upper and lower branches $S_a^{\pm}$ and middle repelling branch S_r, separated by upper and lower fold curves $L^{\pm}$. That is,

$$S = S_a^- \cup L^- \cup S_r \cup L^+ \cup S_a^+.$$

Assumption 2.2. The points $p \in L^{\pm}$ are jump points (regular fold points), i.e. (2.12) holds and the reduced flow near the folds is directed towards the folds (see Section 2.4).

Let $P(L^{\pm}) \subset S_a^{\mp}$ be the projection of the fold curves $L^{\pm}$ along fast fibers of the layer problem on the opposite attracting branch $S_a^{\mp}$.

Assumption 2.3. The reduced flow is transverse to the curves $P(L^{\pm}) \subset S_a^{\mp}$.

Under the assumptions above, a singular relaxation orbit Γ of system (2.24) is a piecewise smooth closed curve (see Figure 2.6(a))

$$\Gamma = \Gamma_a^- \cup \Gamma_f^- \cup \Gamma_a^+ \cup \Gamma_f^+,$$

consisting of:

(i) A slow orbit segment Γ_a^- that follows the slow flow on S_a^- up to L^-.
(ii) A fast jump Γ_f^- from L^- up to the upper attracting sheet S_a^+.
(iii) A slow orbit segment Γ_a^+ that follows the slow flow on S_a^+ up to L^+.
(iv) A fast jump Γ_f^+ from L^+ down to the lower attracting sheet S_a^-.

Assumption 2.4. There exists a singular periodic attractor Γ for system (2.24).

Initial conditions generically start away from S, and the layer flow brings trajectories onto an attracting sheet of S where the dynamics switch to those of the reduced problem. Solutions then follow the reduced flow along S until they reach one of the folds where they jump off S, switching once again to the fast dynamics. Under Assumption 2.4 and after sufficiently many iterations of this sequence, trajectories (in the domain of attraction) converge to Γ. GSPT guarantees that, for sufficiently small ε, the singular orbit Γ persists as a periodic orbit Γ_ε of the fully perturbed problem (2.24):

Theorem 2.14 (**Persistence of Relaxation Orbits** [**120**])**.** *Assume system* (2.24) *satisfies assumptions 1–4. Then there exists a locally unique relaxation orbit* Γ_ε *of system* (2.24)*, which is* $\mathcal{O}(\varepsilon^{2/3})$ *close to* Γ *for* $0 < \varepsilon \ll 1$.

Remark 2.22. The periodic orbit Γ_ε of (2.24) retains the same basic characteristics as its singular counterpart (i.e. alternation between slow and fast phases). The fast jumps initiate in $\mathcal{O}(\varepsilon^{2/3})$ neighbourhoods of the fold curves [**71, 120**] (Theorem 2.7). Such periodic solutions that switch between slow and fast motions are called *relaxation oscillations*.

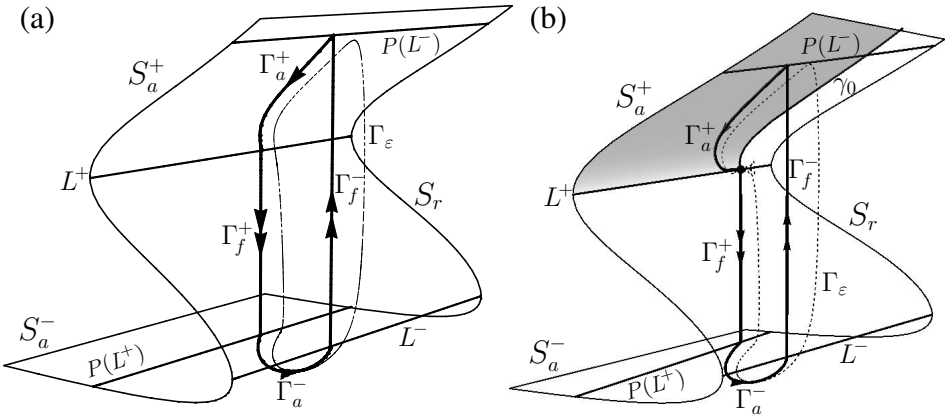

Figure 2.6. Singular (a) relaxation orbit and (b) MMO orbit Γ with corresponding non-singular trajectory Γ_ε (dashed). The fast up-jump Γ_f^- in (b) projects Γ into the funnel (shaded) of the folded node. Note the small oscillations of Γ_ε around the folded node.

2.6.2. Canard-Induced MMOs. Suppose now that we relax Assumption 2.2 and allow for folded singularities.

Assumption 2.5. There exists a folded node p on the upper fold curve L^+ and all other points on $L^\pm$ are jump (regular fold) points.

Remark 2.23. Obviously, assumption 2.5 can be modified to allow for multiple folded singularities of various types along the fold curves. Here, we assume there is only one folded node on the upper fold curve for the sake of illustration.

Under assumptions 2.1, 2.3 and 2.5, system (2.24) may possess a singular periodic orbit, Γ, consisting of:

(i) A slow orbit segment Γ_a^- that follows the slow flow on S_a^- up to L^-.
(ii) A fast jump Γ_f^- from L^- up to the upper attracting sheet S_a^+.
(iii) A slow orbit segment Γ_a^+ that flows along S_a^+ up to the folded node $p \in L^+$.
(iv) A fast jump Γ_f^+ from $p \in L^+$ down to the lower attracting sheet S_a^-.

Note the small but crucial difference to the singular relaxation orbit previously constructed: the slow orbit segment on S_a^+ terminates at the folded node.

Assumption 2.6. There exists a singular periodic attractor Γ for system (2.24), where Γ has a fast fiber segment based at the folded node.

Theorem 2.15 (**Canard-Induced MMOs** [**14**])**.** *Suppose system* (2.24) *satisfies assumptions 2.1, 2.3, 2.5 and 2.6.*

(i) There exist MMOs Γ_ε *with signature* 1^s*,* $s = s_{\max}$ *if* Γ_a^+ *is in the interior of the funnel of the folded node.*

(ii) MMOs Γ_ε with signature L^s, $s < s_{\max}$ and $L \geq 1$ are possible (depending on the global return onto S_a^+) if Γ_a^+ is a segment of the strong canard.

GSPT again guarantees that the singular orbit Γ persists as a periodic orbit Γ_ε of the fully perturbed problem. The difference is that there are small oscillations (due to canards) about the folded node superimposed on the relaxation oscillations. That is, there is an alternation between small-amplitude oscillatory phases (associated with canard dynamics) and large-amplitude relaxation type excursions. Thus, we have MMOs. We say that the MMOs are *canard-induced*. For an extensive survey of canard-induced MMOs, we refer to [**27**].

Remark 2.24. Away from the folded node, Γ and Γ_ε are $\mathcal{O}(\varepsilon)$ close as in the relaxation oscillator. Near the folded node, Γ and Γ_ε are $\mathcal{O}(\sqrt{\varepsilon})$ close (cf. the relaxation oscillator).

An important diagnostic of canard-induced MMOs is the distance, d, of the phase point of global return trajectories on $P(L^-)$ to the strong canard [**14**]. A negative d denotes orbits that land outside the funnel (relaxation oscillations) and a positive d denotes orbits that land inside the funnel of the folded node (MMOs). The border $d = 0$ marks the boundary between MMOs and relaxation oscillations, and indicates that a part of the singular orbit is a segment of the strong canard. Thus, for a canard-induced MMO to exist, we require:

(i) A folded node singularity of the reduced flow.
(ii) A singular periodic orbit with fast fiber segment at the folded node, which automatically guarantees that the global return lies within the funnel of the folded node.

The MMOs (Figure 2.6(b)) are the result of the interaction between local and global mechanisms. The small amplitude oscillations are caused by a local twisting of trajectories near a folded node singularity [**119, 140, 143**]. The large relaxation type spikes arise from the global return of trajectories. We will show in Chapter 3 that the MMOs in Figure 1.5 are canard-induced.

2.6.3. Hopf-Induced MMOs. Recall that the most common causes of loss of normal hyperbolicity are fold and Hopf bifurcations of the layer problem. We now examine how MMOs can be generated by fast subsystem Hopf bifurcations. Note that, in general, a Hopf bifurcation of the layer problem does not imply a Hopf bifurcation of the fully perturbed problem. Consider the 2-fast/1-slow problem

$$\begin{aligned} \dot{x} &= f_1(x, y, z, \varepsilon), \\ \dot{y} &= \varepsilon\, g(x, y, z, \varepsilon), \\ \dot{z} &= f_2(x, y, z, \varepsilon), \end{aligned} \tag{2.25}$$

where f_1, f_2 and g are analytic functions. We make the following assumptions on (2.25):

Assumption 2.7. System (2.25) has critical manifold $\mathcal{Z}$ with complex eigenvalues, which loses hyperbolicity at a (super- or subcritical) Hopf bifurcation $\mathcal{Z}^H$. Near $\mathcal{Z}^H$, we write

$$\mathcal{Z} = \mathcal{Z}_a \cup \mathcal{Z}^H \cup \mathcal{Z}_r,$$

where $\mathcal{Z}_a$ and $\mathcal{Z}_r$ denote the parts of $\mathcal{Z}$ with eigenvalues having negative and positive real parts, respectively.

Assumption 2.8. The reduced flow of (2.25) moves trajectories from $\mathcal{Z}_a$ to $\mathcal{Z}_r$ through $\mathcal{Z}^H$.

In the singular limit, the slow variable y is a fixed parameter of the layer problem. Away from the singular limit, the slow variable becomes a dynamic quantity that drifts through the vicinity of the Hopf bifurcation $\mathcal{Z}^H$ and the behaviour of the dynamical system depends on a parameter that changes slowly in time. In such dynamic bifurcation problems, one often

observes a *bifurcation delay*, where solutions that pass over a bifurcation point do not immediately leave the repulsive curve of stationary points but continue to stay in a neighbourhood of the stationary points for a surprisingly long time [**93**].

Remark 2.25. In 2D slow/fast systems, the canard phenomenon is degenerate and only occurs in an exponentially small parameter interval. In that case, only those trajectories exponentially close to the maximal canard experience bifurcation delay. In 3D slow/fast systems, canards are generic and all trajectories in the funnel of a folded node observe a delay. That is, the generalized canard mechanism is just another manifestation of bifurcation delay.

One very useful diagnostic in the theory of dynamic bifurcations is the way-in/way-out (or entry-exit) function:

Definition 2.17. Let $(x_0, y_0, z_0) \in \mathcal{Z}_a$. The *way-in/way-out function*, $\psi(y_0)$, is the function implicitly defined by the relation

$$\int_{y_0}^{\psi(y_0)} \operatorname{Re} \lambda(s, 0)\, ds = 0, \tag{2.26}$$

where $\lambda(y, \varepsilon)$ denotes the eigenvalues of the linearization of (2.25) about $\mathcal{Z}$, so that $\lambda(y, 0)$ denotes the eigenvalues of the layer problem of (2.25) about $\mathcal{Z}$.

Intuitively, the way-in/way-out function is interpreted as the moment when the expansion on the repelling manifold counterbalances the accumulative contraction on the attracting manifold. The implication is that a solution of (2.25) starting at y_0 will remain in a small neighbourhood of $\mathcal{Z}$ at least up to ψ. This is summarized in the following:

Theorem 2.16 (Delayed Loss of Stability for a Dynamic Hopf [91, 92]). *Consider* (2.25) *under Assumptions 2.7 and 2.8. Let* (x_0, y_0, z_0) *be an initial condition such that* $\operatorname{Re} \lambda(y_0, 0) < 0$ *and* (x_0, z_0) *is* $\mathcal{O}(\varepsilon)$ *close to* $\mathcal{Z}$ *at* y_0*. Then the trajectory of* (x_0, z_0) *stays* $\mathcal{O}(\varepsilon)$ *close to* $\mathcal{Z}$ *for all* $y \leq \psi(y_0)$*, where* $\psi(y_0)$ *is the way-in/way-out function* (2.26)*.*

Remark 2.26. Stability loss delay does not hold for non-analytic systems (see [**93**]).

Trajectories that approach $\mathcal{Z}_a$ a distance $\mathcal{O}(1)$ from $\mathcal{Z}^H$ are attracted to and oscillate around $\mathcal{Z}_a$. Trajectories become exponentially close to $\mathcal{Z}_a$ on the slow timescale as they pass close to $\mathcal{Z}^H$. As the trajectories pass over to $\mathcal{Z}_r$, the layer equations undergo a Hopf bifurcation, but in analytic systems the trajectories remain close to $\mathcal{Z}_r$ for $\mathcal{O}(1)$ times (i.e. they stay close for $\mathcal{O}(1)$ distances beyond $\mathcal{Z}^H$). The delay occurs because the trajectory is exponentially close to $\mathcal{Z}$ and must be repelled before it can follow limit cycles of the layer problem. That is, trajectories destabilize when the expansion on $\mathcal{Z}_r$ counteracts the accumulative contraction on $\mathcal{Z}_a$. Thus, the further a trajectory is from $\mathcal{Z}^H$ on $\mathcal{Z}_a$, the longer the delay on $\mathcal{Z}_r$ before it is repelled. However, there is a maximal distance that trajectories may trace $\mathcal{Z}_r$ before they must escape via fast directions.

Definition 2.18. Let $\psi(y_0)$ be as defined in (2.26). The *maximal delay* or *buffer point*, y_B, is

$$y_B := \lim_{y_0 \to y_a^{\max}} \psi(y_0),$$

where $y_a^{\max}$ is the furthest point (possibly infinity) of $\mathcal{Z}_a$ from $\mathcal{Z}^H$.

Remark 2.27. The buffer point implies that phase points that were attracted to $\mathcal{Z}$ at different moments before y_B will escape from $\mathcal{Z}$ simultaneously at y_B.

The amplitude and number of small oscillations due to the slow passage through the dynamic Hopf are related to the size of the perturbation. For small ε, the passage through $\mathcal{Z}^H$ is slow and there is a substantial amount of time for trajectories to oscillate but those

oscillations are small and difficult to observe due to the strong attraction to $\mathcal{Z}_a$. Any oscillatory behaviour becomes visible just before the trajectory jumps away from $\mathcal{Z}_r$. When ε is increased, the timescale separation weakens, making the slow variable faster. Consequently, the drift through $\mathcal{Z}^H$ is faster, there is less time for the trajectories to oscillate and the attraction to $\mathcal{Z}_a$ is weaker. Thus, the trajectories have less time to be pulled into $\mathcal{Z}_a$ and so the observed oscillations are larger and fewer. Moreover, as the trajectory drifts through $\mathcal{Z}^H$, the real part of the eigenvalues increases through zero. As such, the small oscillations have decreasing amplitude (on $\mathcal{Z}_a$) and increasing amplitude (on $\mathcal{Z}_r$).

We now examine one set of conditions (corresponding to those encountered in Chapter 4) in which the dynamic Hopf can generate MMOs.

Assumption 2.9. The critical manifold is 'Z-shaped', with fold points $\mathscr{L}^{\pm}$ separating the upper, middle and lower branches, and with a Hopf bifurcation $\mathcal{Z}^H$ on the upper branch. Moreover, $y^H < y^+$, where y^+ and y^H are the y-coordinates of $\mathscr{L}^+$ and $\mathcal{Z}^H$, respectively. That is,

$$\mathcal{Z} = \mathcal{Z}_a^- \cup \mathscr{L}^- \cup \mathcal{Z}_r^- \cup \mathscr{L}^+ \cup \mathcal{Z}_r^+ \cup \mathcal{Z}^H \cup \mathcal{Z}_a^+.$$

The attracting branches of the critical manifold have graph representations $(x_a^{\pm}(y), y, z_a^{\pm}(y))$ for $y \in I^{\pm}$, where $I^+ \cap I^- \neq \emptyset$ (i.e. $\mathcal{Z}$ has bistable regions).

Assumption 2.10. System (2.25) has an equilibrium on $\mathcal{Z}_r$ not in the vicinity of $\mathcal{Z}^H$ or $\mathscr{L}^{\pm}$.

Under assumptions 2.9 and 2.10, system (2.25) may possess a singular periodic orbit, Γ, consisting of:

(i) A slow orbit segment Γ_a^- that follows the slow flow on $\mathcal{Z}_a^-$ up to $\mathscr{L}^-$.
(ii) A fast jump Γ_f^- from L^- up to the upper attracting branch $\mathcal{Z}_a^+$.
(iii) A slow orbit segment Γ_a^+ that flows along $\mathcal{Z}_a^+$ up to the Hopf bifurcation $\mathcal{Z}^H$.
(iv) A fast jump Γ_f^+ from $\mathcal{Z}^H$ down to the lower attracting branch $\mathcal{Z}_a^-$.

Assumption 2.11. There exists a singular periodic attractor Γ for system (2.25), where Γ has fast fiber segment based at the Hopf bifurcation of the layer problem of (2.25).

Theorem 2.17. *Consider system* (2.25) *under assumptions 2.9–2.11. For* $0 < \varepsilon \ll 1$*, there exist MMOs* Γ_ε *with signature* 1^s, $s \geq 0$.

GSPT establishes the persistence of the singular orbit Γ for $0 < \varepsilon \ll 1$. The resulting MMOs Γ_ε depend crucially on the criticality of the Hopf bifurcation of the layer problem. In the supercritical case, the small oscillations of the MMO closely follow the stable limit cycles that emanate from $\mathcal{Z}^H$ (as in plateau bursting). In the subcritical case, the small oscillations are transient oscillations generated by the unstable limit cycles emanating from the subcritical Hopf (as in pseudo-plateau bursting). Theorem 2.17 is illustrated in the super/subcritical case (in the bursting context) in Figure 1.4(a) and (b), respectively.

Remark 2.28. The small oscillations of the MMOs Γ_ε arise from the slow passage through a dynamic Hopf bifurcation. We say that the MMOs of Theorem 2.17 are *Hopf-induced*.

2.6.4. Return Maps In Slow/Fast Systems. Discrete dynamical systems arise naturally from flows: one can observe the flow at fixed time intervals (strobing) or record the coordinates of the flow when a special event occurs (Poincaré section). Often in the study of periodic orbits of continuous dynamical systems, Poincaré maps are used to convert the problem into a discrete dynamical system that has state space one dimension smaller than the original state space. The Poincaré map allows the stability of orbits to be determined in a process that resembles the linearization procedure used to determine the stability of equilibria.

We proceed now to define the Poincaré map in the context of the slow/fast system (2.24). Let ϕ_t denote the flow of (2.24) and let γ be a periodic orbit of ϕ_t. Let $\Sigma \subset \mathbb{R}^3$ be a 2D local

cross-section such that the flow is everywhere transverse to Σ. Let $p = \gamma \cap \Sigma$ and assume that p is unique (if not, restrict Σ so that p is unique).

Definition 2.19. The *first return* or *Poincaré map* is the mapping

$$\Pi_\varepsilon : U \subset \Sigma \to \Sigma,$$
$$q \mapsto \phi_\tau(q),$$

where U is a neighbourhood of p, $\tau = \tau(q)$ is the smallest positive time taken for the orbit $\phi_t(q)$ based at q to first return to Σ.

Remark 2.29. We use the ε subscript in Π_ε to indicate that the return map is being calculated for the fully perturbed problem (i.e. $\varepsilon > 0$). We will define singular analogues of Π_ε in Chapter 3. The return time $\tau = \tau(q)$ need not be equal to the period $T(p)$ of the periodic orbit γ. However, $\tau(q)$ converges to $T(p)$ as $q \to p$.

Clearly, p is a fixed point of the map Π_ε, the stability of which reflects the stability of the periodic orbit γ for the flow ϕ_t. In slow/fast systems, the Poincaré map has the advantage that trajectories decay to S_a^ε exponentially fast so that cross sections to S_a^ε quickly evolve to exponentially thin strips that can be approximated by curves. That is, in 3D slow/fast systems, the return map is closely approximated by a 1D curve. We use this to our benefit in practice by taking a curve of initial conditions on S_a^ε and flowing them forward to obtain a suitable approximation of the dynamics (Figure 2.7(a)).

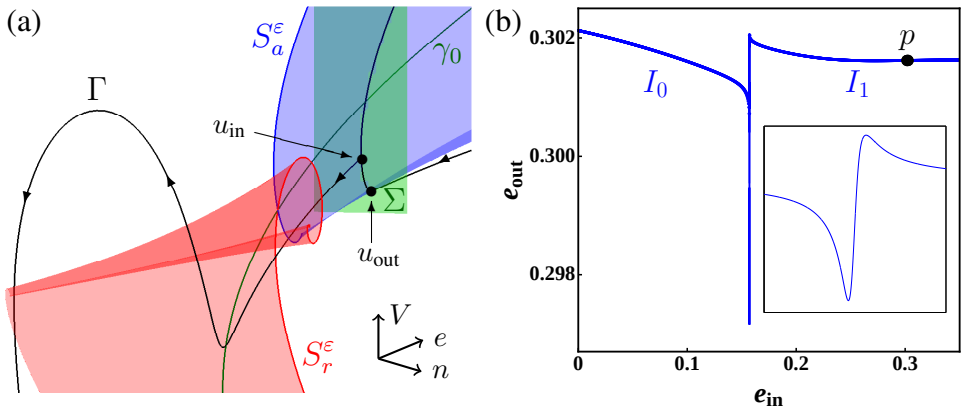

Figure 2.7. Return map construction for a system of the form (2.24) with 1^1 MMO attractor (see Chapter 3). Here, V is fast and (n, e) are the slow directions. (a) The first returns of the points of $S_a^\varepsilon \cap \Sigma$ are computed. Initial conditions $u_{\text{in}} = (V_{\text{in}}, n_\Sigma, e_{\text{in}})$ are mapped to $u_{\text{out}} = (V_{\text{out}}, n_\Sigma, e_{\text{out}})$. (b) Associated return map (inset: zoom of the nearly vertical region separating rotational sectors I_0 and I_1). The fixed point p of the map falls in the rotational sector I_1 and is stable.

Figure 2.7(b) shows a typical return map generated by a slow/fast system (2.24) that has a canard-induced MMO attractor with signature 1^1. Trajectories that follow the maximal strong canard on opposite sides of S_r^ε are torn apart and follow very different evolutions. This gives rise to rapid expansion in the return maps. Hence, we observe nearly vertical segments in Π_ε, corresponding to the exponentially close family of canards associated to the maximal strong canard. Initial conditions on one side of the strong canard execute a small oscillation in their forward orbit and initial conditions on the other side of the strong canard have no rotations. That is, the maximal strong canard demarcates the rotational sectors I_0 and I_1. A more detailed analysis of the return maps and the bifurcation sequences involved in the creation and crossing of folded node type canards will be studied in Chapter 3.

2.7. Computation of Invariant Slow Manifolds and Canards

An important aspect of GSPT and canard theory in practice is numerically implementing all of the relevant geometric features. The numerical method used to compute the attracting and repelling slow manifolds, such as in Figure 2.4, involves reformulating the singular perturbation problem as a boundary value problem (BVP) and using homotopic continuation to generate a family of solutions that form a mesh of the surface. Here, we outline the method in the context of the leading order dynamics of the folded node/folded saddle normal form (2.17) and refer to [**23, 24, 25**] for additional details (with further examples) and to the AUTO demo files [**32**], which provide sample codes.

To compute the invariant slow manifolds, S_a^ε and S_r^ε, we first rescale (2.17)

$$\begin{aligned} \dot{x} &= T\left(\frac{1}{2}\mu y - (\mu+1)z\right), \\ \dot{y} &= T, \\ \dot{z} &= \frac{T}{\varepsilon}(x+z^2), \end{aligned} \tag{2.27}$$

where the overdot denotes differentiation with respect to the new time variable and the free parameter T is the actual integration time. Thus the integration time of any solution is rescaled to unity. For the computation of the attracting slow manifold S_a^ε, we continue solutions of (2.27) subject to boundary conditions which ensure that solutions lie (approximately) on S_a^ε. To do this, we choose a curve on the attracting sheet S_a of the critical manifold that is sufficiently far from the fold L:

$$\mathbf{u}(0) \in \Sigma_a := \{(x,y,z) \in S_a : z = -0.3\}, \tag{2.28}$$

where $\mathbf{u} = (x,y,z)$. To ensure the relevant part of S_a^ε is computed near the folded singularity, the right endpoint $\mathbf{u}(1)$ is restricted to a plane through the folded singularity with the requirement that the plane is transverse to the flow. A suitable choice is to take the plane of constant y passing through the folded singularity

$$\mathbf{u}(1) \in \Sigma := \{(x,y,z) : y = 0\}. \tag{2.29}$$

Before S_a^ε can be calculated, note that a solution of (2.27) subject to (2.29) is the trivial orbit segment given by the folded singularity.

We now use homotopic continuation to construct a first solution of the BVP (2.27) subject to (2.28) and (2.29). In the first step, we start with the trivial solution at the folded singularity and continue the orbit in T subject to the modified boundary condition

$$\mathbf{u}(0) \in \{(x,y,z) \in L\},$$

until the endpoint $\mathbf{u}(0)$ is at some predetermined distance from the folded singularity. In other words, we grow the orbit segment out from the folded singularity along the fold. In Figure 2.4, the calculation was terminated when the endpoint reached $y = -2$. In the second step, we continue the orbit segment in T subject to the new boundary condition

$$\mathbf{u}(0) \in \{(x,y,z) \in S_a : y = -2\},$$

until the endpoint $\mathbf{u}(0)$ reaches Σ_a. That is, we grow the orbit segment along the attracting sheet of the critical manifold approximately parallel to the plane Σ. The last solution obtained from the homotopy is the start solution for the BVP defined by (2.27) subject to (2.28) and (2.29). Numerical continuation in T then generates the surface S_a^ε (see Figure 2.8).

The repelling slow manifold is computed analogously but with negative T, which has the effect of reversing the direction of the flow. The boundary conditions are chosen to ensure

that solutions lie close to S_r^ε. To continue orbits with negative T in practice, we simply swap the boundary conditions. Thus, the BVP for the repelling slow manifold is (2.27) subject to

$$\mathbf{u}(0) \in \Sigma,$$
$$\mathbf{u}(1) \in \Sigma_r := \{(x, y, z) \in S_r : z = 0.3\}.$$

As in the computation for S_a^ε, the trivial orbit segment at the folded singularity is used as a starting solution for a 2-step homotopy process to find a first solution to the BVP. In the first stage, we move solutions along the fold L until $y(1) = 2$. From there, the second stage of the homotopy moves solutions along S_r, parallel to Σ, until Σ_r is reached (see Figure 2.8).

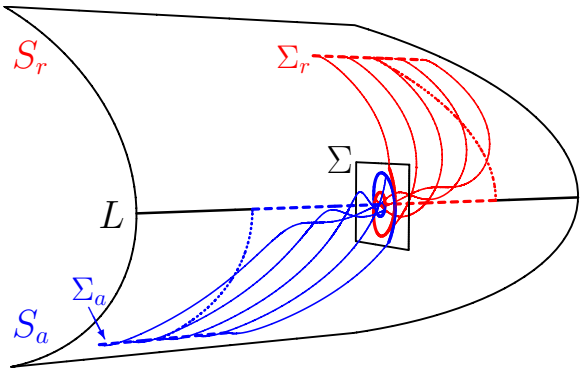

Figure 2.8. Computation of the slow manifolds S_a^ε and S_r^ε near a folded node. Starting at the folded node, orbits are grown homotopically (red and blue, dashed) along L and then parallel to the section Σ. Initial conditions from Σ_a and Σ_r are flowed forward and backward, respectively, to Σ. These trajectories (red and blue, solid) form a mesh of the surface.

The advantage of terminating the computation of S_a^ε and S_r^ε in the cross-section Σ is that the maximal canards are easily identifiable. In terms of the BVP, canards are solutions of (2.27) subject to the boundary conditions

$$\mathbf{u}(0) \in \Sigma_a \text{ and } \mathbf{u}(1) \in \Sigma_r.$$

A solution of this BVP is computed by finding orbit segments $\mathbf{u}_a \in S_a^\varepsilon$ and $\mathbf{u}_r \in S_r^\varepsilon$ that match in the plane Σ. We concatenate $\mathbf{u}_a$ with the reverse of $\mathbf{u}_r$ (so that the integration time is positive), rescale the resulting orbit back to the time interval $[0, 1]$ and continue the solution. Provided $|\mathbf{u}_a(0) - \mathbf{u}_r(0)|$ is sufficiently small, a Newton step in AUTO generates a solution of the BVP, which represents the respective canard solution.

CHAPTER 3

Bifurcations of Canard-Induced MMOs

MMOs are complex oscillatory waveforms that naturally occur in physiologically relevant dynamical processes. In Chapter 1, we showed that our pituitary cell model (1.4) generates two types of MMOs (dynamic and calcium-conducting). In this chapter, we study the calcium-conducting MMOs in a 3D reduction of (1.4). Using the combined power of bifurcation theory and GSPT, we show that the pseudo-plateau bursting is a canard-induced MMO and study bifurcations of the MMOs under variations of key parameters. To do this, a global return map induced by the flow of the equations is constructed and a qualitative analysis given. The canards act as separatrices in the return maps, organizing the dynamics along the Poincaré section. We examine the bifurcations of the MMOs from the viewpoint of the return maps, which informs our geometric intuition of the bursting and explains the different observed MMO patterns. This chapter is documented in [**134, 135**].

Authors' Contributions: The analysis in [**134**] was done by TV, RB, and JT (only the work by TV is presented herein). The manuscript of [**134**] was written and edited by all authors. The analysis and manuscript of [**135**] were done by TV, and edited by all authors.

3.1. Motivation

In most bursting models, the bursting oscillations are driven by the slow, systematic variation in the calcium concentration c [**81, 128, 146**]. However, in the pituitary lactotroph model (1.4), the bursting can persist almost unaltered when c is fixed (Figure 1.6). This suggests an intrinsic bursting mechanism independent of the calcium. Early treatments of (1.4) focused on these novel calcium-conducting bursts by fixing c [**130**]. Mathematically, this is equivalent to taking the singular limit $\delta \to 0$ in system (1.4) and examining the dynamics of the (V, n, e) subsystem with parameter c. The value at which c is fixed is chosen via averaging (see Chapter 4). In that case, the calcium-dependent SK current becomes a constant conductance current that arises from the leakage of potassium ions through the cell membrane and plays a significant part in determining the resting membrane potential of the cell [**56, 62**]. Thus, the SK current becomes a passive leak current

$$I_L = g_L(V - V_K),$$

where g_L is the leak conductance, which we set at $g_L = 0.3$ nS. To further reduce and simplify the model for calcium-conducting bursts, we remove the BK current ($g_{BK} = 0$ nS), which corresponds (in an experimental setting) to the introduction of pharmacological agents such as paxilline or iberiotoxin (which are known BK channel blockers – see Chapter 6). In that case, the pituitary cell model reduces to

$$\begin{aligned} \varepsilon \dot{V} &= f(V, n, e) \equiv -\frac{1}{g_{\max}} \left(I_{Ca} + I_K + I_A + I_L \right), \\ \dot{n} &= g_1(V, n) \equiv \frac{k_t}{\tau_n}(n_\infty(V) - n), \\ \dot{e} &= g_2(V, e) \equiv \frac{k_t}{\tau_e}(e_\infty(V) - e), \end{aligned} \tag{3.1}$$

where $\varepsilon = \frac{C_m}{k_t g_{\max}} \ll 1$, t is the (dimensionless) slow time and the dot denotes a t derivative.

Remark 3.1. Note that in (1.4), the timescale of n is given by τ_n/λ. In (3.1), we absorb the λ factor into the definition of τ_n and set $\tau_n = 40$ ms.

System (3.1) provides a minimal description for the calcium-conducting bursts [**130**]. The key parameters of interest are the conductance of the delayed rectifier channels g_K and the conductance of the A-type channels g_A. Together, these parameters control the amplitude and number of spikes per burst as we discuss later. Note that the membrane capacitance C_m plays the role of the singular perturbation parameter so that we use ε and C_m interchangeably.

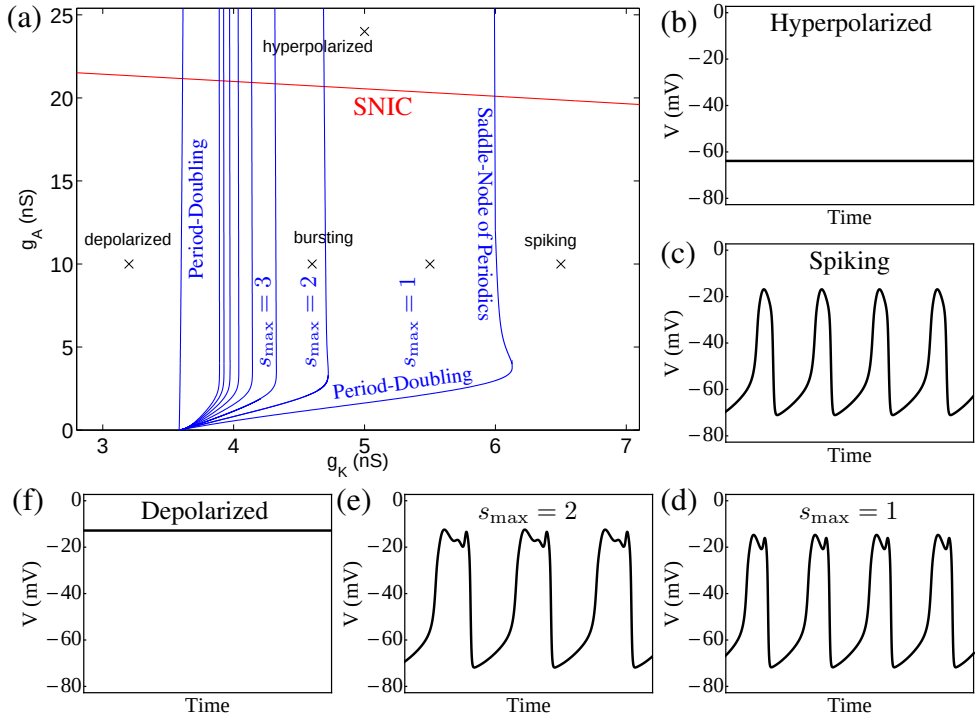

Figure 3.1. Bifurcation structure of (3.1) for $C_m = 2$ pF. (a) Two-parameter (g_K, g_A) diagram showing the curves that delimit the various system behaviours. (b) Hyperpolarized steady state ($g_K = 5$ nS, $g_A = 24$ nS). (c) Typical spiking pattern ($g_K = 6.5$ nS, $g_A = 10$ nS). (d) Typical 1^1 MMO ($g_K = 5.5$ nS, $g_A = 10$ nS). (e) Typical 1^2 MMO ($g_K = 4.6$ nS, $g_A = 10$ nS). (f) Depolarized steady state ($g_K = 3.2$ nS, $g_A = 10$ nS). The (g_K, g_A) coordinates for panels (b)–(f) are indicated by crosses in panel (a).

We wish to determine how the bursting relates to other states of the system, such as spiking or quiescence (hyperpolarized or depolarized equilibria), and to determine how the number of spikes in a burst varies with parameters. To this end, we construct a 2-parameter (g_K, g_A)-bifurcation diagram (Figure 3.1(a)). Here, we briefly describe the bifurcation structure of system (3.1) that motivates this chapter and refer to Section 3.2 for a detailed analysis. The bursting region is enclosed by the period-doubling, saddle-node of periodics and saddle-node on invariant circle (SNIC) curves. Within the bursting region, the number of small oscillations s increases (so that the bursting waveform broadens) with decreasing g_K (compare Figures 3.1(d) and (e)). Surrounding the bursting region are regions of depolarized steady states (Figure 3.1(f)), hyperpolarized steady states (Figure 3.1(b)) and spiking behaviour (Figure 3.1(c)). Whilst the bifurcation analysis provides boundaries for the bursting region in parameter space, it does not explain the rationale for these boundaries.

There are two primary goals to this chapter. The first is to show that the pseudo-plateau bursting is a canard-induced MMO. That is, using GSPT, we demonstrate the genesis of

the bursting rhythm, identify the region in parameter space where it exists and show how the number of small amplitude oscillations (or spikes) varies in parameter space. In so doing, we identify the mechanism for this type of pseudo-plateau bursting, and also perform analyses at the singular limit to explain behaviours seen away from this limit. The second major goal is to explain the bifurcation structure of (3.1) (as shown in Figure 3.1) by way of canard-induced MMOs. Such studies have been performed previously on plateau bursting [**126**] and more recently on pseudo-plateau bursting [**95, 129**], but ours is the first case study to examine MMOs under the creation and crossing of folded node type canards.

The outline of the chapter is as follows. In Section 3.2 we provide a detailed investigation of the bifurcation structure of pseudo-plateau bursting similar to [**95**] to determine the regions in parameter space where spike transitions occur. Following the work done in [**141, 142**] for a stellate cell model, we focus primarily on 1^s and related MMO patterns. In Section 3.3 we perform a geometric singular perturbation analysis wherein the 3D system (3.1) is formally decomposed into a 2D slow subsystem coupled to a 1D fast subsystem. In particular, we show that the bursting is a canard-induced MMO. This slow/fast analysis helps us understand the pattern of spike additions and the dynamics underlying them. The comparison of the singular limit predictions with the observed MMO boundaries shows that the singular limit analysis is able to predict these different MMO boundaries sufficiently well.

In Section 3.4, we construct a global return map [**51, 53, 77, 85, 141, 142**] induced by the flow of (3.1) as an alternative method for understanding the spike-adding transitions. In Section 3.5 we investigate the bifurcation sequences of the return maps, which explain the bifurcation structure of the MMOs observed in Section 3.2. Again, certain topological features of the return maps can be predicted from the corresponding singular limit return maps and, hence, explain the bifurcation structure of interest. Thus, the bifurcation analysis of system (3.1) provides a view of the sequence of spike-adding transitions and the associated periodic bursting solutions, whilst the slow/fast analysis and 1D return maps help us understand why the spike-adding transitions occur. We follow in Section 3.6 with a discussion.

3.2. Bifurcations of MMOs

In this section, we perform a full system bifurcation analysis of system (3.1) with respect to the maximal conductances of the delayed rectifier (g_K) and A-type currents (g_A). The aim of this section is to examine the detailed bifurcation structure of (3.1) and ultimately show how Figure 3.1 was constructed. We place particular emphasis on identifying a common sequence of bifurcations from stable 1^s to 1^{s+1} MMO patterns, $s \geq 0$.

3.2.1. Horizontal bifurcations. By fixing $C_m = 2$ pF, $g_A = 4$ nS, we consider only those bifurcations that arise from variations in g_K, the biophysical parameter that controls the repolarizing current I_K. Using AUTO [**31, 32**], a bifurcation diagram was calculated as shown in Figure 3.2, where g_K is the principal continuation parameter and L_2 norm refers to the standard Euclidean norm for equilibria or the L_2 norm for periodic solutions.

The spiking family ($s = 0$, Figure 3.2) connects to the depolarized equilibrium curve E_D at subcritical Hopf bifurcations (HB) at $g_K \approx 3.67$ nS and $g_K \approx 36.99$ nS (only one Hopf bifurcation is shown). The equilibrium is a depolarized steady state for small g_K. After the first Hopf it becomes a saddle and after the second Hopf it is hyperpolarized. The first bursting family ($s = 1$) connects to the spiking family at period doubling (PD) points at $g_K \approx 6.127$ nS and $g_K \approx 3.592$ nS. The rest of the MMO families are isolated closed curves of periodic orbits. These isolas are born in saddle-node of periodic orbits (SN) bifurcations in a neighbourhood of $g_K \approx 3.592$ nS and possess stable plateau regions which never overlap. Between each pair of MMO families $s = n$ and $s = n + 1$ ($n = 0, 1, 2, \ldots$), there is a small interval where neither branch is stable. In these g_K intervals, we find isolas of more

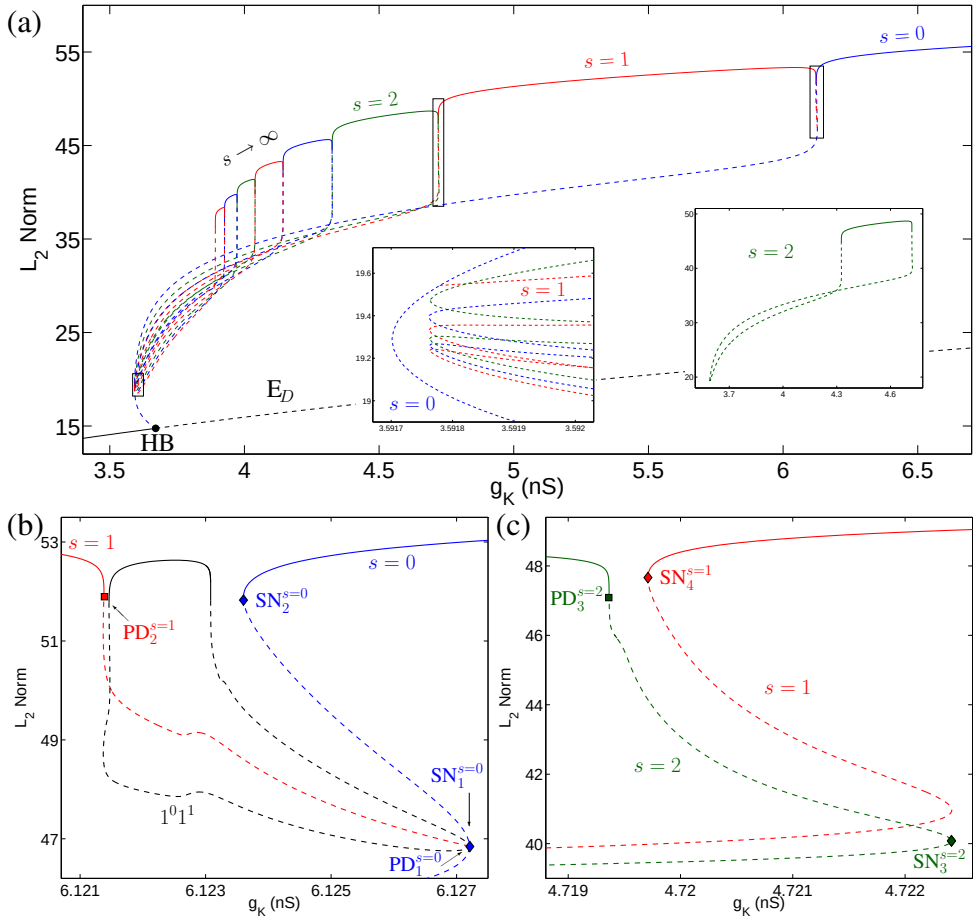

Figure 3.2. Bifurcations of (3.1) along $g_A = 4$ nS for $C_m = 2$ pF. (a) Left inset: neighbourhood of the saddle-node of periodics of the bursting families for $s \geq 2$. Only the branch $s = 1$ connects to the Hopf branch at a PD. Right inset: the $s = 2$ bursting family is a closed isola of periodic orbits. This is true for all bursting families $s \geq 2$. (b) Region between the spiking ($s = 0$) and first bursting ($s = 1$) families where an isola of orbits with signature 1^01^1 have been computed. Note that the $s = 1$ branch connects to the $s = 0$ branch at a PD. (c) Transition region between $s = 1$ and $s = 2$ MMOs.

complicated MMO patterns. The MMO signature in these parameter intervals is always some mixture of 1^n and 1^{n+1}. Figure 3.2(b) shows one of these isolas with signature 1^01^1. The stability plateau of the MMOs in these parameter intervals decreases rapidly with the complexity of the MMO signature.

Figure 3.2(b) shows the g_K window where the $s = 0$ and $s = 1$ curves meet along with the 1^01^1 MMO. In order of decreasing g_K, there are 4 significant bifurcations for the $s = 0$ and $s = 1$ branches. The SN point on the spiking branch at $g_K \approx 6.127$ nS labelled $\mathrm{SN}_1^{s=0}$ marks the location where the first bursting family and additional isolas of mixed MMO type are born. There is also a PD bifurcation labelled $\mathrm{PD}_1^{s=0}$ at almost the same g_K value. The spiking branch $s = 0$ remains stable until the SN point marked by $\mathrm{SN}_2^{s=0}$ at $g_K \approx 6.1235$ nS is reached. Then there is a PD point labelled $\mathrm{PD}_2^{s=1}$ at $g_K \approx 6.1213$ nS where the $s = 1$ bursting branch becomes stable. The parameter window between $\mathrm{PD}_2^{s=1}$ and $\mathrm{SN}_2^{s=0}$ is filled with stable branches of isolas with mixed MMO signature (only branch shown is 1^01^1).

The transition from the $s = 1$ bursting branch to the $s = 2$ bursting branch differs slightly from the spiking to bursting transition as the $s = 1$ and $s = 2$ families do not connect to each other (Figure 3.2(c)). The 1^2 isola is born as an unstable branch for decreasing g_K in

a SN bifurcation (labelled $SN_3^{s=2}$) whilst the 1^1 branch remains stable. The $s = 1$ branch then destabilises at the SN point $SN_4^{s=1}$ and another parameter window of complex isolas is encountered where the stable MMOs have signatures which are mixtures of 1^1 and 1^2. As g_K decreases further, the $s = 2$ branch becomes stable at the PD point $PD_3^{s=2}$.

There are additional bifurcations of the $s = 1$ and $s = 2$ curves that have been omitted as they have little bearing on later results. For the remaining transitions between MMO families, the sequence of bifurcations is the same. Thus it is sufficient to consider only the transition from spiking to bursting and from $s = 1$ to $s = 2$ to understand the bifurcation structure of the MMOs away from the SN region near $g_K \approx 3.59$ nS (inset Figure 3.2(a)).

3.2.2. Vertical bifurcations. By fixing $g_K = 4.1$ nS, we now consider bifurcations that arise due to variations in g_A, the biophysical parameter that controls the sub-threshold current I_A. The resulting bifurcation diagrams for $C_m = 2$ pF and $C_m = 0.1$ pF are shown in Figures 3.3 and 3.4, respectively. As before, we consider (and label) only those bifurcations which are crucial to our discussion.

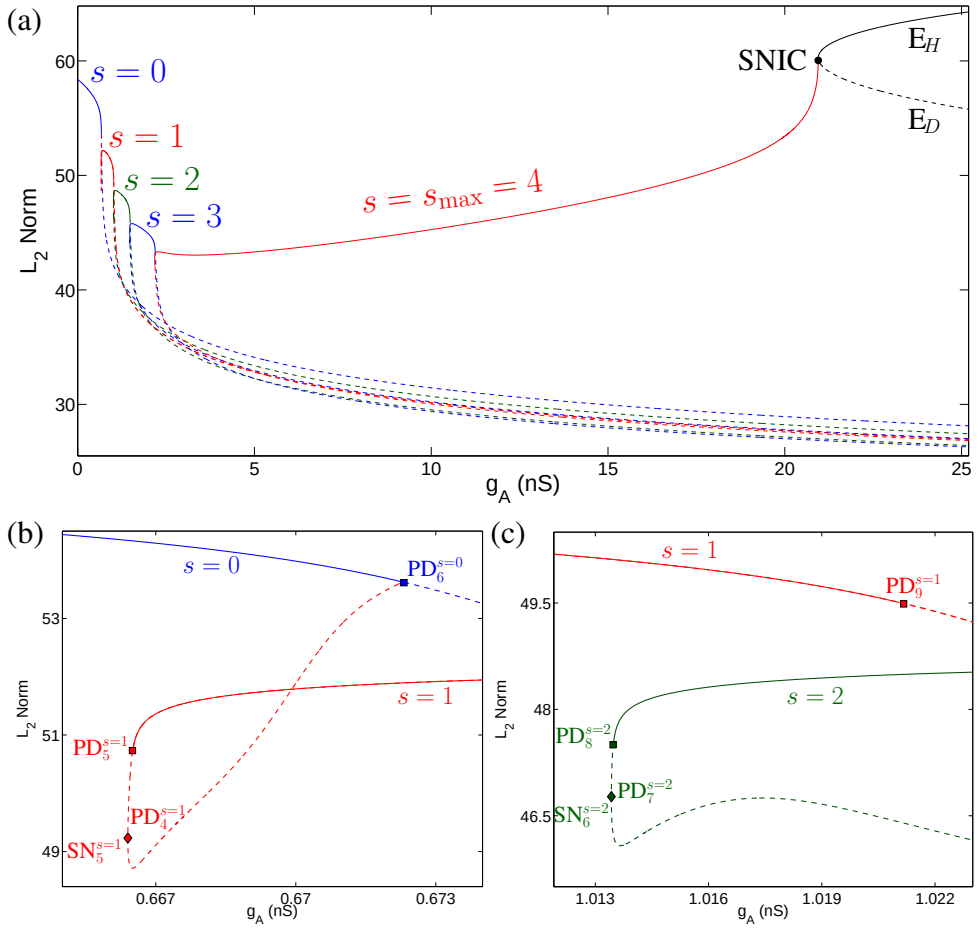

Figure 3.3. (a) Bifurcations of MMOs along $g_K = 4.1$ nS for $C_m = 2$ pF where $s_{\max} = 4$. (b) Blown-up view of the transition from spiking to bursting. (c) Transition region between $s = 1$ and $s = 2$ MMOs: we observe regions of bistability.

For $C_m = 2$ pF, the $s = 1$ bursting family connects to the spiking branch at a PD point and the remaining MMO branches are disconnected. Unlike the horizontal case, there are no parameter windows in which more complex MMO patterns can be found. Instead, there are regions in which the stable plateau of neighbouring MMO branches may overlap and the system exhibits bistability between two different bursting states (Figure 3.3(b) and (c)).

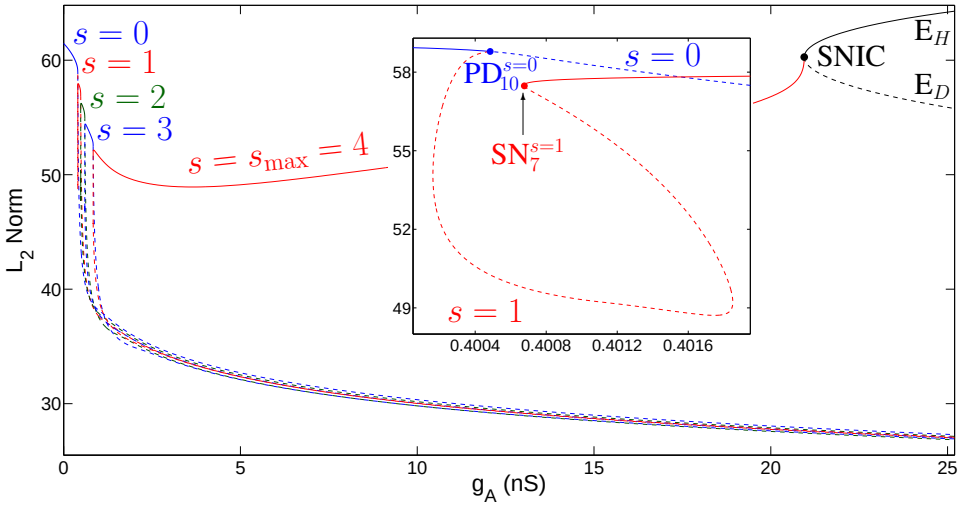

Figure 3.4. Bifurcations of MMOs along $g_K = 4.1$ nS for $C_m = 0.1$ pF where $s_{\max} = 4$. Inset: there is no overlap between the stable portions of the MMO branches (cf. Figure 3.3).

These bistable parameter windows shrink as C_m decreases. For sufficiently small C_m, the stable branches no longer overlap (Figure 3.4 inset) and parameter windows with more complex MMOs can be found (not shown). All bursting families terminate in homoclinics (not shown) for g_A values well outside the physiologically meaningful domain ($g_A > 500$ nS).

For $C_m = 2$ pF, the sequence of bifurcations in the transition from spiking to bursting (in the direction of increasing g_A) is commenced by the $\text{SN}_5^{s=1}$ point where the 1^1 orbit is created (Figure 3.3(b)). The upper branch immediately loses stability in a PD bifurcation $\text{PD}_4^{s=1}$ at virtually the same g_A value. The $s = 1$ MMO curve becomes stable again at another PD point $\text{PD}_5^{s=1}$ whilst the spiking branch also remains stable. This bistability endures until a PD point $\text{PD}_6^{s=0}$ is reached on the $s = 0$ branch where the 1^1 family connects with the 1^0 family. Beyond this point, the 1^1 family is stable and the 1^0 branch is unstable.

For the change from $s = 1$ to $s = 2$ for $C_m = 2$ pF, the 1^2 family is born in the $\text{SN}_6^{s=2}$ point with a stable upper branch and an unstable lower branch. The stable upper branch rapidly loses stability at a PD point $\text{PD}_7^{s=2}$ in Figure 3.3(c) (so that both the SN and PD points virtually coincide). The upper branch of the $s = 2$ curve eventually regains stability at another PD point $\text{PD}_8^{s=2}$. There is a small bistable window before the $s = 1$ MMO becomes unstable in a PD bifurcation $\text{PD}_9^{s=1}$. Subsequently, the $s = 1$ MMO remains unstable and the $s = 2$ MMO remains stable until the next MMO transition. The sequence of bifurcations from the $s = n$ to the $s = n + 1$ branch ($n = 1, \ldots, s_{\max} - 2$, where $s_{\max}$ is the maximum number of small oscillations observed) is similar. In our case, $s_{max} = 4$ and the above description of bifurcation sequences covers the $s = 2$ to $s = 3$ transition.

The last transition from the $s_{\max} - 1$ branch to the $s_{\max}$ branch requires special attention. The $s_{\max}$ branch is born in a SN point in the usual way, but the upper branch is born stable and remains so. Bistability between $s_{\max} - 1$ and $s_{\max}$ exists until the $s_{\max} - 1$ family loses stability via a PD bifurcation. The $s_{\max}$ branch remains stable until it terminates in a saddle-node on invariant circle (SNIC) bifurcation (Figures 3.3 and 3.4), after which the attractor of the system is a hyperpolarized state (labelled E_H in Figures 3.3 and 3.4).

3.2.3. The MMO regime. In light of Sections 3.2.1 and 3.2.2, Figure 3.5(a) shows the (g_K, g_A) diagram (Figure 3.1(a)) for $C_m = 2$ pF. We also include the corresponding (g_K, g_A)-bifurcation diagram for $C_m = 0$ pF in Figure 3.5(b) (for easier comparison between the $C_m = 2$ pF and $C_m = 0$ pF figures), but defer the discussion to Section 3.3.

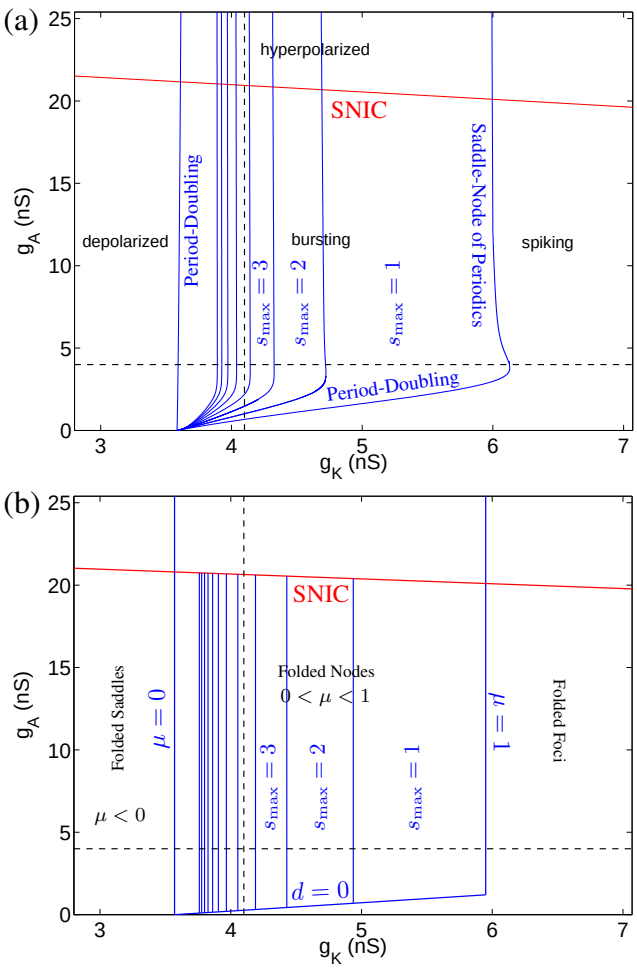

Figure 3.5. MMO boundaries in (g_K, g_A) space: (a) observed in the full 3D system (3.1) and (b) predicted from the singular limit (see Section 3.3.2). Vertical lines in (b) between $\mu = 0$ and $\mu = 1$ indicate candidate boundaries for the rotational sectors in (3.1) corresponding to odd integer values of μ^{-1}. Horizontal dashed lines correspond to $g_A = 4$ nS (Figure 3.2). Vertical dashed lines correspond to $g_K = 4.1$ nS (Figure 3.3).

For the $C_m = 2$ pF diagram (Figure 3.5(a)), we calculated the bursting boundaries using numerical continuation [**31, 79**]. The rightmost boundary is a curve of SN points which follows $\mathrm{SN}_2^{s=0}$ (Figure 3.2(b)) in (g_K, g_A) and marks the location where the spiking family destabilises. Note that a (g_K, g_A)-continuation of $\mathrm{SN}_1^{s=0}$ generates a similar curve to the right of $\mathrm{SN}_2^{s=0}$ (not shown). In fact, the $\mathrm{SN}_1^{s=0}$ and $\mathrm{SN}_2^{s=0}$ curves coalesce at a limit point near the corner of the bursting regime. The left and lower boundaries of the bursting regime form a single curve of PD points. These arise from a 2-parameter continuation of $\mathrm{PD}_6^{s=0}$ (Figure 3.3(b)). The $\mathrm{PD}_6^{s=0}$ point also generates a nearly vertical right border (not shown), which virtually sits on top of the $\mathrm{SN}_1^{s=0}$ border (cf. Figure 3.2(b)). Moreover, the right boundary generated by $\mathrm{PD}_6^{s=0}$ passes through the curve of SN points. To clarify, in Figure 3.5(a) we depict the right and lower boundaries of the MMO region as the $\mathrm{SN}_2^{s=0}$ branch and the $\mathrm{PD}_6^{s=0}$ branch up to its intersection with the $\mathrm{SN}_2^{s=0}$ branch.

There is a very thin strip in the $s_{\max} = 1$ sector where the MMO signature is some combination of 1^0 and 1^1. This thin strip is delimited on the right by the $\mathrm{SN}_2^{s=0}$ branch and on the left by a PD branch obtained from continuation of $\mathrm{PD}_2^{s=1}$ (not shown). For g_A away from the lower PD border, the $\mathrm{PD}_2^{s=1}$ branch sits to the left of the $\mathrm{SN}_2^{s=0}$ branch (hence the

complex MMO region). For smaller g_A, the situation is reversed and the $\text{PD}_2^{s=1}$ branch sits to the right of the $\text{SN}_2^{s=0}$ branch thus indicating bistable MMO regions (see Figure 3.3(b)).

As shown in Section 3.2.1, a 1^n MMO destabilises at a SN point whilst the adjacent 1^{n+1} MMO stabilises shortly after at a PD point. Two parameter continuation of these PD points generates a first approximation to the boundaries between MMO regimes. For instance, continuation of $\text{PD}_3^{s=2}$ (Figure 3.2(c)) gives the border between $s_{\max} = 1$ and $s_{\max} = 2$. Continuation of $\text{SN}_4^{s=1}$ (not shown) would generate a boundary very close to (and to the right of) the $\text{PD}_3^{s=2}$ border. We could then use this to identify the thin wedges in parameter space where the complex MMO patterns appear. Similarly, continuation of the PD points in Figure 3.3 where the $s = n$ branch destabilizes and the $s = n+1$ branch stabilizes generates thin strips in (g_K, g_A) space where bistability holds. In either case (complex MMOs or bistability), the strip covered in the (g_K, g_A) plane is extremely thin. As such we concern ourselves with the boundaries where a spike is added to the MMO pattern.

From the bifurcation analysis we have identified the regions in parameter space where the spike transitions occur in the bursting. We turn our attention now to the question of what causes these transitions. We use GSPT as the basis of our understanding.

3.3. Geometric Singular Perturbation Analysis of MMOs

System (3.1) is a slow/fast system written over the slow timescale t. Switching to a (dimensionless) fast timescale $\tau = t/\varepsilon$ yields an equivalent representation of (3.1):

$$\begin{aligned} V' &= f(V, n, e), \\ n' &= \varepsilon\, g_1(V, n), \\ e' &= \varepsilon\, g_2(V, e), \end{aligned} \tag{3.2}$$

where the prime denotes a τ derivative. Here we apply GSPT and canard theory (Chapter 2) to (3.1) to demonstrate the origin of the MMOs. Dynamically, (3.1) can be partitioned into slow and fast subsystems by taking the singular limit $\varepsilon \to 0$ ($C_m \to 0$) on the slow and fast timescales, respectively. The 2D reduced system given by $\varepsilon \to 0$ ($C_m \to 0$) in (3.1), is

$$\begin{aligned} 0 &= f(V, n, e), \\ \dot{n} &= g_1(V, n), \\ \dot{e} &= g_2(V, e). \end{aligned} \tag{3.3}$$

The 1D layer problem, given by $\varepsilon \to 0$ ($C_m \to 0$) in (3.2), is

$$V' = f(V, n, e), \tag{3.4}$$

with parameters (n, e). GSPT **[41, 68]** pieces together the information obtained from the lower dimensional subproblems (3.3), (3.4) to provide a unified global description of (3.1).

3.3.1. The reduced and layer problems. The critical manifold of the layer flow (3.4),

$$S := \left\{(V, n, e) \in \mathbb{R}^3 : f(V, n, e) = 0\right\}, \tag{3.5}$$

is a folded surface with respect to the fast variable V as shown, e.g., in Figures 3.6 and 3.7. This follows directly from the stability analysis of the 2D set of equilibria in (3.4), which possesses a subset of equilibria with a zero eigenvalue. In the physiological range of (n, e) this subset consists of two disjoint sets, the 1D fold curves

$$L^{\pm} := \left\{(V, n, e) \in S : f_V(V, n, e) = 0\right\}, \tag{3.6}$$

which divide S into attracting ($S_a^{\pm}$) and repelling (S_r) sheets. There also exist parameter sets of (g_K, g_A) where the two fold curves $L^{\pm}$ join in the physiological domain. In that case, the critical manifold forms a cusp (not shown here; see [**134**]).

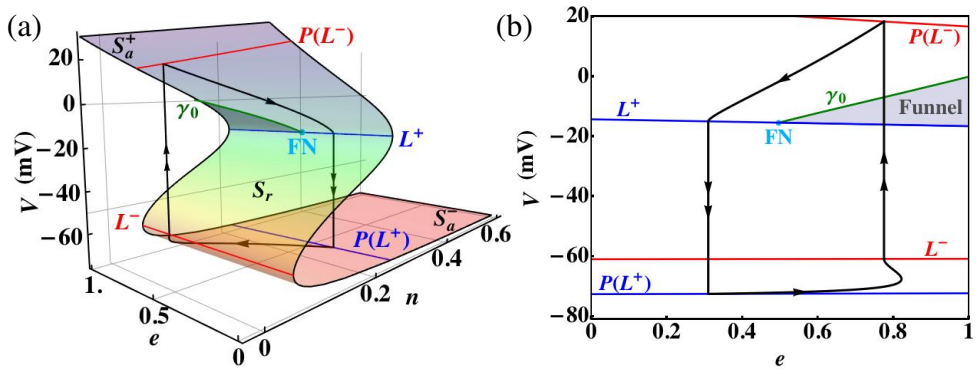

Figure 3.6. Singular spiking orbit for $g_K = 4.1$ nS, $g_A = 0.2$ nS: (a) 3D view and (b) projection onto the (V, e)-plane. The fast jumps (double arrow) join with the slow segments (single arrow) on the attracting sheets $S_a^{\pm}$. The fold curves $L^{\pm}$ and their projections $P(L^{\pm})$ indicate where the reduced flow jumps and where it lands, respectively. The grey shaded region between L^+ and the strong canard γ_0 is the funnel of the folded node (FN).

The critical manifold S is both the manifold of equilibria for the layer problem (3.4) and the phase space of the reduced problem (3.3), which describes the slow evolution along S. Since n (and e) enter $f(V, n, e)$ linearly, S has, e.g., a graph representation $n = n(V, e)$. As a result, a complete description of (3.3) can be obtained in the (V, e) coordinate chart. The resulting equations are

$$\begin{aligned} -f_V \dot{V} &= f_n g_1 + f_e g_2, \\ \dot{e} &= g_2, \end{aligned} \tag{3.7}$$

where $n = n(V, e)$ satisfies (3.5). The finite time blow-up of solutions along $L^{\pm}$ can be removed by rescaling time ($t = -f_V s$) to give the desingularized system

$$\begin{aligned} \dot{V} &= f_n g_1 + f_e g_2 \equiv F, \\ \dot{e} &= -f_V g_2, \end{aligned} \tag{3.8}$$

where the dot now denotes s derivatives. The flow of (3.8) is equivalent to (3.7) on $S_a^{\pm}$ but has the wrong orientation on S_r due to time rescaling. The desingularized system (3.8) has two kinds of equilibria: *ordinary* ($g_1 = g_2 = 0$) and *folded* ($F = f_V = 0$). In our model system, there is a single folded singularity on the upper fold curve L^+, which can be of node, saddle or focus type, depending on parameters. Folded node singularities are especially important to the bursting model (3.1) since they allow for canard solutions (Section 2.5), which in turn, can lead to canard-induced MMOs (Section 2.6).

3.3.2. Singular periodic orbits, relaxation oscillations and MMOs. Using the reduced and layer flows, singular periodic orbits can be constructed as continuous concatenations of slow and fast orbit segments. Singular periodic orbits which hit L^+ at a jump point (Figure 3.6) correspond to relaxation oscillations [**120**]. Singular periodic orbits which are filtered into the folded node on L^+ (Figure 3.7) are singular representations of MMOs (Section 2.6). Recall the two important diagnostics of a canard-induced MMO [**14, 119, 140**]:

(i) The eigenvalue ratio μ of the folded node, which essentially bounds the number of small oscillations, s, about the folded node (see (2.20)): $0 \le s \le s_{\max} := \lfloor \frac{\mu+1}{2\mu} \rfloor$.

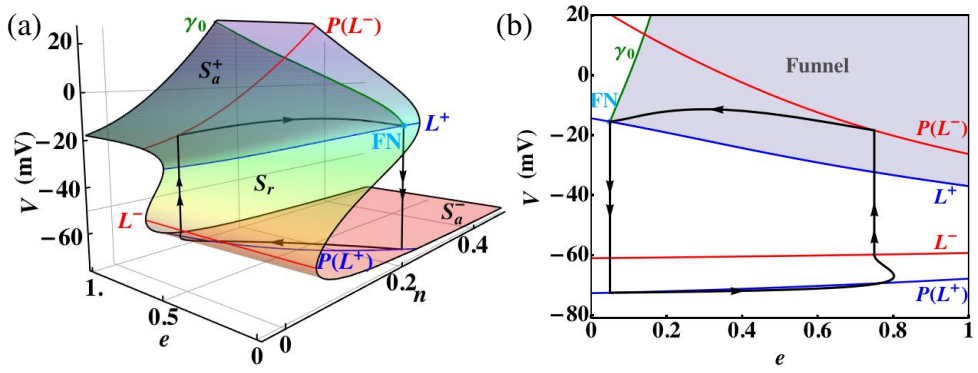

Figure 3.7. Singular MMO for $g_K = 4.1$ nS, $g_A = 2$ nS: (a) 3D view and (b) projection onto the (V, e)-plane. The main difference to the singular spiking orbit is that the fast up jump projects the singular orbit into the funnel of the folded node.

(ii) The distance d of global return trajectories on $P(L^-)$ to the strong canard γ_0.

Variation of the biophysical parameter g_K affects the repolarizing current in the active phase, the dynamics of which are associated with the local oscillations in the MMOs. Consequently, g_K controls (almost exclusively) the eigenvalue ratio μ. Similarly, variation of the biophysical parameter g_A affects the sub-threshold current in the silent phase, the dynamics of which are associated with the global resetting properties. As a result, g_A controls (almost exclusively) the distance d [**134**]. As such, we use (g_K, g_A) and (μ, d) interchangeably.

We can now justify our choice of the special horizontal and vertical directions in Section 3.2. By fixing $g_A = 4$ nS and $C_m = 2$ pF (Section 3.2.1), d is also essentially fixed provided we stay away from the lower MMO boundary in Figure 3.5(a). The only bifurcations that arise as g_K varies are due to changes in μ. By fixing $g_K = 4.1$ nS and $C_m = 2$ pF (Section 3.2.2), μ is fixed and the only quantity that varies is d (through variations in g_A). In particular, there is a maximum number of small oscillations; for $g_K = 4.1$ nS, and $C_m = 2$ pF resp. $C_m = 0.1$ pF, we find $s_{\max} = 4$ (Figure 3.3 resp. 3.4), which matches the singular limit prediction, i.e. $s_{\max} = 4$ in (2.20) for this specific example where $\mu \approx 0.122$.

In general, we wish to demonstrate that the singular limit systems ((3.3) and (3.4)) predict the behaviour of the full system (3.1) sufficiently well. Figure 3.5(b) shows a 2-parameter bifurcation diagram based on our singular limit analysis. The right $\mu = 1$ border of the MMO regime corresponds to a degenerate folded node where 2 nonzero eigenvalues merge. To the right of the $\mu = 1$ border we have folded foci which possess no canards and hence we predict relaxation oscillations. The left border $\mu = 0$ denotes a FSN II [**76, 119**] of the reduced flow (see Section 2.5.3). To the left of the $\mu = 0$ border we have a folded saddle on L^+ and a stable node on S_a^+, corresponding to a stable depolarized state of (3.1).

The $d = 0$ border indicates whether or not the global return mechanism projects the phase point of the singular orbits into the funnel. Below the $d = 0$ line, orbits land outside the funnel and relaxation oscillations are produced. Increasing d to positive values moves the phase point into the funnel so that MMOs are produced. The upper boundary of the MMO regime is a curve of SNIC bifurcations. Crossing this curve towards increased g_A annihilates the singular orbit and a stable hyperpolarized state becomes the attractor. The predictive power of GSPT for the boundaries of the MMO regime is evident from Figure 3.5.

3.3.3. The geometry of MMOs. We now examine the geometry of (3.1) away from the singular limit to explain the appearance of the small oscillations in a MMO. Fenichel theory [**41, 68**] guarantees that the regions of $S_a^\pm$, S_r that are $\mathcal{O}(1)$ away from $L^\pm$ perturb to invariant slow manifolds $S_{a,\varepsilon}^\pm$, $S_{r,\varepsilon}$ which are $\mathcal{O}(\varepsilon)$ close to their singular counterparts. The flow on

these perturbed manifolds is a smooth $\mathcal{O}(\varepsilon)$ perturbation of the reduced flow (Section 2.1). Extending $S^+_{a,\varepsilon}$ and $S_{r,\varepsilon}$ by the flow of (3.1) into the vicinity of a folded node results in a local twisting of the manifolds [**119, 140**] (Section 2.5). This geometric feature produces the small spikes seen during the active phase of a burst. Representative slow manifolds calculated up to a plane $\Sigma_e : e = e_{FN}$ passing through the folded node are depicted in Figure 3.8. The procedure for computing $S^+_{a,\varepsilon}$ and $S_{r,\varepsilon}$ is outlined in Section 2.7.

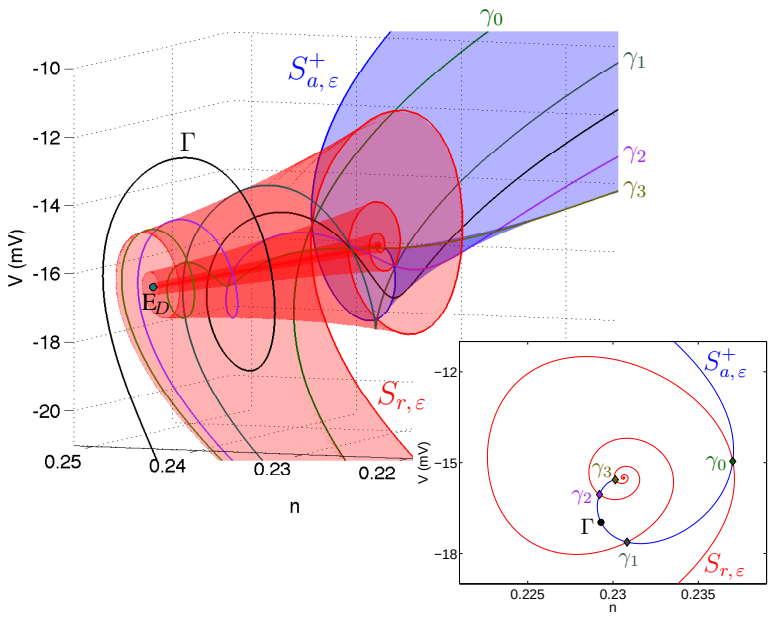

Figure 3.8. Slow manifolds $S^+_{a,\varepsilon}$ and $S_{r,\varepsilon}$ for $g_K = 4.1$ nS, $g_A = 1.2$ nS and $C_m = 2$ pF extended to cross-section $\Sigma_e : e \approx 0.083$ through the folded node. The intersections are maximal canards: the primary strong canard γ_0 and the secondary canards $\gamma_l, l = 1, 2, 3$. Each canard is consecutively separated by a full rotation. The attractor Γ of (3.1) is a 1^2 MMO and lies between γ_1 and γ_2 in rotational sector I_2. Also shown is a saddle equilibrium E_D on $S_{r,\varepsilon}$ (teal filled circle). Inset: intersection of $S^+_{a,\varepsilon}$ and $S_{r,\varepsilon}$ with cross-section Σ_e.

The rotational properties of the slow manifolds are closely related to the existence of canards in (3.1). The primary strong and weak canards, γ_0 and γ_w, correspond to the eigendirections of the folded node. The remaining $s_{\max} - 1$ secondary canards γ_l partition the funnel region between γ_0 and γ_w into $s_{\max}$ subsectors $I_k, k \in [1, \ldots, s_{\max}]$ each with different rotational properties. The rotations occur in $\mathcal{O}(\sqrt{\varepsilon})$ neighbourhoods of the folded node. At $\mathcal{O}(1)$ distances from L^+, the secondary canards are $\mathcal{O}(\varepsilon^{(1-\mu)/2})$ close to γ_0 whilst the maximal rotation sector has $\mathcal{O}(1)$ width. In the singular limit, all secondary canards collapse onto γ_0 [**14, 140**]. The vertical bifurcation diagrams (Figures 3.3 and 3.4) give an indication of the width of the rotational sectors I_k. For $g_K = 4.1$ nS, $C_m = 2$ pF (Figure 3.3), the maximal rotation sector I_4 is significantly larger than sectors I_1, I_2 and I_3. As C_m decreases the secondary canards approach γ_0 and the corresponding sectors decline in width (Figure 3.4), except for the maximal rotation sector I_4 which (almost) covers the entire MMO regime.

Figure 3.8 shows the maximal canards that connect $S^+_{a,\varepsilon}$ and $S_{r,\varepsilon}$. The green trajectory is the primary strong canard γ_0 and it makes one twist (half-rotation). The dark slate grey orbit is the first secondary canard γ_1, which makes 3 twists. The purple canard is γ_2, which makes 5 twists about the axis of rotation and the olive canard γ_3 is the third secondary canard, which makes 7 twists. Also shown are the saddle equilibrium E_D (teal point) of the system, which lies on $S_{r,\varepsilon}$ and the unique trajectory Γ (black) of the system for the given parameter values corresponding to a 1^2 MMO which lies in rotational sector I_2 bounded by γ_1 and γ_2.

These secondary canards explain the boundaries shown in the interior of the MMO region in Figure 3.5. In the singular limit diagram, Figure 3.5(b), the vertical lines in the interior of the bursting region which occur at resonant values of μ^{-1} indicate candidate boundaries for the rotational sectors since a maximal canard bifurcates from γ_w for odd integer μ^{-1} [**140**]. In order of decreasing g_K, the first vertical line in the interior of the MMO regime in Figure 3.5(b) corresponds to $\mu^{-1} = 3$. The next vertical line occurs at the g_K value for which $\mu^{-1} = 5$ and so on. A comparison of the singular and non-singular diagrams (Figures 3.5(b) and (a)) reveals a one-to-one correspondence between boundaries of the different MMO regions. Since all secondary canards collapse onto γ_0 ($d = 0$) in the singular limit, the almost linear segments of the interior MMO boundaries in Figure 3.5(a) collapse onto the $d = 0$ curve in Figure 3.5(b) and we are left with only the vertical segments in Figure 3.5(b).

We turn now to more qualitative methods based on the singular perturbation analysis to further our understanding of the spike-adding transitions in the MMO patterns.

3.4. Return Maps of MMOs

Return maps provide a tool to analyze periodic orbits and their stability [**46**] (see Section 2.6.4) and can be used to understand the dynamics in a simple and elegant way. The essential ingredient that the return map formulation developed here depends upon is the exponential contraction of the system along $S_{a,\varepsilon}$ [**27, 51, 53, 77, 85, 141, 142**]. Sections transverse to $S_{a,\varepsilon}$ quickly evolve to exponentially thin strips that can be approximated by curves. Thus, the flow map through an appropriately chosen section is strongly contracting and hence is almost 1D. Here we detail the formulation of singular and non-singular return maps which cover the essential dynamics. Our work is an amalgamation of [**77, 141, 142**] and [**53**] who use singular and non-singular return maps, respectively. In contrast to [**53, 141, 142**] who use a cross-section through the folded node (i.e. use the blow-up technique), we choose a cross-section that keeps the analysis simple and retains the essential dynamics for both $\varepsilon = 0$ and $\varepsilon \neq 0$. We show that vital information can be extracted from the singular limit return map. Hence we use the singular limit as a predictor for the non-singular case.

3.4.1. Singular return maps. Following [**77, 141**], we construct a singular return map to characterize the dynamics of the singular orbits [**50, 55, 120**]. For the reduced and layer flows, we define the following maps which track local and global properties of the flow:

- Trajectories of the reduced problem (3.3) starting from $P(L^-)$ outside the funnel can reach L^+ at a jump point and follow the layer flow (3.4) to S_a^-. Trajectories then follow the slow flow on S_a^- to L^- where they jump and return to $P(L^-)$. This map tracks the returns of jump points (see, e.g., Figure 3.6) and we denote it by
$$\Pi_J : P(L^-) \to L^+ \to P(L^+) \to L^- \to P(L^-).$$
- Trajectories of (3.3) starting from $P(L^-)$ inside the funnel reach L^+ at the folded node, FN $\in L^+$. Since these trajectories do not represent canards for $C_m \neq 0$, they jump in an $O(\sqrt{\varepsilon})$ neighbourhood of FN [**14, 140**]. Hence, we do not extend these singular canards onto S_r but let them jump at FN to S_a^-. They then follow the reduced flow on S_a^- to L^- where they jump and return to $P(L^-)$. This map tracks the returns of points in the interior of the funnel (see, e.g., Figure 3.7) and we denote it by
$$\Pi_F : P(L^-) \to FN \to P(L^+) \to L^- \to P(L^-).$$
- The strong canard γ_0 represents all rotational canards for $\varepsilon = 0$ and hence, trajectories of (3.3) can track γ_0 on S_r. These canard trajectories can jump off γ_0 at any point

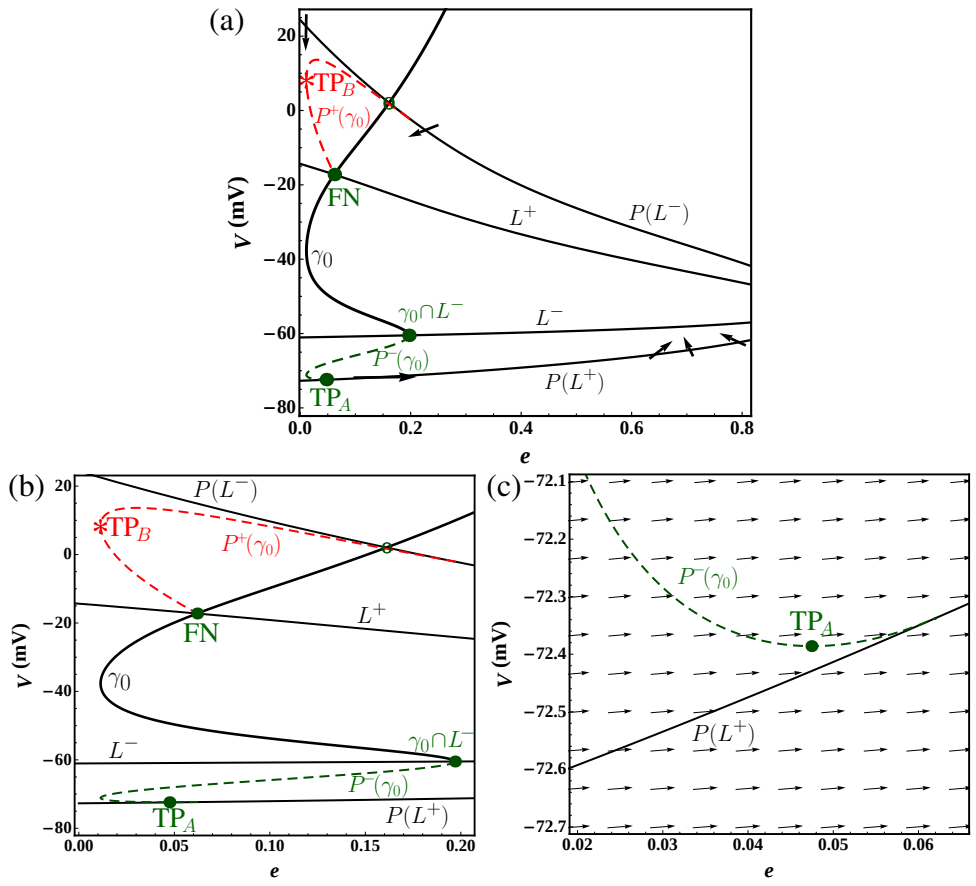

Figure 3.9. Reduced flow (3.3) for $g_K = 5$ nS and $g_A = 4$ nS: panels (b) and (c) are zooms. $P^{\pm}(\gamma_0)$ (red and green dashed curves, respectively) are the projections of γ_0 onto $S_a^{\pm}$, respectively. Note, (3.3) has a tangency with $P^+(\gamma_0)$ (red asterix TP$_B$) and $P^-(\gamma_0)$ (green circle TP$_A$).

on $\gamma_0 \cap S_r$ to S_a^- and flow into L^- before jumping to $P(L^-)$. The returns of these 'jump-away' canards are monitored via this map, denoted by

$$\Pi_A : \gamma_0 \cap S_r \to S_a^- \to L^- \to P(L^-).$$

- Trajectories of (3.3) tracking $\gamma_0 \cap S_r$ can jump up to S_a^+, flow into L^+ and subsequently return to $P(L^-)$. This map follows the returns of the 'jump-back' canards and we denote it by

$$\Pi_B : \gamma_0 \cap S_r \to S_a^+ \to L^+ \to P(L^+) \to L^- \to P(L^-).$$

We construct the first return map $\Pi_0 : \Sigma_0 \to \Sigma_0$ as the union of Π_J, Π_F, Π_A and Π_B. We take $\Sigma_0 = P(L^-)$ as the section so that the map is naturally parametrized by the coordinate e. To completely understand Π_0, the geometry of the reduced system must be examined in detail. Figure 3.9 shows the projection of the reduced flow (3.3) on the (V, e) plane for $g_K = 5$ nS, $g_A = 4$ nS with γ_0 on both attracting and repelling sheets of the critical manifold. The reduced flow along $P(L^-)$ is towards L^+. The reduced flow along $P(L^+)$ is away from L^- for small values of e (see Figure 3.9(c)) and towards L^- for larger values of e. This implies a point of tangency of the reduced flow with $P(L^+)$ for some $\tilde{e}$. Moreover, since e_{FN} is small and the reduced flow along $P(L^+)$ is directed away from L^- for small e, we have $\tilde{e} > e_{FN}$.

Consider two jump points $P_1(V_1, e_1)$ and $P_2(V_2, e_2)$ on L^+ with $0 < e_1 < e_2 < e_{FN}$. On jumping down to $P(L^+)$ the orientation $e_1 < e_2 < e_{FN}$ is preserved. However, since the

reduced flow is away from L^- for small e and towards L^- for larger e, this orientation is reversed when P_1 and P_2 are flowed forward to L^-. That is, the e coordinate of P_2 is to the left of the e coordinate of P_1 under the flow of (3.7). Thus if we track points described by Π_J, we observe a decreasing segment in Π_0 due to the orientation flip caused by the reduced flow on S_a^-. The corresponding (slightly) decreasing branch labelled I_0 is shown in Figure 3.10(a). Next, note that Π_F maps the whole funnel segment on $P(L^-)$ to a single value. This implies a horizontal segment in Π_0 which we observe as the branch I_1 in Figure 3.10(a).

The maps Π_A and Π_B create vertical segments in Π_0 due to canards [**11, 142**]. Thus, the singular map Π_0 is multivalued and not well-defined. We track the first returns of $\gamma_0 \cap S_r$ to deduce the vertical extent of these segments. Both start at FN, which is the beginning of the canard segment onto S_r. We start with the jump-away canards. As we follow γ_0 on S_r the returns initially increase from FN until they reach TP_A (Figure 3.9(c)), where the projections of the jump-away canards, $P^-(\gamma_0)$, have a tangency with the reduced flow. This point defines the maximum of the green vertical segment in Figure 3.10(a). As we follow γ_0 further on S_r the returns decrease monotonically until we reach the endpoint $\gamma_0 \cap L^-$. The endpoint $\gamma_0 \cap L^-$ jumps-back to S_a^+, landing exactly on $P(L^-)$, and corresponds to the minimum of the canard branch on Π_0 (Figure 3.10(a)). Simply put, the jump-away canards that follow $\gamma_0 \cap S_r$ furthest have the greatest vertical extent in the return map.

The projections of the jump-back canards, $P^+(\gamma_0)$, also have a tangency (TP_B in Figure 3.9) with the reduced flow. This introduces a corresponding turning point (TP_B in Figure 3.10(a)) in Π_0. We track the returns of $\gamma_0 \cap S_r$ once more, along with the return of the tangency. The jump-back canards start at the canard point FN where all branches of Π_0 intersect. As we travel along $\gamma_0 \cap S_r$ towards the endpoint on L^-, the returns of the jump-back canards increase until we encounter a maximum, corresponding to the tangency TP_B. As we trace $\gamma_0 \cap S_r$ further, the returns start to decrease from the maximum. If the projection $P^+(\gamma_0)$ lies outside the singular funnel, then the return of the endpoint $\gamma_0 \cap L^-$ is above the canard point of the map. If $P^+(\gamma_0)$ falls inside the singular funnel then the jump-back canards start at FN, increase to a maximum and then decrease back to FN.

Remark 3.2. The initial point $\gamma_0 \cap P(L^-)$ which tracks the strong canard may jump off $\gamma_0 \cap S_r$ precisely to $\gamma_0 \cap P^+(\gamma_0)$ (open circle in Figures 3.9(a) and (b)), thus generating a periodic jump-back canard cycle, which cannot be detected by Π_0. This return of canards to the funnel can generate chaotic invariant sets [**142**].

Note for $\mu = 1$, the strong and weak canards coincide and as μ decreases, the primary canards separate. Neither of them connect to the saddle E_D on S_r (not shown) and both travel along S_r towards L^-. Consequently, the singular returns for the weak canard γ_w are similar to those of the strong canard γ_0. In particular, the returns of γ_w form vertical branches in Π_0 attached to some point e_w in the singular funnel. The further μ decreases from 1, the further e_w moves away from FN into the funnel. Analogous to the strong canard, the endpoints of the vertical branches associated with γ_w are the turning point corresponding to the jump-back weak canard and the termination of γ_w on the lower fold L^-.

3.4.2. Non-singular return maps. For the fully perturbed problem (3.1) we define a similar first return map $\Pi_\varepsilon : \Sigma \to \Sigma$, where Σ is a suitably chosen cross section transverse to the flow far from the fold, and $\varepsilon = \frac{C_m}{k_t g_{\max}}$. The typical choice in numerical simulations was to take the section as a line of initial conditions on $S_{a,\varepsilon}^+$ with fixed coordinate n:

$$\Sigma = \left\{(V, n, e) \in S_{a,\varepsilon}^+ : n = n_\sigma,\ n_\sigma \text{ constant}\right\}.$$

We choose n_σ so that we are close to the landing point of trajectories that jump up to $S_{a,\varepsilon}^+$ from $S_{a,\varepsilon}^-$. In most instances, we take $n_\sigma = 0.04$. As in the singular case, this choice of

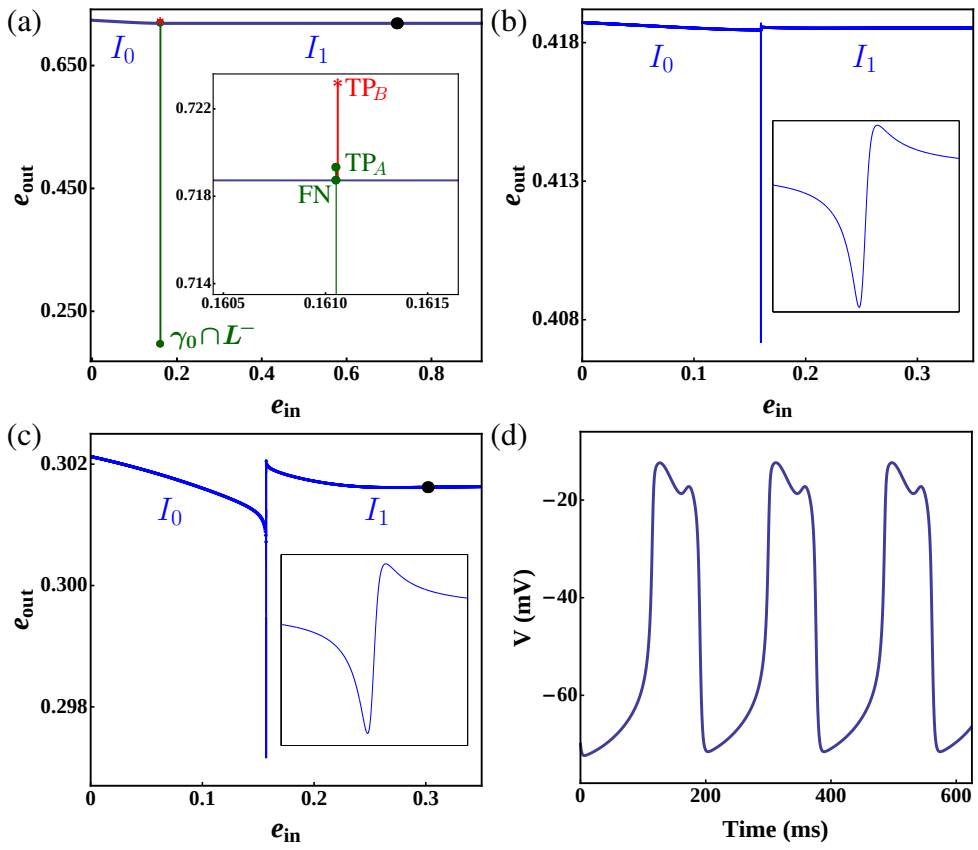

Figure 3.10. Return maps Π_ε for $g_K = 5$ nS, $g_A = 4$ nS and (a) $C_m = 0$ pF with inset showing the jump-back (red) and jump-away (green) canards. (b) $C_m = 0.2$ pF with inset showing a caricature of the vertical segment at the strong canard. (c) $C_m = 2$ pF. Panel (d) shows the attractor for $C_m = 2$ pF, a 1^1 MMO (as predicted). Fixed points are indicated by black markers. Note in (b) the fixed point lies outside the regime covered by Π_ε.

Σ leads to a map naturally parametrized by e. Note that such a section will cross $P(L^-)$. Thus, it only covers the return map between 0 and $e_{\max}$ where $e_{\max} < 1$. Nonetheless, the essential dynamics are covered. In particular, we observe all the attractors (relaxation and mixed mode oscillators) of the system.

Panels (b) and (c) of Figure 3.10 show the map Π_ε for $C_m = 0.2$ pF and $C_m = 2$ pF, respectively. As C_m increases, the vertical extent of the maps decreases rapidly but the structure of the singular return map Π_0 itself is preserved. The maximum associated with the turning point TP$_B$ in Π_0 persists under small perturbations as a local maximum of Π_ε. The fixed point (indicated by black markers) of the maps lies in rotational sector I_1 and the associated MMO pattern is indeed a 1^1 MMO (Figure 3.10(d)).

The apparent jump in the perturbed maps Π_ε is the strong canard, which divides trajectories between relaxation oscillations and MMOs. These regions of rapid expansion in Π_ε reflect the instability of trajectories flowing along the canards on $S_{r,\varepsilon}$ for various times before jumping to $S^{\pm}_{a,\varepsilon}$ [**53**]. The vertical extent of these near vertical segments is not clear from the simulations due to the stiffness of the problem. To clarify, each seemingly disjoint branch of the map Π_ε is in fact continuously connected to each other. Limitations in the numerical integration scheme prevents these segments of rapid variation from being computed using initial value solvers. We use boundary value solvers instead to compute the canard segments.

The procedure for computing Π_ε involves 2 parts: computing the regular parts of Π_ε away from canards and approximating the (nearly vertical) exponentially thin segments near

a canard. As in the computation of canards (Section 2.7), we rescale solutions to the time interval $[0, 1]$. For the regular parts of Π_ε, we require initial conditions on $S^+_{a,\varepsilon}$ with $n = n_\sigma$. To initialize the computation, we take a line of initial conditions on S^+_a far from Σ:

$$\mathbf{u}(0) \in \left\{(V, n, e) \in S^+_a : V = 100\right\}.$$

This line of initial conditions is then flowed forward until they hit the section Σ, at which point the calculation is terminated. That is,

$$\mathbf{u}(1) \in \Sigma = \left\{(V, n, e) : n = n_\sigma,\ n_\sigma \text{ constant}\right\}.$$

Exponential contraction of (3.1) ensures that this curve is sufficiently close to $S^+_{a,\varepsilon}$. We use the curve $S^+_{a,\varepsilon} \cap \Sigma$ as the initial conditions in Π_ε and flow them forward until they return to Σ. This produces a return map naturally parametrized by e. For any maximal canards crossed, there is a seemingly discontinuous jump and the map appears to have disjoint branches. The distance Δe between the distinct branches (where there is no data) is nonzero and depends on the number of points used to compute Π_ε. The more points used to parametrize $S^+_{a,\varepsilon} \cap \Sigma$, the smaller the 'gap' Δe. In our calculations, we typically used 2000 points.

By continuity of solutions of (3.1), all branches of the map are in fact continuously connected to each other by exponentially thin canard segments. To compute these canard segments, we first use AUTO to identify the maximal canards (Section 2.7). The endpoint of the canard on S_r is then extended as close to the lower fold curve L^- as possible to give an indication of the vertical extent of the canards. We also extend the endpoint of the canards on S^+_a out to the section $\Sigma_V : V = 100$ and then flow it forward to obtain the corresponding canard point on $S^+_{a,\varepsilon} \cap \Sigma$. The canard point in $S^+_{a,\varepsilon} \cap \Sigma$ always sits in the interval of width Δe between the distinct branches of Π_ε.

We then take the points of the canard on $S_{r,\varepsilon}$ and perturb them in either V direction (towards either $S^\pm_{a,\varepsilon}$). Those points that sit above $S_{r,\varepsilon}$ jump-back to $S^+_{a,\varepsilon}$ whilst those that sit below $S_{r,\varepsilon}$ jump-away to $S^-_{a,\varepsilon}$. The returns of these points to the section Σ give the returns of the jump-back and jump-away canards. To complete the computation of the return map, we must determine the initial conditions in Σ corresponding to the jump-back and jump-away canards. Since it is impossible to trace the returns of these canards to their origin in the section Σ, we use interpolation to approximate the distribution of these returns in a neighbourhood of the canard point. As in [**53**] we terminate the canard branch when it intersects the regular part of Π_ε so that we have a continuous map.

3.5. Bifurcations of the Return Maps

We now use the singular and non-singular return maps Π_0 and Π_ε to track the bifurcations of MMOs in the lactotroph model (3.1) and show that the return maps cover the essential dynamics. Our work differs from [**53**] who employ kneading theory and numerical analysis for a qualitative and quantitative description of the bifurcation sequence related to a FSN II. Here, we (qualitatively) describe the bifurcation sequences associated with the primary and secondary canards of a folded node. To our knowledge, there have been no prior studies of the bifurcation sequences of folded node type canards using return maps, especially near their creation (birth) at $\mu = 1$. As in Section 3.2, we focus on the horizontal and vertical directions in the 2-parameter diagram (Figures 3.2, 3.3 and 3.5). That is, we track the bifurcations which arise from variations in μ and d via the return maps.

3.5.1. Horizontal bifurcations - variation of μ and birth of canards. Fixing $g_A = 4$ nS, the distance d from the strong canard is essentially fixed as g_K varies and so the bifurcations of interest in this scenario are the ones that arise from the creation of canards.

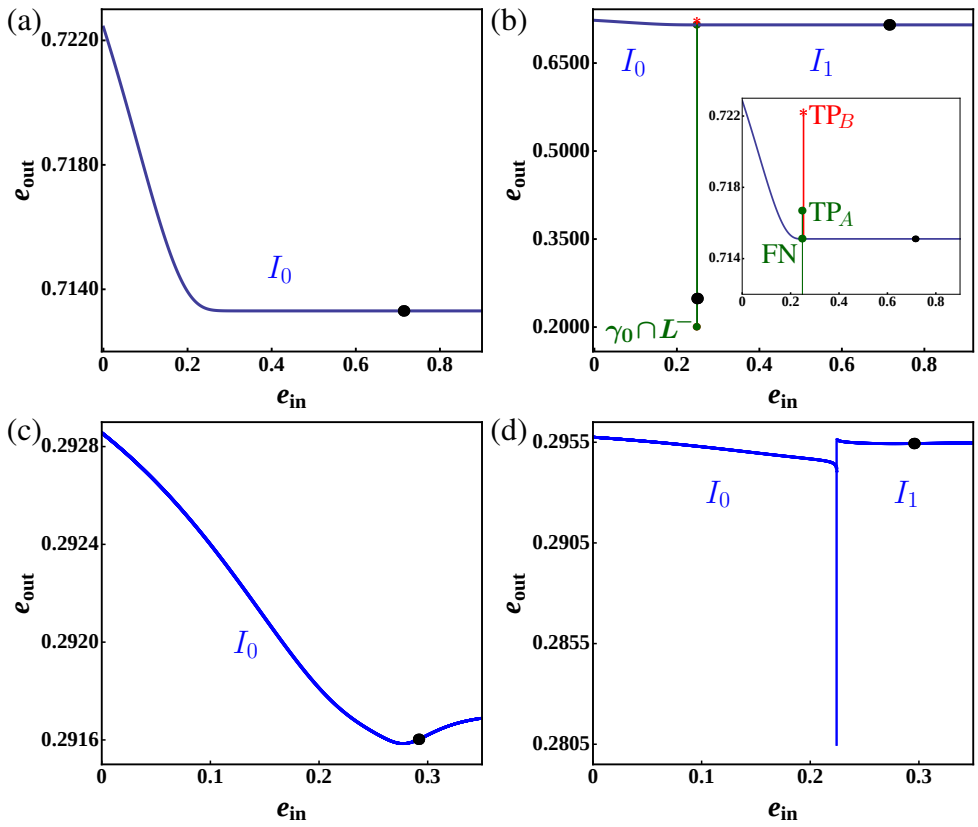

Figure 3.11. Return maps Π_ε for $g_A = 4$ nS: (a) $C_m = 0$ pF, $g_K = 6.2$ nS, (b) $C_m = 0$ pF, $g_K = 5.8$ nS, (c) $C_m = 2$ pF, $g_K = 6.2$ nS, (d) $C_m = 2$ pF, $g_K = 5.8$ nS. Fixed points are indicated by black dots.

For large g_K, the reduced system has folded foci on L^+ (Figure 3.5), there are no canards and the singular limit map Π_0 is well defined (Figure 3.11(a), $g_K = 6.2$ nS). The dynamics are strongly attracting to a stable fixed point of Π_0, representing relaxation oscillations. The associated perturbed map Π_ε (Figure 3.11(c)) preserves this structure of Π_0. Namely, Π_ε is regular, well-defined and has a single fixed point representing a relaxation oscillator.

As g_K decreases so that μ becomes real, i.e. $\mu < 1$, the singular system has a folded node. There are two fixed points of the associated return map Π_0 with the stable one falling in the funnel region I_1 (Figure 3.11(b), $g_K = 5.8$ nS). For $C_m = 2$ pF, the corresponding Π_ε map is multimodal with two distinct branches, separated by near vertical jumps (Figure 3.11(d)). The left branch is the spiking branch (I_0). Initial conditions on this part of the map exhibit a relaxation oscillation in their tra nsient solution. The right I_1 branch of the map corresponds to a 1^1 bursting oscillation which is observed for $g_K = 5.8$ nS (Figure 3.2(a)) and is expected from the singular limit prediction.

To understand the bifurcation sequence in Figure 3.2(b), we examine the unfolding of Π_ε as g_K decreases (Figure 3.12). Before the degenerate folded node, Π_ε is regular with a local minimum occurring in a neighbourhood of the folded singularity (Figure 3.12(a)). As g_K decreases (with μ still complex), this local minimum sharpens becoming almost cusp-like and signalling the formation of a canard (Figure 3.12(b)). When g_K reaches the degenerate folded node, $\mu = 1$, the slow manifolds $S^+_{a,\varepsilon}$ and $S_{r,\varepsilon}$ are tangential signalling the birth of the primary canards ('vertical branches' in Figure 3.12(c)-(d)), which quickly separate as μ decreases (Figure 3.12(e)-(f)).

Note that just after the bifurcation, Π_ε has 3 distinct branches, I_0, I_1 and I_0 (Figure 3.12(c)-(e)). Figure 3.13(a) shows the slow manifolds in the cross-section $\Sigma_e : e = e_{FN}$.

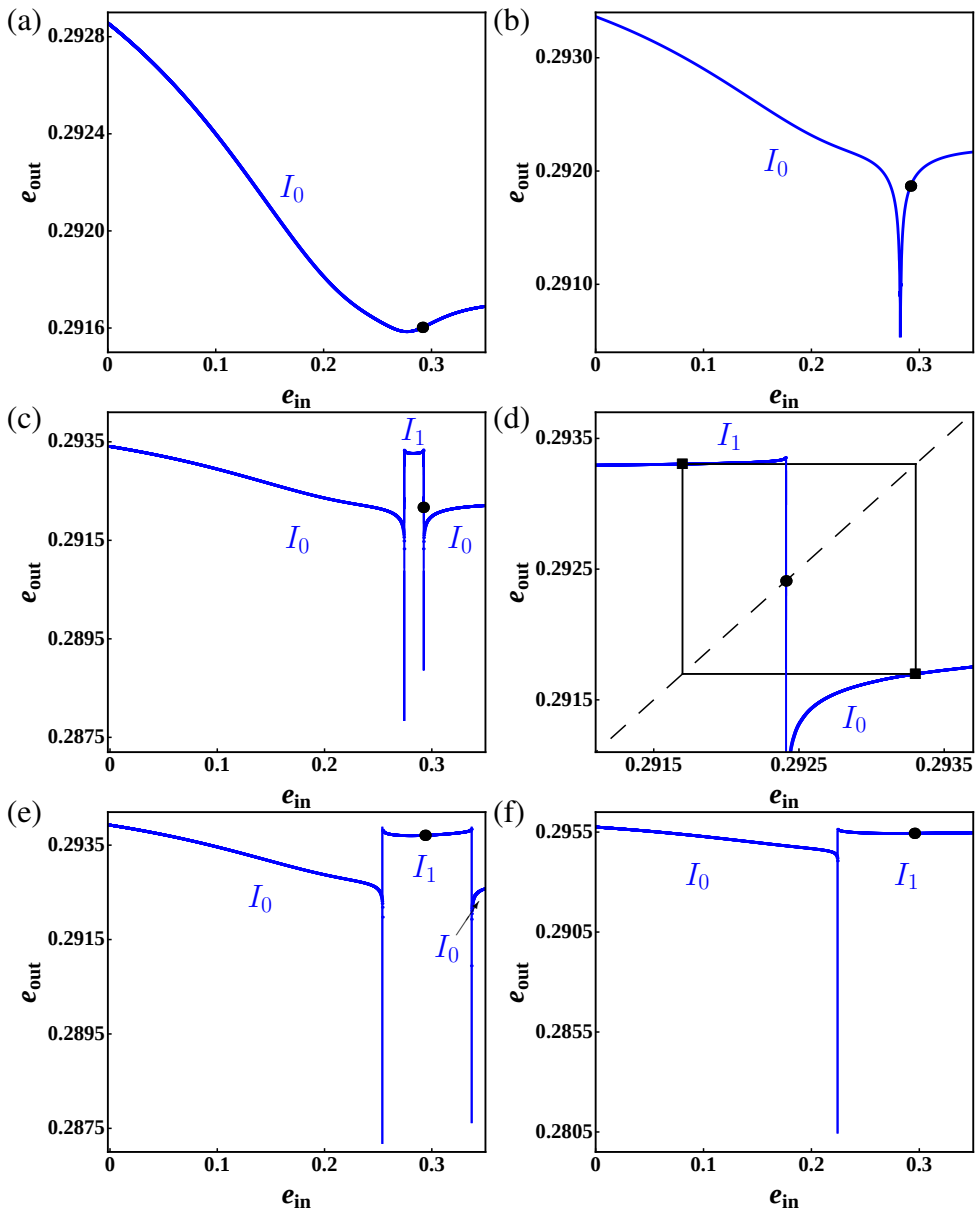

Figure 3.12. Return maps Π_ε for $C_m = 2$ pF and $g_A = 4$ nS: (a) $g_K = 6.2$ nS, 1^0 spiking, (b) $g_K = 6.12824$ nS, 1^0 spiking, (c) $g_K = 6.1225$ nS, $1^0 1^1$ MMOs, (d) Zoom of right vertical segment in (c), (e) $g_K = 6.05$ nS, 1^1 MMOs, (f) $g_K = 5.8$ nS, 1^1 MMOs. The strong (weak) canard corresponds to the left (right) vertical segment. Fixed points (black dots) move from I_0 to I_1. In (d), the $1^0 1^1$ MMO is represented in the maps as a 2-cycle.

Subsector I_1 is the segment of $S^+_{a,\varepsilon}$ bound by γ_0 and γ_w. The two distinct I_0 subsectors are identified as the disjoint parts of $S^+_{a,\varepsilon}$ outside I_1. Also shown are solutions $\Gamma_1, \Gamma_2, \Gamma_3$, taken from the sectors I_0, I_1 and I_0, respectively (Figure 3.13(b)). The orbit Γ_1 starts on $S^+_{a,\varepsilon}$ 'prior' to γ_0, i.e. outside the funnel, and jumps away to more negative V without rotation. The orbit Γ_2 lies in the funnel region between γ_0 and γ_w, and makes a single transient rotation. The orbit Γ_3 starts on $S^+_{a,\varepsilon}$ 'after' the weak canard and like Γ_1, has a spiking transient. As g_K decreases, the I_1 branch quickly expands to larger e values and the right I_0 branch is eventually pushed out of the domain covered by the map (Figure 3.12(f)).

The reason for the difference between Γ_2 and Γ_3 is as follows: for $1 < \mu^{-1} < 2$, $S^+_{a,\varepsilon}$ makes a twist around the weak canard. Then the sector I_1 lies above $S_{r,\varepsilon}$ after passage near

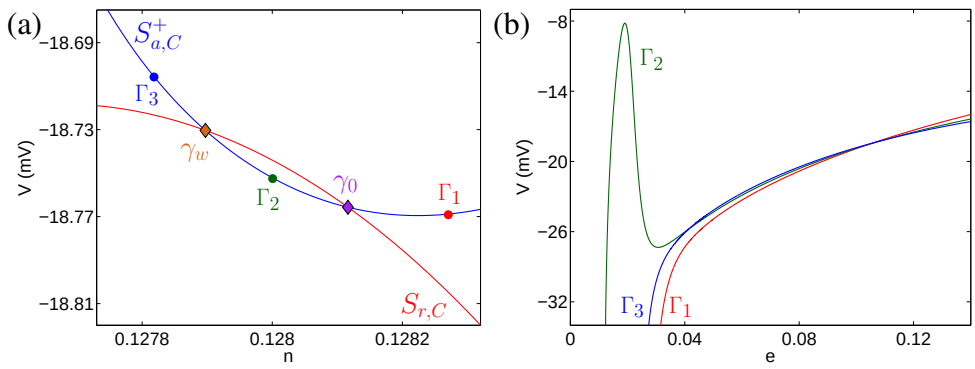

Figure 3.13. Trajectories with different rotational properties for $C_m = 2$ pF, $g_K = 6.1225$ nS and $g_A = 4$ nS. (a) Zoom of $S^+_{a,\varepsilon} \cap \Sigma_e$ and $S_{r,\varepsilon} \cap \Sigma_e$. (b) Orbits $\Gamma_1, \Gamma_3 \in I_0$ and $\Gamma_2 \in I_1$.

the folded node and hence jumps back to $S^+_{a,\varepsilon}$ where it finishes a full rotation before jumping to $S^-_{a,\varepsilon}$, which explains the rotation number $s = 1$. On the other hand, the sector I_0 bound by γ_w and the fold L^+ lies (after passage of the folded node) below $S_{r,\varepsilon}$ and hence jumps to $S^-_{a,\varepsilon}$ without any extra rotation, which accounts for the rotation number $s = 0$. The two different behaviours can be clearly observed in Figure 3.13(b). More generally, initial conditions between γ_w and L^+ rotate $s_{\max} - 1$ times before jumping away (see Section 3.5.3).

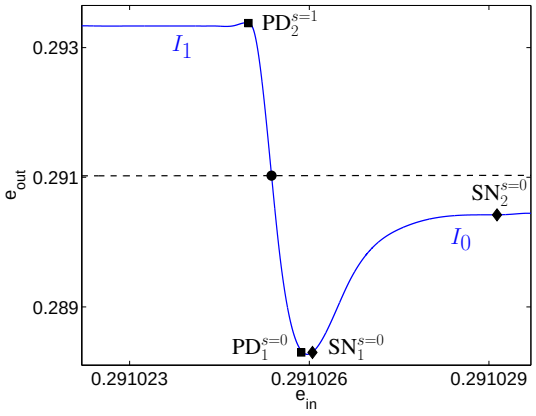

Figure 3.14. Zoom of return map Π_ε for $g_A = 4$ nS, $C_m = 2$ pF, $g_K = 6.1235$ nS. The fixed point (black dot) is highly unstable and the attractor is a $(1^0)^4 1^1$ MMO (not shown).

Figure 3.14 shows a zoom of the return map Π_ε for $g_K = 6.1235$ nS near the vertical branch associated with the weak canard. Recall from Section 3.4.1 that the local maximum in Figure 3.14 is due to a turning point in the jump-back weak canard and the local minimum is due to the termination of the jump-away weak canard. Here, rather than consider a bifurcation diagram, we consider a single snapshot of a 3-parameter family of maps. Since the local topological structure of the map is preserved under changes in the bifurcation parameter, the only thing that changes is the position of the diagonal relative to the map. Hence we proceed on the understanding that the indicated bifurcations occur when a fixed point, i.e., an intersection of the map with the diagonal, crosses the special points.

We observe that the diagonal 'moves up' relative to the map as g_K decreases. For $g_K > 6.127$ nS there is a stable fixed point to the right of the local minimum. As g_K decreases the diagonal will first touch the map at the $SN_1^{s=0}$ point which is followed immediately by the $PD_1^{s=0}$ point where the newly created stable fixed point loses its stability. As g_K decreases further, the stable spiking branch $s = 0$ loses its stability at the $SN_2^{s=0}$ point. The 1^1 MMO

branch then becomes stable at $\mathrm{PD}_2^{s=1}$. In between the $\mathrm{SN}_2^{s=0}$ and the $\mathrm{PD}_2^{s=1}$ points, there is a parameter window in which there are no stable fixed points and the MMO attractor is an n-cycle with k period-n points on the $s=0$ branch and $(n-k)$ period-n points on the $s=1$ branch, where k is typically either 1 or $n-1$. The stable $1^0 1^1$ MMO pattern is identified in the map shown in Figure 3.12(d) as a 2-cycle. This explains precisely the sequence of bifurcations detected in Figure 3.2, which is closely related to the birth of canards.

3.5.2. Vertical bifurcations - variation of d and crossing of strong canard. Fixing $g_K = 4.1$ nS, the maximal number of rotations is $s_{\max} = 4$. We construct Π_0 and Π_ε, and explore the bifurcations associated with the passage of d as it crosses zero. The return maps before and after this bifurcation sequence are shown in Figure 3.15 for $C_m = 0,\ 2$ pF.

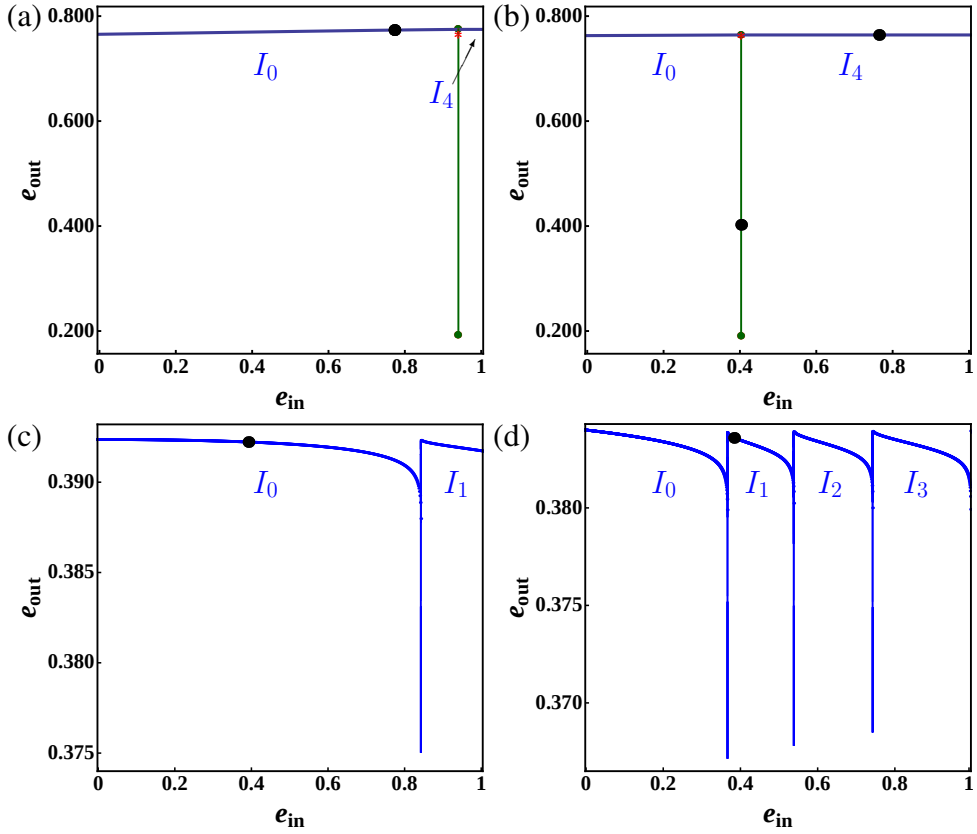

Figure 3.15. Return maps Π_ε for $g_K = 4.1$ nS where $s_{\max} = 4$: (a) $C_m = 0$ pF, $g_A = 0.3$ nS ($\delta < 0$), (b) $C_m = 0$ pF, $g_A = 0.7$ nS ($\delta > 0$), (c) $C_m = 2$ pF, $g_A = 0.3$ nS, (d) $C_m = 2$ pF, $g_A = 0.7$ nS. The fixed point (black dots) shifts from sector I_0 to I_1.

For $g_A = 0.3$ nS, the distance d of the global returns from the strong canard is negative and the trajectories exhibit relaxation oscillations. The corresponding maps (Figure 3.15(a) and (c)) reflect these dynamics. The fixed point (black dot) of the singular map Π_0 sits to the left of the canard point (Figure 3.15(a)). Thus the attractor is a relaxation orbit.

For $g_A = 0.7$ nS and $C_m = 0$ pF, d is positive. The singular map Π_0 (Figure 3.15(b)) has two fixed points: one stable on the maximal rotation branch I_4 and one highly unstable on the canard branch. As the perturbation is switched on, the secondary canards (represented in the singular limit by γ_0) bifurcate out of γ_0. The non-singular map Π_ε has five distinct branches, each separated by nearly vertical segments (Figure 3.15(d) shows only three branches – the other two exist outside the physiological domain $e > 1$). The leftmost branch I_0 corresponds to relaxation oscillations where the global return trajectories land outside the funnel (i.e.

$d < 0$). The I_1 branch of Π_ε is the region of the funnel where MMO patterns only have one small oscillation. The subsequent branches progressively move through the rotational sectors until the maximal rotation sector I_4 is reached. The stable fixed point of the map occurs on the I_1 branch and this is reflected in the observed 1^1 MMO pattern.

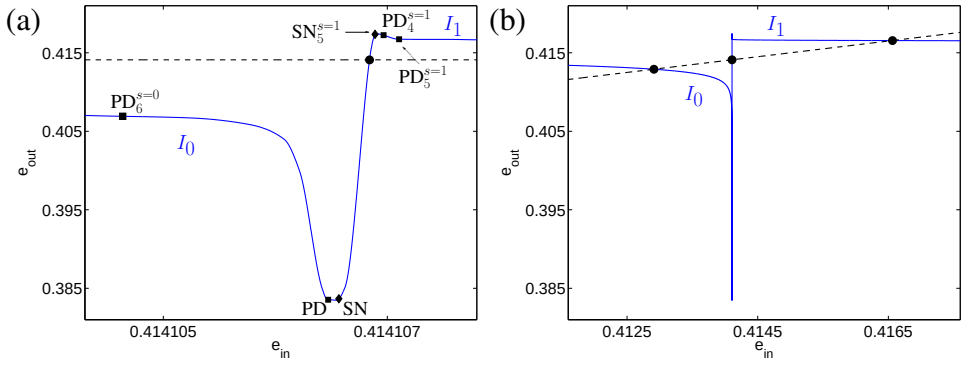

Figure 3.16. Return map Π_ε for $g_K = 4.1$ nS, $C_m = 2$ pF, $g_A = 0.672$ nS where $s_{\max} = 4$. The fixed point (black dots) shifts from the left spiking branch to the $s = 1$ bursting branch.

When g_A is small, only the spiking and first bursting branches of Π_ε lie in the physiological domain (Figure 3.15(c)). As g_A increases, the branches of the map contract and shift to smaller e so that higher order bursting branches enter the physiological domain (Figure 3.15(d)). Consequently, the fixed point occurs closer to the MMO branches. The transition from I_0 to I_1 can be observed in Figure 3.16 (which is a snapshot of Π_ε for fixed (C_m, g_K, g_A) rather than a bifurcation diagram; cf. Figure 3.14). As g_A continues to increase, the first intersection of the diagonal with the $s = 1$ branch occurs when Π_ε has slope 1 (bifurcation point $SN_5^{s=1}$) just before the local maximum of the jump-back canards (see also Figure 3.3(c)).

As g_A increases further, the $s = 1$ branch of the map becomes stable as the diagonal passes through a point with slope -1 ($PD_4^{s=1}$) to the right of the maximum associated with the jump-back canards. Thereafter, there is a window of g_A values for which there are two stable fixed points, one on the spiking branch $s = 0$ and the other on the $s = 1$ bursting branch (Figure 3.16(b)). There is also an highly unstable fixed point on the canard branch. As g_A moves to larger values still, the fixed point on the spiking family loses stability at $PD_6^{s=0}$ point (Figure 3.3(c)) and the $s = 1$ MMO is the only attractor of the system. Thus the return maps Π_ε predict the sequence of bifurcations shown in Figure 3.3 and the bistability of the MMO orbits.

3.5.3. Crossing and creation of secondary canards. To complete the discussion of the return maps, we examine the structure of Π_ε under two circumstances: when a trajectory crosses a secondary canard into a different rotational sector (vertical bifurcations) and when a secondary canard bifurcates from the primary weak canard (horizontal bifurcations). As seen in Section 3.2, the bifurcation structure of (3.1) follows similar trends in the transitions between MMO families under variations in d and μ. The return map Π_ε reflects this as shown in Figure 3.17.

Variations in d have the effect of shifting the map relative to the diagonal but have virtually no impact on the structure (topology) of the map. For $g_K = 4.1$ nS, the maximal number of rotations is $s_{\max} = 4$ so the return map Π_ε has 5 branches. Starting with g_A small, increasing g_A shifts the diagonal to the right relative to the map so that the fixed points shift to MMO branches with higher rotation number. In terms of the funnel, orbits are pushed away from the strong canard, moving deeper into the rotational subsectors. Bistable MMO orbits can also be detected near the switch from one rotational subsector to another. These

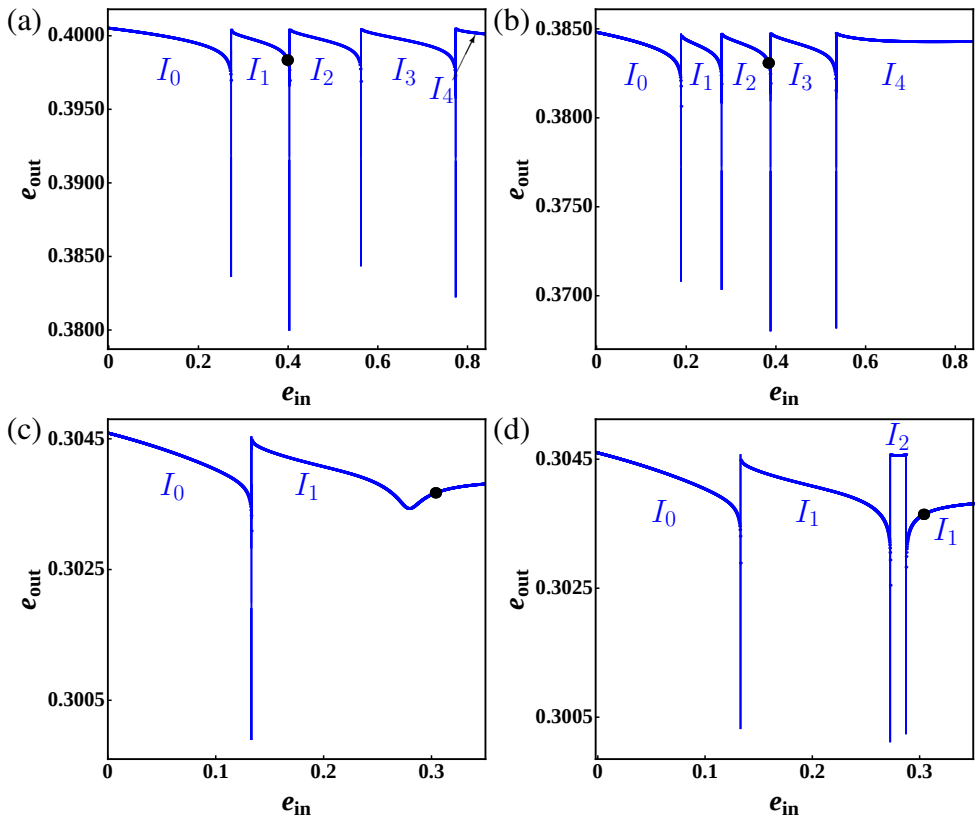

Figure 3.17. Return maps Π_ε for $C_m = 2$ pF under variations in d and μ: (a) $g_K = 4.1$ nS, $g_A = 1$ nS, (b) $g_K = 4.1$ nS, $g_A = 1.45$ nS, (c) $g_K = 4.723$ nS, $g_A = 4$ nS, (d) $g_K = 4.722$ nS, $g_A = 4$ nS. Black dots denote fixed points of the map.

manifest in the maps as two stable fixed points occurring on adjacent MMO branches. The bifurcations that occur arise as the trajectories cross the canards.

In the crossing from $s = 1$ to $s = 2$ (Figure 3.17(a)), the diagonal initially intersects the $s = 1$ branch at a stable fixed point. As the diagonal 'moves to the right' relative to the map under increases in g_A (we again think of the map frozen since its topological structure is preserved under parameter changes), it encounters the stable $s = 2$ branch at the $\text{SN}_6^{s=2}$ point (Figure 3.3(c)). This stability is short-lived as the diagonal 'shifts right' (relative to Π_ε) and encounters the $\text{PD}_7^{s=2}$ point where the $s = 2$ branch turns unstable. The concavity of the $s = 2$ branch allows the slope to decrease from -1 and then increase back to -1 so that the $s = 2$ MMOs regain their stability via another PD indicated by the point $\text{PD}_8^{s=2}$ in Figure 3.3(c). As the diagonal shifts further to the right (relative to the map), the fixed point on the $s = 1$ MMO branch passes through the PD point $\text{PD}_9^{s=1}$ and becomes unstable. This is exactly the bifurcation sequence shown in Figure 3.3(c).

Under variations in μ, secondary canards bifurcate from γ_w thus forming new branches in the map. The creation of these new branches introduces almost vertical segments in Π_ε. For $g_K = 4.723$ nS, the 1^1 MMO is the attractor and is represented by a stable fixed point on the I_1 branch of Π_ε (Figure 3.17(c)). The I_1 branch has a local minimum, which as g_K decreases, becomes significantly sharper until it reaches a SN bifurcation corresponding to $\text{SN}_3^{s=2}$ in Figure 3.2(c). At this point the I_1 branch breaks into two distinct branches with an additional, newly created I_2 branch in between (Figure 3.17(d)). The left vertical boundary of I_2 corresponds to the newly created secondary canard γ_1. The right vertical boundary corresponds to γ_w. Note that the rightmost I_1 branch is the subsector bound by γ_w and the fold (cf. Figure 3.12(c) at the $\mu = 1$ bifurcation). As in the $\mu = 1$ case, the

SN point corresponds to a tangency between $S^+_{a,\varepsilon}$ and $S_{r,\varepsilon}$, which then perturbs to transverse intersections. As g_K decreases further, the I_2 branch rapidly expands to larger e values and the right I_1 branch is pushed out of the physiological domain. In this process, the right I_1 branch loses stability at $\mathrm{SN}_4^{s=1}$ in Figure 3.2(c). The I_2 branch then becomes stable at $\mathrm{PD}_3^{s=2}$. The return map Π_ε and the associated bifurcation sequence (Figure 3.2(c)) in this case is analogous to the situation in Figure 3.14 (Section 3.5.1).

3.6. Discussion

MMOs in multiple timescale systems are the result of the combined interaction between a local mechanism and a global mechanism. The local mechanism is the folded node of the reduced flow (3.3), which causes a local twisting of the slow manifolds and hence local rotations of trajectories. The global mechanism is the global return which re-injects trajectories into the funnel region and thus resets the dynamics after completion of the local passage. In this chapter, we showed that the calcium-conducting bursts were canard-induced MMOs and we studied their bifurcation structure.

Using geometric singular perturbation analysis, we demonstrated the origin of the MMO, identified the region in parameter space where it exists, and showed how the number of small amplitude oscillations varies in parameter space. The curves in the (g_K, g_A) parameter space that bound the MMO region in the singular limit correspond one-to-one with those that bound the bursting region away from the singular limit. Thus, the analysis performed at the singular limit not only reveals the subtle mechanism of bursting, but also provides information on the extent of bursting that is consistent with the bifurcation analysis of the full system.

Importantly, the singular perturbation analysis provides information on features that were not apparent from the bifurcation analysis of the full system. While the full system analysis provided boundaries for the bursting region in parameter space, it did not fully explain the rationale for these boundaries. The singular perturbation analysis gave a clear rationale, in terms of the properties of the folded node singularity and the curves delimiting the singular funnel. It was clear from the singular analysis that the appropriate parameter space to work in was (μ, d) space. Also, the singular analysis provided information on how the number of spikes in a burst varies in parameter space: information that could not be obtained from the bifurcation analysis of the full system (but required numerical simulation).

While the singular perturbation analysis has many virtues, it also has limitations. Most obviously, the singular analysis is only guaranteed to be valid for sufficiently small C_m. Also, the analysis is most effective when there are no more than two slow variables. Thus, the singular analysis has limitations that are not present in the full system bifurcation analysis. This emphasizes the power of combining the two analysis techniques: singular perturbation analysis to understand the oscillation mechanism and extent in parameter space, and full system bifurcation analysis to extend the singular analysis to the non-singular situation that is likely a more accurate description of the biological system.

We then employed bifurcation analysis, GSPT and return map analysis to examine the bifurcation structure of the canard-induced MMOs. Each technique provided substantial information and it was their combination that allowed us to understand the phenomenon of spike-adding in pseudo-plateau bursters. We constructed singular and non-singular return maps Π_0 and Π_ε so that we could study the dynamics in the setting of 1D maps. This relied on the geometry and exponential contraction of (3.1). The exponential contraction reduces the problem of studying the bifurcations of MMOs under variations of ε, μ and d to the study of bifurcations in a 3-parameter family of maps. The resulting maps Π_ε were multimodal and seemingly discontinuous. The distinct branches of Π_ε arise from the canard orbits.

Trajectories that follow a maximal canard on opposite sides of $S_{r,\varepsilon}$ are torn apart and follow very different evolutions, thus causing the rapid vertical expansion in the maps.

One of the strengths of the return map formulation is that the partitioning of the funnel can be characterized in a simple way. The canard trajectories act as separatrices in the return maps, clearly dividing trajectories with differing numbers of twists around the weak canard. The main insight obtained from Π_0 is the extent of the vertical segments of the canards in Π_ε. Moreover, the turning points of Π_0 on S_a^+ have a one-to-one correspondence with local extrema in Π_ε. The main bifurcation sequences detected consist of only SN and PD points. In studying the transitions between MMO branches, this is sufficient. However as $\mu \to 0$ (FSN type II), different tools are needed to explain the bifurcation structure near the singular Hopf bifurcation [**52, 76**] of system (3.1): a task we leave to future work.

CHAPTER 4

Multiple Geometric Viewpoints of Mixed Mode Dynamics

The pituitary lactotroph model (1.3) produces two types of (pseudo-plateau) bursts: one in which the calcium drives the bursts and another in which the calcium follows them. Multiple methods from dynamical systems theory have been used to understand the bursting. The classic 2-timescale approach treats the calcium concentration as a slowly varying parameter and considers a parametrized family of fast subsystems. A more novel and successful 2-timescale approach divides the system so that there is only one fast variable and shows that the bursting arises from canard dynamics. Both methods can be effective analytic tools but there has been little justification for one approach over the other. In this chapter, we use (1.3) to demonstrate that the two approaches are different unfoldings of a 3-timescale system. We show that elementary applications of GSPT in the 2-timescale and 3-timescale methods provides us with substantial predictive power. We use that predictive power to explain the transient and long-term dynamics of (1.3). This chapter was published in [**136**].

Authors' Contributions: The analysis in this chapter was performed by TV. MW assisted in the structuring of the manuscript. The manuscript was written by TV, and edited by TV, RB, and MW.

4.1. Motivation

The discovery of dynamic and calcium-conducting MMOs [**130**] marked the juncture at which studies of (1.3) diverged. Early treatments focused on the calcium-conducting MMOs in a 3D reduction of (1.3) since they were novel (Chapter 3) [**134, 135**]. However, due to the physiological importance of calcium, attention was eventually given again to the bursting with variable calcium (in another 3D reduction of (1.3)) [**123**]. In both cases, the theory of canard-induced MMOs showed that the bursting arose from canard dynamics. In spite of these advances, the two 3D reductions of (1.3) remain as fairly separate entities. There has been virtually no work done to reconcile the results from the two 3D reductions and form a coherent picture. In this chapter, we tie the various threads from [**121, 130, 134, 123, 135**] and provide a first step towards a unified picture of the dynamics of (1.3).

Using GSPT [**41, 68**], we have shown that the (calcium-conducting) pseudo-plateau bursting in (3.1) [**134, 123**] was a canard-induced MMO [**14, 15**]. A vital feature of the analysis was the multiple timescale structure of the governing equations. In this chapter, we extend the results of Chapter 3 to the $0 < \delta \ll 1$ regime and focus on MMOs in the 3-timescale version of the model, which we reproduce here for convenience:

$$\begin{aligned} \varepsilon \frac{dV}{dt_I} &= f(V, n, e, c), \\ \frac{dn}{dt_I} &= g_1(V, n), \\ \frac{de}{dt_I} &= g_2(V, e), \\ \frac{dc}{dt_I} &= \delta h(V, c), \end{aligned} \tag{4.1}$$

where $0 < \varepsilon, \delta \ll 1$, f, g_1, g_2 and h are smooth functions and t_I is the dimensionless time (see Chapter 1). The variables (V, n, e, c) vary over different timescales with V fast, (n, e) intermediate and c slow. In its current form, system (4.1) is written such that the motions in V are $\mathcal{O}(\varepsilon^{-1})$, the motions in (n, e) are $\mathcal{O}(1)$ and the motions in c are $\mathcal{O}(\delta)$. Thus, over $\mathcal{O}(1)$ time intervals, (4.1) naturally highlights the motions in the intermediate variables (n, e). We say that (4.1) is written over an intermediate timescale. An equivalent description of the dynamics can be obtained by rescaling time ($t_I = \varepsilon\, t_F$) to obtain the fast system

$$\begin{aligned} \frac{dV}{dt_F} &= f(V, n, e, c), \\ \frac{dn}{dt_F} &= \varepsilon\, g_1(V, n), \\ \frac{de}{dt_F} &= \varepsilon\, g_2(V, e), \\ \frac{dc}{dt_F} &= \varepsilon\, \delta\, h(V, c). \end{aligned} \tag{4.2}$$

Alternatively, we can obtain a different viewpoint of the dynamics by rescaling time ($t_S = \delta t_I$) to give the equivalent slow system

$$\begin{aligned} \varepsilon\, \delta\, \frac{dV}{dt_S} &= f(V, n, e, c), \\ \delta\, \frac{dn}{dt_S} &= g_1(V, n), \\ \delta\, \frac{de}{dt_S} &= g_2(V, e), \\ \frac{dc}{dt_S} &= h(V, c). \end{aligned} \tag{4.3}$$

Systems (4.1), (4.2) and (4.3) stress the notion that the choice of reference scale k_t in the non-dimensionalization process is not important. The multi-timescale structure is an intrinsic feature of the model and (4.1), (4.2) and (4.3) simply reflect different choices of k_t.

Such 3-timescale systems as (4.1) have received little attention [**67, 74, 75**] and are typically treated as 2-timescale problems, which is the natural setting for GSPT [**41, 68**]. However, the presence of two perturbation parameters means that there are various ways in which the theory can be implemented. One particular implementation uses ε as the singular perturbation parameter whilst keeping δ fixed (1-fast/3-slow pathway of Figure 4.1). System (4.1) is then partitioned into a fast subsystem described by the V dynamics and a slow subsystem described by the (n, e, c) dynamics. Another viewpoint of (4.1) utilizes δ as the singular perturbation parameter with ε fixed (3-fast/1-slow pathway of Figure 4.1), creating a family of fast (V, n, e) subsystems parametrized by the slow variable c.

This asymptotic approach with perturbation parameter δ is the standard approach to bursting oscillations [**98, 99**] in systems (4.1) with a single slow variable c [**6, 81, 10, 121, 128, 116**]. Bursts are classified according to the fast (V, n, e) subsystem bifurcations (with respect to c) involved in the initiation/termination of the active phase. Plateau bursting and various features of pseudo-plateau bursting such as resetting properties [**116**] and burst termination due to fast subsystem manifolds [**94**] are well understood in the classic approach (see Section 1.1). More recent studies [**134, 123, 125**] make use of ε as the perturbation parameter and complement the classic slow/fast analysis. Key organizing structures are the invariant slow manifolds and their intersections (canard solutions) [**23, 119, 140**]. The theory of canard-induced MMOs [**14**] then provides the theoretical basis for understanding burst

phenomena such as the transition from spiking (relaxation oscillations) to bursting (MMOs) and how spike-adding bifurcations can occur (Chapter 3). The two slow/fast analysis techniques yield key insights into the mixed mode dynamics of pseudo-plateau bursting. Comparative analyses of the two slow/fast methods have been performed [**123**], however, there have been few attempts to reconcile these approaches [**125**] in the context of (4.1).

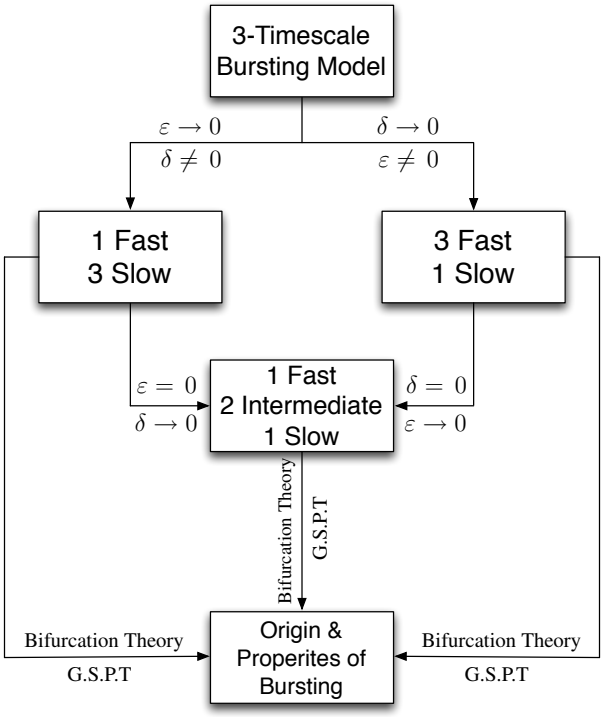

Figure 4.1. Schematic diagram of the multiple geometric analyses of pseudo-plateau bursting.

There are multiple goals to this chapter. First and foremost, we wish to broaden the scope of GSPT by showing that elementary applications of the theory can be a powerful analytical tool in understanding 3-timescale problems. We compare the familiar 2-timescale methods with a 3-timescale analysis (1-fast/2-intermediate/1-slow path of Figure 4.1) and demonstrate the efficacy of each technique. In conjunction with this, we illustrate our assertions by analyzing the 3-timescale model (4.1) [**121, 130**] and show that our multiple geometric viewpoints provide a fairly complete view of the dynamics. Physiologically, we are motivated by a desire to understand a complex neuroendocrine cell model. Mathematically, we are interested in the relationship between multiple analytical techniques. Our work complements [**125**], in which the relationship between geometric features of the 2-fast/1-slow and 1-fast/2-slow analysis techniques is demonstrated in a 3D reduction of (4.1).

The outline of the chapter is as follows: in Section 4.2, we investigate the bifurcation structure of (4.1) and identify the regions in parameter space where MMOs exist. Section 4.2 serves as a preamble to the main results of this chapter, which are presented in Sections 4.3–4.5. Section 4.3 details a slow/fast analysis in which there is 1 fast variable and 3 slow variables, examples of which are currently scarce [**58, 59**]. We then recall the standard slow/fast analysis in Section 4.4, where everything is treated as fast except for a single slow variable. The crux of this chapter lies in Section 4.5, where we perform a geometric singular perturbation analysis of the full 3-timescale problem (4.1). We formulate our analysis in a general way to emphasize that our approach can easily be adapted to other 3-timescale problems. We show that the 3-timescale decomposition inherits the strengths of the 2-timescale methodologies, affording us a remarkable degree of control and predictive power. Sections

4.3–4.5 highlight an unusual degeneracy about which the small oscillations of the MMOs are localized. In Section 4.6, we examine this degeneracy more closely whilst comparing the three analytical approaches. We conclude the chapter in Section 4.7 with a discussion.

4.2. Full System Bifurcation Analysis

The first step towards a classification of the dynamics is a full system bifurcation analysis, which complements slow/fast analysis techniques and views the MMOs as periodic solutions with complex structure [**104, 129**]. In [**134, 123, 135**], careful bifurcation analyses were performed for reductions of (4.1) that focused on calcium-conducting MMOs (with $\delta \to 0$ and c removed – see Section 3.2) or dynamic MMOs (with $g_A = 0$ nS and e decoupled) but not both. We now extend the bifurcation analysis to (4.1) with $0 < \delta \ll 1$.

4.2.1. The Three Conductances. Using AUTO [**31, 32**], the bifurcation structure of the lactotroph model (4.1) was calculated for each of the three conductances g_K, g_{BK} and g_A (Figure 4.2). In each case, we set $f_c = 0.01$ (so that $\delta = 0.032$). The L_2 norm refers, as before, to either the standard Euclidean norm for equilibria or the L_2 norm for periodic orbits.

Figure 4.2(a) shows the bifurcation structure of (4.1) with continuation parameter g_K. Here, we are considering bifurcations that arise from variations in the repolarizing current I_K. For small g_K, the depolarized equilibrium (labelled Dep) is attracting (black curve) and destablizes at a subcritical Hopf bifurcation (denoted HB_{g_K}) at $g_K \approx 0.576$ nS. Emanating from HB_{g_K} is the spiking branch ($s=0$), which terminates outside the physiological domain at another subcritical Hopf point. The $s=1$ bursting branch connects with the spiking branch at period doubling (PD) points. The $s=2$ branch is born at a saddle-node of periodics (SN) at $g_K \approx 0.613$ nS and is a closed isola of MMOs. The bursting families $s = k, k > 2$ (not shown) have the same configuration as the $s=2$ case with ever-decreasing stability plateaus. These closed isolas are all born in SN points in a neighbourhood of the PD point where the spiking and first bursting branches connect (at $g_K \approx 0.617$ nS). Situated between the $s = k$ and $s = k+1$ ($k \geq 0$) bursting families are isolas of MMOs with signatures that are some mixture of 1^k and 1^{k+1} patterns (not shown; cf. Section 3.2).

Figure 4.2(b) shows bifurcations of (4.1) with respect to g_{BK}, the biophysical parameter that controls the BK current and reliably increases c (with increasing g_{BK}) [**121**]. The bifurcation structure of g_{BK} has a reversed orientation to the g_K bifurcation structure, but the core elements are the same. There is a curve of (depolarized) equilibria (black curve) that loses stability at a subcritical Hopf bifurcation ($\text{HB}_{g_{\text{BK}}}$) at $g_{BK} \approx 2.499$ nS. Spiking orbits (blue curve) arise from $\text{HB}_{g_{\text{BK}}}$ and are stable for the smallest g_{BK} values. As g_{BK} is increased from 0 nS, we encounter the various MMO families. The $s = 1$ branch (red curve) connects with the $s = 0$ branch at PD points and the remaining bursting families are disjoint, closed curves. The isolas are born in SN points in a neighbourhood of the PD point where the $s = 0$ and $s = 1$ branches connect (at $g_{BK} \approx 2.338$ nS). As before, there exist MMO families with complex signature between each bursting family.

Figure 4.2(c) shows a bifurcation diagram of (4.1) with continuation parameter g_A. The bifurcations we are treating in this case are due to variations in the sub-threshold current I_A. The g_A bifurcation structure is inherently different from the g_K and g_{BK} structures. In the g_A case, there is no Hopf bifurcation. The depolarized steady state (black curve) bifurcates at a saddle-node on invariant circle (SNIC) bifurcation well beyond the physiological domain (not shown) where it meets a hyperpolarized steady state. Like the g_{BK} case, the spiking orbits (blue curve) are stable for the smallest g_A values. The first bursting family (red curve) arises from the spiking branch at a PD point at $g_A \approx 0.316$ nS but terminates (at large g_A) at a homoclinic point. The remaining MMO families are disjoint, but not closed. In fact, they

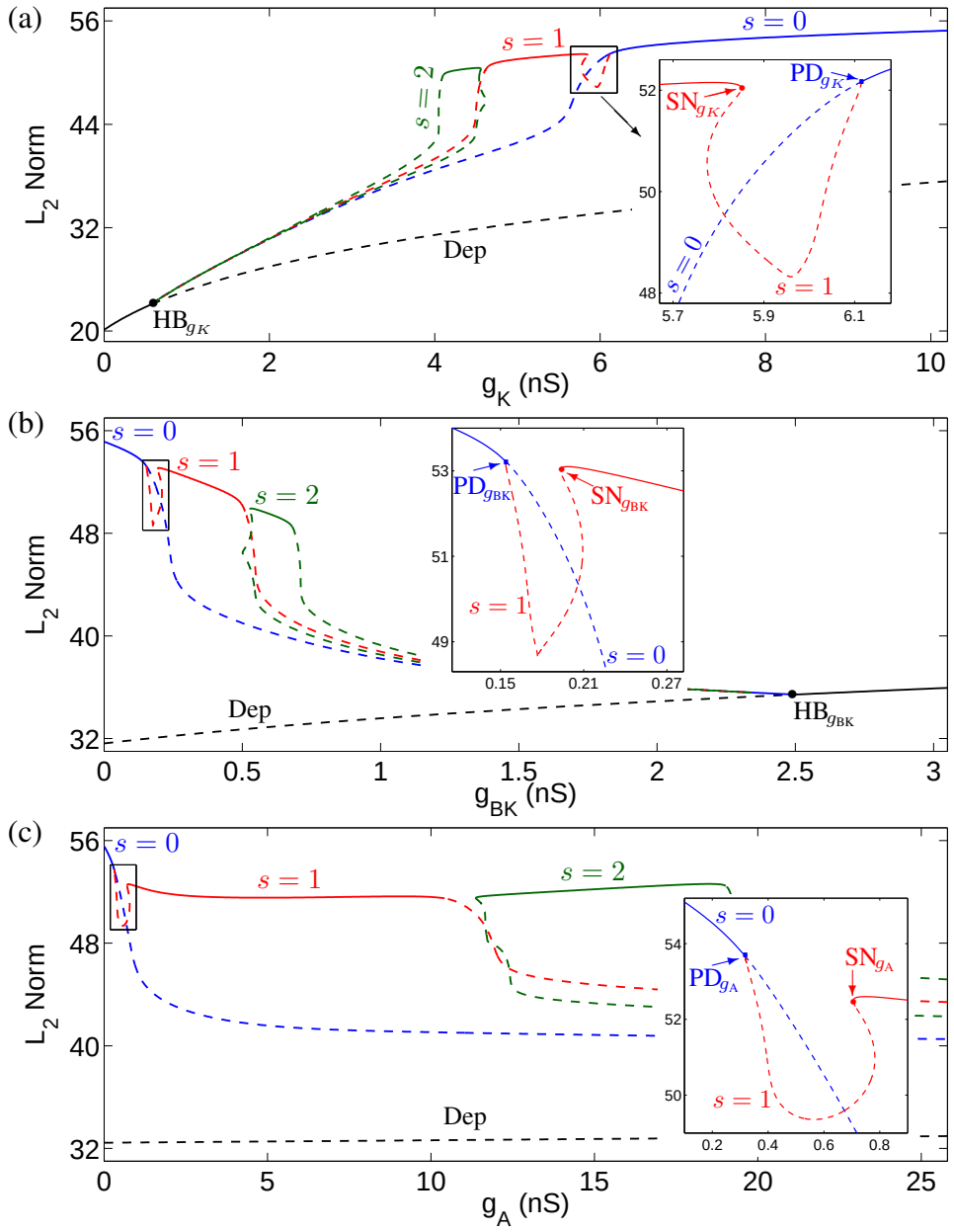

Figure 4.2. One parameter bifurcation structure of (4.1) with $C_m = 2$ pF and $f_c = 0.01$, showing the depolarized steady states (black), spiking (blue), and bursting families (red and green). (a) $g_{BK} = 0.4$ nS, $g_A = 4$ nS. (b) $g_K = 5$ nS, $g_A = 4$ nS. (c) $g_K = 5$ nS, $g_{BK} = 0.4$ nS. Insets: transition between spiking ($s = 0$) and bursting ($s = 1$) branches.

all terminate at homoclinics far outside the physiological domain. Unlike the g_K and g_{BK} cases, there is a maximal MMO family (not shown). This maximal bursting family has the largest stability plateau and terminates at the SNIC point (cf. Figure 3.3).

In each panel of Figure 4.2, there is an inset that shows the transition from the spiking branch (blue, $s = 0$) to the first bursting branch (red, $s = 1$). In each case the spiking branch loses stability at a PD point, labelled PD_{g_x}, where $x \in \{K, BK, A\}$. The $s = 1$ branch does not immediately become stable and there is a window of complex MMO families. The $s = 1$ branch eventually becomes stable at the SN point, denoted SN_{g_x} with $x \in \{K, BK, A\}$. This window of complex MMOs sitting between adjacent bursting families vanishes as the perturbation parameter C_m is decreased. In fact, for sufficiently small C_m (i.e. ε), the adjacent MMO branches overlap and there is bistability (cf. Section 3.2.2 [**135**]).

4.2.2. The Bursting Boundaries. Using the one-parameter diagrams (Figure 4.2), we can now construct 2-parameter diagrams to identify the regions in parameter space where MMOs exist (Figure 4.3) relative to other types of dynamical behaviour. We concentrate on the bursting boundaries and save refinements of our 2-parameter diagrams for future work.

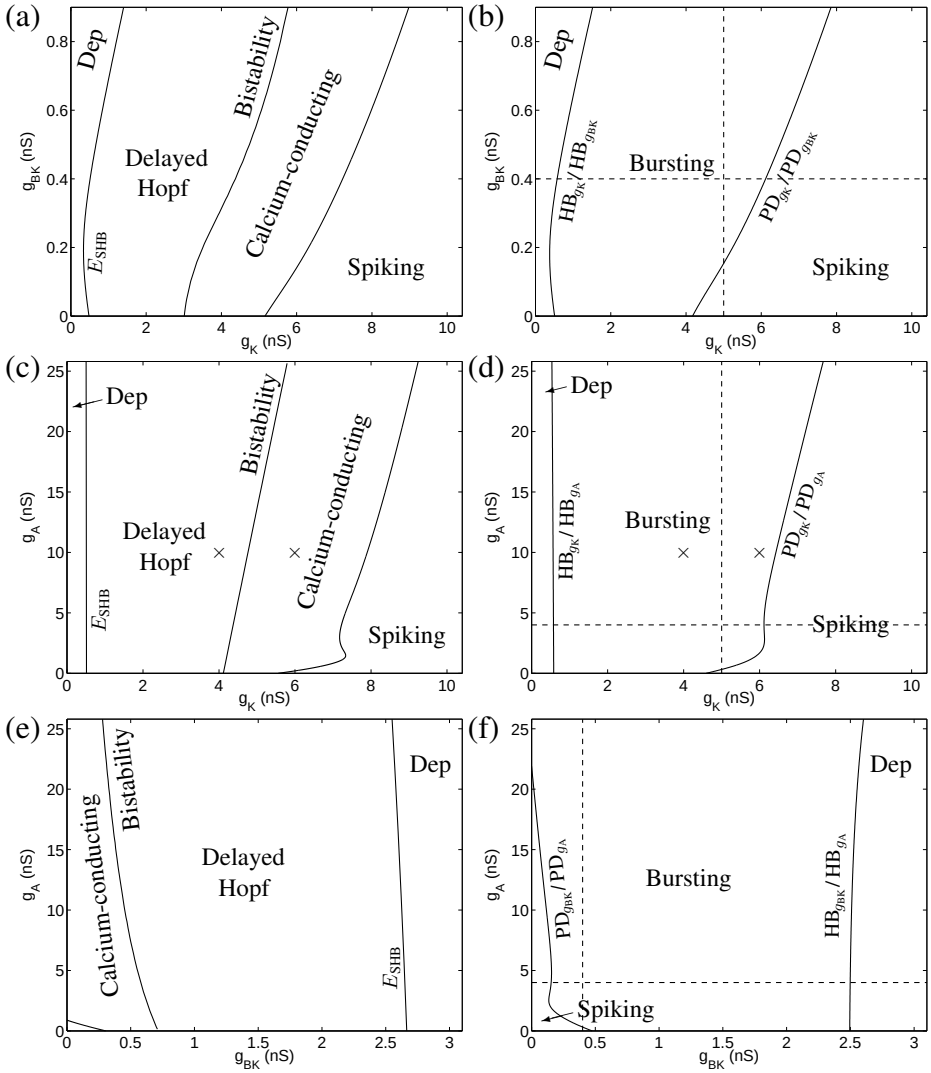

Figure 4.3. Two parameter bifurcation structure of (4.1). In (a) and (b), $g_A = 4$ nS. In (c) and (d), $g_{BK} = 0.4$ nS. In (e) and (f), $g_K = 5$ nS. Panels (a), (c) and (e) have $C_m = 0$ pF and $f_c = 0$ whilst panels (b), (d) and (f) have $C_m = 2$ pF and $f_c = 0.01$. The MMO boundaries are generated by continuing the PD and Hopf points from Section 4.2.1 (see text for details). The crosses in panels (c) and (d) indicate the positions of Figures 1.6(a) and (b). The dashed lines denote the 1D slices taken in Figure 4.2.

In Figure 4.3, we show diagrams for the singular limit $(\varepsilon, \delta) \to (0, 0)$ (panels (a), (c) and (e)) but defer the discussion to Section 4.5. Panel (b) shows the (g_K, g_{BK}) diagram for $g_A = 4$ nS, $C_m = 2$ pF and $f_c = 0.01$. In the physiologically relevant domain, there are three distinct types of behaviour: spiking, bursting and depolarized steady states. The spiking and bursting regions are separated by the PD_{g_K}/$\text{PD}_{g_{\text{BK}}}$ curve, which can be calculated by 2-parameter continuation of either the PD_{g_K} or $\text{PD}_{g_{\text{BK}}}$ point. In any case, we choose the PD point instead of the SN point as the spiking/bursting boundary since the PD point is where the spiking branch destablizes and gives way to trajectories that are mixtures of spikes and bursts. Note that continuation of the SN point would generate essentially the same boundary.

The other boundary that delimits the MMO regime is the HB_{g_K}/$HB_{g_{BK}}$ curve, which was obtained from a 2-parameter continuation of the HB_{g_K} (or $HB_{g_{BK}}$) point.

In Figure 4.3(d), $g_{BK} = 0.4$ nS and in Figure 4.3(f), $g_K = 5$ nS. As in panel (b), the main types of dynamical behaviour in panels (d) and (f) are spiking, bursting and depolarization. The spiking and bursting behaviour in (d) are separated by the PD_{g_K}/PD_{g_A} curve and in (f) the border is the $PD_{g_{BK}}$/PD_{g_A} curve. Moreover, the divide between spiking and depolarization arises from continuation of the Hopf bifurcation (the HB_{g_K}/HB_{g_A} curve in (d) and the $HB_{g_{BK}}$/HB_{g_A} curve in (f)). Note in Figures 4.3(d) and (f) that the 1D g_A slice taken in Figure 4.2(c) never intersects a Hopf bifurcation.

Thus, we have identified the regions in parameter space where MMOs exist. In addition, we can deduce that the bursting waveform broadens ($s \to \infty$) when the parameters approach the HB boundary. Conversely, the bursting waveform narrows ($s \to 0$) when the spiking/bursting boundary is approached. In other words, our diagrams suggest that g_A has little effect on the number of small oscillations and that s is primarily determined by g_K and g_{BK} (cf. Section 3.3.2). We now concern ourselves with the question of the origin and properties of the MMOs. At the core of our approach is GSPT.

4.3. The ε-Viewpoint

In this section we consider a timescale splitting of (4.1) in which there is only one fast variable and everything else is considered slow (1-fast/3-slow path of Figure 4.1). Such decompositions have been used to explain neuronal dynamics [**33, 38, 101, 104, 141**] and intracellular calcium dynamics [**58, 59**]. This section adds to the currently sparse literature of examples of dealing with systems that have more than 2 slow variables [**58, 59, 143**]. The 1-fast/k-slow approach has been applied to 3D reductions of (4.1) in which $k = 2$ (Chapter 3 and [**123**]). The addition of a third slow variable does not significantly change the procedure.

4.3.1. Geometric Singular Perturbation Analysis. For a fixed δ, (4.1) is a singularly perturbed problem with perturbation parameter ε where V is fast and (n, e, c) are 'slow'. The fast system is given by (4.2) and an equivalent 'slow' system is given by (4.1) (or (4.3)). Taking the singular limit $\varepsilon \to 0$ on the fast timescale t_F gives the 1D layer problem

$$\frac{dV}{dt_F} = f(V, n, e, c), \tag{4.4}$$

where (n, e, c) are parameters. The singular limit $\varepsilon \to 0$ in the 'slow' system (i.e. on the intermediate timescale t_I) gives the 3D reduced problem:

$$\begin{aligned} 0 &= f(V, n, e, c), \\ \frac{dn}{dt_I} &= g_1(V, n), \\ \frac{de}{dt_I} &= g_2(V, e), \\ \frac{dc}{dt_I} &= \delta h(V, c). \end{aligned} \tag{4.5}$$

Remark 4.1. Note in (4.5) that c operates on a slower timescale than the other variables. That is, (4.5) is itself singularly perturbed with small parameter δ. We demonstrate in this section what information can be gleaned from the 2-timescale methodology with ε as the principal perturbation parameter. In Section 4.5, we acknowledge the 3-timescale structure of (4.1) and show that we can use the extra timescale to gain greater predictive power.

The aim of GSPT is to concatenate the information obtained from the lower dimensional subproblems (4.4) and (4.5) to provide a unified global description of (4.1). As usual, we start with a bifurcation analysis of the 1D layer problem (4.4). The critical manifold is

$$S := \left\{(V, n, e, c) \in \mathbb{R}^4 : f(V, n, e, c) = 0\right\}. \tag{4.6}$$

In our model system, S is a 3D folded manifold with 2D *fold surface*:

$$L := \left\{(V, n, e, c) \in S : f_V(V, n, e, c) = 0\right\}, \tag{4.7}$$

which divides S into attracting sheets S_a ($f_V < 0$) and repelling sheets S_r ($f_V > 0$).

The critical manifold S is not only the manifold of equilibria of (4.4), but is also the phase space of (4.5), interfacing between the layer and reduced problems, (4.4) and (4.5), respectively. Projection of (4.5) onto a slow-fast variable base, (V, e, c) say, gives:

$$\begin{aligned} -f_V \frac{dV}{dt_I} &= f_n\, g_1(V, n) + f_e\, g_2(V, e) + \delta f_c\, h(V, c) \equiv F_\delta(V, n, e, c), \\ \frac{de}{dt_I} &= g_2(V, e), \\ \frac{dc}{dt_I} &= \delta h(V, c), \end{aligned} \tag{4.8}$$

where n satisfies (4.6). Desingularization (i.e. a time rescaling $dt_I = -f_V\, ds_I$) removes the singular term at the fold and gives the desingularized system

$$\begin{aligned} \frac{dV}{ds_I} &= F_\delta(V, n, e, c), \\ \frac{de}{ds_I} &= -f_V\, g_2(V, e), \\ \frac{dc}{ds_I} &= -\delta\, f_V\, h(V, c). \end{aligned} \tag{4.9}$$

The ordinary singularities E and folded singularities M_δ of (4.9) are given by

$$\begin{aligned} E &:= \left\{(V, n, e, c) \in S : g_1(V, n) = g_2(V, e) = h(V, c) = 0\right\}, \\ M_\delta &:= \left\{(V, n, e, c) \in L : F_\delta(V, n, e, c) = 0\right\}. \end{aligned}$$

The ordinary singularities correspond to actual equilibria of (4.1). The points on the curve M_δ are special points of (4.8) where there is potentially a cancellation of a simple zero, allowing trajectories of the reduced problem to cross L with nonzero speed. The persistence of these singular canards [**119, 140**] under small perturbations gives rise to complex dynamics, such as in [**11, 17, 24, 33, 39, 58, 84, 85, 100, 101, 104, 141**].

Remark 4.2. The δ subscript in F_δ and M_δ is a notational convenience used to indicate the δ dependence and does not denote a derivative.

The Jacobian of (4.9) evaluated along M_δ has two linearly dependent rows. Consequently, there will always be a zero eigenvalue with eigenvector tangent to M_δ. The remaining two eigenvalues are used to classify the points of M_δ (Definition 2.7). The boundary between folded saddles and folded nodes is the folded saddle-node (FSN). We are interested in the FSN points because they are the organizing centers for delay phenomena [**76**]. In particular, a FSN II occurs when there is a transcritical bifurcation of ordinary and folded singularities. That is, the set of FSN II points is the set of singular Hopf bifurcations [**2, 4, 51**]:

$$E_{\text{SHB}} := \left\{(V, n, e, c) \in E : f_V(V, n, e, c) = 0\right\}. \tag{4.10}$$

A FSN I corresponds to the coalescence of a folded saddle and a folded node.

Remark 4.3. There are two ways in which a FSN I can occur in (4.9). A FSN I may occur at a fold in the curve of folded singularities M_δ. Alternatively, a FSN I is associated with the change in sign of an eigenvalue when a special curve crosses the fold surface L:

$$M_\delta^{\mathrm{I}} := \{(V,n,e,c) \in L : g_1 = \delta G_1(V,n,e,c,\delta), g_2 = \delta G_2(V,n,e,c,\delta)\}, \tag{4.11}$$

where the functions G_1 and G_2 are computable. The geometric interpretation of (4.11) will become clear in Section 4.5.1 where we make use of the full 3-timescale machinery.

4.3.2. Singular Orbits and Canards. As we saw in Section 4.2.2, the attractor of (4.1) can be in one of three states: spiking, bursting or depolarization. We now use our analysis from Section 4.3.1 to construct singular approximations of (4.1) to understand the transient and long-term evolution for each of the attractors. For convenience, we introduce some notation. We denote solutions of the fully perturbed problem (4.1) by $\Gamma_{(\varepsilon,\delta)}$. We write $\Gamma^x_{(0,\delta)}, x \in \{F, I\}$ to denote trajectories of the fast subsystem (4.4) and 'slow' subsystem (4.5) written over the intermediate timescale t_I. The singular orbits take the form

$$\Gamma^F_{(0,\delta)} \cup \Gamma^I_{(0,\delta)},$$

where $\Gamma^F_{(0,\delta)}$ represents fast jumps in V and $\Gamma^I_{(0,\delta)}$ is the 'slow' flow along S.

Figure 4.4 shows the 1-fast/3-slow singular orbit construction for equilibria and periodic orbits. In each case, the folded singularities M_δ (red), c-nullcline (dashed, black) and full system trajectory $\Gamma_{(\varepsilon,\delta)}$ (black) are plotted. When the attractor is a depolarized steady state (panels (a) and (b)) the singular trajectory is simple, consisting of a fast and 'slow' orbit segment. The fast evolution $\Gamma^F_{(0,\delta)}$ brings the trajectory onto an attracting sheet of S, where the dynamics switch to those of (4.9) We observe that the 'slow' orbit segment $\Gamma^I_{(0,\delta)}$ converges to the equilibrium point E. The full system trajectory $\Gamma_{(\varepsilon,\delta)}$ then shows that the singular orbit is a suitable predictor of the transient evolution to the equilibrium. More precisely, since the singular trajectories stay in normally hyperbolic regions of S, $\Gamma_{(\varepsilon,\delta)}$ is simply an $\mathcal{O}(\varepsilon)$ perturbation of the singular attractor $\Gamma^F_{(0,\delta)} \cup \Gamma^I_{(0,\delta)}$ (by Fenichel theory).

Parameter variations shift the position of the steady state E on S. There eventually comes a point when E crosses the fold surface L and moves from an attracting sheet S_a to a repelling sheet S_r. When E crosses the fold surface L, we have a FSN II bifurcation leading to the birth of limit cycles [**51**]. Figures 4.4(c) and (d) show that the 1-fast/3-slow singular attractor is composed of a fast jump from a folded node together with a 'slow' flow that returns the orbit to the folded node. That is, we have the singular limit representation of a canard-induced (dynamic) MMO [**14**] (Section 2.6.2).

Recall that the canard theory for two slow variables (Section 2.5) extends to k slow variables, $k \geq 2$ (Theorem 2.6) [**143**]. In particular, the number of small oscillations, s, of an MMO is bounded (see (2.20)). In Figures 4.4(c) and (d), the folded node of the singular attractor is $\mathcal{O}(\delta)$ close to a FSN I point M_δ^{I}, i.e. the eigenvalue ratio is $\mu = \mathcal{O}(\delta)$ and $s_{\max}$ is large. However, we typically do not see $s_{\max}$ oscillations and the oscillations occur some distance from the folded node. Figure 4.4(c) shows that the singular MMO approaches the folded node along its weak eigendirection, v_w, which is a linear approximation to the axis of rotation for the small oscillations. Thus, trajectories close to v_w do not visibly oscillate until they are some maximal distance from the folded node and are repelled. In light of this, we see that the offset between singular and non-singular trajectories around the folded node (most prominent in Figure 4.4(c)) is due to the delay effects associated with passage through twisted slow manifolds near a folded node.

Figure 4.4(d) shows that the folded node is not the only region where there is disparity between $\Gamma_{(\varepsilon,\delta)}$ and its singular counterpart. At the 'slow'-fast transition near $e \approx 0.4$, $\Gamma_{(\varepsilon,\delta)}$ deviates significantly from the predicted path before it realigns with the 'slow' orbit segment.

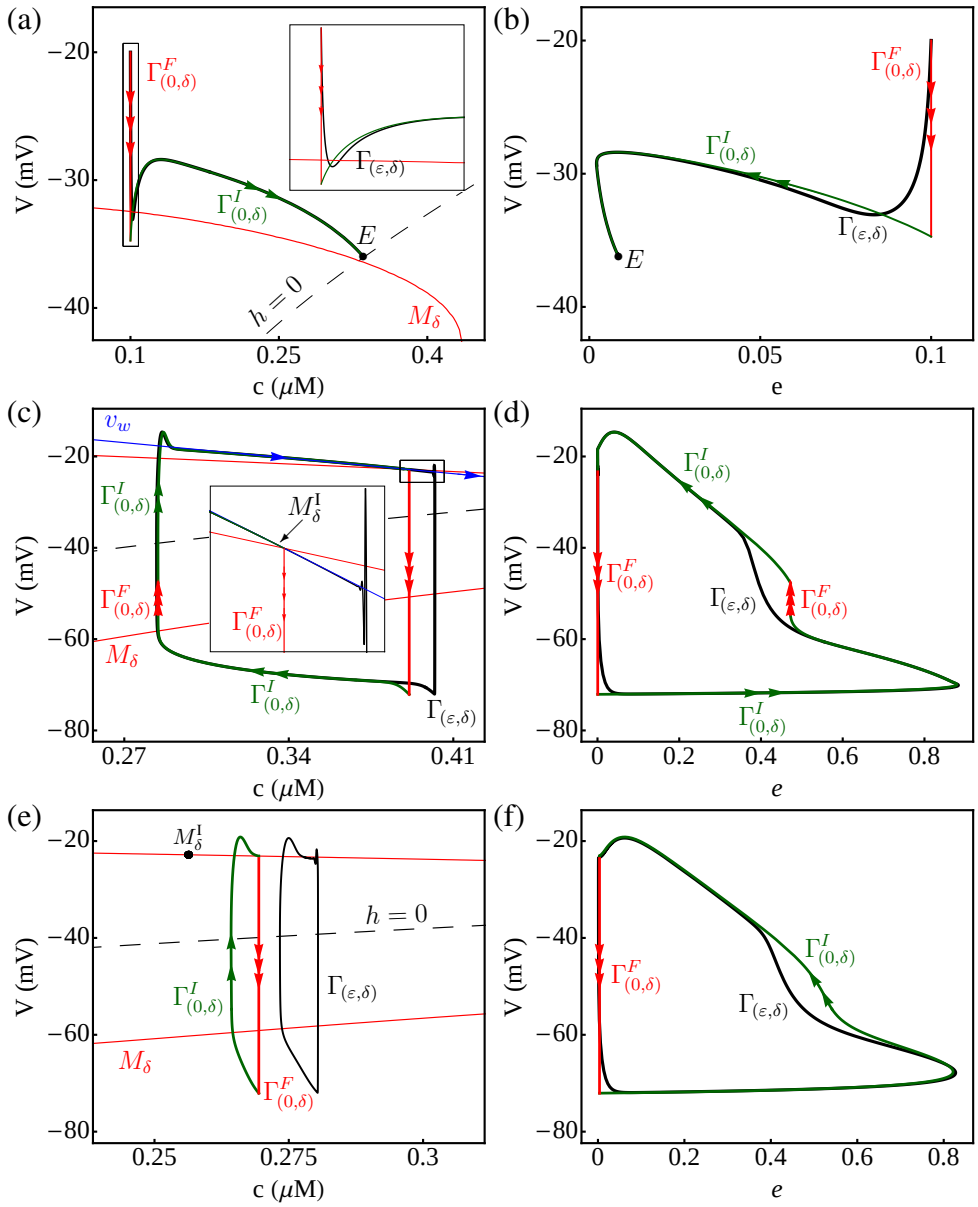

Figure 4.4. Singular orbit construction $\Gamma^F_{(0,\delta)} \cup \Gamma^I_{(0,\delta)}$ for equilibria (top row) and periodic orbits (middle and bottom rows) projected onto the (V, c) plane (left column) and the (V, e) plane (right column). For (a) and (b), $g_K = 5$ nS, $g_{BK} = 3$ nS and $g_A = 10$ nS. The full system trajectory $\Gamma_{(\varepsilon,\delta)}$ (black) has $C_m = 2$ pF and $f_c = 0.01$. For panels (c) and (d), $g_K = 3$ nS, $g_{BK} = 0.4$ nS, $g_A = 8$ nS. Panels (e) and (f) have $g_K = 5$ nS, $g_{BK} = 0.4$ nS, $g_A = 8$ nS. The solution of (4.1) in panels (c)-(f) has $C_m = 0.2$ pF and $f_c = 0.001$.

To understand the discrepancy, we note that S is folded with fold surface L, which is itself folded with a curve, C, of cusp bifurcations (not shown). This creates an unusual scenario in a neighbourhood of C, where trajectories either encounter L with ever-shortening fast up-jumps or avoid L entirely by circumventing C (as in Figure 4.4(f)). The scenario depicted in Figure 4.4(d) shows that the singular orbits are close to C (since $\Gamma^F_{(0,\delta)}$ is so short) and consequently, $\Gamma_{(\varepsilon,\delta)}$ exhibits slow passage effects associated with a cusp. Currently, cusp singularities in slow/fast systems have only been treated for the case of a single cusp point [**13**], whereas our system presents a whole curve of them. Numerically, we observe that small perturbations to C change the geometry of the trajectory significantly (as highlighted by Figures 4.4(d) and (f)) but the precise details are unknown and left to future work.

As far as the 1-fast/3-slow decomposition is concerned, there is no intrinsic difference between dynamic MMOs (where the slow calcium variations drive the bursts) and calcium-conducting MMOs (where the calcium oscillations follow the burst, rather than drive it). In both cases, the singular orbit is a concatenation of 'slow' and fast segments that join continuously at a folded node. The main observation is that dynamic MMOs have $\mu = \mathcal{O}(\delta)$, whilst calcium-conducting MMOs have μ above some threshold. Figure 4.4(e) suggests that the singular orbit is not a very good predictor of the full system calcium-conducting MMO. Figure 4.4(f) counterbalances this and reveals that the (V, c) projection is a special projection in which the approximation error is most pronounced. As before, $\Gamma_{(\varepsilon,\delta)}$ is $\mathcal{O}(\varepsilon)$ close to $\Gamma^F_{(0,\delta)} \cup \Gamma^I_{(0,\delta)}$, except near the folded node and the cusp (which is circumvented in this case).

The other attractor we need to consider is the spiking orbit (not shown). Once again, properties of folded nodes can be used to tell the difference between the spiking and MMO attractors. Each folded node of M_δ possesses a 2D funnel and together, these form a 3D funnel volume for M_δ. Singular orbits that land inside the funnel volume on their fast upstroke will jump at one of the folded nodes of M_δ and so correspond to MMOs. Singular orbits that land outside the funnel volume return to L at a regular jump point. In that case the singular orbit is a relaxation oscillation and corresponds to spiking trajectories of the full system.

Remark 4.4. The funnel of the folded nodes of M_δ is a theoretical construct that loses practical utility as the number of slow variables increases. The concept is only truly effective in the case of 2 slow variables where M_δ is a single point, the funnel is a 2D region and everything can be visualized (see Sections 2.5, 3.3.3 and 4.5.5). In practice, a simpler way of identifying a spiking trajectory is to monitor F_δ at the upper jump point of the singular orbit. If $F_\delta \neq 0$ at the upper jump point, then the singular orbit hits L at a regular jump point.

We have now computed the main objects essential to a 1-fast/3-slow geometric singular perturbation analysis. The bursting is the result of canard dynamics associated with a folded node [**14, 119, 140**]. This 1-fast/3-slow decomposition is new in the sense that only relatively recently has it become an established method in mathematical neuroscience for understanding bursting phenomena. Early work on the analysis of bursting used an alternative slow/fast analysis. The next section reviews the main components of this traditional approach.

4.4. The δ-Viewpoint

The classic slow/fast analysis, pioneered by [**98**], treats δ as the principal perturbation parameter. It has been used to great effect in unravelling the dynamics of plateau bursting in pancreatic islets [**7**], trigeminal motoneurons [**21**] and neonatal CA3 hippocampal principal neurons [**105**]. It is also useful in explaining how pseudo-plateau bursting can be converted to plateau bursting [**124**]. Here, we review the classic approach and apply it to (4.1). In this viewpoint, the system is partitioned such that c is the sole slow variable and everything else is relatively fast [**6, 81, 94**] (3-fast/1-slow path of Figure 4.1). In the language of GSPT, (4.1) is singularly perturbed with small perturbation parameter δ and fixed nonzero ε.

4.4.1. Geometric Singular Perturbation Analysis.

When using δ as the perturbation parameter, (4.1) can be considered to have fast variables (V, n, e) and slow variable c. In this 3-fast/1-slow analysis, the equivalent 'fast' and slow systems are given by (4.1) (or (4.2))

and (4.3), respectively. The singular limit $\delta \to 0$ in (4.1) gives the 3D layer problem

$$\begin{aligned} \varepsilon \frac{dV}{dt_I} &= f(V,n,e,c), \\ \frac{dn}{dt_I} &= g_1(V,n), \\ \frac{de}{dt_I} &= g_2(V,e), \end{aligned} \tag{4.12}$$

where c is a parameter. The singular limit $\delta \to 0$ in (4.3), i.e. on the slow timescale t_S, gives the 1D reduced problem

$$\begin{aligned} 0 &= f(V,n,e,c), \\ 0 &= g_1(V,n), \\ 0 &= g_2(V,e), \\ \frac{dc}{dt_S} &= h(V,c). \end{aligned} \tag{4.13}$$

Remark 4.5. Obviously, the layer problem (4.12) of the 3-fast/1-slow method is singularly perturbed with small parameter ε. In fact, it is precisely the 3D model reduction of (4.1) dealt with in Chapter 3. Our objective here is to illustrate the strengths and weaknesses of the 2-timescale method with perturbation parameter δ. As such, we defer discussion of the full 3-timescale structure to Section 4.5.

To understand the dynamics of the simpler subsystems (4.12) and (4.13), we proceed with a bifurcation analysis. The critical manifold of the 3D layer problem is

$$\mathcal{Z} := \left\{ (V,n,e,c) \in \mathbb{R}^4 : f(V,n,e,c) = g_1(V,n) = g_2(V,e) = 0 \right\}, \tag{4.14}$$

which is a 1D subset of the critical manifold S. Often, we deal with critical manifolds $\mathcal{Z}$ which are folded curves with isolated fold points $\mathscr{L}$ defined by

$$\mathscr{L} := \left\{ (V,n,e,c) \in \mathcal{Z} : \det \begin{pmatrix} f_V & f_n & f_e \\ g_{1V} & g_{1n} & 0 \\ g_{2V} & 0 & g_{2e} \end{pmatrix} = 0 \right\}. \tag{4.15}$$

In the classic slow/fast analysis, $\mathcal{Z}$ is known as the 'z-curve' and the fold points $\mathcal{L}$ are called the 'knees'. The other generic codimension-1 bifurcation we may encounter is the Andronov-Hopf bifurcation. Hopf bifurcations of (4.12) are given by the condition:

$$\mathcal{Z}^H := \left\{ (V,n,e,c) \in \mathcal{Z} : f_V = \varepsilon\, H(V,n,e,c,\varepsilon) \right\}, \tag{4.16}$$

where $H(V,n,e,c,\varepsilon)$ can be computed explicitly. Note that the Hopf bifurcation points $\mathcal{Z}^H$ are $\mathcal{O}(\varepsilon)$ close to the fold surface L of the 1-fast/3-slow approach. Note further that there are other Hopf bifurcations on $\mathcal{Z}$ but these have been found (numerically) to occur on the repelling branch $\mathcal{Z}_r$ of $\mathcal{Z}$ and so we will only concentrate on those Hopfs that are $\mathcal{O}(\varepsilon)$ close to the fold surface L. The criticality of the fast subsystem Hopf typically differentiates between plateau and pseudo-plateau bursting [**116, 95, 129, 124**]. In our model system, $\mathcal{Z}^H$ has always been found (numerically) to be subcritical so that the associated bursts are pseudo-plateau type.

System (4.13) describes the slow motions on the restricted phase space $\mathcal{Z}$. A complete description of (4.13) is obtained by projection:

$$\frac{d}{dt_S} \begin{pmatrix} V \\ n \\ e \end{pmatrix} = - \begin{pmatrix} f_V & f_n & f_e \\ g_{1V} & g_{1n} & 0 \\ g_{2V} & 0 & g_{2e} \end{pmatrix}^{-1} \begin{pmatrix} f_c h \\ 0 \\ 0 \end{pmatrix} = \frac{1}{\det A} \begin{pmatrix} -g_{1n} g_{2e} \\ g_{1V} g_{2e} \\ g_{1n} g_{2V} \end{pmatrix} f_c h, \tag{4.17}$$

where A is the matrix appearing in (4.15). The slow flow along $\mathcal{Z}$ is singular at the folds $\mathscr{L}$. For our model, the only singularities of the slow subsystem are the equilibria E of the fully perturbed problem. It is conceivable however that there are discrete parameter values, g_* say, where the full system equilibrium coincides with a fold point $\mathscr{L}$ and a singular Hopf bifurcation may occur [**95**]. That is, it is possible that the set

$$\mathscr{L} \cap E = \{(V, n, e, c) \in \mathscr{L} : h(V, c) = 0\},$$

is non-empty and a canard point of (4.17) exists, making canard solutions feasible in an exponentially small parameter window around g_*. Despite this, such canard points have no bearing on the full system dynamics since they have always been found (numerically) to occur on $\mathcal{Z}_r$. This is due to the geometric structure of $\mathcal{Z}$ wherein the Hopf point $\mathcal{Z}^H$ occurs at a more depolarized voltage level than the fold points $\mathscr{L}$. Consequently, any canard points must occur on $\mathcal{Z}_r$ and the singular attractor of (4.12) and (4.13) never visits the canard point. As such, (4.1) has no (observable) canard dynamics with respect to the slow-fast decomposition (4.12)–(4.13) and the oscillatory behaviour cannot be due to a folded node. The oscillation mechanism must be encoded then in the layer problem (4.12).

4.4.2. Singular Orbits and Bifurcations. We now proceed to construct singular orbits as in the previous section to extract information about the dynamics. The singular orbits

$$\Gamma^I_{(\varepsilon,0)} \cup \Gamma^S_{(\varepsilon,0)},$$

are once again continuous concatenations of solutions of (4.12) and (4.13), denoted by $\Gamma^I_{(\varepsilon,0)}$ and $\Gamma^S_{(\varepsilon,0)}$, respectively. Figure 4.5 shows the 3-fast/1-slow singular orbit construction for equilibria and for dynamic MMOs.

In Figures 4.5(a) and (b), the equilibrium E of (4.1) sits on $\mathcal{Z}_a$. Initial conditions generically start away from $\mathcal{Z}$ and so the first part of the transient evolution is a rapid motion $\Gamma^I_{(\varepsilon,0)}$ towards $\mathcal{Z}$. Due to the slow/fast structure of (4.12), the 'fast' orbit segment initially overshoots $\mathcal{Z}$ before settling down to it. The slow flow $\Gamma^S_{(\varepsilon,0)}$ along $\mathcal{Z}_a$ brings the trajectory to E before it can reach either the Hopf point $\mathcal{Z}^H$ or the fold point $\mathscr{L}$. Since the singular orbit stays away from bifurcations of the 'fast' and slow subsystems, Fenichel theory guarantees that the full system trajectory $\Gamma_{(\varepsilon,\delta)}$ is an $\mathcal{O}(\delta)$ perturbation of $\Gamma^I_{(\varepsilon,0)} \cup \Gamma^S_{(\varepsilon,0)}$. Note that the asymptotic matching in this case occurs at $\mathcal{Z}$, where the reduced problem (outer solution) and layer problem (inner solution) overlap (cf. Figures 4.4(a) and (b)).

Parameter variations move E through $\mathcal{Z}^H$ and the attractor becomes a limit cycle. The singular dynamic MMO attractor is an hysteresis loop that alternates between the attracting branches of $\mathcal{Z}$ (Figures 4.5(c) and (d)). The singular orbit jumps at the fold point $\mathscr{L}^-$ and at the (subcritical) Hopf bifurcation $\mathcal{Z}^H$, and satisfies Assumptions 2.9–2.11. By Theorem 2.17, the full system trajectory $\Gamma_{(\varepsilon,\delta)}$ is a Hopf-induced MMO. Hence, according to the 3-fast/1-slow analysis, the oscillation mechanism of dynamic MMOs is a delayed Hopf bifurcation [**3, 27, 54**]. The inset of Figure 4.5(c) shows that $\Gamma_{(\varepsilon,\delta)}$ experiences bifurcation delay and traces $\mathcal{Z}_r$ some distance before it oscillates and jumps to a different branch of $\mathcal{Z}$. Typically, the small oscillations associated with the passage through the Hopf are below a visible threshold due to exponential attraction to $\mathcal{Z}_a$ (Section 2.6.3), resulting in trajectories that are virtually indistinguishable from $\mathcal{Z}$.

Remark 4.6. Apart from the fast subsystem Hopf point, the other bifurcation point in the singular orbit is the fold point $\mathscr{L}^-$. The behaviour of $\Gamma_{(\varepsilon,\delta)}$ in a neighbourhood of $\mathscr{L}^-$ is that of classic fold behaviour [**71, 120**]. That is, $\Gamma_{(\varepsilon,\delta)}$ and the layer solution that jumps from $\mathscr{L}^-$ are $\mathcal{O}(\delta^{2/3})$ close (Theorem 2.7). At $\mathcal{O}(1)$ distances from the singular points $\mathcal{Z}^H$ and $\mathscr{L}^-$, the full system trajectory is $\mathcal{O}(\delta)$ close to $\Gamma^I_{(\varepsilon,0)} \cup \Gamma^S_{(\varepsilon,0)}$.

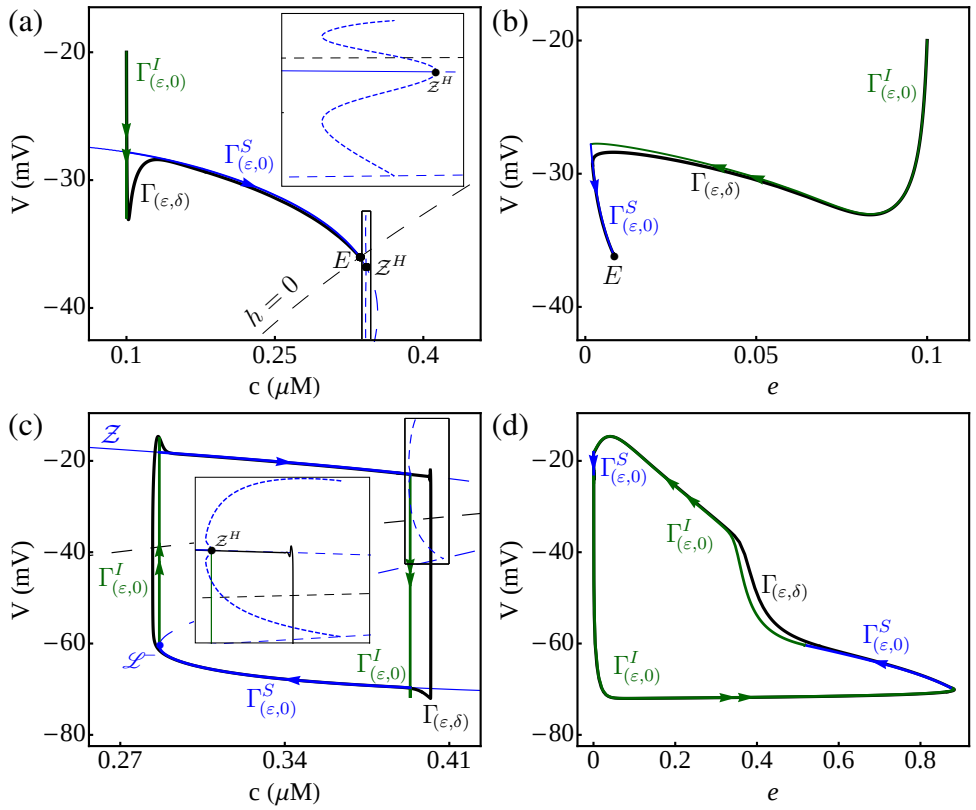

Figure 4.5. Singular orbit and bifurcation diagram (with respect to c) for equilibria (top row) and dynamic MMOs (bottom row). Parameter values in (a) and (b) are $g_K = 5$ nS, $g_{BK} = 3$ nS and $g_A = 10$ nS with $C_m = 2$ pF and $f_c = 0.01$ for $\Gamma_{(\varepsilon,\delta)}$ (cf. Figures 4.4(a) and (b)). In (c) and (d), $g_K = 3$ nS, $g_{BK} = 0.4$ nS and $g_A = 8$ nS with $C_m = 0.2$ pF and $f_c = 0.001$ for $\Gamma_{(\varepsilon,\delta)}$ (cf. Figures 4.4(c) and (d)). In both cases, there is an unstable spiking branch (blue, dashed) emanating from the subcritical Hopf bifurcation of (4.12).

4.4.3. The Distinction Between MMO Types. As noted in Figure 4.5(c), the singular dynamic MMO orbit is an hysteresis cycle that jumps at the thresholds $\mathscr{L}^-$ and $\mathcal{Z}^H$, where $\mathscr{L}^-$ sits to the left of $\mathcal{Z}^H$ in the (V, c) projection. Under variation of the conductances (g_K, g_{BK}, g_A), the relative positions of $\mathscr{L}^-$ and $\mathcal{Z}^H$ change. We immediately see an issue: what happens when $\mathscr{L}^-$ sits to the right of $\mathcal{Z}^H$ so that the bistable region of $\mathcal{Z}$ disappears?

Figure 4.6 is a prototypical example of a scenario in which the fold point $\mathscr{L}^-$ sits to the right of the Hopf point $\mathcal{Z}^H$. The attractor $\Gamma_{(\varepsilon,\delta)}$ of the fully perturbed problem (4.1) sits in the c-interval between the two bifurcation points. Transients of (4.1) closely trace $\mathcal{Z}$ until they encounter either $\mathscr{L}^-$ or $\mathcal{Z}^H$, at which point they start bursting (Figure 4.6(a)). The transient bursting exhibits differing numbers of small oscillations, depending on the position of the trajectory in phase space. An explanation of this dynamical behaviour using GSPT requires more work than in previous scenarios.

For our transient singular orbit construction we can, without loss of generality, take an initial condition on $\mathcal{Z}_a$. Transients move (according to (4.13)) along $\mathcal{Z}_a$ until they encounter $\mathscr{L}^-$ or $\mathcal{Z}^H$ (where normal hyperbolicity breaks down). At $\mathscr{L}^-$, the layer flow description (4.12) takes over and it generates a stable MMO, $\Gamma^1_{(\varepsilon,0)}$, with fixed c. Similarly, at $\mathcal{Z}^H$ the layer problem (4.12) produces a stable MMO, $\Gamma^2_{(\varepsilon,0)}$, with c fixed at $\mathcal{Z}^H$ (Figures 4.6(b) and (c)). We then find that for every fixed c-value between $\mathcal{Z}^H$ and $\mathscr{L}^-$, the attractor of (4.12) is a MMO (not shown). In short, when there is no bistability in $\mathcal{Z}$, the 3-fast/1-slow splitting predicts a torus of MMOs of calcium-conducting type between $\mathcal{Z}^H$ and $\mathscr{L}^-$.

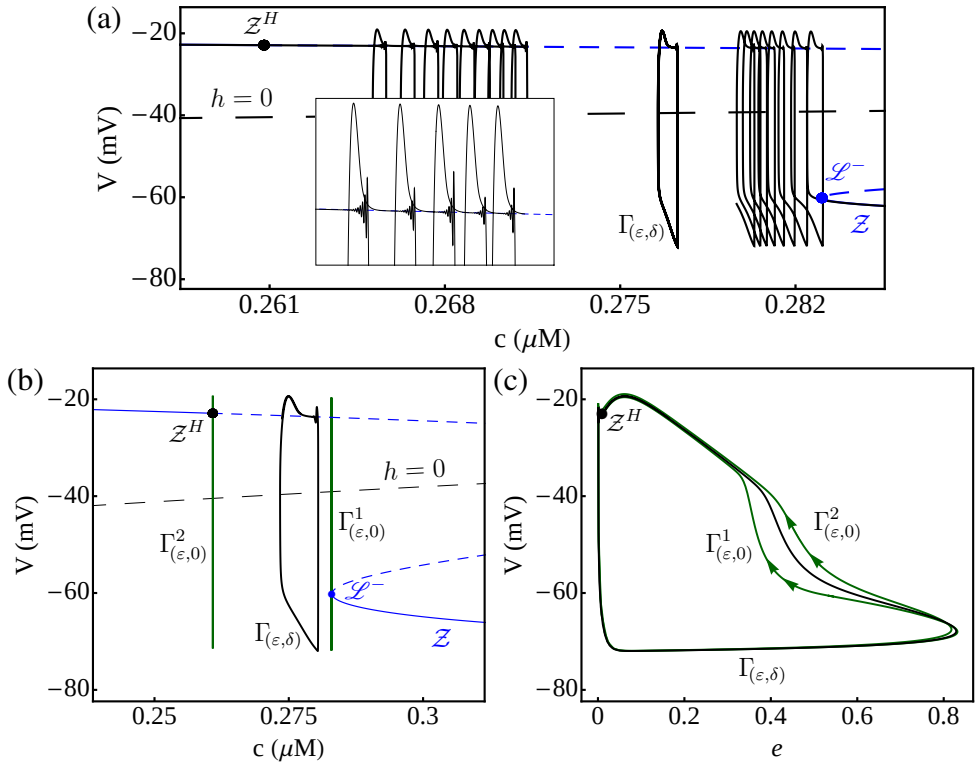

Figure 4.6. Geometric configuration of $\mathcal{Z}$ in which there is no bistability for $g_K = 5$ nS, $g_{BK} = 0.4$ nS and $g_A = 8$ nS (cf. Figures 4.4(e) and (f)). In (a) the transient evolution to the attractor of (4.1) with $C_m = 0.2$ pF, $f_c = 0.0001$ exhibits a variety of bursts. In (b) there is a c-interval of stable singular MMOs bounded by $\Gamma^1_{(0,0)}$ and $\Gamma^2_{(0,0)}$ (see text). The attractor of the fully perturbed problem $\Gamma_{(\varepsilon,\delta)}$ for $C_m = 0.2$ pF, $f_c = 0.001$ lies somewhere in this c-interval. (c) The (V, e) projection shows a clearer picture of the periodic orbits.

Remark 4.7. Recall from Section 4.3.2 that there is a curve of cusp bifurcations in the 1-fast/3-slow splitting, where the trajectories deviate significantly from the singular limit predictions. Figure 4.6(c) shows that the cusp continues to play a role in shaping the trajectories. However, in the 3-fast/1-slow setting, the cusp cannot be detected and hence the disparity between singular and non-singular orbits cannot be explained.

Within this torus of stable singular MMOs, there is an unique singular attractor that $\Gamma_{(\varepsilon,\delta)}$ converges to in the singular limit $\delta \to 0$. To locate this singular attractor, we use averaging. A rigorous discussion of the averaging method is presented in [**107**] and we refer to [**6, 10**] for examples of the method applied to singular perturbation problems. In the context of (4.1), the autonomous averaged equation (to leading order) for the slow motions is

$$\frac{dc}{dt_I} = \delta \frac{1}{T(c)} \int_0^{T(c)} h(V_{(\varepsilon,0)}(s,c),c)\, ds \equiv \delta \overline{h}(c), \tag{4.18}$$

where $V_{(\varepsilon,0)}(t,c)$ is the V-coordinate of the MMO attractor of (4.12) with period $T(c)$ for a fixed c between $\mathcal{Z}^H$ and $\mathcal{L}^-$. We are interested in equilibria of (4.18), where there is no net drift in c.

Figure 4.7 shows how the averaging method can be used to approximate the MMO attractor of (4.1). In panel (a), the averaged vector field $\overline{h}(c)$ is plotted over the c-interval between $\mathcal{Z}^H$ and $\mathcal{L}^-$. We can immediately see that the averaged equation (4.18) has a single stable equilibrium at $\overline{c} \approx 0.277$ μM. We then use $\overline{c}$ in the layer problem (4.12) to generate a stable singular MMO. Panel (b) shows the bifurcation structure of (4.12) with respect to c. The critical manifold $\mathcal{Z}$ is unstable over the c-interval between $\mathcal{Z}^H$ and $\mathcal{L}^-$. Emanating from

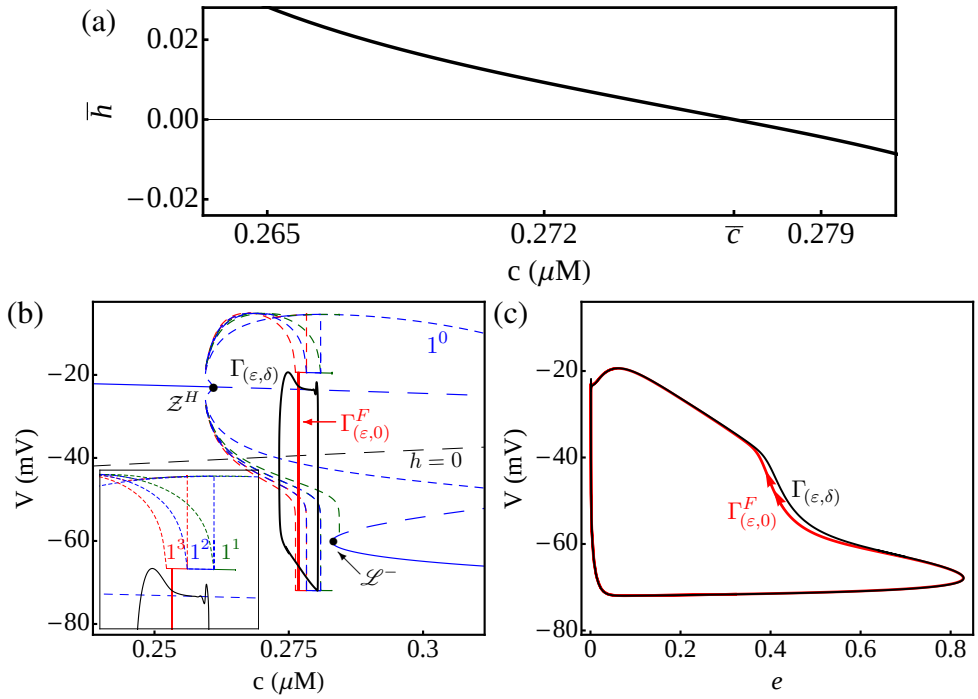

Figure 4.7. The averaging method for the parameter set given in Figure 4.6. (a) The function $\overline{h}(c)$ plotted over the c-interval between $\mathcal{Z}^H$ and $\mathscr{L}^-$ shows that (4.18) has an unique stable equilibrium. (b) Bifurcation structure of the layer problem (4.12). The maxima and minima of the various MMO families are shown. The spiking family comes from the Hopf $\mathcal{Z}^H$ and the MMO families with $s \geq 1$ are born nearby. (c) The singular averaged MMO attractor (red, $\Gamma^F_{(\varepsilon,0)}$) is a good approximation of the full system trajectory $\Gamma_{(\varepsilon,\delta)}$.

$\mathcal{Z}^H$ is the unstable spiking branch (labelled 1^0), which terminates in homoclinic points on the unstable branch of $\mathcal{Z}$. There exist stable MMO families in the c-interval between $\mathcal{Z}^H$ and $\mathscr{L}^-$. These are computed in AUTO using c as the continuation parameter.

In Figure 4.7, the MMO family for $s = 1$ (green) has a small window of stability and terminates at homoclinics. The adjacent MMO branch for $s = 2$ (blue) is a closed isola of orbits. Similarly, the $s = 3$ branch (red) is an isola of MMOs with a stability window adjacent to the stability window of the $s = 2$ branch. Further calculations show that there are additional MMO families within the c-interval between $\mathcal{Z}^H$ and $\mathscr{L}^-$. The number of small oscillations s increases as c tends towards $\mathcal{Z}^H$. The singular averaged attractor, $\Gamma^F_{(\varepsilon,0)}$, is then superimposed on the bifurcation diagram in Figure 4.7. We observe that $\Gamma^F_{(\varepsilon,0)}$ lies in the stable window of the 1^3 MMOs and that $\Gamma_{(\varepsilon,\delta)}$ is itself a 1^3 MMO. Moreover, since the singular orbit $\Gamma^F_{(\varepsilon,0)}$ with $c = \overline{c}$ never runs into any singularities, Fenichel theory holds and $\Gamma_{(\varepsilon,\delta)}$ is an $\mathcal{O}(\delta)$ perturbation of the averaged singular orbit. In this way, we can use the singular limit $\delta \to 0$ to predict the full system dynamics.

Variations in the conductances change the bifurcation structure of (4.12). By choosing parameter sets closer to the spiking/bursting boundary (see Figure 4.3), the MMO families are pushed to lower c values. That is, the MMO branches with large s are squeezed into ever-decreasing neighbourhoods of $\mathcal{Z}^H$. The averaged singular MMO moves through these MMO families towards the fold point $\mathscr{L}^-$ and thus traverses the MMOs with smaller s. Eventually, the $s = 0$ branch itself becomes stable and the averaged MMO trajectory lies in the stability plateau of the spiking family.

Thus, the 3-fast/1-slow analysis can be used to explain the main dynamical behaviours of (4.1): depolarized steady states, (dynamic and calcium-conducting) MMOs and spiking.

In particular, the bifurcation structure of $\mathcal{Z}$ provides a simple test for dynamic or calcium-conducting MMOs. A Hopf bifurcation in the layer problem explains the oscillation mechanism of dynamic MMOs. For calcium-conducting MMOs however, the singular analysis does not provide any clear oscillation mechanism.

4.5. The Three Timescale Problem

So far we have taken two different approaches to the analysis of the 3-timescale problem (4.1). In the 1-fast/3-slow approach, the MMOs were due to canards. Canard theory provided a strong theoretical framework to explain the delay phenomena but had no way of distinguishing between dynamic and calcium-conducting MMOs. In the 3-fast/1-slow approach, we had a simple criterion to differentiate the MMO types based on the geometric configuration of $\mathcal{Z}$ but we did not have a clear oscillation mechanism. In each case, we alluded to the presence of the third timescale (but made no use of it). In this section, we finally acknowledge the 3-timescale structure of (4.1) and perform a geometric singular perturbation analysis (1-fast/2-intermediate/1-slow path of Figure 4.1). Analyses of 3-timescale problems are currently rare [**67, 74, 75, 125**] and a rigorous theoretical framework has yet to be developed. Regardless, we demonstrate that our approach is effective for dealing with 3-timescale problems. In particular, we show that the 3-timescale analysis combines the information from 2-timescale methodologies, affording us greater predictive power than any of the 2-timescale approaches.

4.5.1. Geometric Singular Perturbation Analysis. Recall that the lactotroph model (4.1) is a 3-timescale problem with fast variable V, intermediate variables (n, e) and slow variable c. We have observed in the transient evolution of (4.1) that the fastest timescale initially dominates the evolution. The slower timescales come into effect when the trajectory enters some special neighbourhood of phase space (either S or $\mathcal{Z}$). With this in mind, we proceed to define the singular subsystems of the 3-timescale problem in the order in which we expect to encounter them.

The double limit $(\varepsilon, \delta) \to (0, 0)$ on the fast timescale gives the *fast subsystem*, which is the approximation of (4.1) in which the intermediate and slow variables (n, e, c) move so slowly (compared to V) that they are fixed. The fast subsystem is precisely the layer problem (4.4) of the 1-fast/3-slow approach. The double limit on the intermediate timescale t_I gives the 2D *intermediate subsystem*:

$$\begin{aligned} 0 &= f(V, n, e, c), \\ \frac{dn}{dt_I} &= g_1(V, n), \\ \frac{de}{dt_I} &= g_2(V, e), \\ \frac{dc}{dt_I} &= 0, \end{aligned} \tag{4.19}$$

an approximation of (4.1) in which V is sufficiently rapid that it immediately responds to changes in state and c is sufficiently slow that it has no motion. Note that (4.19) is the $\delta \to 0$ limit of the 3D reduced problem (4.5) of the 1-fast/3-slow splitting. It is also the $\varepsilon \to 0$ limit of the 3D layer problem (4.12) of the 3-fast/1-slow decomposition. Thus, we can interpret the intermediate subsystem (4.19) as the interaction between the 1-fast/3-slow and 3-fast/1-slow analyses. What that means, as we will show, is that all the geometric structures encountered previously persist in the double limit.

We inherit the 3D critical manifold S (and its 2D fold surface L), which serves as a manifold of equilibria of the fast subsystem and as the phase space of (4.19). Projection and desingularization of (4.19) give a complete description of the nontrivial flow on S:

$$\begin{aligned}\frac{dV}{ds_I} &= F_0(V,n,e,c) \equiv f_n\, g_1 + f_e\, g_2,\\ \frac{de}{ds_I} &= -f_V\, g_2(V,e),\\ \frac{dc}{ds_I} &= 0,\end{aligned} \tag{4.20}$$

where n is determined by (4.6). The desingularized system (4.20) inherits the curve of folded singularities M_0, where M_0 is simply the $\delta \to 0$ limit of M_δ:

$$M_0 := \{(V,n,e,c) \in L : F_0(V,n,e,c) = 0\}. \tag{4.21}$$

The ordinary singularities E of (4.9) do not persist as singularities of (4.20). The $\delta \to 0$ limit frees system (4.20) from the requirement that $h = 0$ for an ordinary singularity. Thus, the $\delta \to 0$ analogue of the ordinary singularities for (4.20) is in fact the critical manifold $\mathcal{Z}$ of the 3-fast/1-slow splitting.

Remark 4.8. The persistence of the curve of folded singularities in the desingularized system (4.20) gives us access to canard theory, which provides an oscillation mechanism for the MMOs. Moreover, the presence of the critical manifold $\mathcal{Z}$ in (4.20) provides the geometric information needed to distinguish between dynamic and calcium-conducting MMOs.

The critical manifold $\mathcal{Z}$ forms a 1D subset of the critical manifold S. As such, we expect bifurcations of (4.20) at bifurcations of (4.4), i.e. at the fold surface L. This can be easily verified by computing the determinant of the Jacobian of (4.20) evaluated along $\mathcal{Z}$:

$$\det \begin{pmatrix} \partial_V(F_0) & \partial_e(F_0) \\ \partial_V(-f_V g_2) & \partial_e(-f_V g_2) \end{pmatrix}\Bigg|_{\mathcal{Z}} = -f_V f_n\, g_{1V} g_{2e}.$$

In particular, along the fold surface L, system (4.20) possesses a zero eigenvalue. Thus, the attracting branch $\mathcal{Z}_a$ of $\mathcal{Z}$ is the subset of $\mathcal{Z}$ embedded in S_a along which the eigenvalues have negative real part. The repelling branch $\mathcal{Z}_r$ of $\mathcal{Z}$ is the subset of $\mathcal{Z}$ (embedded in either S_a or S_r) along which at least one eigenvalue has positive real part.

Remark 4.9. In principle, we should also consider Hopf bifurcations along $\mathcal{Z}$. Numerical studies show that Hopf bifurcations of (4.20) usually occur on the repelling branch $\mathcal{Z}_r$.

The curve of folded singularities M_0 consists of folded nodes, saddles and foci. The FSN points can be located by examining the Jacobian determinant of (4.20) evaluated along M_0:

$$\det \begin{pmatrix} \partial_V(F_0) & \partial_e(F_0) \\ \partial_V(-f_V g_2) & \partial_e(-f_V g_2) \end{pmatrix}\Bigg|_{M_0} = g_2\left(F_{0e} f_{VV} - F_{0V} f_{Ve}\right).$$

There are two ways in which a FSN I may occur: either $F_{0e} f_{VV} - F_{0V} f_{Ve} = 0$ or $g_2 = 0$. The first case corresponds to actual folds in the curve M_0. In the case $g_2 = 0$, the condition $F_0 = 0$ simplifies to $g_1 = 0$ and thus the corresponding FSN I points are defined by

$$M_0^{\mathrm{I}} := M_0 \cap \mathcal{Z} = \{(V,n,e,c) \in \mathcal{Z} : f_V(V,n,e,c) = 0\}. \tag{4.22}$$

Geometrically, the set M_0^{I} has two interpretations. First, the FSN I points M_0^{I} represent direct interactions between geometric structures of the 1-fast/3-slow (M_0) and 3-fast/1-slow ($\mathcal{Z}$) analyses, respectively. Second, the FSN I points M_0^{I} correspond to crossings of the critical manifold $\mathcal{Z}$ over the fold surface L.

Remark 4.10. The geometric meaning of (4.11) is now clear. The curve defined by

$$\mathcal{Z}_\delta := \{(V, n, e, c) \in S : g_1 = \delta G_1, g_2 = \delta G_2\}$$

is an $\mathcal{O}(\delta)$ perturbation of the critical manifold $\mathcal{Z}$.

We note that the points of M_0^{I} are the $\varepsilon \to 0$ limit of the Hopf bifurcation points $\mathcal{Z}^H$, defined by (4.16), encountered in the 3-fast/1-slow layer problem. Moreover, M_0^{I} is the $\delta \to 0$ counterpart of the FSN I points M_δ^{I}, defined by (4.11), in the 1-fast/3-slow splitting (cf. [**125**]). We further note that, as far as (4.20) is concerned, the FSN II points (4.10) are codimension-2 bifurcations (in fact, they are special cases of FSN I points M_0^{I}).

The *slow subsystem* approximation of (4.1) assumes that (V, n, e) are so rapid when compared with c that they immediately settle down to their steady state under changes in c. The slow subsystem is obtained from the double limit $(\varepsilon, \delta) \to (0, 0)$ of the slow system (4.3) and is identical to (4.13). As before, $\mathcal{Z}$ is both the manifold of equilibria of (4.20) and the phase space of the slow subsystem, and the fold points $\mathscr{L}$ are points where the slow flow (4.13) (but not the intermediate flow (4.19)) is singular. The only equilibria of (4.13) are the true equilibria E of (4.1).

4.5.2. Transients and the Depolarized Steady State. As before, we use our geometric singular perturbation analysis to unravel the dynamics of (4.1). We now write $\Gamma^x_{(0,0)}$, $x \in \{F, I, S\}$ to denote solutions of the fast, intermediate and slow subsystems (4.4), (4.19) and (4.13), respectively. Our singular orbits take the form

$$\Gamma^F_{(0,0)} \cup \Gamma^I_{(0,0)} \cup \Gamma^S_{(0,0)}.$$

As usual, solutions of the fully perturbed problem are denoted by $\Gamma_{(\varepsilon,\delta)}$.

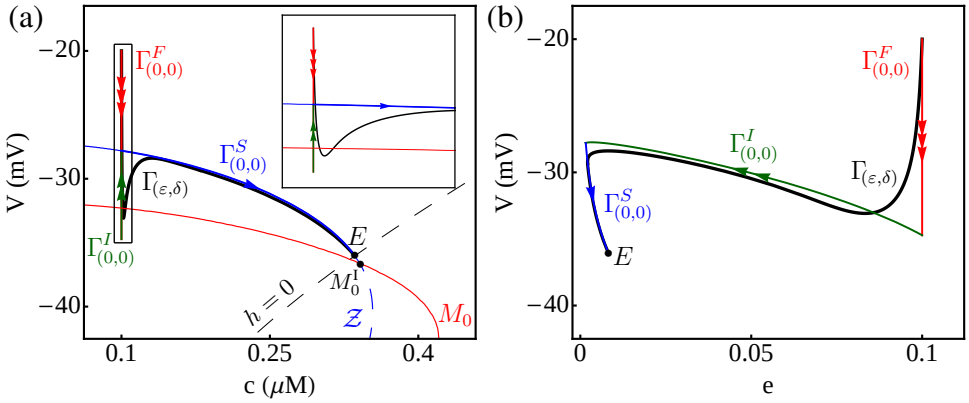

Figure 4.8. Singular orbit construction for a stable equilibrium projected into (a) (V, c) and (b) (V, e). The parameters are $g_K = 5$ nS, $g_{BK} = 3$ nS and $g_A = 10$ nS (cf. Figures 4.4 and 4.5, panels (a) and (b)). The solution $\Gamma_{(\varepsilon,\delta)}$ of (4.1) with $C_m = 2$ pF and $f_c = 0.01$ (black curve) is approximated by solutions of the fast (red, $\Gamma^F_{(0,0)}$), intermediate (green, $\Gamma^I_{(0,0)}$) and slow (blue, $\Gamma^S_{(0,0)}$) subsystems.

Figure 4.8 shows the singular orbit construction in the case when system (4.1) has a stable depolarized steady state. We first identify the main objects from our geometric singular perturbation analysis: the critical manifold $\mathcal{Z}$ intersects the curve of folded singularities M_0 at the FSN I point M_0^{I}. This marks the switch from an attracting branch to a repelling branch (of both S and $\mathcal{Z}$). Both $\mathcal{Z}$ and M_0 are folded. The fold point $\mathscr{L}$ in $\mathcal{Z}$ (not labelled) at $c \approx 0.355$ μM occurs when an eigenvalue changes sign, so that there is a saddle on one side and an unstable node on the other. The fold in M_0 (also not labelled) at $c \approx 0.421$ μM is another FSN I point. The intersection of $\mathcal{Z}$ with the c-nullcline corresponds to a true

equilibrium E of (4.1). In Figure 4.8, E lies on the attracting sheets S_a and $\mathcal{Z}_a$ and so is a stable equilibrium of the full system for sufficiently small perturbations.

We now explain the transient evolution to the attractor starting from arbitrary initial conditions. Since an initial condition is (generically) off the critical manifold S, the fast dynamics (4.4) dominate and there is a rapid evolution $\Gamma^F_{(0,0)}$ to an attracting branch of S (red, 3 arrows). This is succeeded by an intermediate decay $\Gamma^I_{(0,0)}$ (green, 2 arrows) towards $\mathcal{Z}$. For the example illustrated in Figure 4.8, the intermediate flow $\Gamma^I_{(0,0)}$ explains the overshoot previously seen in Figure 4.5(a). Once the trajectory is on $\mathcal{Z}$, the slow flow description (4.13) takes over and the slow drift $\Gamma^S_{(0,0)}$ either brings the orbit to the depolarized equilibrium E (blue, 1 arrow) or to the lower fold point $\mathscr{L}^-$, depending on initial conditions. In the case of the fold point, the intermediate and fast subsystems describe the return of the trajectory to the upper attracting branch of $\mathcal{Z}$ where the slow flow once again brings the trajectory to E.

Remark 4.11. Even though the fold point $\mathscr{L}^-$ is embedded in the critical manifold S, the results from classic studies of fold points hold [**88, 120, 131, 143**]. This can be shown formally by computing a normal form for $\mathscr{L}^-$. The main result in the context of our 4D 3-timescale problem is that there is a 2D slow/intermediate subsystem that is precisely the classic fold problem and the remaining intermediate and fast directions are hyperbolic.

Since the singular orbit in Figure 4.8 does not involve any bifurcations of the fast, intermediate or slow subsystems, the full system trajectory is an $\mathcal{O}(\varepsilon, \delta)$ perturbation of the singular attractor. Bearing in mind the results of Sections 4.3.2 and 4.4.2, we can actually make more precise asymptotic statements. At the interface where $\Gamma^F_{(0,0)}$ and $\Gamma^I_{(0,0)}$ meet, the fast timescale switches to the intermediate timescale and the dominant perturbation parameter is ε. This ε-dominance manifests as a non-uniform sensitivity of the trajectories to perturbations in ε and δ in a neighbourhood of the timescale switch. That is, small changes in δ have virtually no effect on $\Gamma_{(\varepsilon,\delta)}$ near the fast-intermediate timescale transition whilst small changes in ε quickly move $\Gamma_{(\varepsilon,\delta)}$ away from the singular limit prediction. Similarly, the intermediate-slow timescale switch (where $\Gamma^I_{(0,0)}$ and $\Gamma^S_{(0,0)}$ meet) is dominated by δ. Small changes in ε have very minor impact on $\Gamma_{(\varepsilon,\delta)}$ near the intermediate-slow transition whereas small changes in δ cause more substantial deviations.

4.5.3. Bursting With Dynamic Calcium. Recall from Sections 4.3 and 4.4 that the transition from stable depolarized steady states, E, to MMOs occurred when the equilibrium crossed from a stable branch of the critical manifold to an unstable one. The transition either occurred via a FSN II (1-fast/3-slow case) or via a Hopf bifurcation $\mathcal{Z}^H$ (3-fast/1-slow case). In the double limit, $\mathcal{Z}^H$ moves to the fold surface L, becoming a FSN I M_0^{I} in the process. Thus, when E crosses from S_a to S_r, it also crosses from $\mathcal{Z}_a$ to $\mathcal{Z}_r$ at the same time. Hence, the switch from depolarized steady states to MMOs still occurs via a FSN II.

As we saw in Section 4.5.2, any transient flow towards $\mathcal{Z}$ can be explained using the fast and intermediate subsystems. We now focus on the singular MMO attractor and examine its key features (Figure 4.9). The singular MMO consists of seven distinct orbit segments. Starting at $\mathscr{L}^-$, the intermediate flow (4.19) brings the trajectory to the fold surface L. From there, the fast fibers project the trajectory onto a different attracting manifold S_a. The intermediate timescale then dominates and the trajectory is brought into $\mathcal{Z}_a$ (along the weak eigendirection of a node of $\mathcal{Z}$). The trajectory then travels along $\mathcal{Z}_a$ according to (4.13) until it hits the FSN I point M_0^{I}. From M_0^{I}, the trajectory jumps off S_a to an alternate attracting branch of S. Yet another intermediate flow returns the orbit to $\mathcal{Z}$ (again, via the weak eigendirection of a node of $\mathcal{Z}$). The slow subsystem then describes the motion of the trajectory until it returns to $\mathscr{L}^-$, thus completing the singular MMO attractor. The full system attractor, $\Gamma_{(\varepsilon,\delta)}$, is a perturbation of this singular orbit.

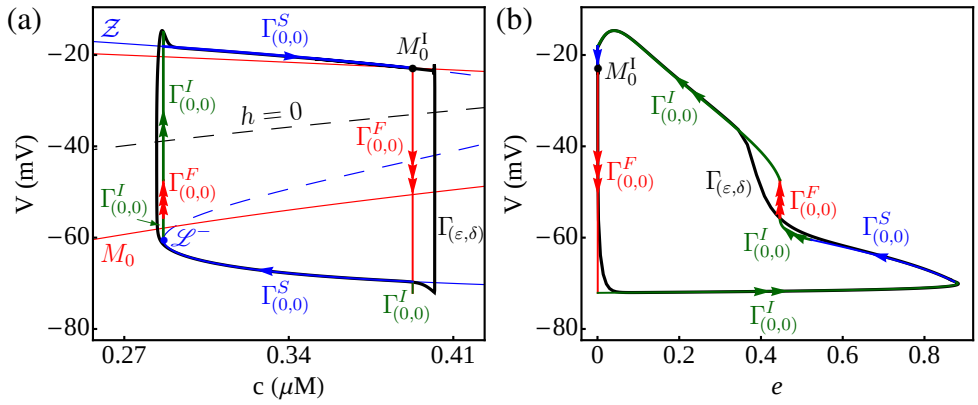

Figure 4.9. Singular orbit construction for a dynamic MMO with $g_K = 3$ nS, $g_{BK} = 0.4$ nS and $g_A = 8$ nS (cf. Figures 4.4 and 4.5, panels (c) and (d)). A solution $\Gamma_{(\varepsilon,\delta)}$ (black) of (4.1) for $C_m = 0.2$ pF and $f_c = 0.001$ is shown along with the singularities $\mathcal{Z}$ and M_0 of (4.20). There are three FSN I points (only one of which is labelled M_0^{I}). The singular MMO is a concatenation of seven distinct orbit segments.

Within our singular MMO attractor, there are 3 special regions where normal hyperbolicity breaks down. The first is the fold point $\mathscr{L}^-$, which exhibits classic fold behaviour [**71**]. This is where the trajectory transitions from the slow timescale to the intermediate timescale and δ is the important perturbation parameter. Trajectories $\Gamma_{(\varepsilon,\delta)}$ are $\mathcal{O}(\delta^{2/3})$ perturbations of the singular orbit in a neighbourhood of $\mathscr{L}^-$. The second non-hyperbolic region encountered is the fold surface L, where the intermediate-fast timescale switch occurs and ε is the important perturbation parameter. Trajectories typically exhibit classic fold behaviour near L (Theorem 2.7) [**120**]. In our case however, the fast up-jump is close to a cusp (see Section 4.3.2) and $\Gamma_{(\varepsilon,\delta)}$ deviates significantly from the singular orbit in this region. The third non-hyperbolic region is the FSN I point M_0^{I}, which is new and specific to 3-timescale problems. The small oscillations of the MMO occur in a neighbourhood of M_0^{I}. Naïvely, we expect the oscillation mechanism to be related to folded singularities. This is only partly true. We defer detailed discussion of how the FSN I point M_0^{I} unfolds to Section 4.6.

As is clear from Figure 4.9, the limiting subsystems are an excellent approximation of the fully perturbed problem. Away from the singularities $\mathscr{L}^-$, L and M_0^{I}, the full system trajectory $\Gamma_{(\varepsilon,\delta)}$ is $\mathcal{O}(\varepsilon)$ close by to $\Gamma^F_{(0,0)} \cup \Gamma^I_{(0,0)}$. As in Section 4.5.2, the perturbative effects of ε and δ are non-uniform and δ has very weak influence on the shape of trajectories around the fast-intermediate timescale transition. Similarly, $\Gamma_{(\varepsilon,\delta)}$ is $\mathcal{O}(\delta)$ close by to $\Gamma^I_{(0,0)} \cup \Gamma^S_{(0,0)}$ and ε has virtually no effect on the shape of orbits around the intermediate-slow timescale transition. The singular dynamic MMO attractor is an hysteresis cycle that alternates between stable branches of $\mathcal{Z}$ (and S). The benefit of the 3-timescale splitting is that we have access to additional information about the shape of the trajectory that we did not have in the 2-timescale splittings. On the other hand, the 3-timescale decomposition retains the degeneracies of the 1-fast/3-slow and 3-fast/1-slow methodologies, making the singular orbit construction more difficult.

4.5.4. Calcium-Conducting Bursts. The geometric configuration of $\mathcal{Z}$ is an important factor in determining the type of MMO attractor. As we saw in Section 4.4.3, parameter variations alter the structure of $\mathcal{Z}$ and when bistability of $\mathcal{Z}$ no longer holds, the MMO attractor changes dramatically. To reiterate the main points of Section 4.4.3, there was a torus of stable singular MMOs between the fold point $\mathscr{L}^-$ and the Hopf point $\mathcal{Z}^H$. The unique attractor was situated somewhere between these two points. The method of averaging was identified as the appropriate analytic tool to locate the MMO attractor.

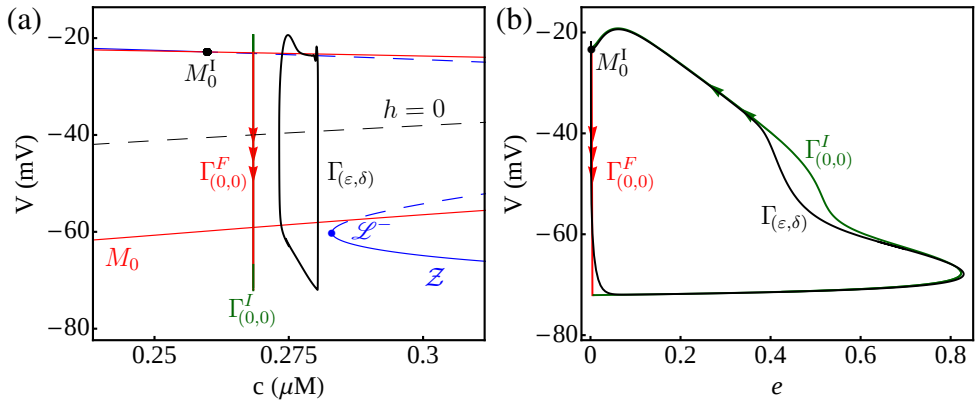

Figure 4.10. Singular orbit construction via averaging for a calcium-conducting MMO. The parameters are $g_K = 5$ nS, $g_{BK} = 0.4$ nS and $g_A = 8$ nS (cf. Figures 4.4(e)–(f) and 4.7(b)–(c)) with $C_m = 0.2$ pF and $f_c = 0.001$ for the full system trajectory. The oscillation region is bordered by the fold point $\mathscr{L}^-$ and the FSN I point M_0^{I}.

These properties persist in the double limit $(\varepsilon, \delta) \to (0, 0)$ with the Hopf bifurcation $\mathcal{Z}^H$ replaced by the FSN I point M_0^{I} (Figure 4.10). The net effect of the averaging process is to remove the slowest variable so that the remaining (V, n, e) subsystem is a classic 2-timescale problem. We immediately inherit the results established in Chapter 3. Namely, the singular orbit $\Gamma^F_{(0,0)} \cup \Gamma^I_{(0,0)}$ satisfies the criteria for a canard-induced MMO: the presence of a folded node and a global re-injection mechanism that resets the system dynamics after passage through the canard point [**14**]. The small oscillations in the calcium-conducting MMOs can then be explained by examining the geometry of the (V, n, e) subsystem away from the singular limit $\varepsilon = 0$ (Section 3.3.3). We illustrate this in Figure 4.11 by showing how the attracting and repelling manifolds S_a and S_r unfold for nonzero ε.

Remark 4.12. In comparing Figures 4.10(a) and 4.7(b), it is clear that the averaged singular MMO undergoes a leftward shift as $\varepsilon \to 0$. Note in (4.18) that the averaging takes the ε dependence into consideration. As a result, the averaged orbit computed in Section 4.4.3 fully accounts for the slow passage effects induced by the canard dynamics in the active phase. As $\varepsilon \to 0$ however, the small oscillations near the folded node disappear (recall the $\mathcal{O}(\varepsilon^{1/2})$ dependence) and the time spent in the active phase is underestimated. Consequently, as $\varepsilon \to 0$ the silent phase has greater contribution than the active phase to the averaged orbit and the singular MMO shifts to lower c values.

Recall from Section 4.4.3 that the transient evolution to the calcium-conducting MMO attractor exhibited a wide variety of bursts. The 3-timescale decomposition allows for a complete explanation of the transient behaviour using canard theory. For the parameter set in Figure 4.10, the eigenvalue ratio of the folded node of the attractor is $\mu \approx 0.041$ and $s_{\max} = 12$. At the FSN I point M_0^{I}, $\mu = 0$. As c increases, μ increases until it eventually reaches $\mu = 1$ (beyond $\mathscr{L}^-$), where the folded nodes of M_0 become folded foci. Transients of (4.1) that pass through a neighbourhood of M_0^{I} undergo a large number of small oscillations. As the trajectory slowly drifts towards the attractor, it encounters a different folded node (with larger μ) every time it returns to M_0. Thus, $s_{\max}$ gradually decreases until the attractor is reached (see Figure 4.6(a)). A similar argument shows that there is a monotonic increase in $s_{\max}$ for those transients of (4.1) that approach the attractor via $\mathscr{L}^-$.

Remark 4.13. An understanding of the transient evolution allows us to predict how our model system responds to external stimuli such as a calcium pulse. We contend that this can be experimentally significant since the transient evolution can distinguish between the two

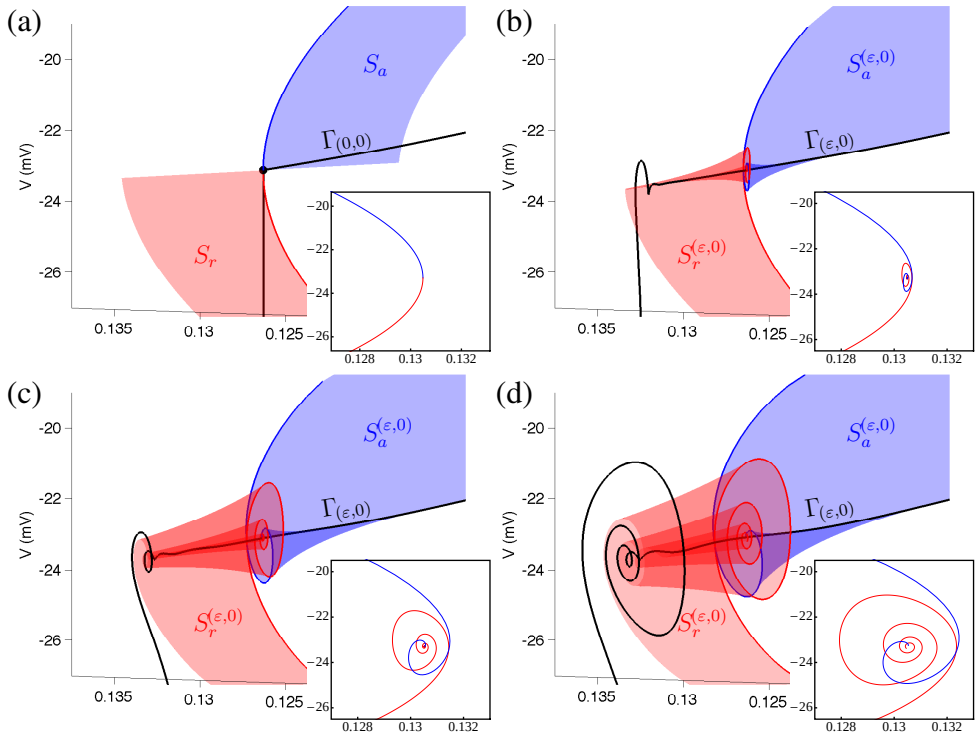

Figure 4.11. Unfolding of the slow attracting (blue) and repelling (red) manifolds for fixed $c = \bar{c}$, calculated up to a section passing through the folded node. The insets show the intersection of the manifolds with a hyperplane through the folded node. The maximal canards correspond to the intersections of the attracting and repelling surfaces. Parameter values are as in Figure 4.10 with (a) $C_m = 0$ pF, (b) $C_m = 0.1$ pF, (c) $C_m = 0.5$ pF and (d) $C_m = 1$ pF.

MMO types. Transients featuring pseudo-plateau bursts with a wide variety of small oscillations are associated with calcium-conducting MMOs. Meanwhile, transients that simply decay to a slow flow along $\mathcal{Z}$ are characteristic features of dynamic MMOs.

Thus, the 3-timescale decomposition provides the geometric information necessary to identify calcium-conducting MMOs and the theoretical framework (canard theory) to explain their oscillatory behaviour. We observe that when there is no bistability, the singular MMO construction only consists of intermediate and fast orbit segments. In other words, since we can average out the c-dynamics, we are effectively down to a 2-timescale problem.

4.5.5. Spiking Orbits. Spiking behaviour always falls (for sufficiently small ε) into parameter regimes where there is no bistability of $\mathcal{Z}$ and we are able to discard a slow direction (via averaging). Consequently, we again deal with a family of 2-timescale problems with parameter c. To determine the difference between spiking and bursting, we first note that the curve of folded singularities M_0 possesses degenerate folded nodes (DFNs), where folded nodes turn into folded foci. Obviously, if the averaged singular attractor is fixed at a c value such that M_0 has a folded focus, then the corresponding full system trajectory will be a spiking pattern. If the averaged singular attractor has c value such that M_0 has a folded node, there is no guarantee that the singular orbit will converge to that folded node. Trajectories that land inside the funnel of the folded node inevitably pass through the folded node. Trajectories that land outside the funnel encounter the fold surface L at a jump point instead. The beauty of the double limit $(\varepsilon, \delta) \to (0, 0)$ is that the funnel region (and the spiking/bursting criterion) can be visualized (Figure 4.12).

In Figure 4.12(a), the averaged singular orbit has $\bar{c} \approx 0.2245$ μM and the associated folded singularity has complex eigenvalues. The corresponding singular attractor $\Gamma^F_{(0,0)} \cup$

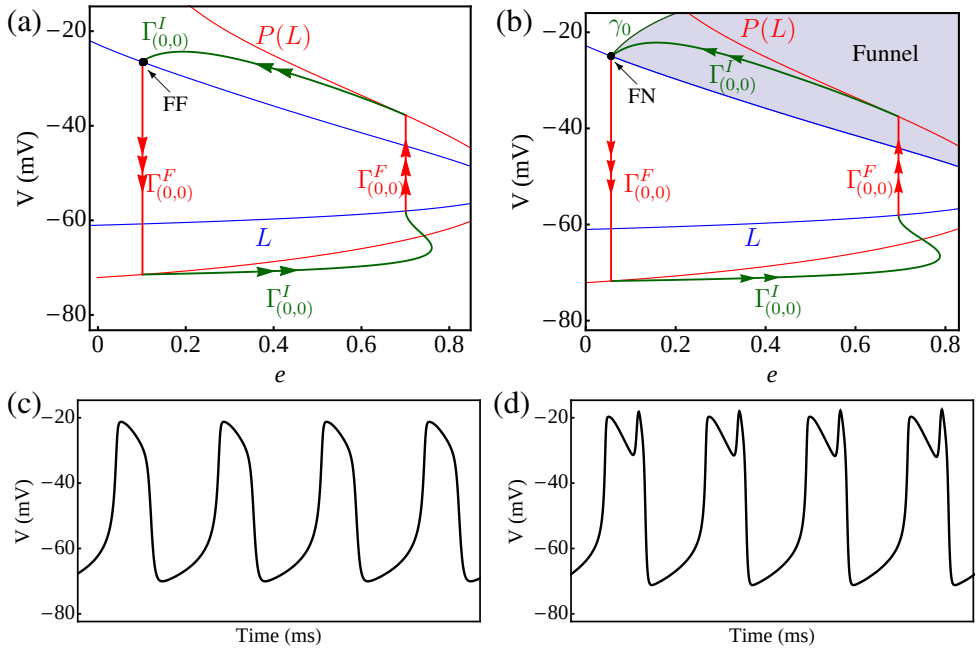

Figure 4.12. The difference between spiking and bursting for $g_{BK} = 0.4$ nS, $g_A = 4$ nS and (a) $g_K = 9$ nS and (b) $g_K = 7$ nS. Panels (a) and (b) are projections into the (V, e) plane. For fixed c, the fold surface L is a curve (blue). Its projection $P(L)$ (red) onto different branches of S is shown to indicate where fast orbit segments land. In (a), the singular attractor hits the folds at regular jump points and the full system orbit (for $C_m = 2$ pF and $f_c = 0.001$) is a relaxation oscillation (panel (c)). In (b), the singular attractor is inside the funnel of the folded node and the full system trajectory is a 1^1 MMO (panel (d)).

$\Gamma^I_{(0,0)}$ with $c = \bar{c}$ is a relaxation oscillator. For the example in Figure 4.12(a), the singular orbit does not actually hit the upper fold at the folded focus but at a regular jump point. The associated time trace of (4.1) shown in Figure 4.12(c) is a spiking pattern, as expected. In Figure 4.12(b), the singular attractor has $\bar{c} \approx 0.2467$ μM and M_0 possesses a folded node with eigenvalue ratio $\mu \approx 0.555$ (and $s_{\max} = 1$). In this case, the fast up-jump projects the singular orbit into the funnel region of the folded node. That is, we have a folded node and a global re-injection mechanism (fast depolarization) that returns trajectories to the funnel region. The associated full system trajectory is a MMO with 1 small oscillation (Figure 4.12(d)) in accordance with the theoretical prediction.

4.5.6. Bifurcation Diagrams. We have shown that the 3-timescale splitting can be used as an effective predictor to explain both the transient dynamics and attractors of (4.1). Our central concern is in identifying the various mechanisms that cause the observed dynamical behaviours (particularly the bursting). We do this by constructing singular 2-parameter diagrams (shown in Figures 4.3(a), (c) and (e)). The singular 2-parameter diagrams are divided into three regions, reflecting the different attractors. The sector marked 'Dep' represents the subset of parameter space where the depolarized steady state is the attractor. The 'Delayed Hopf' region corresponds to the dynamic MMOs. The 'calcium-conducting' region corresponds to the MMOs where averaging can be used to fix the calcium concentration. The singular spiking orbits lie in the spiking region.

The boundary between the equilibrium state and the singular MMO state is the set of FSN II points E_{SHB}, where the equilibrium crosses from an attracting manifold S_a (and $\mathcal{Z}_a$) to a repelling manifold S_r (and $\mathcal{Z}_r$). The division between dynamic and calcium-conducting MMOs is related to the geometric structure of $\mathcal{Z}$. When the stable branches of $\mathcal{Z}$ overlap (denoted 'Delayed Hopf' in Figure 4.3), the singular MMO attractor is an hysteresis cycle.

The small oscillations occur in a neighbourhood of M_0^{I} but the precise oscillation mechanism is unknown. When the stable branches of $\mathcal{Z}$ are separated (labelled 'calcium-conducting'), the calcium variable can be fixed and the small oscillations are associated with folded node canards. The degeneracy where the c-coordinate of $\mathscr{L}^-$ and M_0^{I} coincide (labelled 'Bistability') approximates the boundary between dynamic and calcium-conducting MMOs.

To complete our singular 2-parameter diagrams, we must locate the border between the calcium-conducting MMOs and spiking orbits. The singular spiking attractor can be associated with either a folded focus or a folded node. In the case of a folded node, the singular orbit lands outside the funnel of the folded node. Thus, there are two parts to the border between the singular spiking and MMO orbits. One part of the spiking/MMO boundary consists of the set of singular orbits that jump at a DFN. The other segment of the spiking/MMO boundary is the set of singular orbits that land on the strong canard of a folded node. Figure 4.3 clearly demonstrates that our singular subsystems provide a good first approximation to the dynamics of the fully perturbed problem for sufficiently small (ε, δ).

By using the multiple timescale structure of (4.1) to our advantage, we can explain the dynamics of (4.1). Canard theory in the 1-fast/3-slow approach provides the theoretical basis for the oscillation mechanism. Geometric considerations in the 3-fast/1-slow approach generate a criterion to identify the MMO type. The 3-timescale splitting then gives the best of both worlds and allows the construction of diagrams such as Figure 4.3, which elucidate the cause of the observed attractors of (4.1). However, there are setbacks to the 3-timescale approach. The most obvious is that the dynamic MMOs jump at the FSN I point M_0^{I}, which is a doubly degenerate point where M_δ^{I} and $\mathcal{Z}^H$ merge. The rest of the chapter is concerned with unravelling the oscillation mechanism of dynamic MMOs.

4.6. The Oscillation Mechanism

We have seen that the complex oscillatory waveforms in (4.1) manifest as MMOs of dynamic or calcium-conducting type. In the calcium-conducting case, the small oscillations in the bursts were unequivocally identified as canards. In the dynamic MMO case, the precise oscillation mechanism depends on the chosen geometric viewpoint. The 1-fast/3-slow formulation suggests that the small oscillations are due to canards, whilst the 3-fast/1-slow viewpoint insists that the oscillations are due to a slow passage through a dynamic Hopf bifurcation. In this section we examine the oscillation mechanism for dynamic MMOs more carefully and reconcile the seeming discrepancy.

4.6.1. Perturbations of the FSN I Point M_0^{I}. In Section 4.5 we showed that when bistability of the critical manifold $\mathcal{Z}$ holds, the resulting oscillatory behaviour of (4.1) can be attributed to the FSN I point M_0^{I}. In Section 4.3 we found that the oscillations were associated with folded node singularities with $\mu \approx 0$. More specifically, there was always a FSN I M_δ^{I} that was $\mathcal{O}(\delta)$ close by. In Section 4.4, the oscillatory behaviour emerged from neighbourhoods of a Hopf bifurcation $\mathcal{Z}^H$ that was $\mathcal{O}(\varepsilon)$ close to the fold surface L.

Proposition 4.1. *The FSN I point M_δ^I of the 1-fast/3-slow decomposition and the Hopf bifurcation $\mathcal{Z}^H$ of the 3-fast/1-slow decomposition are different unfoldings of the FSN I point M_0^I of the 3-timescale decomposition.*

Proof. Suppose we have a 2-timescale slow/fast system with k slow and m fast variables that has a locally folded m-dimensional critical manifold S with an $(m-1)$-dimensional manifold of fold points. Suppose further that S possesses an $(m-2)$-dimensional set of generic folded singularities and that the $(m-1)$ nonzero eigenvalues of S along the fold have negative real part. Then, by Theorem 3.1 of [**143**], there exists (after center manifold

reduction) a smooth change of coordinates that transforms the slow/fast system to

$$\begin{aligned}
\varepsilon\,\dot{x} &= y_1(1 + x\mathcal{O}(y_2, z)) + x^2(1 + \mathcal{O}(x, y_1)) + \varepsilon\,\mathcal{O}(x, y_1, y_2, \varepsilon),\\
\dot{y}_1 &= B_2(z)y_2 + C(z)x + \mathcal{O}(y_1, x^2, y_2^2, xy_2) + \varepsilon\,\mathcal{O}(x, y_1, y_2, z),\\
\dot{y}_2 &= A_2(z) + \beta_2 y_2 + \mathcal{O}(x, y_1, \varepsilon),\\
\dot{z} &= A_3(z) + \mathcal{O}(x, y_1, y_2, \varepsilon),
\end{aligned} \tag{4.23}$$

where

$$A_j(z) = a_j + g_{j,1}(z), \quad B_2(z) = b_2 + g_{1,1}(z), \quad C(z) = c + g_{1,2}(z),$$

with $g_{i,j}(0) = 0$ and computable constants $a_2, a_3, b_2, c, \beta_2$, which are generically nonzero.

Using (4.23), we wish to compute a canonical form for a FSN I point M_0^{I}. Without loss of generality, we assume the curves $\mathcal{Z}$ and M_0 cross at the origin (i.e. M_0^{I} is at the origin). This requires $a_2 = 0$ and $a_3 = 0$. We also assume that the folded singularities change from folded nodes (with two negative real eigenvalues) to folded saddles at the FSN I point. A sufficient condition for this is $C(z) < 0$ in a neighbourhood of the origin.

The critical manifold $\mathcal{Z}$ is given parametrically by

$$\mathcal{Z} = \left\{ x = \frac{A_2(z)B_2(z)}{\beta_2 C(z)}, y_1 = -\frac{A_2^2(z)B_2^2(z)}{\beta_2^2 C^2(z)}, y_2 = -\frac{A_2(z)}{\beta_2} \right\}$$

and the curve of folded singularities is defined by

$$M = \{x = 0, y_1 = 0, y_2 = 0\}.$$

A Hopf bifurcation of the (x, y_1, y_2) subsystem is given by the condition

$$A_2(z)B_2(z)\left(2A_2(z)B_2(z) - C^2(z) + \varepsilon\,\beta_2^2 C(z)\right) = 0,$$

together with

$$C(z)\left(2A_2(z)B_2(z) - C^2(z)\right) > 0.$$

The nonzero eigenvalues of the desingularized system of (4.23) with $a_2 = 0, a_3 = 0$ are

$$2\lambda = C(z) \pm \sqrt{C^2(z) - 8A_2(z)B_2(z)}.$$

We thus have both a Hopf bifurcation of the (x, y_1, y_2) subsystem and a FSN of the desingularized system as we pass through M_0^{I} (i.e. as $A_2(z) \to 0$). □

It is beyond our scope to analyze how trajectories perturb in both ε and δ. We conjecture that if δ is sufficiently small, then the small oscillations of the MMO inherit their rotational properties from the dynamic Hopf bifurcation. Alternatively, if δ is sufficiently large, the rotational properties of trajectories are manifestations of the properties of the canards.

Figure 4.13 shows the effect of 'small' and 'large' δ on trajectories $\Gamma_{(\varepsilon,\delta)}$ of (4.1). In panel (a), δ is small enough that the 3-fast/1-slow splitting is valid. The slow drift in c moves $\Gamma_{(\varepsilon,\delta)}$ through the Hopf bifurcation and we see behaviour typical of a delayed Hopf. By increasing δ, we eventually cross a secondary bifurcation and the nature of the orbit changes. Panel (b) shows $\Gamma_{(\varepsilon,\delta)}$ after the secondary bifurcation has been crossed. The trajectory no longer closely follows $\mathcal{Z}$ and undergoes its small oscillations in a neighbourhood of M_δ (about a folded node). Thus, by increasing δ, we have moved from a parameter regime where the 3-fast/1-slow splitting is favoured to a regime where the 1-fast/3-slow splitting is appropriate.

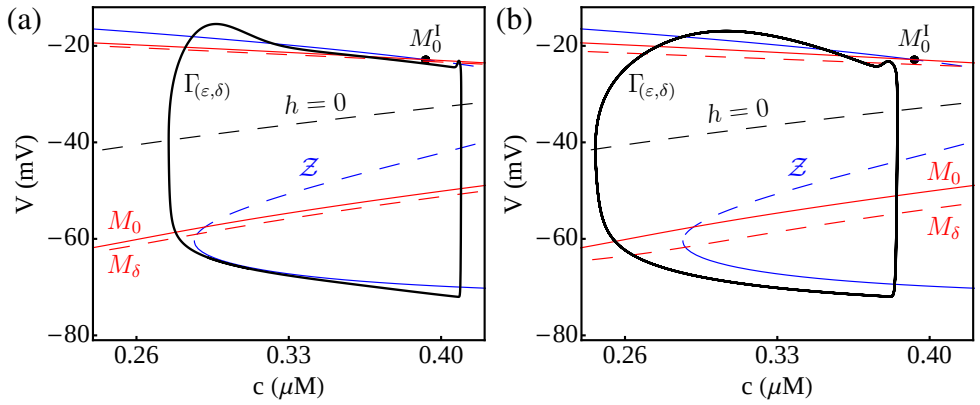

Figure 4.13. Oscillatory behaviour associated with the FSN I M_0^{I} for various δ. The parameters are $g_K = 3$ nS, $g_{BK} = 0.4$ nS, $g_A = 8$ nS, $C_m = 0.2$ pF and (a) $f_c = 0.01$ and (b) $f_c = 0.03$. The singularities $\mathcal{Z}$ and M_0 (red, solid) of (4.20) are shown along with the folded singularities M_δ (red, dashed) of (4.9). (a) When δ is small, the trajectories exhibit properties of the Hopf. (b) When δ is large, the trajectories no longer stick to $\mathcal{Z}$ and the small oscillations arise from canards.

4.6.2. Delayed Hopf Bifurcation and Tourbillon. There exists a subset of parameter space such that the dynamic MMOs exhibit oscillations above an observable threshold. Such dynamic MMOs are called *tourbillon* [**27**]. The burst patterns associated with a tourbillon are qualitatively different from those arising from delayed Hopf or folded node mechanisms (see Figure 4.14). Despite this, a tourbillon is actually just a different manifestation of a dynamic Hopf bifurcation. Recall that MMOs approaching the Hopf $\mathcal{Z}^H$ from an $\mathcal{O}(1)$ distance become exponentially close to $\mathcal{Z}^{(\varepsilon,0)}$ and so display virtually no small oscillations. In the case of a tourbillon, the trajectory approaches the dynamic Hopf bifurcation from a much closer distance. In that case, the real part of the eigenvalues is small and the attraction to $\mathcal{Z}_{(\varepsilon,0)}$ is weak. As a result, the trajectory does not have sufficient time to be exponentially attracted and the oscillations are visible throughout. The speed at which the trajectory traverses the dynamic Hopf region is governed by the slowest timescale. As δ increases, the time spent near the Hopf decreases and hence, the number of observed oscillations decreases.

Figure 4.14 illustrates the difference between the two types of trajectories that pass by a dynamic Hopf bifurcation. Panel (a) depicts a geometric configuration in which $\mathscr{L}^-$ and M_0^{I} are well separated. This means that the full system bursting attractor shows virtually none of its small oscillations. The only observable small oscillation is at the end of the oscillatory regime when the trajectory jumps off the slow manifold. Figure 4.14(b) shows that when $\mathscr{L}^-$ and M_0^{I} are not well separated, the hysteresis loop narrows in width when viewed in the (V, c) projection. This means trajectories return sufficiently close to the Hopf that the rotations occur before the the trajectory can be exponentially attracted to the slow manifold. The amplitude of the small oscillations in a tourbillon initially decreases and eventually increases before the trajectory jumps away. This is because the real part of the eigenvalues is initially negative and increases through zero to positive values.

It becomes clear that when the parameters are chosen such that bistability holds and the fold point $\mathscr{L}^-$ and the FSN I point M_0^{I} are weakly separated, the resulting full system trajectory will (in principle) be a tourbillon. However, for fixed ε, the difference between a tourbillon and a delayed Hopf MMO is not always clear. There is no predefined distance that can be used to differentiate between the two types of dynamic Hopf phenomena.

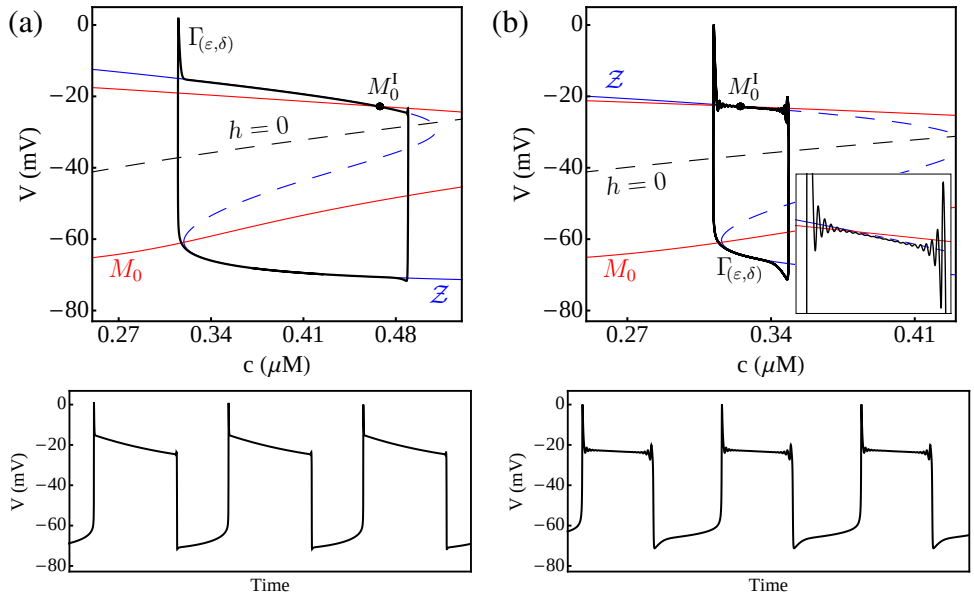

Figure 4.14. The two types of dynamic Hopf bifurcation for $g_{BK} = 0.4$ nS, $g_A = 4$ nS: (a) delayed Hopf bifurcation ($g_K = 2$ nS) and (b) tourbillon ($g_K = 4$ nS). Full system trajectories (black) have $C_m = 2$ pF and $f_c = 0.001$.

4.7. Discussion

MMOs are complex oscillatory waveforms characterized by an alternation between large and small amplitude oscillatory motion. Often appearing in the time course evolution of neural bursting models, MMOs have become a new metric in neuroscience [**38**]. As a result, a thorough understanding of the structure of MMOs and their mechanisms has become a significant interdisciplinary endeavour. An important aspect of MMOs is the multiscale structure of their governing equations, making them amenable to singular perturbation methods. One particular singular perturbation technique that has been used with great success is GSPT. Using this geometric approach, we have examined the transient and long-term dynamics of a 3-timescale neuroendocrine cell model (4.1). Our results show that the early investigations of (4.1) produced limited, non-overlapping views of the mixed mode dynamics in the pituitary cell model.

The dynamics of pseudo-plateau bursting have been of interest to both the cell modelling community and to those interested in MMOs in multiscale systems. Historically, the analysis of bursting in slow/fast systems was pioneered by [**98**] and several treatments of pseudo-plateau bursting followed suit [**94, 95, 116, 129**]. In this traditional 3-fast/1-slow approach, the small oscillations are born from a slow passage through a dynamic Hopf bifurcation [**91, 92, 3**] and the MMOs are hysteresis loops that alternately jump at a fold and a subcritical Hopf (fold/subHopf bursts) [**99, 65**]. We extended the standard slow/fast analysis and computed the additional MMO families that bifurcate from the unstable spiking branch (Figure 4.7). This classic slow/fast analysis is particularly effective for dynamic MMOs and for detecting the switch from dynamic to calcium-conducting MMOs. Away from singularities of the slow and 'fast' subsystems, Fenichel theory guarantees that the singular and non-singular orbits are $\mathcal{O}(\delta)$ close to each other.

An alternative and more recent take on pseudo-plateau bursting complements the classic approach. In the 1-fast/3-slow analysis, a folded critical manifold and canard orbits shape the dynamics. This novel slow/fast analysis is particularly effective in explaining the oscillatory behaviour of calcium-conducting MMOs. We showed that other geometric features such

as a curve of cusp bifurcations could influence the resetting behaviour of MMOs via fast depolarization at a fold or via circumnavigation of the cusps. The full system trajectories were $\mathcal{O}(\varepsilon)$ perturbations of the singular limit predictions in normally hyperbolic regions [**41, 68**]. In a neighbourhood of the fold surface L or a folded node, the asymptotic error estimates were $\mathcal{O}(\varepsilon^{2/3})$ [**71, 120**] and $\mathcal{O}(\varepsilon^{1/2})$ [**14, 140**], respectively. Our work also adds to the currently scarce supply of examples of canard-induced MMOs in systems with more than 2 slow variables [**58, 59**]. In both the 3-fast/1-slow and 1-fast/3-slow analyses, the underlying geometry influences the bursting through a combination of local and global mechanisms. These two slow/fast analyses of (4.1) stem from the inherent 3-timescale structure.

The core focus of this chapter has been the comparison of the relative strengths and weaknesses of these two complementary geometric methods in the context of the 3-timescale singular perturbation problem (4.1). When dealing with such problems, there are always questions of which analysis is appropriate and how the different methods are related [**125**]. In this chapter, we have directly addressed how the classic and novel 2-timescale methods are related in the context of system (4.1). To be precise, they are different unfoldings of the more degenerate 3-timescale decomposition. As to the question of which method is most appropriate, we assert that the 3-timescale decomposition provides the best results asymptotically, independent of the model, as it inherits all of the geometric information contained in the different 2-timescale analyses. As a result, the 3-timescale decomposition provides us with a remarkable degree of control and predictive power.

To the authors' knowledge, there has been little work done on 3-timescale problems [**67, 74, 75**]. In this chapter, we concentrated on 3-timescale problems of the form (1.5), in which there is an obvious ordering of the timescales, i.e.

$$\delta \ll 1 \ll \frac{1}{\varepsilon}.$$

In particular, we analyzed a 3-timescale pituitary lactotroph model using geometric singular perturbation analysis techniques. We have demonstrated the potency of such an approach and formulated our analysis in a general way that easily carries over to other 3-timescale problems. Our analysis showed that, for the most part, each transition of a trajectory could be explained locally by the interaction of 2-timescales only. However, we have also shown that there is a need for the development of a comprehensive theoretical framework for 3-timescale systems. In the 3-timescale formulation, we encountered degeneracies not yet seen before in the form of the FSN I points M_0^{I}, which represent the interaction of objects from the 3-fast/1-slow theory (the critical manifold $\mathcal{Z}$) with objects from the 1-fast/3-slow theory (the folded singularities M_0). The unfolding of M_0^{I} is particularly important because it is new and it marks regions in phase space where all three timescales interact. Moreover, there are elements of the 2-timescale theory that require deeper analysis. For instance, the unfolding of FSN I singularities has yet to be done: a problem we address in the next chapter. In any case, we have shown that there is great benefit in combining GSPT with bifurcation analysis. The moral of the story then, is that it never hurts to look at a problem from multiple points of view.

CHAPTER 5

Canards of Folded Saddle-Node Type I

Folded node canards, folded saddle canards, and their bifurcations have been studied extensively in $\mathbb{R}^3$. The folded saddle-node of type I (FSN I) is the codimension-1 bifurcation that gives rise to folded nodes and folded saddles and has been observed in various applications, such as the forced Van der Pol oscillator and in models of neural excitability. Their dynamics however, are not completely understood. In this chapter, we analyze the local dynamics near a FSN I by combining methods from GSPT (blow-up), and the theory of dynamic bifurcations (analytic continuation into the plane of complex time). We prove the existence of canards, faux canards, and their concatenations near the FSN I. We also show that there is a delayed loss of stability and estimate the expected delay. The contents of this chapter are the focus of [**138**].

Authors' Contributions: The analysis in this chapter was performed by TV with assistance from MW. The results of Section 5.3.1 and the proof of Proposition 5.14 were obtained by MW. The analysis in Section 5.3.2 was done jointly by TV and MW. The manuscript was written by TV, and edited by TV and MW.

5.1. Motivation

Canards are special solutions of slow/fast systems that partition the flow and organize the dynamics in phase space. They are ubiquitous in applications and have been used to explain

- the firing patterns (spiking, bursting and excitability thresholds) of electrically excitable cells in neuroscience [**24, 33, 39, 101, 103, 104, 135**],
- the sudden change in amplitude and period of oscillatory behaviour in chemical reactions [**85, 90, 97**],
- the anomalous delays in response to exogenous pulses of inositol triphosphate in calcium signalling [**58, 59**],
- the critical regimes that separate explosive and non-explosive chemical reactions in combustion problems [**44, 45, 111, 115**],
- and the instability to self-sustained vibrations that can ruin metal cutting processes such as turning, milling and drilling [**17**].

This is just a small sample of the many instances in which the canard phenomenon has been applied and we refer to [**15, 27**] for additional examples. In Chapters 3 and 4, we found that the bursting behaviour of (1.3) was closely related to the existence of folded singularities and canards. In particular, the bursting/depolarized equilibrium boundary was the set of FSN II points, and the dynamic MMOs always passed close to a FSN I point. Motivated by this, we now carefully examine the dynamics around the FSN bifurcation.

Both types of FSN are common in applications, often leading to the onset of complex and chaotic dynamics. FSN I singularities arise in the forced van der Pol oscillator, where they lead to the creation of MMOs [**11, 48, 57, 120**]. The FSN I demarcates the regions in parameter space where bursting occurs in neuroendocrine cell models [**123**]. In Chapter 4, we identified the FSN I points as the regions in phase space where all three timescales interact [**136**]. The FSN I also crops up in a hybrid Morris-Lecar/FitzHugh-Nagumo model, where it

is responsible for creating firing threshold manifolds that differentiate between spiking and quiescent behaviour [**144**]. We remark that the FSN I does not require a Hopf bifurcation to create oscillatory behaviour.

The FSN II is the dynamic unfolding of the 2D singular Hopf bifurcation and explains the rapid transition from $\mathcal{O}(\sqrt{\varepsilon})$-amplitude limit cycles to relaxation oscillations via canard explosion in planar slow/fast systems [**36, 73**]. The FSN II plays an important role in the creation of MMOs [**4, 12, 51**] and frequently occurs in cell models. Some examples include the Hodgkin-Huxley model [**103, 104**], an entorhinal cortex layer II stellate cell model [**101**], models of intracellular calcium dynamics [**59**], and the pituitary lactotroph model (1.3). The occurrence of one type of FSN does not preclude the possibility of the other; both types appear in [**39, 123**] where they enclose the region of parameter space where MMOs occur.

Despite their importance in applications, the dynamics near FSN singularities are not well understood. Both FSN singularities are known to possess canards for $0 < \varepsilon \ll 1$ [**119, 139**]. Recent studies have unravelled the dynamics of the FSN II [**20, 51, 76**] (see Section 2.5.3). In particular, the FSN II has been studied in the $\mu = \mathcal{O}(\varepsilon)$ regme [**51**], in the $\mu = \mathcal{O}(\sqrt{\varepsilon})$ regime [**76**] and in the transition between them [**20**]. However, there is currently no such analogue for the FSN I.

5.1.1. Aims and Outline. The aim of this chapter is to extend canard theory into the FSN I regime with $\mu = \mathcal{O}(\varepsilon^k)$, $k \geq \frac{1}{4}$ (we refer to the blow-up in Section 5.3.3 for an explanation of the ε-dependent neighbourhoods). We seek to analyze the dynamics near the FSN I thereby proving the existence of canards and faux canards. We focus on the delayed loss of stability near the FSN I and provide delay estimates. Unlike the FSN II [**51, 76**], the FSN I has no full system Hopf bifurcation and there is also the possibility for faux canards. This suggests there may be canards that traverse the entire length of the repelling manifold and return to the attracting manifold. This chapter complements the FSN II analysis in [**76**].

The outline of the chapter is as follows. In Section 5.2, we study the FSN I in the forced Van der Pol oscillator and in a hybrid Morris-Lecar/FitzHugh-Nagumo model for neural excitability, showing that it generates complex and unexpected dynamics. We numerically demonstrate canards, faux canards and solutions that are concatenations of canards and faux canards, a study of which motivates the rest of the chapter. In Section 5.3, we examine a normal form for the FSN I, define the associated transition map, and provide a partial blow-up analysis. In particular, we zoom in on an $\mathcal{O}(\varepsilon^{1/4})$ neighbourhood of the FSN I. In so doing, we convert our problem of finding canards into a dynamic Hopf bifurcation problem.

In Section 5.4, we state our main theoretical results whilst pointing out the similarities/differences to the FSN II. We state existence theorems for canards and faux canards in the FSN I limit, and estimate how long we expect solutions to follow the weak canard before escaping via fast directions. The novel results that set the FSN I apart from the FSN II are the existence of faux canards, and the ability for solutions to cross the repelling manifold and return to the attracting side. The numerics in Section 5.2 illustrate the theorems of Section 5.4. Sections 5.2, 5.3 and 5.4 contain the main results of the chapter, whilst Sections 5.5 and 5.6 are devoted to formally proving our assertions.

To prove the existence of canards and study their properties, we follow the approach of [**91, 92**] for dynamic bifurcation problems and analytically continue solutions into the plane of complex time in Section 5.5. We examine special paths along which the system has an adiabatic invariant. That is, we study the linearized complex flow along elliptic paths, where solutions neither grow nor decay. In Section 5.6, we extend the results of Section 5.5 to the complex nonlinear flow. In this way, we are able to track the invariant manifolds across the dynamic bifurcations and hence show the existence of $\mathcal{O}(\varepsilon^{-1/4})$ canards and faux canards, and study the associated bifurcation delay. We conclude in Section 5.7 with a discussion.

5.2. The FSN I In Practice

The FSN I is the codimension-1 bifurcation of the reduced flow that separates folded saddle and folded node regimes. We are interested in the local dynamics of the FSN I because it is the organizing center for delay phenomena. A canonical form for the FSN I [**76**] is

$$\begin{aligned} \dot{x} &= -z + \delta\left(\alpha - y^2\right) + \mathcal{O}(x, \varepsilon, z(y+z), y^3), \\ \dot{y} &= 1 + \mathcal{O}(x, y, z, \varepsilon), \\ \varepsilon\,\dot{z} &= x + z^2 + \mathcal{O}(z^3, xz^2, xyz, \varepsilon(x+y+z), \varepsilon^2), \end{aligned} \tag{5.1}$$

with parameters $\alpha \in \mathbb{R}$ and $\delta = \pm 1$ (cf. system (2.17) for $\mu = 0$). In this section, we provide a brief geometric singular perturbation analysis of (5.1), highlighting the main differences between the two FSN I subcases ($\delta = \pm 1$). We numerically demonstrate canards and faux canards in the FSN I limit in the forced Van der Pol (VdP) oscillator ($\delta = -1$ subcase), and in a hybrid Morris-Lecar/FitzHugh-Nagumo model for excitability in the firing patterns of neurons ($\delta = 1$ subcase).

Remark 5.1. For $\alpha > 0$, system (5.1) can be transformed to system (2.17) by translating one of the folded singularities to the origin. By translating the folded node to the origin, we can express the parameter α in terms of the eigenvalue ratio μ of the folded node

$$\mu = \frac{-1 + \sqrt{1 - 16\sqrt{\alpha}}}{-1 - \sqrt{1 - 16\sqrt{\alpha}}}, \quad \text{or} \quad \alpha = \frac{\mu^2}{16(1+\mu)^4}.$$

We choose to work with (5.1) to retain symmetry at leading order.

5.2.1. Geometric Singular Perturbation Analysis. Fast fibers of the layer problem of (5.1) move trajectories towards or away from the 2D critical manifold, which is given to leading order by the parabolic cylinder $S = \{(x, y, z) : x = -z^2\}$, with attracting sheet S_a ($z < 0$), repelling sheet S_r ($z > 0$), and fold curve L given by the y-axis. The reduced flow is the $\varepsilon \to 0$ limit of (5.1). Projection and desingularization give

$$\begin{aligned} \dot{y} &= -2z(1 + \mathcal{O}(z)), \\ \dot{z} &= -z + \delta\left(\alpha - y^2\right) + \mathcal{O}(x, z(y+z)), \end{aligned} \tag{5.2}$$

which has folded singularities at $(y, z) = (\pm\sqrt{\alpha}, 0)$ for $\alpha > 0$. These merge to the FSN I for $\alpha = 0$ and disappear for $\alpha < 0$. If $\delta = 1$, the folded singularity at $(-\sqrt{\alpha}, 0)$ is a folded node and the folded singularity at $(\sqrt{\alpha}, 0)$ is a folded saddle. The funnel of the folded node is bounded by the folded node strong canard Γ_s^n and L (Figure 5.1(a)). If $\delta = -1$, the folded singularities are reversed and the funnel is enclosed by Γ_s^n, the folded saddle canard Γ_s^s and L (Figure 5.1(b)). When α is large enough, the folded node and folded saddle are sufficiently separated that the bifurcation theory of folded nodes [**140**] applies without modification. For $\alpha > 0$, the unstable manifold of the folded saddle forms a heteroclinic connection with the folded node and trajectories near the unstable manifold of the folded saddle rotate about the folded node [**52**]. We take this heteroclinic to be the primary weak canard.

For $\alpha = 0$, we see that δ controls the position of the center manifold W^C. For $\delta = 1$, W^C lies on S_a, the funnel region persists and we expect a family of canard solutions. For $\delta = -1$, the funnel region shrinks to zero and W^C lies on S_r. In this case, we expect only those initial conditions close to the strong canard will be influenced by the dynamics near the FSN I singularity. Both scenarios have been observed in applications. The $\delta = 1$ situation occurs in [**144**] whilst the $\delta = -1$ configuration has been found in [**39, 119, 123**]. In fact, the bifurcations associated with secondary canards near the FSN I with $\delta = -1$ were studied numerically in [**52**]. We now investigate the two FSN I subcases in two model systems.

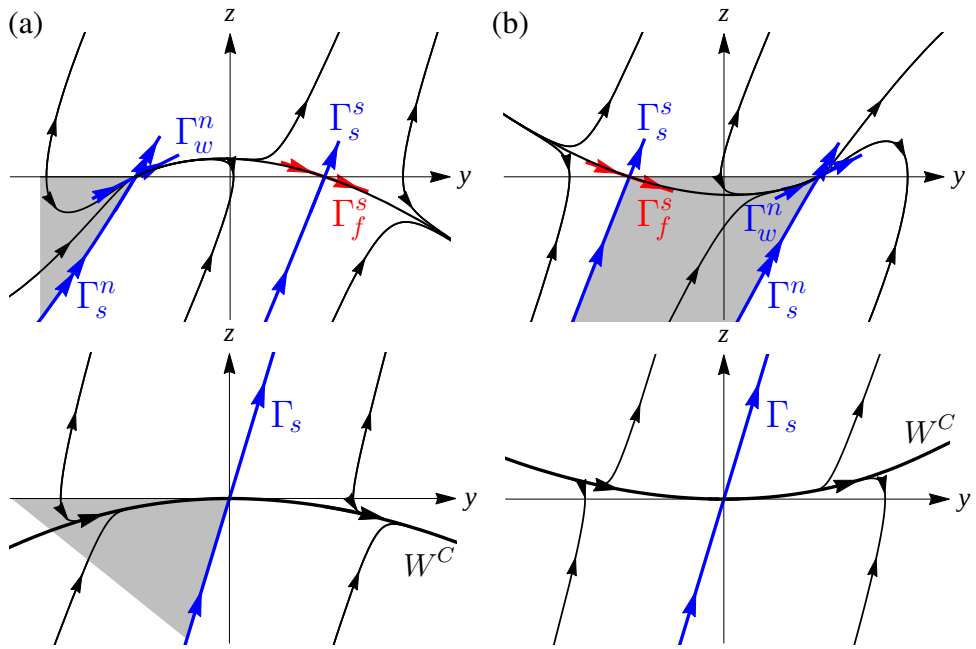

Figure 5.1. Reduced flow of (5.1) for (a) $\delta = 1$ and (b) $\delta = -1$. In (a), the funnel (shaded) persists in the FSN I limit $\alpha \to 0$ (bottom row) and the center manifold W^C is on S_a. In (b), the funnel disappears and W^C is on S_r. The folded node strong and weak canards are denoted by Γ_s^n and Γ_w^n, respectively. The folded saddle true and faux canards are labelled as Γ_s^n and Γ_f^n, respectively

5.2.2. Example: The Forced Van der Pol Oscillator. The VdP oscillator is a basic model for oscillatory processes in physics, electronics, biology, neurology, sociology and economics. With strong nonlinear damping effects, it is the prototypical example of a relaxation oscillator. The most prominent variant of the VdP oscillator is the forced VdP equation:

$$\begin{aligned} \dot{x} &= -z + A\cos y, \\ \dot{y} &= \omega, \\ \varepsilon\,\dot{z} &= x - \frac{1}{3}z^3 + z, \end{aligned} \tag{5.3}$$

where $\varepsilon^{-1/2}$ is the damping factor, A is the forcing amplitude and $\omega > 0$ is the slow drive frequency. The external signal models a periodically varying driving force, such as a heart being driven by a pacemaker. Detailed studies of (5.3) have been done in the geometric singular perturbations context [**11, 48, 57, 120**]. Our goal here is to illustrate the existence of canards and faux canards near the FSN I limit.

We start by identifying the geometric structures of (5.3). The critical manifold is

$$S = \left\{ (x, y, z) : x = \frac{z^3}{3} - z \right\},$$

with folds at $z = \pm 1$, which separate the attracting sheets ($|z| > 1$) from the repelling sheet ($|z| < 1$). The reduced flow is given by

$$\begin{aligned} \dot{y} &= \omega, \\ (z^2 - 1)\dot{z} &= -z + A\cos y. \end{aligned}$$

For $A < 1$, there are no folded singularities and the attractor of the system is a relaxation oscillator. For $A = 1$, there is a FSN I at $(y, z) = (0, 1)$ which splits into a folded saddle and

a folded node for $A > 1$. The folded saddle is located at $(y, z) = (-\cos^{-1}(A^{-1}), 1)$ and the folded node at $(y, z) = (\cos^{-1}(A^{-1}), 1)$. Note that folded nodes only exist for

$$A < A_{\text{DFN}} := \sqrt{1 + (64\omega^2)^{-1}},$$

which ensures the eigenvalues of the desingularized system are real. The configuration of (5.3) is such that the reduced flow is directed from the folded saddle towards the folded node. As such, the FSN I in (5.3) has center manifold on S_r (i.e. $\delta = -1$ in the normal form).

Remark 5.2. Since the forcing term is periodic, there are infinitely many pairs of folded singularities (i.e. there is a pair of folded singularities on each of the folds, and these live in the space $\mathbb{R}^2 \times \mathbb{S}^1$). All pairs have the folded saddle to folded node ($\delta = -1$) configuration.

We make the following (numerical) observation: solutions of (5.3) with $1 < A < A_{\text{DFN}}$ (and ε sufficiently small) on S_a tend towards the submanifold defined by

$$CM := \{(x, y, z) \in S : z = A \cos y\},$$

as shown in Figure 5.2. We will show in Section 5.3.3 that CM is the zero order approximation to the primary weak canard, which we take to be the heteroclinic between the folded node and folded saddle.

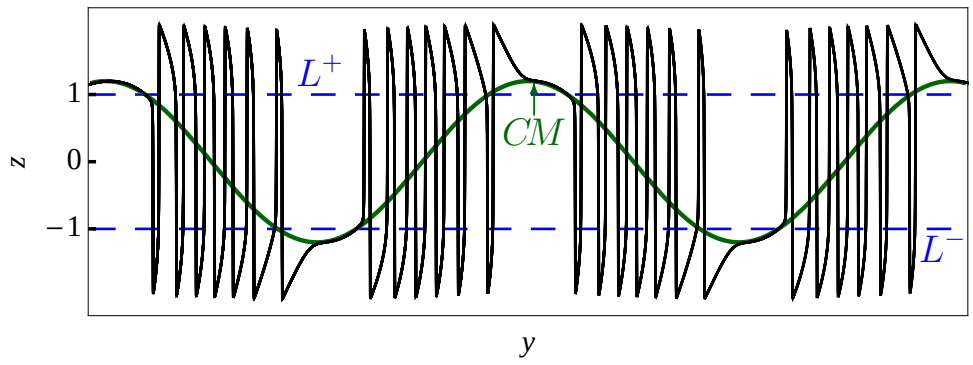

Figure 5.2. Attractor of (5.3) for $\varepsilon = 0.01$, $\omega = 0.15$ and $A = 1.2$. Trajectories become slaved to the segments of CM (green) that lie on an attracting sheet of S.

We are interested in the behaviour of solutions near the FSN I limit ($A = 1$). Using initial value solvers, it is very easy to find transient solutions of (5.3) that are initially $\mathcal{O}(\varepsilon^{1/4})$ close to CM on S_r, and pass from S_r to S_a via the folded saddle (we again refer to the blow-up in Section 5.3.3 for an explanation of the ε-dependent neighbourhoods). These faux canards exhibit small oscillations that have growing amplitude on S_r and decaying amplitude on S_a, evocative of a slow passage through a dynamic Hopf bifurcation [**2, 3, 4, 91, 92**] (but in reverse). Once they are on S_a, the trajectories follow CM until they reach the fold and return to S_r. Depending on the initial conditions, some of these solutions may continue to follow S_r for $\mathcal{O}(1)$ times on the slow timescale before they subsequently jump to an attracting branch of S. Boundary value solvers can be used to extend the solutions on S_r further and in the case of (5.3), can extend solutions along the entire length of S_r (Figure 5.3).

The special canard orbit in Figure 5.3 is highly unstable. In practice, most solutions fall off S_r before they can pass through the folded saddle and return to S_a. As a result, the attractor of the forced VdP oscillator near a FSN I is either a relaxation oscillation interspersed with delays (Figure 5.2) or a MMO (not shown). In either case, the delay occurs whenever the attractor falls into the funnel region enclosed by the fold curve, the folded node strong canard and the folded saddle canard. The delay itself is due to the slow passage effects associated with the folded node. The difference between a simple delay and a full MMO is

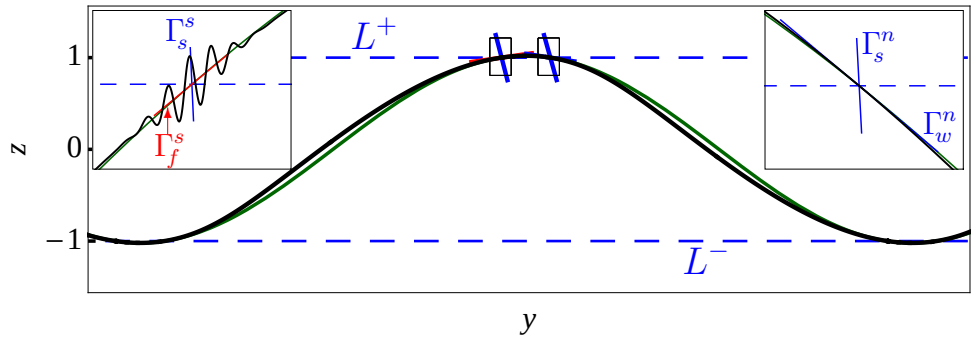

Figure 5.3. Special canard orbit (black) of (5.3) with $\varepsilon = 0.0001, \omega = 0.1$ and $A = 1 + 2\sqrt{\varepsilon} = 1.02$ that stays uniformly $\mathcal{O}(\varepsilon^{1/4})$ close to CM (green) projected onto the (y, z) plane. The folds $L^{\pm}$ intersect CM at folded saddle (left inset) and folded node (right inset) singularities. The stable and unstable eigendirections of the folded singularities are included. The small oscillations near the folded nodes are virtually imperceptible.

the size of the perturbation, which determines the oscillation amplitude ($\mathcal{O}(\sqrt{\varepsilon})$ for folded nodes).

5.2.3. Non-autonomous Excitable System With Dynamic Protocols. An excitable system is one that is typically silent (i.e. at steady state) but can produce a transient oscillation in response to an external stimulus. In the neuroscience context, these transient oscillations are action potentials. The notion of excitability is useful for understanding the firing behaviours of neurons, which are responsible for transmitting information through the nervous system. We study the FSN I in a hybrid Morris-Lecar/FitzHugh-Nagumo model for neural excitability with slow external drive $I(\varepsilon t)$ [**144**]:

$$\begin{aligned} \dot{v} &= v(v-a)(b-v) - w + I(s), \\ \dot{w} &= \varepsilon(w_\infty(v) - w), \\ \dot{s} &= \varepsilon, \end{aligned} \tag{5.4}$$

where $s \in \mathbb{R}$ is the (dimensionless) slow time, $w \in \mathbb{R}$ is a slow recovery variable and $v \in \mathbb{R}$ is the (dimensionless) fast voltage. The external slow drive is a mollified step protocol

$$I(s) = \frac{1}{2} I_1 \left(1 + \tanh\left(\frac{s - s_0}{s_1}\right)\right), \quad s \in [s_-, s_+],$$

where $[s_-, s_+]$ is a sufficiently large interval centered around s_0. For $s < s_-$, we take $I(s) = 0$ and for $s > s_+$, $I(s) = I_1$. The activation function is given by

$$w_\infty(v) = \frac{1}{2}\left(1 + \tanh\left(\frac{v - v_1}{v_2}\right)\right).$$

We set $a = -0.5, b = 1, I_1 = 0.09, s_0 = 0, v_1 = -0.1, v_2 = 0.1$ and take s_1 to be the bifurcation parameter. Geometrically, the most important features of (5.4) are the cubic shaped critical manifold

$$S := \left\{(v, w, s) \in \mathbb{R}^3 : w = v(v-a)(b-v) + I(s)\right\},$$

(to allow switching between active and silent states) and the sigmoidal activation function $w_\infty(v)$, which determines the number of equilibria the unforced ($I(s) \equiv 0$) system can have. Note the non-autonomous system (5.4) has no equilibria. The dynamic drive however can create folded singularities. This can in turn generate folded node and folded saddle canards, which provide a useful metric for excitability.

System (5.4) possesses a folded critical manifold S with folds located at

$$v_L^{\pm} = \frac{1}{3}\left(a + b \pm \sqrt{a^2 - ab + b^2}\right),$$

and lower attracting sheet S_a^- ($v < v_L^-$), upper attracting sheet S_a^+ ($v > v_L^+$) and repelling sheet S_r enclosed by the folds. Projection and desingularization of the reduced flow on S gives:

$$\begin{aligned}\dot{s} &= -f'(v),\\ \dot{v} &= f(v) + I(s) - w_\infty(v) + I'(s),\end{aligned}$$

where $f(v) := v(v-a)(b-v)$. As in the forced VdP example, we define the submanifold

$$CM := \{(v, w, s) \in S : w = w_\infty(v)\},$$

with the understanding that it will play the role of the primary weak canard.

The reduced flow on S has no ordinary singularities but the dynamic drive can create folded singularities. More precisely, for $s_1 > s_{\text{FSN}} \approx 0.829$, there are no folded singularities, no canards and hence no firing behaviour. For $s_1 = s_{\text{FSN}}$, the reduced flow of (5.4) has a FSN I singularity. For $0.7813 \lesssim s_1 < s_{\text{FSN}}$, the reduced flow has a pair of folded singularities on the lower fold curve. These folded singularities are oriented such that the flow is directed from folded node to folded saddle (i.e. $\delta = 1$ in the normal form). For $0 < s_1 \lesssim 0.7813$, the folded node becomes a folded focus and only the folded saddle canard persists.

We focus on trajectories that start somewhere on S_a^-. For $s_1 > s_{\text{FSN}}$, (5.4) has no folded singularities. The reduced flow on S_a^- is directed away from L^- and any trajectory starting on S_a^- never leaves S_a^-. Thus, in the absence of any additional stimulus, the system is quiescent. For $s_1 \lesssim 0.7813$, there is a folded focus and a folded saddle on L^-. Since folded foci have no canards, only the folded saddle canard Γ_s^s influences the firing behaviour. In fact, Γ_s^s plays the role of a firing threshold manifold [**144**]. Trajectories enclosed by Γ_s^s and L^- transiently spike; all other trajectories stay on S_a^- and remain quiescent.

Near the FSN I, the transient firing criterion is not so simple. There is a folded node strong canard Γ_s^n as well as the folded saddle canard Γ_s^s. Both canards emanate from their respective folded singularities and in system (5.4) turn back towards the fold. The trapping region of each canard is quite small and the phase space is divided into three distinct regions. Trajectories on S_a^- not enclosed by Γ_s^s never pass through either of the folded singularities and remain silent (Figure 5.4(a)). Most solutions in the region between Γ_s^n and Γ_s^s reach L^- and elicit a transient spike (Figure 5.4(b)).

In the region between Γ_s^n and L^-, trajectories are filtered through the folded node where they oscillate around CM. These solutions follow CM on S_r for various distances before being repelled, resulting in transient MMOs (Figure 5.4(c)). Some of these trace $CM \cap S_r$ and return to S_a^- in a neighbourhood of the folded saddle, where the slow flow directs them away from L^- so that they remain quiescent (Figure 5.4(d)). Thus, care must be taken with the firing threshold criterion near the FSN I limit since trajectories can tunnel through the fold via (folded node) canards and return to S_a^- via (folded saddle) faux canards.

Remark 5.3. Another possibility is that solutions filtered through the folded node make it over to Γ_s^s, follow it some distance on S_r and jump back to S_a^- (see Figure 5.11 and [**96**]).

As the system parameter s_1 is moved away from the FSN I limit, the folded node and folded saddle separate. Most initial conditions in the region between Γ_s^n and CM jump away from CM before they can return to S_a^- (Figure 5.4(e)). However, the primary weak canard can still make it all the way through (see Figure 5.4(f), where an approximation of the weak canard is virtually indistinguishable from CM).

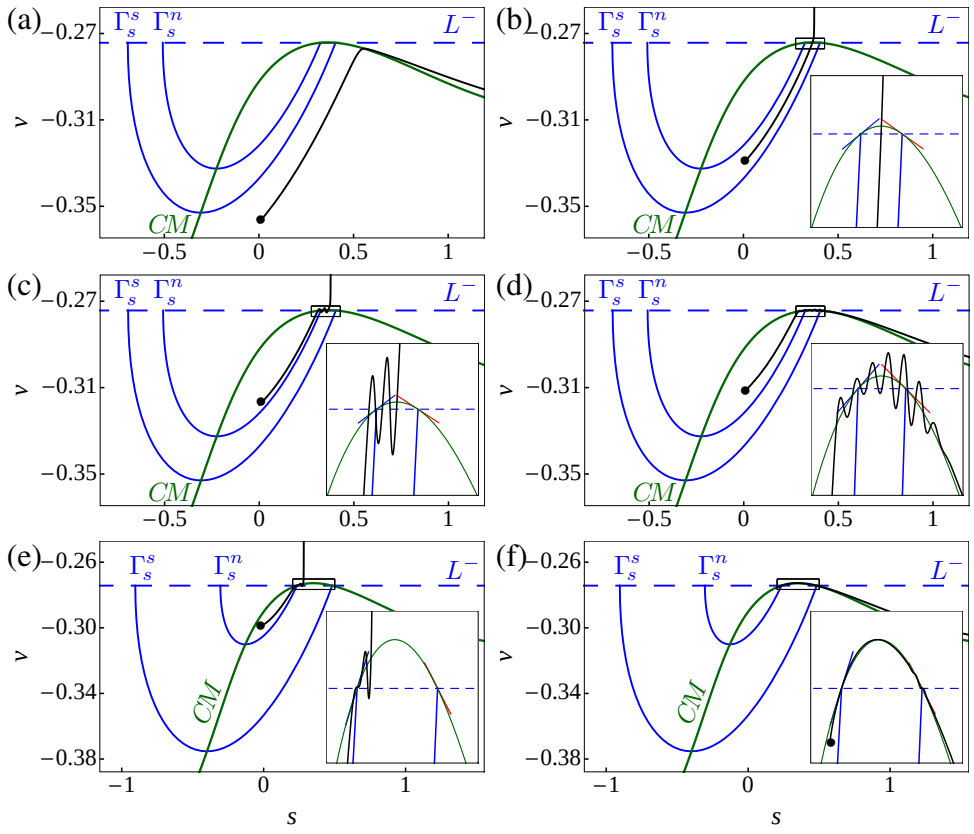

Figure 5.4. Canards, faux canards, spiking and MMOs in the excitability model (5.4). Parameters were set at $\varepsilon = 0.00001$, $s_1 = s_{\text{FSN}} - 0.5\sqrt{\varepsilon}$ for (a)–(d), and $s_1 = s_{\text{FSN}} - 5\sqrt{\varepsilon}$ for panels (e) and (f). Insets show magnified views of the region around the folded singularities. We fix $s(0) = 0$ (except for panel (f), where $s(0) = 0.2$) and move $v(0)$ through the different regions on S_a^-. Initial conditions are marked by black dots.

5.3. Blow-up Analysis of the FSN I

We have (numerically) demonstrated the existence of canards and faux canards near the FSN I limit in two model systems. The canards and faux canards oscillate near their respective folded singularities and can (surprisingly) connect to each other, allowing trajectories starting on S_a to cross over to S_r and eventually return to S_a (and vice versa). Motivated by these observations, we now turn to the theoretical problem of formally proving the existence of canards and faux canards in (5.1), and studying their properties near the FSN I limit. In this section, we define the flow map induced by (5.1), and perform a partial blow-up analysis. This section serves as a prelude to the analysis and results in the remainder of the chapter.

5.3.1. Transition Map. We introduce the transition map $\Pi : \Sigma_1 \to \Sigma_4$, induced by the flow of (5.1) with cross-sections

$$\Sigma_1 := \{(x, y, z) : x = -\sigma_1, \sigma_1 > 0\}, \quad \Sigma_4 := \{(x, y, z) : z = \sigma_4, \sigma_4 > 0\}.$$

Fenichel theory [**41, 68**] guarantees that the regions of S_a and S_r that are $\mathcal{O}(1)$ away from L perturb to invariant slow manifolds S_a^ε and S_r^ε, which are $\mathcal{O}(\varepsilon)$ close to their singular counterparts. Moreover, the slow flow on S_a^ε and S_r^ε is a smooth $\mathcal{O}(\varepsilon)$ perturbation of the reduced flow on S (Section 2.1). The blow-up technique extends Fenichel theory into $\mathcal{O}(\sqrt{\varepsilon})$ neighbourhoods of L. To analyze the map Π in these neighbourhoods (and the flow past the fold), we introduce intermediate ε-dependent cross-sections (Figure 5.5)

$$\Sigma_2 := \{(x, y, z) : x = -\varepsilon\, \sigma_2, \sigma_2 > 0\}, \quad \Sigma_3 := \left\{(x, y, z) : z = \sqrt{\varepsilon}\sigma_3, \sigma_3 > 0\right\},$$

which are used in the blow-up analysis of folded singularities (see [**14, 119, 140**] for details).

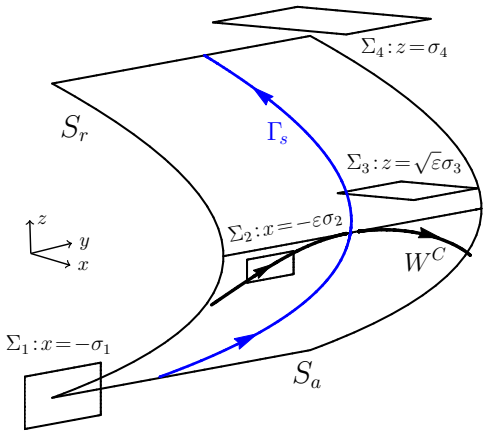

Figure 5.5. Cross-sections Σ_1 – Σ_4 to the flow of (5.1) in the FSN I limit for the subcase $\delta = 1$.

We have the following result, valid up to Σ_2 or up to Σ_3:

Proposition 5.1. *For system* (5.1) *the sets* $S_a^{\varepsilon^{1/4}}$ *and* $S_r^{\varepsilon^{1/4}}$ *are smooth locally invariant normally hyperbolic manifolds and* $\mathcal{O}(\varepsilon^{1/4})$ *smooth perturbations of* S. *The flow on* $S_a^{\varepsilon^{1/4}}$ *and* $S_r^{\varepsilon^{1/4}}$ *is an* $\mathcal{O}(\varepsilon^{1/4})$ *perturbation of the reduced flow.*

The reason why $S_a^{\varepsilon^{1/4}}$ and $S_r^{\varepsilon^{1/4}}$ are $\mathcal{O}(\varepsilon^{1/4})$ perturbations of S will become apparent in Section 5.3.3. An important property of $S_a^{\varepsilon^{1/4}}$ and $S_r^{\varepsilon^{1/4}}$ is that they grow algebraically in backward and forward time, respectively. In fact, $S_a^{\varepsilon^{1/4}}$ and $S_r^{\varepsilon^{1/4}}$ approach the parabolic cylinder $x = -z^2$ as $t \to \mp\infty$, respectively.

5.3.2. Blow-up & Entry Chart. To analyze the map Π, we introduce a suitable (spherical) blow-up transformation and analyze the dynamics on the sphere by treating the flow in various charts. Recall that the most important chart in the singular perturbations context is the classical chart κ_2 corresponding to an ε-dependent rescaling of the vector field (see Section 5.3.3). In chart κ_2, the parameter α is rescaled as $\alpha = \sqrt{\varepsilon}\alpha_2$ so that $\lim_{\varepsilon\to 0}\alpha = 0$ and we have a FSN I singularity for all $\alpha = \mathcal{O}(\sqrt{\varepsilon})$. With this in mind, we set $\alpha = \sqrt{\varepsilon}\alpha_2$ in (5.1). For the FSN I singularity of (5.1) with $\alpha = \sqrt{\varepsilon}\alpha_2$, the blow-up transformation is

$$(x, y, z, \varepsilon) = (r^4\overline{x}, r\overline{y}, r^2\overline{z}, r^4\overline{\varepsilon}), \tag{5.5}$$

with $(\overline{x}, \overline{y}, \overline{z}, \overline{\varepsilon}) \in \mathbb{S}^3$. We concentrate on charts κ_1 and κ_2 defined by $\overline{x} = -1$ and $\overline{\varepsilon} = 1$, respectively (recall from Figure 2.3(b) that these charts are sufficient to capture the incoming, outgoing and flow on the blown-up sphere itself).

We begin our analysis of Π by examining the transition from Σ_1 to Σ_2. To do this, consider (5.5) with $\overline{x} = -1$ and let $\Pi_1 : \Sigma_1 \to \Sigma_2$ be the associated map. The sections Σ_1 and Σ_2 are given by $r_1 = \sigma_1^{1/4}$ and $r_1 = (\sigma_2\,\varepsilon)^{1/4}$, respectively. Transformation and desingularization (i.e. rescaling time by $\frac{1}{4}r_1^2$) of system (5.1) on the fast timescale with $\alpha = \sqrt{\varepsilon}\alpha_2$ gives:

$$\begin{aligned}
\dot{r}_1 &= -r_1\,\varepsilon_1\left(-z_1 + \delta(\sqrt{\varepsilon_1}\alpha_2 - y_1^2) + \mathcal{O}(r_1, \varepsilon_1)\right),\\
\dot{y}_1 &= 4r_1\,\varepsilon_1 + \varepsilon_1\,y_1\left(-z_1 + \delta(\sqrt{\varepsilon_1}\alpha_2 - y_1^2) + \mathcal{O}(\varepsilon_1)\right) + \mathcal{O}(r_1^2),\\
\dot{z}_1 &= 4(-1 + z_1^2) + 2\,\varepsilon_1\,z_1\left(-z_1 + \delta(\sqrt{\varepsilon_1}\alpha_2 - y_1^2) + \mathcal{O}(r_1, \varepsilon_1)\right),\\
\dot{\varepsilon}_1 &= 4\,\varepsilon_1^2\left(-z_1 + \delta(\sqrt{\varepsilon_1}\alpha_2 - y_1^2) + \mathcal{O}(r_1, \varepsilon_1)\right).
\end{aligned} \tag{5.6}$$

This has two invariant subspaces $r_1 = 0$ and $\varepsilon_1 = 0$. Their intersection contains the lines of equilibria $L_{a,1} = (0, y_1, -1, 0)$ and $L_{r,1} = (0, y_1, 1, 0)$, which have nonzero eigenvalue ∓ 2, respectively. In the invariant subspace $\varepsilon_1 = 0$, system (5.6) has normally hyperbolic surfaces $S_{a,1}$ and $S_{r,1}$ of equilibria, which emanate from $L_{a,1}$ and $L_{r,1}$, respectively. Note that $S_{a,1}$ and $S_{r,1}$ correspond to the attracting and repelling branches of the critical manifold S. In the invariant subspace $r_1 = 0$, there exist 2D center manifolds $C_{a,1}$ and $C_{r,1}$ of $L_{a,1}$ and $L_{r,1}$, respectively, which can be viewed as the extensions of $S_{a,1}$ and $S_{r,1}$ on the blown-up locus.

Proposition 5.2 ([**119, 140**]). *The following hold for system* (5.6)*:*

(i) There exists an attracting 3D center manifold $M_{a,1}$ of the line of equilibria $L_{a,1}$, containing the surface of equilibria $S_{a,1}$ and the center manifold $C_{a,1}$. The branch of $C_{a,1}$ in $r_1 = 0, \varepsilon_1 \geq 0$ is unique for $1 + \delta(\sqrt{\varepsilon_1}\alpha_2 - y_1^2) > 0$.

(ii) There exists a repelling 3D center manifold $M_{r,1}$ of the line of equilibria $L_{r,1}$, containing the surface of equilibria $S_{r,1}$ and the center manifold $C_{r,1}$. The branch of $C_{r,1}$ in $r_1 = 0, \varepsilon_1 \geq 0$ is unique for $-1 + \delta(\sqrt{\varepsilon_1}\alpha_2 - y_1^2) < 0$.

System (5.6) is the blow-up of system (5.1) over the fast timescale. To obtain the corresponding slow flow on the center manifold $M_{a,1}$ given by $z_1^-(r_1, y_1, \varepsilon_1) = -1 + \mathcal{O}(r_1, \varepsilon_1)$, we substitute z_1^- into (5.6) and desingularize (i.e. rescale time by ε_1):

$$\begin{aligned} \dot{r}_1 &= -r_1 \left(1 + \delta(\sqrt{\varepsilon_1}\alpha_2 - y_1^2) + \mathcal{O}(r_1, \varepsilon_1)\right), \\ \dot{y}_1 &= 4r_1 + y_1(1 + \delta(\sqrt{\varepsilon_1}\alpha_2 - y_1^2) + \mathcal{O}(r_1, \varepsilon_1)), \\ \dot{\varepsilon}_1 &= 4\,\varepsilon_1 \left(1 + \delta(\sqrt{\varepsilon_1}\alpha_2 - y_1^2) + \mathcal{O}(r_1, \varepsilon_1)\right). \end{aligned} \tag{5.7}$$

In the invariant subspace $\varepsilon_1 = 0$, (5.7) is the desingularized flow (5.2) on S_a for $\alpha = 0$. For $\delta = 1$, there is a saddle at the origin and saddle-nodes at $(0, \pm 1, 0)$. The attracting eigendirection of the saddle corresponds to the strong eigendirection Γ_s of the FSN I whilst the center directions of the saddle-nodes correspond to the center directions W^C of the FSN I. That is, the blow-up splits the strong and center directions of the FSN I.

In the invariant subspace $r_1 = 0$, there is a saddle at the origin and two branches of equilibria $W^C_\pm = \left(0, \pm\sqrt{\alpha_2\sqrt{\varepsilon_1}+1}, \varepsilon_1\right)$ which are both center-stable and correspond to the center directions of the FSN I. Note that the (y_1, ε_1) problem is singularly perturbed since $W^C_\pm$ is invariant. Trajectories approach $W^C_\pm$ along its stable eigendirection and the flow on $W^C_\pm$ is determined by a center manifold computation.

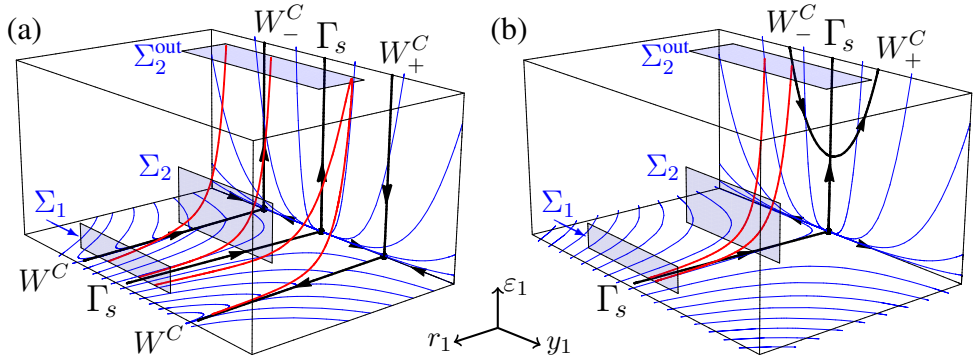

Figure 5.6. Dynamics in chart κ_1 for $\alpha_2 > 0$ and (a) $\delta = 1$, and (b) $\delta = -1$.

Estimating the transition time from Σ_1 to Σ_2 by the linearization of the saddle at the origin gives $T_s = \mathcal{O}\left(\log \varepsilon^{-1/4}\right)$. The expansion in y_1 implies that all initial conditions in Σ_1 that are $\mathcal{O}\left(\varepsilon^{1/4}\right)$ close to Γ_s will be mapped into an $\mathcal{O}(1)$ neighbourhood of Γ_s in Σ_2. The leading

order flow on the center manifold of $(0,-1,0)$ gives the transition time from Σ_1 to Σ_2 as $T_c = \mathcal{O}\left(\varepsilon^{-1/4}\right)$. Thus, all initial conditions in Σ_1 that are $\mathcal{O}(1)$ close to the center eigendirection and some arbitrarily small but fixed distance from Γ_s map to Σ_2 in an $\mathcal{O}\left(\exp\left(-\varepsilon^{-1/4}\right)\right)$ neighbourhood of the center eigendirection. By continuity of Π_1, all initial conditions in Σ_1 cover the whole segment between the strong and center eigendirections in Σ_2 (up to exponentially small error) under the map Π_1 (Figure 5.6(a)).

For $\delta = -1$, there is only a saddle at the origin in the invariant subspace $\{\varepsilon_1 = 0\}$. In the invariant subspace $\{r_1 = 0\}$, there are two additional branches of equilibria $W^C_{\pm} = \left(0, \pm\sqrt{\alpha_2\sqrt{\varepsilon_1}-1}, \varepsilon_1\right)$ which only exist for $\varepsilon_1 > \alpha_2^{-2}$ and are both center-stable (Figure 5.6(b)). These can be viewed as the pre-images of the folded node weak canard and the folded saddle faux canard in chart κ_1, respectively.

We identify an exit section $\Sigma_2^{\text{out}} : \varepsilon_1 = \sigma_2^{-1}$ for when solutions in κ_1 enter κ_2. The transition estimates near the saddle are as above so that initial conditions $\mathcal{O}(\varepsilon^{1/4})$ close to Γ_s in Σ_1 expand to an $\mathcal{O}(1)$ interval around Γ_s in Σ_2 (Figure 5.6(b)). The restricted map $\Pi_1^{\text{out}} : \Sigma_1 \to \Sigma_2 \cap \Sigma_2^{\text{out}}$ gives the additional constraint $\varepsilon_1(0) = \mathcal{O}(\varepsilon)$ so that $\varepsilon_1(T_s) = \sigma_2^{-1}$. We will show in Section 5.3.4 that this implies only initial conditions $\mathcal{O}(\varepsilon^{1/4})$ close to Γ_s in Σ_1 enter the domain of attraction of the dynamics in κ_2 (i.e. the funnel).

5.3.3. Zoom of the FSN I. We now examine the flow past the fold curve (i.e. the transition from Σ_2 to Σ_3) by setting $\overline{\varepsilon} = 1$ in (5.5), which gives

$$x = \varepsilon\, x_2, \quad y = \varepsilon^{1/4}\, y_2, \quad z = \sqrt{\varepsilon} z_2, \tag{5.8}$$

since $\varepsilon = r_2^4$. The directional blow-up (5.8) is an ε-dependent zoom of the vector field near the FSN I. Recall that $\alpha = \sqrt{\varepsilon}\alpha_2$. In terms of the eigenvalue ratio of the folded node, $\alpha = \mathcal{O}(\sqrt{\varepsilon})$ corresponds to $\mu = \mathcal{O}(\varepsilon^{1/4})$.

Remark 5.4. The change of coordinates between chart κ_1 and κ_2 (see Definition 2.15) is given by

$$\begin{aligned}
\kappa_{12}(x_2, y_2, z_2, r_2) &= \left(r_2(-x_2)^{1/4}, (-x_2)^{-1/4} y_2, (-x_2)^{-1/2} z_2, -x_2^{-1}\right), \quad x_2 < 0, \\
\kappa_{21}(r_1, y_1, z_1, \varepsilon_1) &= \left(-\varepsilon_1^{-1}, \varepsilon_1^{-1/4}\, y_1, \varepsilon_1^{-1/2}\, z_1, r_1\, \varepsilon_1^{1/4}\right), \quad \varepsilon_1 > 0.
\end{aligned}$$

Transformation and desingularization (i.e. $t = \sqrt{\varepsilon} t_2$) converts the 1-fast/2-slow system (5.1) into the 2-fast/1-slow system

$$\begin{aligned}
\dot{x_2} &= -z_2 + \delta\left(\alpha_2 - y_2^2\right) + \mathcal{O}(\varepsilon^{1/4}), \\
\dot{y_2} &= \varepsilon^{1/4}\left(1 + \mathcal{O}(\varepsilon^{1/4})\right), \\
\dot{z_2} &= x_2 + z_2^2 + \mathcal{O}(\varepsilon^{1/4}),
\end{aligned} \tag{5.9}$$

which describes the dynamics in an $\mathcal{O}(\varepsilon^{1/4})$ neighbourhood of the FSN I singularity. The associated layer problem of (5.9) is given by

$$\begin{aligned}
\dot{x_2} &= -z_2 + \delta\left(\alpha_2 - y_2^2\right), \\
\dot{z_2} &= x_2 + z_2^2,
\end{aligned} \tag{5.10}$$

with parameter y_2. The 1D critical manifold CM of equilibria is defined by

$$CM := \left\{\left(-(\alpha_2 - y_2^2)^2, y_2, \delta(\alpha_2 - y_2^2)\right) : y_2 \in \mathbb{R}\right\}. \tag{5.11}$$

Linear stability analysis shows that the eigenvalues of (5.10) along CM are

$$\lambda = \delta(\alpha_2 - y_2^2) \pm \sqrt{(\alpha_2 - y_2^2)^2 - 1}. \tag{5.12}$$

For $\alpha_2 < 0$, CM is always stable (or unstable) and we do not expect any unusual dynamics. For $\alpha_2 > 0$, the stability of CM changes via Hopf bifurcations at $y_2 = \pm\sqrt{\alpha_2}$. Thus, the folded singularities of (5.1) correspond to Hopf bifurcations of (5.10). For $0 < \alpha_2 < 1$, the eigenvalue structure of CM for $|y_2| < \sqrt{\alpha_2}$ is elliptic (i.e. complex). For $\alpha_2 > 1$, the eigenvalue structure of CM switches between elliptic (complex) and hyperbolic (real), as shown in Figure 5.7.

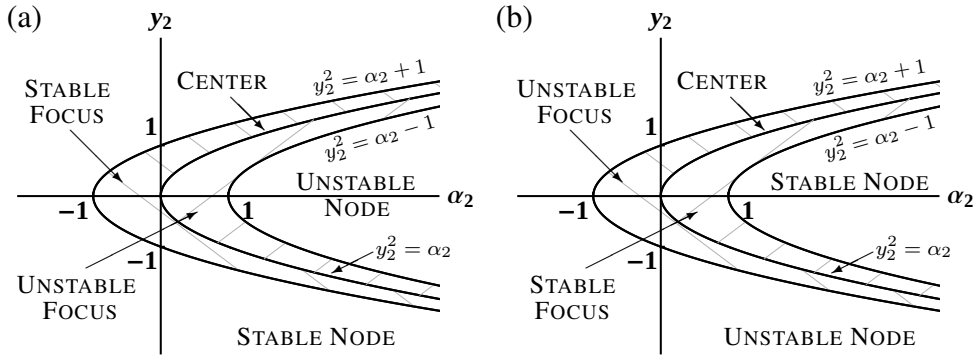

Figure 5.7. Eigenvalue structure of (5.10) along CM for (a) $\delta = 1$ and (b) $\delta = -1$.

The reduced flow of the blown-up vector field (5.9) is given by

$$\begin{aligned} 0 &= -z_2 + \delta\left(\alpha_2 - y_2^2\right), \\ \dot{y_2} &= 1, \\ 0 &= x_2 + z_2^2, \end{aligned} \tag{5.13}$$

and simply describes the slow passage along CM. In particular, the reduced flow moves trajectories through Hopf bifurcations of the layer problem (5.10) leading to delayed loss of stability [**93**] (Theorem 2.16).

Remark 5.5. Note that $\alpha = \mathcal{O}(\sqrt{\varepsilon})$ is the lowest order at which there is any delay. For $\alpha = \mathcal{O}(\varepsilon^k), k > 1/2$, the Hopf bifurcations collapse to the origin and the stability of CM does not change when the reduced flow crosses $y_2 = 0$. That is, all rescalings $\alpha = \mathcal{O}(\varepsilon^k), k > 1/2$ are encapsulated in the case $\alpha_2 = 0$.

Away from CM, two explicit algebraic solutions can be computed for the layer problem:

$$\gamma_\pm(t_2) = \left(-\frac{1}{4}t_2^2 + \frac{1}{2}, \pm\sqrt{\alpha_2}, \frac{1}{2}t_2\right), \tag{5.14}$$

where $\gamma_\pm$ correspond to the eigenvalue $\lambda = -1$ of the linearization of the desingularized flow (5.2) for the FSN I ($\alpha = 0$). The importance of these solutions is that they connect the attracting and repelling slow manifolds, $S_{a,2}$ and $S_{r,2}$, of the unperturbed problem of (5.9), as illustrated in Figure 5.8.

Remark 5.6. We use $S_{a,2}$ and $S_{r,2}$ to denote the $\varepsilon \to 0$ limit of $S_a^{\varepsilon^{1/4}}$ and $S_r^{\varepsilon^{1/4}}$ in (5.9). The manifolds $S_{a,2}$ and $S_{r,2}$ can be described as a union of special solutions of the layer problem (5.10), indexed over the slow variable y_2 (see Section 5.6.2).

These special solutions are viewed as pre-images of a folded node strong canard (at $y_2 = -\delta\sqrt{\alpha_2}$) and of a folded saddle canard (at $y_2 = \delta\sqrt{\alpha_2}$).

Proposition 5.3 ([**119**])**.** *The singular strong canards $\gamma_\pm$ always perturb to maximal strong canards of folded node/folded saddle type for $0 < \varepsilon \ll 1$.*

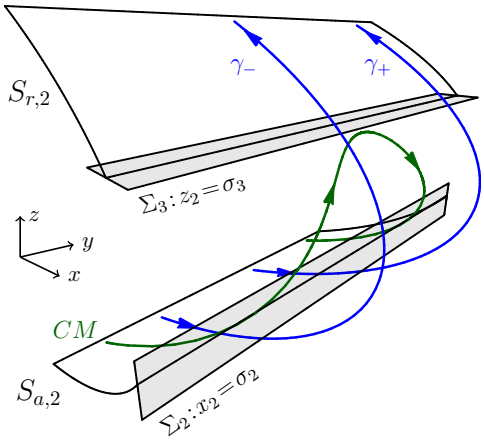

Figure 5.8. Invariant manifolds $S_{a,2}$ and $S_{r,2}$ extended up to Σ_2 and Σ_3, respectively for $\delta = 1$. The canards $\gamma_\pm$ connect the manifolds whilst CM approximates the connection between the folded node weak canard and the folded saddle faux canard. Note that CM can reach $S_{r,2}$ for sufficiently 'large' α_2.

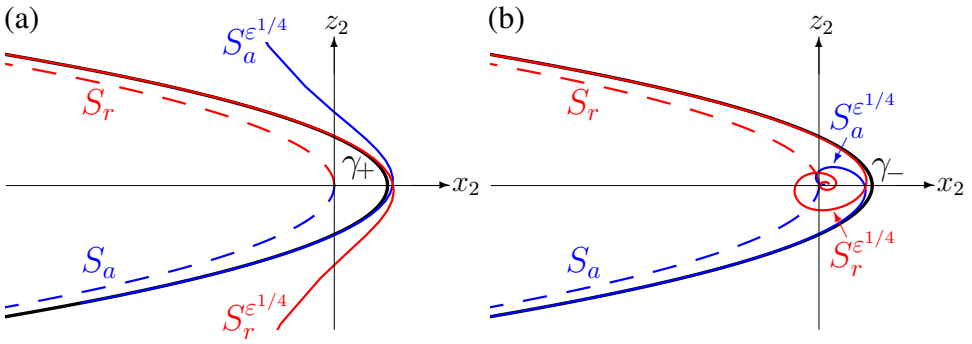

Figure 5.9. Slow manifolds of (5.9) for $\delta = 1$, $\alpha_2 = 0.25$ and $\varepsilon = 1 \times 10^{-5}$, shown in the cross-section (a) $y_2 = \sqrt{\alpha_2}$ (folded saddle) and (b) $y_2 = -\sqrt{\alpha_2}$ (folded node). The singular canards $\gamma_\pm$ (black) perturb to nearby maximal canards. The (x_2, z_2) regions shown correspond to $\mathcal{O}(\varepsilon) \times \mathcal{O}(\sqrt{\varepsilon})$ neighbourhoods in the (x, z) coordinates of (5.1).

Proposition 5.3 is illustrated in Figure 5.9 (cf. Figure 2.4). Solutions exponentially close to $\gamma_\pm$ in Σ_2 will cross the fold and follow the repelling manifold for $\mathcal{O}(1)$ times on the slow timescale before being repelled. All other points in Σ_2 within the funnel region and not exponentially close to either of the canards will be quickly attracted to CM.

Like $\gamma_\pm$, CM connects the attracting and repelling manifolds. The difference is that CM returns to the manifold on which it started. Unlike the FSN II, there are no equilibria nearby so that solutions can, in principle, follow CM indefinitely. Note that CM can be viewed as the concatenation of the folded node primary weak canard and the folded saddle faux canard. To simplify our analysis of the dynamics around CM, we rectify CM to the y_2-axis.

Lemma 5.1. *There exists a smooth change of coordinates that transforms* (5.9) *to the system*

$$\begin{aligned} \dot{x_2} &= -z_2 + \mathcal{O}(\sqrt{\varepsilon}, \varepsilon^{1/4} x_2, \varepsilon^{1/4} z_2), \\ \dot{y_2} &= \varepsilon^{1/4}, \\ \dot{z_2} &= x_2 + 2\delta(\alpha_2 - y_2^2) z_2 + z_2^2 + \mathcal{O}(\sqrt{\varepsilon}, \varepsilon^{1/4} x_2, \varepsilon^{1/4} z_2). \end{aligned} \tag{5.15}$$

Proof. Let $(\overline{x}_2, \overline{z}_2) = (x_2 + (\alpha_2 - y_2^2)^2, z_2 - \delta(\alpha_2 - y_2^2))$. Then (5.9) becomes

$$\begin{aligned}
\overline{x}_2' &= -\overline{z}_2 + \mathcal{O}(\varepsilon^{1/4}),\\
y_2' &= \varepsilon^{1/4}(1 + \mathcal{O}(\varepsilon\, x_2, \varepsilon^{1/4}\, y_2, \varepsilon^{1/2}\, z_2, \varepsilon)),\\
\overline{z}_2' &= \overline{x}_2 + 2\delta(\alpha_2 - y_2^2)\overline{z}_2 + \overline{z}_2^2 + \mathcal{O}(\varepsilon^{1/4}),
\end{aligned}$$

where CM is the y_2 axis. Let $\Phi = (1 + \mathcal{O}(\varepsilon\, x_2, \varepsilon^{1/4}\, y_2, \varepsilon^{1/2}\, z_2, \varepsilon))^{-1}$, which is positive in the domain of interest. Rescaling time by Φ, expanding Φ and dropping the bars, we have:

$$\begin{aligned}
x_2' &= -z_2 + \varepsilon^{1/4}\varphi_1(y_2) + \mathcal{O}(\sqrt{\varepsilon}, \varepsilon^{1/4}x_2, \varepsilon^{1/4}z_2),\\
y_2' &= \varepsilon^{1/4},\\
z_2' &= x_2 + 2\delta(\alpha_2 - y_2^2)z_2 + z_2^2 + \varepsilon^{1/4}\varphi_2(y_2) + \mathcal{O}(\sqrt{\varepsilon}, \varepsilon^{1/4}x_2, \varepsilon^{1/4}z_2).
\end{aligned}$$

Let $\tilde{z}_2 = z_2 - \varepsilon^{1/4}\varphi_1(y_2)$. Then the system transforms to

$$\begin{aligned}
x_2' &= -\tilde{z}_2 + \mathcal{O}(\sqrt{\varepsilon}, \varepsilon^{1/4}x_2, \varepsilon^{1/4}\tilde{z}_2),\\
y_2' &= \varepsilon^{1/4},\\
\tilde{z}_2' &= x_2 + 2\delta(\alpha_2 - y_2^2)\tilde{z}_2 + \tilde{z}_2^2 + \varepsilon^{1/4}\tilde{\varphi}_2 + \mathcal{O}(\sqrt{\varepsilon}, \varepsilon^{1/4}x_2, \varepsilon^{1/4}\tilde{z}_2),
\end{aligned}$$

where $\tilde{\varphi}_2 = \varphi_2 + 2\varphi_1\tilde{z}_2 + 2\delta(\alpha_2 - y_2^2)\varphi_1$. Setting $\tilde{x}_2 = x_2 + \varepsilon^{1/4}\tilde{\varphi}_2$ leads to the result. □

The y_2-axis of (5.9) is invariant only to leading order, whereas in (5.15), it is invariant to order $\mathcal{O}(\varepsilon^{1/4})$. This control over the leading order terms will be needed in our analysis. We now define the eigenvalues of the linearization of (5.15) along CM (i.e. the y_2-axis) up to order $\mathcal{O}(\varepsilon^{1/4})$:

$$\begin{aligned}
\lambda(y_2, \alpha_2, \varepsilon^{1/4}) &:= \delta(\alpha_2 - y_2^2) - i\sqrt{1 - (\alpha_2 - y_2^2)^2} + \varepsilon^{1/4}\, h_1(y_2),\\
\nu(y_2, \alpha_2, \varepsilon^{1/4}) &:= \delta(\alpha_2 - y_2^2) + i\sqrt{1 - (\alpha_2 - y_2^2)^2} + \varepsilon^{1/4}\, h_2(y_2).
\end{aligned} \tag{5.16}$$

The zero order terms $\lambda(y_2, \alpha_2, 0)$ and $\nu(y_2, \alpha_2, 0)$ are precisely the eigenvalues of (5.10).

Definition 5.1. The integrals

$$I_\lambda(s_0, s_1) := \int_{s_0}^{s_1} \operatorname{Re}\lambda(s, \alpha_2, 0)\, ds, \quad I_\nu(s_0, s_1) := \int_{s_0}^{s_1} \operatorname{Re}\nu(s, \alpha_2, 0)\, ds, \tag{5.17}$$

measure the (leading order) expansion/contraction properties of (5.15) along CM.

Note that $I_\lambda = I_\nu$ when the eigenvalues are elliptic but not when they are hyperbolic.

We have the following view of the dynamics: let $\overline{I}$ be a y_2 interval where the eigenvalues $\lambda(y_2, \alpha_2, 0)$ and $\nu(y_2, \alpha_2, 0)$ are real and negative. The rescaled system (5.15) has strong and weak stable foliations, W^{ss} and W^s, along CM (Figure 5.10). In $\overline{I}$, the weak stable foliation is equivalent to the invariant manifold $S_{a,2}$ locally near CM. Similarly, if the eigenvalues are real and positive, there exists a weak unstable foliation W^u along CM, which is locally equivalent to $S_{r,2}$. Fenichel theory guarantees that these weak stable and unstable foliations (and hence $S_{a,2}$ and $S_{r,2}$) persist as $S_a^{\varepsilon^{1/4}}$ and $S_r^{\varepsilon^{1/4}}$, respectively. In regions where the eigenvalues are complex, there are no preferred directions to follow and we must find an alternative way of identifying and tracking the manifolds.

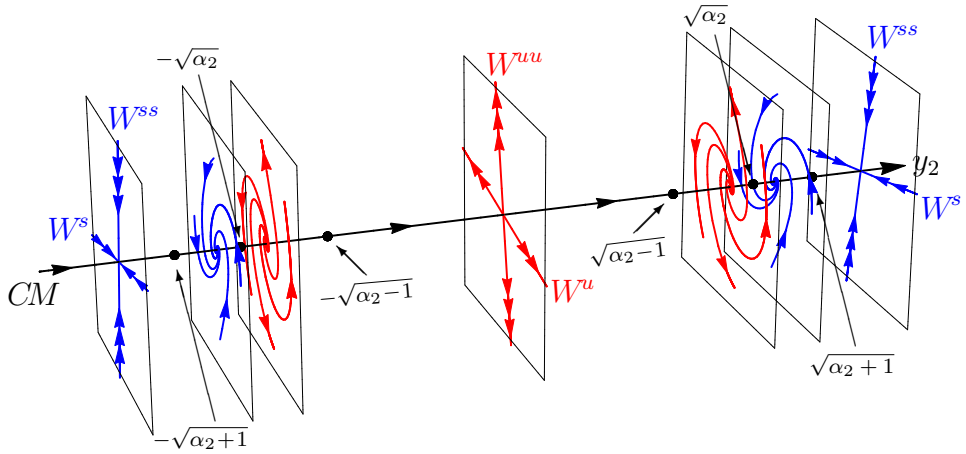

Figure 5.10. System (5.15) for $\delta = 1$ and $\alpha_2 > 1$. CM is the y_2-axis. Each cross-section shows a different regime of (5.15) (cf. Figure 5.7). W^s and W^u can be viewed as foliations of $S_{a,2}$ and $S_{r,2}$, respectively.

5.3.4. Connecting Charts κ_1 and κ_2. We now rewrite the special solutions $\gamma_\pm$ and CM from chart κ_2 in the entry chart κ_1. To do this, we require the change of coordinates κ_{12} that take solutions in κ_2 and map them to κ_1. For the FSN I, the change of coordinates is

$$r_1 = r_2(-x_2)^{1/4}, \quad y_1 = \frac{y_2}{(-x_2)^{1/4}}, \quad z_1 = \frac{z_2}{\sqrt{-x_2}} \quad \varepsilon_1 = -\frac{1}{x_2},$$

for $x_2 < 0$. A simple calculation shows that

$$\lim_{t_2 \to -\infty} \kappa_{12}(\gamma_\pm(t_2)) = (0, 0, -1, 0)$$

so that the strong canards $\gamma_\pm$ both emanate from the origin of (5.7) in κ_1 (for both $\delta = \pm 1$). Transforming the weak canard CM to κ_1 gives:

$$\kappa_{12}(CM) = \left(0, \frac{y_2}{((\alpha_2 - y_2^2)^2)^{1/4}}, \frac{\delta(\alpha_2 - y_2^2)}{\sqrt{(\alpha_2 - y_2^2)^2}}, \frac{1}{(\alpha_2 - y_2^2)^2}\right),$$

which shows that, for $\delta = 1$, CM emanates from the saddle-nodes of (5.7) in κ_1 (Figure 5.6). For $\delta = -1$, the only part of $\kappa_{12}(CM)$ that enters κ_1 with $z_1 < 0$ is the segment of $\kappa_{12}(CM)$ that has $|y_2| < \sqrt{\alpha_2}$. Note that $\varepsilon_1 \to \alpha_2^{-2}$ as $y_2 \to 0$ and $\varepsilon_1 \to \infty$ as $y_2 \to \pm\sqrt{\alpha_2}$. That is, since the center manifold of the FSN I lies on S_r, CM only extends a finite distance into κ_1 with $z_1 = -1$.

Note that $\kappa_{21}(\Sigma_2^{\text{out}}) = \Sigma_2 : z_2 = -\sqrt{\sigma_2}$, where $\kappa_{21} = \kappa_{12}^{-1}$. For $\delta = -1$, the domain D_2 of attraction of CM in chart κ_2 is the y_2-interval $(-\sqrt{\alpha_2}, \sqrt{\alpha_2})$, which is $\mathcal{O}(1)$ since $\alpha_2 = \mathcal{O}(1)$ by assumption. The inverse change of coordinates $\kappa_{21} = \kappa_{12}^{-1}$ shows that $D_1 = \kappa_{21}(D_2)$ is the $\mathcal{O}(\varepsilon^{1/4}) \times \mathcal{O}(1) \times \{\sigma_2^{-1}\}$ region in $(r_1, y_1, \varepsilon_1)$ in chart κ_1. As we showed in Section 5.3.2, D_1 comes from an $\mathcal{O}(\varepsilon^{1/4})$ neighbourhood of the strong canard Γ_s in Σ_1, with $\varepsilon_1 = \mathcal{O}(\varepsilon)$. That is, only those initial conditions $\mathcal{O}(\varepsilon^{1/4})$ close to the strong canard in Σ_1 enter the domain of attraction of CM in chart κ_2.

5.4. Statement of Main Results

Using blow-up, we have shown the existence of maximal strong canards near the FSN I and established that solutions within the funnel not exponentially close to the strong canards become exponentially close to CM in Σ_2. The task now is to figure out what the behaviour of solutions near CM is (i.e. to understand the behaviour of the weak and secondary canards). In this section, we state the main theoretical results of this work, leaving the proofs of our

assertions to Sections 5.5 and 5.6. We have two kinds of results: existence of canards and faux canards (Sections 5.4.1 and 5.4.2), and estimates of bifurcation delay (Section 5.4.3) due to Hopf bifurcations of the layer problem of the blown-up system (5.9).

We consider trajectories starting in some hyperbolic region of CM and ask whether a trajectory starting close to CM remains close or separates (i.e. follows fast directions). The issue is whether the separation happens in hyperbolic or elliptic regions of CM and the two cases must be handled separately. If the separation occurs in hyperbolic regions ($\alpha_2 > 1$), then the weak stable and unstable foliations for CM are equivalent to the invariant manifolds $S_{a,2}$ and $S_{r,2}$, and we can track the evolution using the linear subspaces (see Section 5.6.3). If the separation occurs in elliptic regions ($0 < \alpha_2 < 1$), then we cannot track $S_{a,2}$ and $S_{r,2}$ using the linear subspaces and we must rely on special properties of the layer flow (see Section 5.6.2). We call the interval $0 < \alpha_2 < 1$ the near-field and the interval $\alpha_2 > 1$ the far-field. To aid our analysis, we introduce the auxiliary cross-sections

$$\Sigma_2^{\pm} := \left\{ (x_2, y_2, z_2) : y_2 = y_{2,0}, y_{2,0} \approx \pm\sqrt{\alpha_2 + \sqrt{\sigma_2}} \right\},$$

where $y_{2,0}$ is in a hyperbolic region of CM and $\Sigma_2^{\pm}$ are approximately equivalent to Σ_2.

5.4.1. Existence of Canards and Faux Canards in the Near-Field.

Theorem 5.1 (Existence of canards). *Let $0 < \alpha_2 < 1$.*

(i) For $\delta = 1$, suppose $y_{2,0}$ is chosen to define Σ_2^- and $y_{2,*}$ is such that $I_\lambda(y_{2,0}, y_{2,*}) = 0$, with $|y_{2,*}| < \sqrt{\alpha_2}$. There exists a canard originating in $S_a^\varepsilon \cap \Sigma_1$, passing through $S_a^{\varepsilon^{1/4}} \cap \Sigma_2^-$ an $\mathcal{O}(\varepsilon^{1/4})$ distance from CM and continuing to a point in $S_r^{\varepsilon^{1/4}}$ near $y_{2,*}$.

(ii) For $\delta = -1$, suppose $y_{2,0}$ is chosen to define Σ_2^+ and $y_{2,*}$ is such that $I_\nu(y_{2,*}, y_{2,0}) = 0$, with $|y_{2,*}| < \sqrt{\alpha_2}$. There exists a canard $\mathcal{O}(\varepsilon^{1/4})$ close to CM connecting $S_a^{\varepsilon^{1/4}}$ near $y_{2,*}$ to $S_r^{\varepsilon^{1/4}} \cap \Sigma_2^+$ and continuing to a point in $S_r^\varepsilon \cap \Sigma_1$.

Proof. Section 5.6.2. □

Remark 5.7. We prove in Section 5.5.4 that such a $y_{2,*}$ exists for every $y_{2,0}$, $|y_{2,0}| > \sqrt{\alpha_2}$.

Theorem 5.2 (Existence of faux canards). *Let $0 < \alpha_2 < 1$ and $\Sigma_* : y_2 = y_{2,*}$.*

(i) For $\delta = 1$, suppose $y_{2,0}$ is chosen to define Σ_2^+ and $y_{2,*}$ is such that $I_\lambda(y_{2,*}, y_{2,0}) = 0$, with $|y_{2,*}| < \sqrt{\alpha_2}$. There exists a faux canard $\mathcal{O}(\varepsilon^{1/4})$ close to CM connecting $S_r^{\varepsilon^{1/4}} \cap \Sigma_*$ to $S_a^{\varepsilon^{1/4}} \cap \Sigma_2^+$.

(ii) For $\delta = -1$, suppose $y_{2,0}$ is chosen to define Σ_2^- and $y_{2,*}$ is such that $I_\nu(y_{2,0}, y_{2,*}) = 0$, with $|y_{2,*}| < \sqrt{\alpha_2}$. There exists a faux canard $\mathcal{O}(\varepsilon^{1/4})$ close to CM connecting $S_r^{\varepsilon^{1/4}} \cap \Sigma_2^-$ to $S_a^{\varepsilon^{1/4}} \cap \Sigma_*$.

Proof. Section 5.6.2. □

Corollary 5.1. *For $\delta = 1$, there exist canard solutions that originate in $S_a^\varepsilon \cap \Sigma_1$ and remain $\mathcal{O}(\varepsilon^{1/4})$ close to CM for all y_2. For $\delta = -1$, there exist faux canard solutions that connect $S_r^{\varepsilon^{1/4}} \cap \Sigma_2^-$ to $S_r^{\varepsilon^{1/4}} \cap \Sigma_2^+$.*

Theorem 5.1 states the existence of canards in the near-field, where CM_r is elliptic (cf. Theorem 3.1 of [**76**] for the FSN II). Theorem 5.2 is the corresponding statement for faux canards, which is a novel result. Corollary 5.1 is new and unique to the FSN I context. Corollary 5.1 implies there are canards and faux canards that connect since trajectories starting on S_a cross over to S_r and eventually return to S_a (for $\delta = 1$). Similarly for $\delta = -1$.

5.4.2. Existence of Canards and Faux Canards in the Far-Field. In the far-field limit ($\alpha_2 > 1$), the eigenvalue structure of the layer problem (5.10) along CM alternates between elliptic and hyperbolic. When this hyperbolic structure does not influence the dynamics, the existence theorems (and their proofs) for canards and faux canards are essentially unaltered.

Theorem 5.3 (**Existence of canards: elliptic case**). *Let* $\alpha_2 > 1$.

(i) For $\delta = 1$*, Theorem 5.1(i) holds with* $y_{2,*} \in (-\sqrt{\alpha_2}, -\sqrt{\alpha_2 - 1})$.
(ii) For $\delta = -1$*, Theorem 5.1(ii) holds with* $y_{2,*} \in (\sqrt{\alpha_2 - 1}, \sqrt{\alpha_2})$.

Theorem 5.4 (**Existence of faux canards: elliptic case**). *Let* $\alpha_2 > 1$.

(i) For $\delta = 1$*, Theorem 5.2(i) holds with* $y_{2,*} \in (\sqrt{\alpha_2 - 1}, \sqrt{\alpha_2})$.
(ii) For $\delta = -1$*, Theorem 5.2(ii) holds with* $y_{2,*} \in (-\sqrt{\alpha_2}, -\sqrt{\alpha_2 - 1})$.

When the hyperbolic structure of CM does influence the dynamics, we have existence results, but cannot determine where the canards originate since they may turn back towards the fold (see Figure 5.1). We fix an interval $A := [\alpha_{2,0}, \alpha_{2,1}]$ with $1 < \alpha_{2,0} < \alpha_{2,1}$.

Theorem 5.5 (**Existence of canards: hyperbolic case**). *Let* $\Sigma_* : y_2 = y_{2,*}$*. For most* $\alpha_2 \in A$ *(an open set of almost full measure), there exists a canard uniformly* $\mathcal{O}(\varepsilon^{1/4})$ *close to* CM *that*

(i) for $\delta = 1$*, connects* $S_a^{\varepsilon^{1/4}} \cap \Sigma_2^-$ *to* $S_r^{\varepsilon^{1/4}} \cap \Sigma_*$*, where* $y_{2,0}$ *defines* Σ_2^- *and* $y_{2,*} \in (-\sqrt{\alpha_2 - 1}, 0]$ *is such that* $I_\lambda(y_{2,0}, -\sqrt{\alpha_2 + 1}) + I_\nu(-\sqrt{\alpha_2 + 1}, y_{2,*}) = 0$.
(ii) for $\delta = -1$*, connects* $S_a^{\varepsilon^{1/4}} \cap \Sigma_*$ *to* $S_r^{\varepsilon^{1/4}} \cap \Sigma_2^+$*, where* $y_{2,0}$ *defines* Σ_2^+ *and* $y_{2,*} \in [0, \sqrt{\alpha_2 - 1})$ *is such that* $I_\lambda(y_{2,*}, \sqrt{\alpha_2 + 1}) + I_\nu(\sqrt{\alpha_2 + 1}, y_{2,0}) = 0$.

Proof. Section 5.6.3. □

Theorem 5.6 (**Existence of faux canards: hyperbolic case**). *Let* $\Sigma_* : y_2 = y_{2,*}$*. For most* $\alpha_2 \in A$ *(an open set of almost full measure), there exists a faux canard uniformly* $\mathcal{O}(\varepsilon^{1/4})$ *close to* CM *that*

(i) for $\delta = 1$*, connects* $S_r^{\varepsilon^{1/4}} \cap \Sigma_*$ *to* $S_a^{\varepsilon^{1/4}} \cap \Sigma_2^+$*, where* $y_{2,0}$ *defines* Σ_2^+ *and* $y_{2,*} \in [0, \sqrt{\alpha_2 - 1})$ *is such that* $I_\nu(y_{2,*}, \sqrt{\alpha_2 + 1}) + I_\lambda(\sqrt{\alpha_2 + 1}, y_{2,0}) = 0$.
(ii) for $\delta = -1$*, connects* $S_r^{\varepsilon^{1/4}} \cap \Sigma_2^-$ *to* $S_a^{\varepsilon^{1/4}} \cap \Sigma_*$*, where* $y_{2,0}$ *defines* Σ_2^- *and* $y_{2,*} \in (-\sqrt{\alpha_2 - 1}, 0]$ *is such that* $I_\nu(y_{2,0}, -\sqrt{\alpha_2 + 1}) + I_\lambda(-\sqrt{\alpha_2 + 1}, y_{2,*}) = 0$.

Proof. Section 5.6.3. □

Corollary 5.2. *For* $\delta = 1$*, there exist canard solutions* $\mathcal{O}(\varepsilon^{1/4})$ *close to* CM *that connect* $S_a^{\varepsilon^{1/4}} \cap \Sigma_2^-$ *to* $S_a^{\varepsilon^{1/4}} \cap \Sigma_2^+$ *and continue to a point in* $S_a^\varepsilon \cap \Sigma_1$*. For* $\delta = -1$*, there exist faux canard solutions* $\mathcal{O}(\varepsilon^{1/4})$ *close to* CM *that connect* $S_r^{\varepsilon^{1/4}} \cap \Sigma_2^-$ *to* $S_r^{\varepsilon^{1/4}} \cap \Sigma_2^+$.

The existence of canards in the far-field (Theorem 5.5) is the FSN I equivalent of Theorem 3.2 from [**76**] for the FSN II. The existence of faux canards (Theorem 5.6), and the existence of solutions which are concatenations of canards and faux canards (Corollary 5.2) is unique to the FSN I.

Remark 5.8. It is possible that trajectories starting on S_a tunnel through to S_r via CM until they reach some exponentially small neighbourhood of the folded saddle canard Γ_s^s. From there, these special solutions trace Γ_s^s on S_r for some time before they jump back to S_a (see [**96**], where such solutions that follow canard segments of different folded singularities are called composite canards). Such solutions are only found in exponentially small parameter windows, reminiscent of a canard explosion (Figure 5.11).

Our next result concerns the number of canards (i.e. small oscillations) near the FSN I.

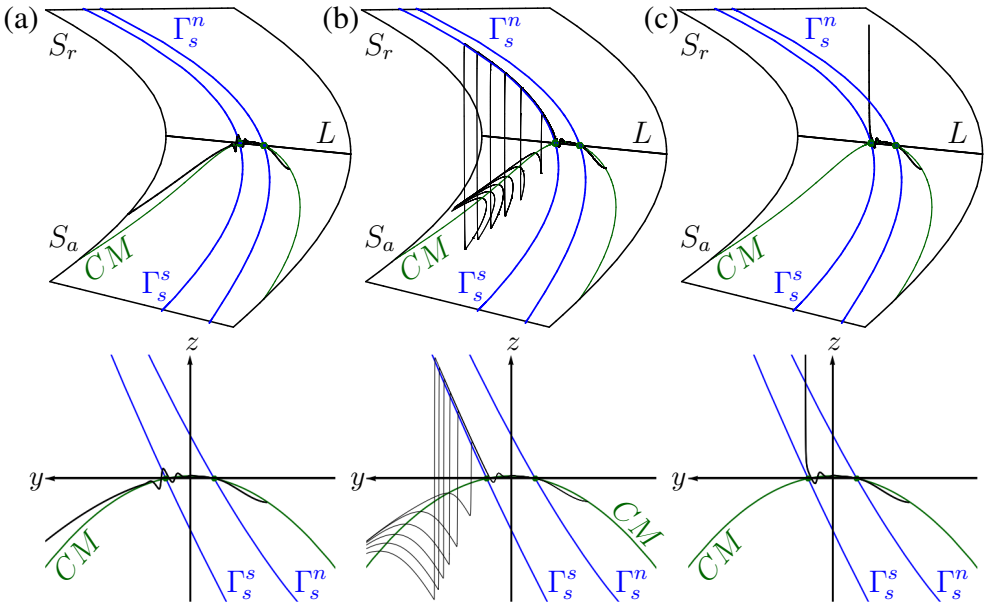

Figure 5.11. Transition through a 'canard explosion' near the FSN I limit in (5.1) for $\delta = 1, \varepsilon = 5 \times 10^{-6}$ and (a) $\alpha = 0.318\sqrt{\varepsilon}$, (b) $\alpha \approx 0.320406\sqrt{\varepsilon}$, and (c) $\alpha = 0.325\sqrt{\varepsilon}$. Γ_s^n and Γ_s^s denote the (singular) folded node strong canard and folded saddle canard, respectively. Top row: trajectories on S. Bottom row: projection onto (y, z). (a) Solutions (black) trace $CM \cap S_r$ entirely (Corollary 5.1). Note the small oscillations about the folded saddle. (b) Solutions in an exponentially small parameter interval around $\alpha \approx 0.320406\sqrt{\varepsilon}$ follow Γ_s^s on S_r for various distances before jumping back to S_a. (c) Solutions escape via a fast direction.

Proposition 5.4. *Let $\alpha_2 > 0$ and suppose a canard (faux canard) solution exists. Then there are $\mathcal{O}(\varepsilon^{-1/4})$ canards (faux canards).*

Proof. Section 5.5.4 (Proposition 5.12). □

Remark 5.9. Recall from Section 2.5.1 that the maximal number of rotations in a neighbourhood of a folded node becomes unbounded in the FSN limit (i.e. as $\mu \to 0$). The FSN II analysis in [**76**] refines this and shows that the number of rotations is $\mathcal{O}(\varepsilon^{-1/2})$. Proposition 5.4 refines the folded node and folded saddle theory for the FSN I case and shows that there are $\mathcal{O}(\varepsilon^{-1/4})$ rotations.

5.4.3. Bifurcation Delay. The benefit of the blow-up transformation (5.8) is that we have converted our problem into a dynamic Hopf bifurcation problem, where the behaviour of the dynamical system depends on a parameter that changes slowly in time (Section 2.6.3). One very useful diagnostic in the theory of dynamic bifurcations is the *way-in/way-out* (or entry-exit) function, $\varphi(y_{2,0}, \alpha_2)$, implicitly defined by

$$I_\lambda(y_{2,0}, \varphi) = 0, \tag{5.18}$$

with entry point $y_{2,0} \in CM_a$ and exit point $\varphi \in CM_r$. Intuitively, the way-in/way-out function is interpreted as the moment when the expansion on CM_r counterbalances the accumulative contraction on CM_a. The implication is that solutions starting at $y_{2,0}$ stay in a small neighbourhood of CM up to φ.

Remark 5.10. The way-in/way-out function (5.18) measures the balance of weak contraction and strong expansion along the weak canard CM for generic solutions. When CM_r is elliptic, $\varphi = y_{2,*}$. However, when CM_r is hyperbolic, $\varphi \neq y_{2,*}$ (Figure 5.12) since the canard-way-in/way-out points $y_{2,*}$ measure weak contraction versus weak expansion along CM (hence the branch switching when evaluating the integrals).

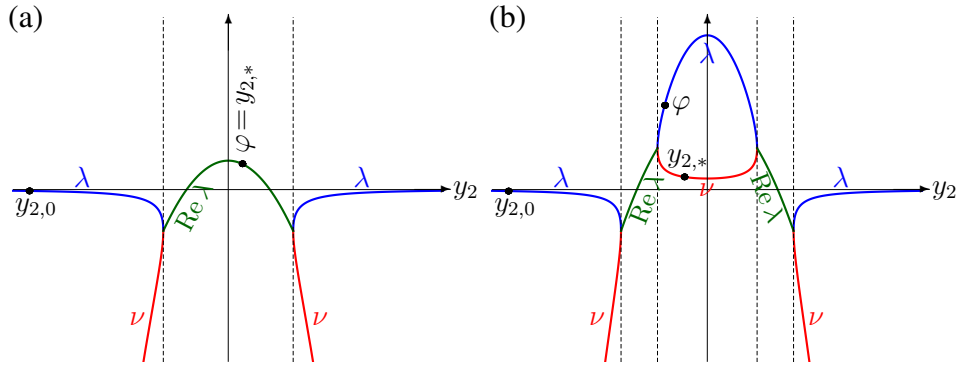

Figure 5.12. Real part of the eigenvalues (5.16) to leading order for $\delta = 1$ and real y_2. The way-in/way-out function for general solutions is indicated by ψ. The canard way-in/way-out points are denoted by $y_{2,*}$. (a) $\alpha_2 = 0.7$: $\psi = y_{2,*}$ (for the same $y_{2,0}$) since CM_r is elliptic and the notion of strong/weak expansion does not apply. (b) $\alpha_2 = 2$: $\psi < y_{2,*}$ since CM_r is hyperbolic. The dashed lines indicate the branch points of $\lambda(y_2, \alpha_2, 0)$.

Using the way-in/way-out function, we now consider how long general solutions can stay close to CM before leaving via fast directions.

Theorem 5.7 (Minimal delay estimates). *Let $\alpha_2 > 0$, and (x_2, y_2, z_2) be a solution of* (5.15) *with initial condition $\mathcal{O}(\varepsilon^{1/4})$ close to CM.*

(i) For $\delta = 1$, let $y_2(0) = y_{2,0}$, where $y_{2,0}$ defines Σ_2^- and $\varphi(y_{2,0}, \alpha_2)$ is defined by (5.18). *Then the solution (x_2, y_2, z_2) stays $\mathcal{O}(\varepsilon^{1/4})$ close to CM for all $y_2 \leq \varphi + o(1)$.*

(ii) For $\delta = -1$, let $y_2(0) = \varphi(y_{2,0}, \alpha_2)$, where $y_{2,0}$ defines Σ_2^+ and φ is defined by (5.18). *Then the solution (x_2, y_2, z_2) stays $\mathcal{O}(\varepsilon^{1/4})$ close to CM for all $y_2 \leq y_{2,0} + o(1)$.*

Proof. Section 5.6.4. □

Remark 5.11. Theorem 5.7 is more general than the classic delayed Hopf result [**91, 92**] (the prototypical example of bifurcation delay) as the eigenvalue used in (5.18) can alternate between elliptic and hyperbolic (cf. Theorem 3.3 of [**76**] for the FSN II).

The way-in/way-out function depends on the distance traversed on CM_a. That is, there is a memory effect and the delay depends on the accumulative contraction. Despite this, there is a maximal distance (the buffer point [**91, 92, 113**]) that solutions can trace CM_r before they must leave the vicinity of CM (see Definition 2.18).

Definition 5.2. For the FSN I the buffer point, $y_{2,B}$, is:

$$y_{2,B} = \begin{cases} \lim\limits_{y_{2,0} \to -\infty} \varphi(y_{2,0}, \alpha_2), & \delta = 1, \\ \lim\limits_{y_{2,0} \to -\sqrt{\alpha_2}} \varphi(y_{2,0}, \alpha_2), & \delta = -1. \end{cases}$$

Note the difference between the subcases $\delta = \pm 1$. In the $\delta = 1$ case, CM_a extends to unbounded y_2. In the $\delta = -1$ case, CM_a is restricted and the contraction can only occur on the interval $|y_2| < \sqrt{\alpha_2}$.

Lemma 5.2. *Suppose $\delta = 1$. For $0 < \alpha_2 < \tilde{\alpha}_2 \approx 0.66$, $y_{2,B} = \sqrt{\alpha_2}$. For $\tilde{\alpha}_2 < \alpha_2 < 1$, $y_{2,B} \in \left(0, \sqrt{\alpha_2}\right)$. For $\alpha_2 > 1$, $y_{2,B} \in (-\sqrt{\alpha_2}, 0)$. Suppose $\delta = -1$. Then $y_{2,B} \in \left(\sqrt{\alpha_2}, 2\sqrt{\alpha_2}\right)$ for all $\alpha_2 > 0$.*

Proof. Section 5.5.4. □

Remark 5.12. An important distinction between the FSN I and the FSN II is the existence of an upper bound on $y_{2,B}$. In the FSN II, there is an ordinary singularity $y_{2,p}$ on CM_r (which

trajectories cannot cross) and $y_{2,B} < y_{2,p}$ [**76**]. In the FSN I, there is no ordinary singularity and $y_{2,B}$ can reach the 'edge' of CM_r. This happens for $\delta = 1$ and $0 < \alpha_2 < \tilde{\alpha_2}$, where $y_{2,B} = \sqrt{\alpha_2}$. We have already seen this in Section 5.2.3, where close to the FSN I limit (i.e. near-field), generic solutions pass from S_a^- to S_r via the folded node weak canard and return to S_a^- via the folded saddle faux canard (Figure 5.4(d)).

We now estimate the maximal delay before trajectories escape a neighbourhood of the FSN I (cf. Theorem 3.5 of [**76**]). For $\delta = 1$, let J_+ be an open subset of $S_a^\varepsilon \cap \Sigma_1$ with closure contained in the open interval $-\sigma_1^{1/4} < y < -2\sqrt{\sigma_1}$ (i.e. between the strong canard and the center manifold – see Figure 5.1). For $\delta = -1$, let J_- be an open subset of $S_a^\varepsilon \cap \Sigma_1$ with closure contained in the open interval $-2\sqrt{\sigma_1} - K\,\varepsilon^{1/4} < y < -2\sqrt{\sigma_1}$ for some $K > 0$ (i.e. $\mathcal{O}(\varepsilon^{1/4})$ close to the strong canard).

Theorem 5.8 (**Maximal delay estimates).** *Let $\alpha_2 > 0$. There exists a function $d(\varepsilon)$ satisfying $\lim_{\varepsilon\to 0} d(\varepsilon) = 0$ such that, given any solution originating in $J_\pm$ (possibly with the exception of an exponentially small interval), the exit point of the solution in Σ_3 satisfies $y_2 \leq y_{2,B} + d(\varepsilon)$.*

Proof. Section 5.6.4. □

Remark 5.13. The difference between the FSN I subcases is most evident in Theorem 5.8. For $\delta = 1$, bifurcation delay near the FSN I is generic since the funnel region persists. For $\delta = -1$, bifurcation delay only occurs for trajectories $\mathcal{O}(\varepsilon^{1/4})$ close to the strong canard in Σ_1. All other points hit the fold and jump.

We define analogous canard-buffers $y_{2,C}$ for the canard-way-in/way-out points $y_{2,*}$:

$$I_\lambda(-\infty, -\sqrt{\alpha_2}) + I_\nu(-\sqrt{\alpha_2}, y_{2,C}) = 0, \qquad \delta = 1,$$
$$I_\lambda(-\sqrt{\alpha_2}, \sqrt{\alpha_2}) + I_\nu(\sqrt{\alpha_2}, y_{2,C}) = 0, \qquad \delta = -1.$$

For $\delta = 1$, we have $y_{2,C} = y_{2,B}$ in the near-field where CM_r is elliptic. For all other cases, $y_{2,B} < y_{2,C}$. That is, the canards can stay in a small neighbourhood of CM beyond $y_{2,B}$ (see Remark 5.10). Using $y_{2,C}$, we derive the following extension of Corollaries 5.1 and 5.2:

Proposition 5.5. *For $\alpha_2 > 0$, there always exists a canard that extends the entire length of CM_r.*

Proof. Section 5.5.4. □

We now relate our theorems back to the FSN I examples in Sections 5.2.2 and 5.2.3. Our principal results are the existence of canards (akin to the FSN II), faux canards and canard-faux canard concatenations (unique to the FSN I). We also provide delay estimates, which are comparable to those of the classic delayed Hopf bifurcation and FSN II, but are also distinct in that the trajectories can extend all the way along CM_r. Figures 5.3 and 5.4 highlight the novel aspects of the FSN I, which we summarize in Table 5.1.

The demonstration of Corollary 5.1 immediately illustrates Theorems 5.1 and 5.2. Similarly, Corollary 5.2 inherently shows Theorems 5.5 and 5.6. Note in Figures 5.3, 5.4(c) and 5.4(d) that the solutions visibly oscillate around the folded saddle, but seemingly pass through the folded node without rotation. Recall that the blow-up (5.8) converts the folded singularities into Hopf bifurcations of (5.10). As such, the canards and faux canards inherit their rotational properties from the dynamic Hopf bifurcations. In particular, the oscillations have growing amplitude on CM_r and decaying amplitude on CM_a. The oscillations near the folded node are below a visible threshold due to exponential attraction to CM_a.

Table 5.1. Demonstration of results in the forced VdP oscillator ($\delta = -1$) and Morris-Lecar/FitzHugh-Nagumo ($\delta = 1$) examples. FN = folded node and FS = folded saddle.

Result	Figure	Description
Cor 5.1	5.4(d), (f)	Canards starting on S_a^- return to S_a^- via the FS faux canard.
Cor 5.2	5.3	Special orbit traces both the FN weak and FS faux canards.
Prop 5.4	5.3, 5.4(d)	There are about 7 oscillations, which is $\mathcal{O}(\varepsilon^{-1/4})$ for the given ε.
Thm 5.8	5.4(d)	Near-field: $y_{2,B} = \sqrt{\alpha_2}$; most solutions trace CM_r all the way.
	5.4(e)	Far-field: $y_{2,B} = 0$; solutions trace CM_r less than halfway.
Prop 5.5	5.3, 5.4(f)	Solution connects FN to FS and traces CM_r completely.

5.5. Linearized Complex Flow

For $\alpha_2 > 0$, the reduced flow (5.13) on CM crosses the Hopf bifurcations of the layer problem (5.10), leading to delayed loss of stability. To find canard solutions near CM, we have to track $S_a^{\varepsilon^{1/4}}$ and $S_r^{\varepsilon^{1/4}}$ across the Hopf bifurcations. Standard methods like Melnikov theory will not work due to the singular nature of (5.15) together with the partially complex eigenvalue structure of (5.10). The benefit of the rescaling (5.8) is that we can analytically continue the vector field into the complex domain (following [**91, 92, 93**]) and look for special (elliptic) paths connecting points on the real y_2-axis. Along such paths, we have control over the growth rates of solutions and can track the invariant manifolds (and hence show transverse intersection). In this section, we complexify our system, show the existence of elliptic paths in the linearization, and study the growth/decay rates and rotational properties.

5.5.1. Complexification. To track the invariant manifolds across the Hopf bifurcations of (5.10), we extend the vector field into the complex domain. To do this, let $(x_2, y_2, z_2) \in \mathbb{C}^3$ and introduce the complex coordinate transformation

$$\begin{aligned} u_2 &= z_2 + i\,\frac{x_2 + \delta(\alpha_2 - y_2^2)z_2 + \mathcal{O}(\varepsilon^{1/4})}{\sqrt{1-(\alpha_2-y_2^2)^2 + \mathcal{O}(\varepsilon^{1/4})}}, \\ v_2 &= z_2 - i\,\frac{x_2 + \delta(\alpha_2 - y_2^2)z_2 + \mathcal{O}(\varepsilon^{1/4})}{\sqrt{1-(\alpha_2-y_2^2)^2 + \mathcal{O}(\varepsilon^{1/4})}}, \end{aligned} \tag{5.19}$$

which brings the linear part of (5.15) into Jordan normal form and $(u_2, v_2, y_2) \in \mathbb{C}^3$. Note that (5.19) is singular for real $|\alpha_2 - y_2^2| = 1$ to leading order. That is, the domain of analyticity must exclude branch points of the square root function. Applying (5.19) to (5.15) gives

$$\begin{aligned} u_2' &= \lambda u_2 + \frac{1}{4}(u_2+v_2)^2\left(1 + i\,\frac{\delta(\alpha_2-y_2^2)+\mathcal{O}(\varepsilon^{1/4})}{\sqrt{1-(\alpha_2-y_2^2)^2+\mathcal{O}(\varepsilon^{1/4})}}\right) + G_1(u_2, v_2, \varepsilon^{1/4}), \\ v_2' &= \nu v_2 + \frac{1}{4}(u_2+v_2)^2\left(1 - i\,\frac{\delta(\alpha_2-y_2^2)+\mathcal{O}(\varepsilon^{1/4})}{\sqrt{1-(\alpha_2-y_2^2)^2+\mathcal{O}(\varepsilon^{1/4})}}\right) + G_2(u_2, v_2, \varepsilon^{1/4}), \\ y_2' &= \varepsilon^{1/4}, \end{aligned} \tag{5.20}$$

where $G_i = \mathcal{O}(\sqrt{\varepsilon}, \varepsilon^{1/4}(|u_2|^2 + |v_2|^2))$, $i = 1, 2$ and we suppress the $(y_2, \alpha_2, \varepsilon^{1/4})$ dependence in λ, ν. We take the standard definition of the square root function given, for $z = |z|\exp(i\theta)$ with $\theta \in [-\pi, \pi)$, by $\sqrt{z} = \sqrt{|z|}\exp(i\theta/2)$, with $\operatorname{Arg}\sqrt{z} \in [-\frac{\pi}{2}, \frac{\pi}{2})$ and branch cut along the negative real axis. Translating this to our problem:

$$\sqrt{1-(\alpha_2-y_2^2)^2} = \sqrt{|1-(\alpha_2-y_2^2)^2|}\exp\left\{i\operatorname{Arg}\sqrt{1-(\alpha_2-y_2^2)^2}\right\},$$

with modulus and argument given by

$$\sqrt{|1-(\alpha_2-y_2^2)^2|} = \left\{\left[(1-\zeta)^2+4a^2b^2\right]\left[(1+\zeta)^2+4a^2b^2\right]\right\}^{1/4},$$
$$\operatorname{Arg}\left(\sqrt{1-(\alpha_2-y_2^2)^2}\right) = \begin{cases} \frac{\pi}{4}-\frac{1}{2}\tan^{-1}\left(\frac{1+4a^2b^2-\zeta^2}{4ab\,\zeta}\right) & \text{if } ab\,\zeta>0, \\ -\frac{\pi}{4}-\frac{1}{2}\tan^{-1}\left(\frac{1+4a^2b^2-\zeta^2}{4ab\,\zeta)}\right) & \text{if } ab\,\zeta\le 0, \end{cases}$$

where $y_2 = a+ib$ with $a,b\in\mathbb{R}$, $\zeta := \alpha_2 - a^2 + b^2$ and $\operatorname{Arg}\left(\sqrt{1-(\alpha_2-y_2^2)^2}\right) \in [-\frac{\pi}{2},\frac{\pi}{2})$. The branch cut of this function along the negative real axis is defined by

$$\operatorname{Im}\left(1-(\alpha_2-y_2^2)^2\right) = 4ab(\alpha_2-(a^2-b^2)) = 0,$$
$$\operatorname{Re}\left(1-(\alpha_2-y_2^2)^2\right) = 1+4a^2b^2-(\alpha_2-(a^2-b^2))^2 < 0.$$

For more detailed derivations, we refer to Section 4.1 of [**76**] and note that our problem is the same (with y_2 from [**76**] replaced by $\alpha_2 - y_2^2$). The domain of analyticity D is the complex y_2-plane with the branch cuts and small discs about the branch points at $y_2 = \pm\sqrt{\alpha_2 \pm 1}$ removed (Figure 5.13). The existence and uniqueness theorems for differential equations hold on D and can be analytically continued to points on the branch cuts.

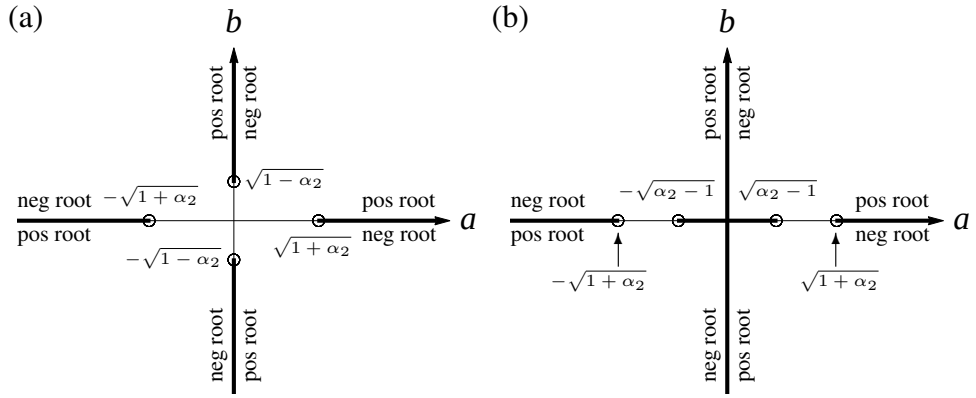

Figure 5.13. Branch cuts (bold lines) of the function $\sqrt{1-(\alpha_2-y_2^2)^2}$ in the complex y_2-plane for (a) $0<\alpha_2<1$ and (b) $\alpha_2>1$. The square root function is independent of δ.

It is important to identify which solutions of (5.20) correspond to real solutions of (5.15). For $y_2\in\mathbb{R}$, if the eigenvalues $\lambda(y_2,\alpha_2,\varepsilon^{1/4}), \nu(y_2,\alpha_2,\varepsilon^{1/4})$ are complex, then we require $u_2 = \overline{v}_2$ for real solutions (x_2,y_2,z_2) of (5.15). If the eigenvalues (5.16) are real, then u_2 and v_2 must be real in order to have real solutions of (5.15).

5.5.2. Linearization. We now study properties of the linear homogeneous flow of (5.20):

$$\begin{aligned} u_2' &= \lambda(y_2,\alpha_2,\varepsilon^{1/4})u_2, \\ v_2' &= \nu(y_2,\alpha_2,\varepsilon^{1/4})v_2, \\ y_2' &= \varepsilon^{1/4}. \end{aligned} \tag{5.21}$$

Alternatively, using y_2 as the complex slow time, we consider the system

$$\begin{aligned} \varepsilon^{1/4}\frac{du_2}{dy_2} &= \lambda(y_2,\alpha_2,0)u_2, \\ \varepsilon^{1/4}\frac{dv_2}{dy_2} &= \nu(y_2,\alpha_2,0)v_2, \end{aligned} \tag{5.22}$$

with the leading order eigenvalues and note that the equations are decoupled. As such, it suffices to study the complex linear homogeneous ODE:

$$\varepsilon^{1/4}\frac{du_2}{dy_2} = \lambda(y_2, \alpha_2, 0)u_2, \tag{5.23}$$

on the slow time y_2. Solutions of (5.23) take the form

$$u_2(y_2) = \tilde{u}_2 \exp\left\{\frac{1}{\varepsilon^{1/4}}\int_\Gamma \lambda(z, \alpha_2, 0)\, dz\right\},$$

with initial condition $u_2(\tilde{y}_2) = \tilde{u}_2$ and contour $\Gamma \subset D$ connecting $\tilde{y}_2$ with y_2. The behaviour of the homogenous solution depends on the form of the exponent

$$\varphi(y_2) = \int_\Gamma \lambda(z, \alpha_2, 0)\, dz,$$

along contours Γ of integration. In particular, we are interested in the special contours:

Definition 5.3. *Elliptic contours* are the level curves of constant growth given by $\operatorname{Re}\varphi =$ constant. *Hyperbolic contours* are the level curves of constant oscillatory behaviour given by $\operatorname{Im}\varphi =$ constant.

We now derive equations for the elliptic contours. Let $y_2(\tau) = a(\tau) + ib(\tau)$ be a contour parametrization. Substituting in Definition 5.3

$$\operatorname{Re}\varphi(a(\tau) + ib(\tau), \alpha_2, 0) = \text{constant},$$

and differentiating both sides with respect to τ gives

$$\operatorname{Re}\lambda(a(\tau) + ib(\tau), \alpha_2, 0)\frac{da}{d\tau} - \operatorname{Im}\lambda(a(\tau) + ib(\tau), \alpha_2, 0)\frac{db}{d\tau} = 0.$$

Rewriting in system form leads to the following evolution equations for the elliptic contours:

$$\begin{aligned} a' &= -\operatorname{Im}\lambda(a(\tau) + ib(\tau), \alpha_2, 0), \\ b' &= -\operatorname{Re}\lambda(a(\tau) + ib(\tau), \alpha_2, 0), \end{aligned} \tag{5.24}$$

where the prime denotes differentiation with respect to τ.

Remark 5.14. Similar evolution equations can be derived for the hyperbolic contours. We omit these since (5.23) has no hyperbolic contours that connect points on the real y_2-axis.

5.5.3. Analysis of the Elliptic Contours.

Proposition 5.6. *For* $0 < \alpha_2 < 1$, (5.24) *has the following properties along the real* y_2*-axis:*

$$\operatorname{sgn} a' \begin{cases} = 0 & |a| \geq \sqrt{\alpha_2 + 1} \\ = 1 & |a| < \sqrt{\alpha_2 + 1} \end{cases}$$

$$\operatorname{sgn} b' \begin{cases} = \operatorname{sgn}\delta & |a| > \sqrt{\alpha_2} \\ = 0 & |a| = \sqrt{\alpha_2} \\ = -\operatorname{sgn}\delta & |a| < \sqrt{\alpha_2} \end{cases}$$

For $\alpha_2 > 1$, (5.24) *has the following properties along the real y_2-axis:*

$$\operatorname{sgn} a' \begin{cases} = 0 & |a| > \sqrt{\alpha_2 + 1} \\ = 1 & \sqrt{\alpha_2 - 1} < |a| < \sqrt{\alpha_2 + 1} \\ = 0 & |a| < \sqrt{\alpha_2 - 1} \end{cases}$$

$$\operatorname{sgn} b' \begin{cases} = \operatorname{sgn} \delta & |a| > \sqrt{\alpha_2} \\ = 0 & |a| = \sqrt{\alpha_2} \\ = -\operatorname{sgn} \delta & |a| < \sqrt{\alpha_2} \end{cases}$$

Proposition 5.7. *For $0 < \alpha_2 < 1$,* (5.24) *has the following properties along the imaginary y_2-axis:*

$$\operatorname{sgn} a' \begin{cases} = 0 & |b| \geq \sqrt{1 - \alpha_2} \\ = 1 & |b| < \sqrt{1 - \alpha_2} \end{cases}$$

$$\operatorname{sgn} b' = -\operatorname{sgn} \delta \qquad b \in \mathbb{R}$$

For $\alpha_2 > 1$, (5.24) *has the following properties along the imaginary y_2-axis:*

$$\operatorname{sgn} a' = 0 \qquad b \in \mathbb{R}$$

$$\operatorname{sgn} b' = -\operatorname{sgn} \delta \quad b \in \mathbb{R}$$

Propositions 5.6 and 5.7 are the FSN I analogues of Propositions 4.1–4.3 from [**76**]. We refer the reader to the appendices of [**76**], where detailed proofs of these results can be found in the FSN II context and point out that our results are obtained by replacing y_2 in [**76**] by $\delta(\alpha_2 - y_2^2)$. Note that for $\alpha_2 > 1$, the elliptic contours cannot cross the imaginary axis. The main point of Proposition 5.6 is that the elliptic contours cross the real axis transversally.

We observe that $\lambda(y_2, \alpha_2, 0)$ has the symmetry $\lambda(y_2, \alpha_2, 0) = \lambda(-y_2, \alpha_2, 0)$, so that the elliptic contours in the first and third quadrants of the complex y_2-plane have the same properties. Similarly, contours in the second and fourth quadrants have the same properties.

Proposition 5.8. *Let $\alpha_2 > 0, \delta = 1$ and $y_2 = a + ib$ with $|y_2| \gg 1$. Then the elliptic contours in the first and third quadrants are respectively forward and backward asymptotic to*

$$K := \left\{ (a, b) \in \mathbb{R}^2 : \frac{a^2}{3} + \frac{C_1}{a} - b^2 = \alpha_2,\ C_1 \textit{ constant} \right\},$$

The elliptic contours in the second and fourth quadrants are respectively backward and forward asymptotic to the family of circles

$$C := \left\{ (a, b) \in \mathbb{R}^2 : (a - C_2)^2 + b^2 = C_2^2 - \alpha_2,\ |C_2| > \sqrt{\alpha_2} \right\}.$$

Proof. Let $z \in \mathbb{C}$. Then, from Appendix E of [**76**], we have:

$$\sqrt{1 - z^2} = \begin{cases} -iz\sqrt{1 - \frac{1}{z^2}} & \operatorname{Im} z > 0, \\ iz\sqrt{1 - \frac{1}{z^2}} & \operatorname{Im} z < 0. \end{cases}$$

Replacing z by $\delta(\alpha_2 - y_2^2)$ gives:

$$\sqrt{1 - (\alpha_2 - y_2^2)^2} = \begin{cases} -i\delta(\alpha_2 - y_2^2)\sqrt{1 - \frac{1}{\delta(\alpha_2 - y_2^2)^2}} & \operatorname{Re} y_2 \operatorname{Im} y_2 < 0, \\ i\delta(\alpha_2 - y_2^2)\sqrt{1 - \frac{1}{\delta(\alpha_2 - y_2^2)^2}} & \operatorname{Re} y_2 \operatorname{Im} y_2 > 0. \end{cases}$$

Now, for $|y_2|$ large, we obtain the following expansions for λ:

$$\lambda = \begin{cases} \frac{1}{2}\frac{1}{\delta(\alpha_2 - y_2^2)} + \mathcal{O}\left(\frac{1}{\delta^3(\alpha_2 - y_2^2)^3}\right) & \text{Re } y_2 \text{ Im } y_2 < 0, \\ 2\delta(\alpha_2 - y_2^2) + \mathcal{O}\left(\frac{1}{\delta(\alpha_2 - y_2^2)}\right) & \text{Re } y_2 \text{ Im } y_2 > 0. \end{cases}$$

Suppose $y_2 = a + ib$ is in the first quadrant. Using the appropriate expansion for λ in (5.24):

$$\begin{aligned} a' &= -4\delta ab, \\ b' &= 2\delta(\alpha_2 - a^2 + b^2). \end{aligned}$$

We can remove the time parametrization and rewrite the system as a single linear equation (in b^2), the general solution of which gives the result. By symmetry of λ, we immediately have the result in the third quadrant.

Suppose that y_2 is in the second quadrant. Then the asymptotic expansion of (5.24) is

$$\begin{aligned} a' &= -\delta\frac{1}{2}\frac{1}{|\alpha_2 - y_2^2|^2}2ab, \\ b' &= -\delta\frac{1}{2}\frac{1}{|\alpha_2 - y_2^2|^2}(\alpha_2 - a^2 + b^2). \end{aligned}$$

Eliminating the parameter τ gives a single linear equation in $\frac{b^2}{a}$ and the result follows. □

Remark 5.15. For $\delta = -1$, the elliptic contours in the first and third quadrants are asymptotic to the circles C whilst the contours in the second and fourth quadrants are asymptotic to the hyperbolae K.

Lemma 5.3. *Let $\alpha_2 > 0$. The elliptic contours are horizontal along the hyperbola*

$$H := \left\{ y_2 = a + ib : \alpha_2 - a^2 + b^2 = 0 \right\}. \tag{5.25}$$

That is, the hyperbola H is precisely the b-nullcline of (5.24).

Corollary 5.3. *There exist critical elliptic paths $\Gamma_\pm$ that touch the real axis tangentially at $y_2 = \pm\sqrt{\alpha_2}$.*

We summarize our analysis of the elliptic contours in Figure 5.14.

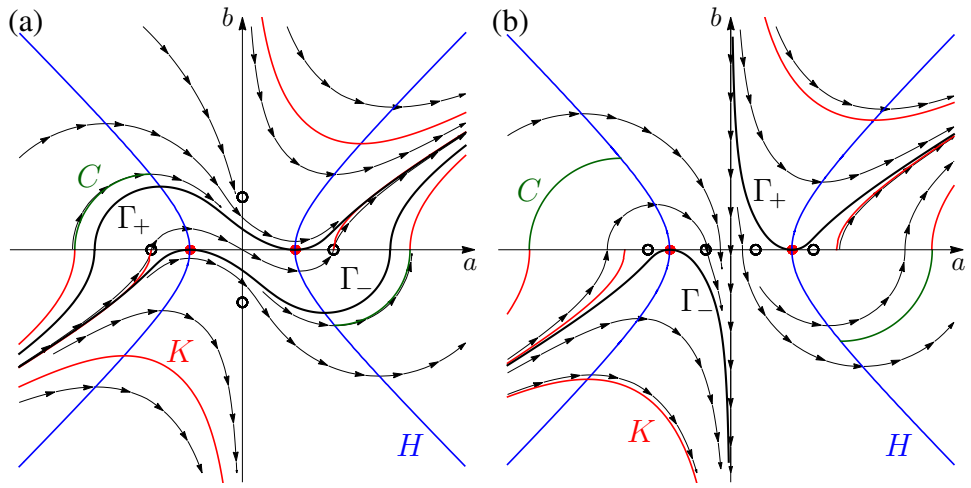

Figure 5.14. Elliptic paths in the complex y_2 plane for $\delta = 1$ for (a) $0 < \alpha < 1$ and (b) $\alpha_2 > 1$. The elliptic contours for $\delta = -1$ are obtained by flipping the image about the real axis.

Remark 5.16. The elliptic contours have symmetries due to the quadratic dependence of $\lambda(y_2, \alpha_2, 0)$ on y_2. The higher order terms in λ will lead to symmetry breaking. We expect that those elliptic contours that are tangent to the imaginary axis at leading order may cross the imaginary axis under perturbation.

We can now state the main results of this section:

Proposition 5.9. *Let $\alpha_2 > 0$ and $y_{2,*} \in (-\sqrt{\alpha_2}, \sqrt{\alpha_2})$ be a point on the real axis. Then there exists an elliptic path Γ_e that connects $y_{2,*}$ to some $y_{2,0}$ where $|y_{2,0}| > \sqrt{\alpha_2}$.*

Proof. Follows from Proposition 5.6 together with Corollary 5.3. □

Corollary 5.4. *For $0 < \alpha_2 < 1$, there exist elliptic paths Γ_e that connect $y_{2,0}^- < -\sqrt{\alpha_2}$ to $y_{2,*} \in (-\sqrt{\alpha_2}, \sqrt{\alpha_2})$ to $y_{2,0}^+ > \sqrt{\alpha_2}$.*

Proof. Follows from Proposition 5.9 together with Proposition 5.7 (i.e. from the fact that the elliptic contours can cross the imaginary axis for $0 < \alpha_2 < 1$). □

5.5.4. Expansion, Contraction and Rotation Along Elliptic Paths. We now study the growth and decay rates along these paths and compute the amount of rotation. To do this, we transform (5.22) along the elliptic paths described by (5.24), resulting in the system

$$\begin{aligned} \varepsilon^{1/4} u_2' &= -i\,\lambda(y_2(\tau), \alpha_2, 0)\,\overline{\lambda}(y_2(\tau), \alpha_2, 0)\,u_2, \\ \varepsilon^{1/4} v_2' &= -i\,\nu(y_2(\tau), \alpha_2, 0)\,\overline{\lambda}(y_2(\tau), \alpha_2, 0)\,v_2. \end{aligned} \tag{5.26}$$

By construction, the eigenvalue of the u_2 equation is purely imaginary (i.e. the growth rate is zero) along the elliptic paths. The same cannot be said for the v_2 equation.

Proposition 5.10. *Let $z = \delta(\alpha_2 - y_2^2)$. The hyperbolic and elliptic components of the v_2 equation are*

$$\begin{aligned} \text{Re}\,\left(-i\,\nu\,\overline{\lambda}\right) &= 2\left(\text{Re}\; z\,\text{Re}\,\sqrt{1-z^2} + \text{Im}\; z\,\text{Im}\,\sqrt{1-z^2}\right), \\ \text{Im}\,\left(-i\,\nu\,\overline{\lambda}\right) &= \sqrt{1-z^2}\overline{\sqrt{1-z^2}} - z\overline{z}. \end{aligned} \tag{5.27}$$

The sign of $\text{Re}\,(-i\nu\overline{\lambda})$ along an elliptic path determines the growth/decay in v_2. That is, the sign of

$$\Xi := 2\left(\text{Re}\; z\,\text{Re}\;\sqrt{1-z^2} + \text{Im}\; z\,\text{Im}\,\sqrt{1-z^2}\right),$$

where $z = \delta(\alpha_2 - y_2^2)$ must be determined (Figure 5.15). This is essentially Lemmas 4.4 and 4.5 of [**76**]. As such, we state the following without proof and refer to [**76**] for details:

Proposition 5.11. *Let $\alpha_2 > 0$. Then*

$$\text{sgn}\;\text{Re}\,(-i\nu\overline{\lambda}) \begin{cases} = \text{sgn}\;\delta & b^2 > a^2 - \alpha_2 \\ = -\,\text{sgn}\;\delta & b^2 < a^2 - \alpha_2. \end{cases}$$

Moreover, $\text{Re}\,(-i\nu\overline{\lambda}) = 0$ along H and along the branch cuts of $\sqrt{1-(\alpha_2 - y_2^2)^2}$.

To study the rotational properties along elliptic paths, we substitute the parametrization $y_2 = y_2(\tau)$ into (5.23). The amount of expansion/contraction, E, and rotation, R, along a path $y_2(\tau), \tau \in [0, T]$ is

$$\begin{aligned} E &:= \frac{1}{\varepsilon^{1/4}} \int_0^T \text{Re}\,\left(\lambda(y_2(\tau), \alpha_2, 0)\frac{dy_2}{d\tau}\right)\,d\tau, \\ R &:= \frac{1}{\varepsilon^{1/4}} \int_0^T \text{Im}\,\left(\lambda(y_2(\tau), \alpha_2, 0)\frac{dy_2}{d\tau}\right)\,d\tau. \end{aligned}$$

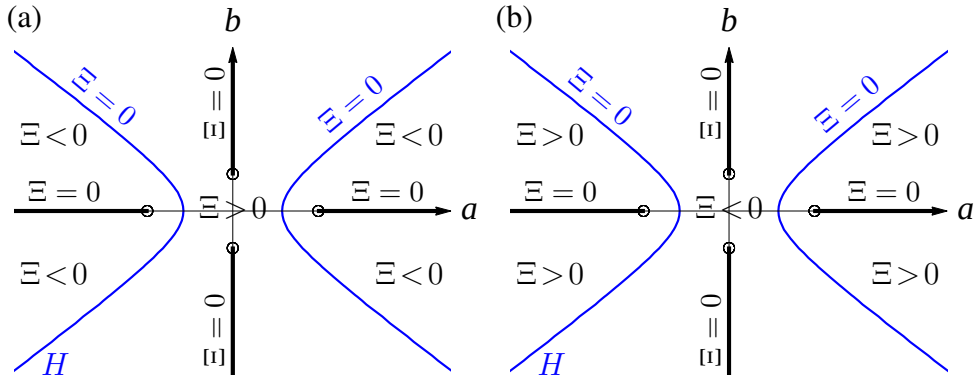

Figure 5.15. Growth and decay rates of the v_2 equation of (5.26) for $0 < \alpha_2 < 1$ for (a) $\delta = 1$ and (b) $\delta = -1$.

These integrals are path independent, allowing us to make the computation along the real axis and the hyperbola H instead of along the elliptic contours. We have:

Proposition 5.12. *Let $\alpha_2 > 0$ and suppose Γ_e is an elliptic path joining $y_{2,0} < -\sqrt{\alpha_2}$ to $y_{2,*} > -\sqrt{\alpha_2}$. There exist constants m, M with $0 < m < M$ such that the amount of rotation, R, along Γ_e is bounded*

$$m\,\varepsilon^{-1/4} \leq R \leq M\,\varepsilon^{-1/4}\,.$$

Proof. Consider the case $0 < \alpha_2 < 1$ and $\delta = 1$. Suppose first that $y_{2,0} < -\sqrt{\alpha_2 + 1}$, $y_{2,*} > \sqrt{\alpha_2 + 1}$ and Γ_e is the elliptic path joining these points. Let $(a^H_\mp, b^H_\mp)$ be the unique points where Γ_e intersects the hyperbola H in the second and fourth quadrants, respectively. Let $R_{\text{real},-}$ denote the amount of rotation along the real axis from $y_{2,0}$ to $-\sqrt{\alpha_2}$. Let $R_{H,-}$ denote the amount of rotation along H from $(-\sqrt{\alpha_2}, 0)$ to (a^H_-, b^H_-). We compute the rotation along Γ_e up to H by computing R_{real} and $R_{H,-}$. For simplicity of notation, we write $\lambda(z) = \lambda(z, \alpha_2, 0)$. We have

$$R_{\text{real},-} + R_{H,-} = \frac{1}{\varepsilon^{1/4}} \left(\int_{y_{2,0}}^{-\sqrt{\alpha_2}} \text{Im}\ \lambda(s)\, ds + \int_{-\sqrt{\alpha_2}}^{a^H_-} \text{Im}\ \lambda(a + i b_H(a)) \frac{db_H}{da}\, da \right),$$

where $b_H(a)$ is a graph representation of H. Similarly, the amount of rotation from (a^H_+, b^H_+) to $(y_{2,*}, 0)$ along the hyperbola and the real axis is

$$R_{\text{real},+} + R_{H,+} = \frac{1}{\varepsilon^{1/4}} \left(\int_{a^H_+}^{\sqrt{\alpha_2}} \text{Im}\ \lambda(a + i b_H(a)) \frac{db_H}{da}\, da + \int_{\sqrt{\alpha_2}}^{y_{2,*}} \text{Im}\ \lambda(s)\, ds \right).$$

To compute the rotation in regions where $\Xi > 0$, we compute the rotation backwards along Γ_e by considering a combination of paths along the real axis and the hyperbola H. Thus, the amount of rotation from (a^H_-, b^H_-) to (a^H_+, b^H_+) computed in backward time is

$$\begin{aligned} \varepsilon^{1/4}(R_{H,+} + R_{\text{real}} + R_{H,-}) = &\int_{a^H_+}^{\sqrt{\alpha_2}} \text{Im}\, \lambda(a + i b_H(a)) \frac{db_H}{da}\, da + \int_{\sqrt{\alpha_2}}^{-\sqrt{\alpha_2}} \text{Im}\ \lambda(s)\, ds \\ &+ \int_{-\sqrt{\alpha_2}}^{a^H_-} \text{Im}\ \lambda(a + i b_H(a)) \frac{db_H}{da}\, da. \end{aligned}$$

Hence, the amount of rotation from $y_{2,0}$ to $y_{2,*}$ along Γ_e is

$$\begin{aligned}\varepsilon^{1/4} R_{\text{total}} &= \varepsilon^{1/4} \left(R_{\text{real},-} + R_{H,-} - R_{H,+} - R_{\text{real}} - R_{H,-} + R_{\text{real},+} + R_{H,+} \right), \\ &= \int_{-\sqrt{1+\alpha_2}}^{\sqrt{1+\alpha_2}} \sqrt{1-(\alpha_2 - s^2)^2}\, ds,\end{aligned}$$

which can be expressed in terms of the complete elliptic integrals of the first and second kinds. In particular, $\varepsilon^{1/4} R_{\text{total}}$ is bounded above and below for all $\alpha_2 > 0$ leading to the conclusion that there are $\mathcal{O}(\varepsilon^{-1/4})$ rotations.

Now, let $y_{2,0} < -\sqrt{\alpha_2}$ and $y_{2,*} > -\sqrt{\alpha_2}$ be the endpoints of the elliptic path Γ_e. Then, by the above arguments, the amount of rotation from $y_{2,0}$ to $y_{2,*}$ is

$$\varepsilon^{1/4} R_{\text{total}} = \int_{s_0}^{s_1} \sqrt{1-(\alpha_2 - s^2)^2}\, ds \leq \int_{-\sqrt{1+\alpha_2}}^{\sqrt{1+\alpha_2}} \sqrt{1-(\alpha_2 - s^2)^2}\, ds,$$

where $s_0 \in [-\sqrt{1+\alpha_2}, -\sqrt{\alpha_2}]$ and $s_1 \in [-\sqrt{\alpha_2}, \sqrt{1+\alpha_2}]$. Similar arguments show boundedness of the rotations for $\alpha_2 > 1$. Also note that $\operatorname{Im} \lambda(y_2, \alpha_2, 0)$ is independent of δ along the real axis so that the above holds for $\delta = -1$. □

Remark 5.17. Proposition 5.12 implies Proposition 5.4. In the FSN II, the number of canards is bounded below by $K\,\varepsilon^{-1/2}$, for some positive constant K [**76**]. Here we have $\mathcal{O}(\varepsilon^{-1/4})$ canards (faux canards) for the FSN I, contingent on the existence of a canard (faux canard) solution. The number of canards becomes unbounded as $\alpha_2 \to 0$, in keeping with the folded node and folded saddle theory as $\mu \to 0$.

We now formally identify a canard-way-in/way-out function that allows us to obtain delay estimates.

Lemma 5.4. *The elliptic contours are the level curves of the Hamiltonian*

$$H(y_2, \alpha_2) = \operatorname{Re}\left(\int_\Gamma \lambda(z, \alpha_2, 0)\, dz \right).$$

Proof. Follows from the Fundamental Theorem of Calculus together with the Cauchy-Riemann equations (see Lemma 4.1 of [**76**]). □

Corollary 5.5. *If $y_{2,0}$ and $y_{2,*}$ are points on the real axis joined by an elliptic path Γ_e, then*

$$\int_{\Gamma_e} \operatorname{Re}\, \lambda(z, \alpha_2, 0)\, dz = 0.$$

Proof. Since H is constant along Γ_e, we have $H(y_{2,0}, \alpha_2) = H(y_{2,*}, \alpha_2)$. Linearity of integration allows the operations of integration and taking the real part to be swapped. □

Remark 5.18. The integral is path independent so we may evaluate it along the real axis. Note that $\lambda(y_2, \alpha_2, 0)$ and $\nu(y_2, \alpha_2, 0)$ represent the same complex function on different sheets of the Riemann surface. Continuity of λ implies that $\lambda(y_2, \alpha_2, 0) \to \nu(y_2, \alpha_2, 0)$ as $y_2 \to \pm\sqrt{\alpha_2 - 1}$ along the real axis in the far-field case, hence the need for branch switching (see Figure 5.12).

Proof of Lemma 5.2. For $\delta = 1$ and $0 < \alpha_2 < 1$, we have $y_{2,B} = y_{2,C}$ and there is always an elliptic path that terminates at $y_{2,*} \in \left(0, \sqrt{\alpha_2}\right]$. There exists a $\tilde{\alpha_2} \approx 0.66$ such that the critical paths $\Gamma_\pm$ connect to the branch points on the imaginary axis. For $\alpha_2 < \tilde{\alpha_2}$, the critical paths cross the imaginary axis and $y_{2,B} = \sqrt{\alpha_2}$ (Figure 5.14(a)). For $\alpha_2 > \tilde{\alpha_2}$, the critical paths do not cross the imaginary axis and $y_{2,B} < \sqrt{\alpha_2}$. For $\delta = 1$ and $\alpha_2 > 1$, the elliptic

contour that terminates at $y_2 = 0$ is the one that originates at $-\infty$ (Figure 5.14(b)) so that $y_{2,B} < y_{2,C} = 0$. For $\delta = -1$, we have:

$$I_\lambda(-\sqrt{\alpha_2}, 2\sqrt{\alpha_2}) \geq \int_{-\sqrt{\alpha_2}}^{2\sqrt{\alpha_2}} (s^2 - \alpha_2)\, ds = 0,$$

which is valid for all $\alpha_2 > 0$, and the result follows. □

Proof of Proposition 5.5. For $\delta = 1$ and $0 < \alpha_2 < 1$, $y_{2,B} \in (0, \sqrt{\alpha_2}]$. Time reversal and symmetry of $\lambda(y_2, \alpha_2, 0)$ imply that there is a faux canard that originates at $+\infty$ and terminates at $y_{2,0} \in [-\sqrt{\alpha_2}, 0)$. For $\delta = 1$ and $\alpha_2 > 1$, $y_{2,C} = 0$. Again, by symmetry, there is a faux canard that connects $y_{2,0} = 0$ and $+\infty$. We obtain the result for $\delta = -1$ by considering the flow in backward time. □

5.6. Existence of Canards and Delay Estimates

In Section 5.5, we studied the linearized complex flow (5.22) and showed the existence of elliptic paths (connecting points on the real axis) along which we have control over the growth/decay of solutions. In this section, we show that the elliptic paths of Section 5.5 perturb to elliptic paths of the nonlinear problem (5.20). Using these perturbed paths, we are able to transport the invariant manifolds $S_a^{\varepsilon^{1/4}}$ and $S_r^{\varepsilon^{1/4}}$ across the dynamic bifurcations and hence prove the theorems of Section 5.4.

5.6.1. Elliptic Paths and Preliminary Estimates. We have shown that there are always elliptic paths defined by (5.24) that are transverse to the real axis. We are therefore guaranteed that the construction of these paths persist under $\mathcal{O}(\varepsilon^{1/4})$ perturbation. In particular, we can construct elliptic paths Γ_e^ε for the perturbed linear homogeneous problem

$$\varepsilon^{1/4} \frac{du_2}{dy_2} = \lambda(y_2, \alpha_2, \varepsilon^{1/4})\, u_2,$$

which are solutions of

$$\begin{aligned} a' &= -\operatorname{Im}\, \lambda(a(\tau) + ib(\tau), \alpha_2, \varepsilon^{1/4}), \\ b' &= -\operatorname{Re}\, \lambda(a(\tau) + ib(\tau), \alpha_2, \varepsilon^{1/4}). \end{aligned}$$

Consequently, Γ_e^ε is $\mathcal{O}(\varepsilon^{1/4})$ close to the unperturbed elliptic path Γ_e.

Proposition 5.13. *Let Γ_e^ε be an elliptic path with parametrization $y_2(\tau)$ starting on the real axis in an $\mathcal{O}(\varepsilon^{1/4})$ neighbourhood of some $y_{2,0}$ and ending on the real axis in an $\mathcal{O}(\varepsilon^{1/4})$ neighbourhood of $y_{2,*}$. Then system* (5.20) *transformed along Γ_e^ε is*

$$\begin{aligned} \varepsilon^{1/4} u_2' &= -i\lambda(\tau, \alpha_2, \varepsilon^{1/4})\, \overline{\lambda}(\tau, \alpha_2, \varepsilon^{1/4})\, u_2 + G_1(\tau, \alpha_2, u_2, v_2), \\ \varepsilon^{1/4} v_2' &= -i\nu(\tau, \alpha_2, \varepsilon^{1/4})\, \overline{\lambda}(\tau, \alpha_2, \varepsilon^{1/4})\, v_2 + G_2(\tau, \alpha_2, u_2, v_2), \end{aligned} \tag{5.28}$$

where the nonlinearities are defined by

$$G_i = \mathcal{O}(\sqrt{\varepsilon}, |u_2|^2 + |v_2|^2), \qquad i = 1, 2.$$

Remark 5.19. The expansion and contraction properties of the linear part of (5.28) are the same as those detailed in Proposition 5.11.

If (5.28) is holomorphic, bounded and Lipschitz in a closed disc around an initial condition, then we have existence and uniqueness of solutions of the corresponding initial value problem [**61**]. Analytic continuation allows us to extend solutions along any path provided the vector field can also be extended along that path. Thus, we have existence and uniqueness of solutions of (5.28) everywhere in the domain of analyticity except possibly along paths connecting to the branch points, where care has to be taken.

The linear flow of system (5.28) is given by

$$\Phi(\tau,\tau_0) := \begin{pmatrix} \exp(-i\,\varepsilon^{-1/4}\int_{\tau_0}^{\tau}\lambda(\sigma)\,\overline{\lambda}(\sigma)\,d\sigma) & 0 \\ 0 & \exp(-i\,\varepsilon^{-1/4}\int_{\tau_0}^{\tau}\nu(\sigma)\,\overline{\lambda}(\sigma)\,d\sigma) \end{pmatrix},$$

where we have suppressed the $(\alpha_2,\varepsilon^{1/4})$ dependence in $\lambda,\overline{\lambda}$ and ν. We can rewrite (5.28) as

$$U_2(\tau,U_0) = \Phi(\tau,0)\,U_0 + \frac{1}{\varepsilon^{1/4}}\int_0^{\tau}\Phi(\tau,\sigma)\,G(U_2(\tau,U_0),\sqrt{\varepsilon})\,d\sigma, \tag{5.29}$$

where $U_2=(u_2,v_2), G=(G_1,G_2)$ and $U_0=(u_2(0),v_2(0))$.

Proposition 5.14. *Let $\alpha_2>0,\delta=1$ and $c\in(0,\frac{1}{4})$ a constant. Suppose $|U_0|=\mathcal{O}(\varepsilon^{1/4+c})$ and $y_2(\tau)$ parametrizes an elliptic path Γ_e^{ε} such that $(\operatorname{Im} y_2)^2 < (\operatorname{Re} y_2)^2-\alpha_2$, i.e. $y_2(\tau)$ parametrizes the part of Γ_e^{ε} where $\operatorname{Re}(-i\nu\overline{\lambda})<0$. Then*

$$U_2(\tau,U_0)=\mathcal{O}(\varepsilon^{1/4}),$$

for all $\tau\in[0,\tau_H]$, where τ_H is such that $y_2(\tau_H)\in H$.

Proof. Consider (5.29) and rewrite the nonlinear terms as

$$G(U_2,\sqrt{\varepsilon}) = G_1(\sqrt{\varepsilon}) + G_2(U_2,\sqrt{\varepsilon}),$$

where $G_1(\sqrt{\varepsilon})=\mathcal{O}(\sqrt{\varepsilon})$ and $G_2(U_2,\sqrt{\varepsilon})=\mathcal{O}(\sqrt{\varepsilon}U_2,U_2^2)$. Then (5.29) becomes

$$U_2(\tau,U_0) = \Phi(\tau,0)\,U_0 + \frac{1}{\varepsilon^{1/4}}\int_0^{\tau}\Phi(\tau,\sigma)\,G_1(\sqrt{\varepsilon})\,d\sigma + \frac{1}{\varepsilon^{1/4}}\int_0^{\tau}\Phi(\tau,\sigma)\,G_2(U_2,\sqrt{\varepsilon}). \tag{5.30}$$

Since we restrict attention to elliptic segments where $\operatorname{Re}(-i\nu\overline{\lambda})<0$, we have $\Phi(\tau,0)\,U_0=\mathcal{O}(\varepsilon^{1/4+c})$. Moreover, $\int_0^{\tau}\Phi(\tau,\sigma)\,d\sigma=\mathcal{O}(\varepsilon^{1/4})$, for $\mathcal{O}(1)$ time τ, so that

$$\int_0^{\tau}\Phi(\tau,\sigma)G_1(\sqrt{\varepsilon})\,d\sigma=\mathcal{O}(\varepsilon^{3/4}).$$

Now, let $U_2=\varepsilon^{1/4+c}\,\widetilde{U}_2$ where $\widetilde{U}_2=\mathcal{O}(1)$. Then

$$G_2(U_2,\sqrt{\varepsilon}) = \varepsilon^{1/2+2c}\,\widetilde{G}_2(\widetilde{U}_2,\sqrt{\varepsilon}),$$

where $\widetilde{G}_2$ is $\mathcal{O}(1)$. In fact, we may assume $|\widetilde{G}_2|\le K_1(\Lambda)$ for all $|\widetilde{U}_2|\le\Lambda$. Substitution in (5.30) leads to the Gronwall-inequality

$$|\widetilde{U}_2| \le K_2 + \varepsilon^c\,K_1(\Lambda)\int_0^{\tau}|\Phi(\tau,\sigma)|\,d\sigma,$$

for some constant $K_2>0$. The implication is that $|\widetilde{U}_2|=\mathcal{O}(1)$ and the result follows. □

Remark 5.20. Analogues of Proposition 5.14 can be shown for elliptic paths in regions where $\operatorname{Re}(-i\nu\overline{\lambda})>0$ by integrating backwards in τ from the real axis to the hyperbola H. Similar estimates can also be shown for $\delta=-1$ by integrating forwards or backwards in τ from the real axis to H.

5.6.2. Near-Field Existence Theorems. We now prove the existence theorems in the near-field limit $0<\alpha_2<1$ (Theorems 5.1 and 5.2). Before we proceed, we first review properties of the layer problem (5.10), which we reproduce here for convenience

$$\begin{aligned} \dot{x}_2 &= p - z_2, \\ \dot{z}_2 &= x_2 + z_2^2, \end{aligned} \tag{5.31}$$

where $p=\delta(\alpha_2-y_2^2)$. For $\delta=1$, we assume $p\in(0,1)$ so that the equilibria of the layer problem are unstable foci (see Figure 5.7 for the corresponding y_2 intervals). For each fixed

p there is an unique trajectory, $S_{r,p}$, which is algebraic in forward time [**71**]. The union of these trajectories $S_{r,p}$ over p provides a close approximation of $S_r^{\varepsilon^{1/4}}$.

The properties of (5.10) near CM were studied in [**76**] by considering the map

$$\Pi_p : \Sigma_p := \left\{(x_2, z_2) : z_2 = p, x_2 < -p^2\right\} \to \Sigma_p.$$

The unstable foci of CM exponentially expand the distance between points in a neighbourhood of CM. More precisely, if $(x_2, p) \in \Sigma_p$ then the number of iterations of Π_p required to be a distance $d > 0$ away from $(-p^2, p)$ is $m = \lfloor -\log|x_2 + p^2| \rfloor$. That is,

$$\text{dist } \left(\Pi_p^m(x_2, p), (-p^2, p)\right) \geq d.$$

Moreover, if $x_{2,0}$ and $x_{2,1}$ are points in Σ_p such that $x_{2,1}$ is on the forward orbit of $x_{2,0}$ but the trajectory of $x_{2,1}$ does not return to Σ_p, then there must be a point $x_{2,*} \in \Sigma_p$ with $x_{2,1} < x_{2,*} < x_{2,0}$ corresponding to $S_{r,p}$. Similar statements hold for $\delta = -1$, in which case we assume $p \in (-1, 0)$ so that the equilibria of (5.31) are stable foci and we consider the layer flow in backward time.

We are now in a position to prove Theorems 5.1 (cf. Theorem 3.1 from [**76**]) and 5.2.

Outline of Proof (Theorem 5.1). For $\delta = 1$, let J_1 be a set of initial conditions in Σ_1 in (x, y, z)-coordinates between the strong canard and center manifold. By Lemma 5.1, CM_a perturbs to $CM_a^{\sqrt{\varepsilon}}$. Exponential contraction of Π_1 onto $CM_a^{\sqrt{\varepsilon}}$ implies one endpoint of $J_2 = \Pi_1(J_1)$ is $\mathcal{O}(\sqrt{\varepsilon})$ close to CM. We choose the other endpoint q of J_1 such that $\Pi_1(q)$ is $\mathcal{O}(\varepsilon^{1/4+c})$. Thus, J_2 is $\mathcal{O}(\varepsilon^{1/4})$ close to CM in Σ_2^- and can be assumed to be contained in a leaf of the weak stable foliation W^s (see Figure 5.10). Let $\Pi_* : \Sigma_2^- \to \Sigma_*$ and assume Π_* transforms to complex (u_2, v_2, y_2)-coordinates. Then we can transport the invariant bundle J_2 to Σ_* using the elliptic path. By Proposition 5.14 and Remark 5.20, $J_* = \Pi_*(J_2)$ is a curve of length $\mathcal{O}(\varepsilon^{1/4})$ in (u_2, v_2) coordinates (i.e. J_* is $\mathcal{O}(\varepsilon^{1/4})$ close to CM). Returning to (x_2, y_2, z_2)-coordinates and using properties of the layer flow (5.31) near an unstable focus, we can show that J_* 'winds out' from CM and intersects $S_r^{\varepsilon^{1/4}}$ transversally. Since the intersection is transverse at zero order, the manifolds will intersect for the fully perturbed problem, which is an $\mathcal{O}(\varepsilon^{1/4}\ln\varepsilon)$ perturbation of the zero order estimate. For $\delta = -1$, we simply consider the flow in backward time.

Outline of Proof (Theorem 5.2). For $\delta = 1$, let $J_2 \subset S_a^{\varepsilon^{1/4}} \cap \Sigma_2$ be an $\mathcal{O}(\varepsilon^{1/4})$ neighbourhood of CM. Assume that the backwards map $\Pi_* : \Sigma_2 \to \Sigma_*$ transforms to (u_2, v_2, y_2) coordinates. Then by Remark 5.20, $J_* = \Pi_*(J_2)$ is also $\mathcal{O}(\varepsilon^{1/4})$. The proof now proceeds as in Theorem 5.1, i.e. by evolving J_* forward under the layer flow (5.31) and showing that J_* winds out from CM, intersecting $S_r^{\varepsilon^{1/4}}$ in the process. For $\delta = -1$, consider the flow in backward time and take $J_2 \subset S_r^{\varepsilon^{1/4}} \cap \Sigma_2$ to be an $\mathcal{O}(\varepsilon^{1/4})$ neighbourhood of CM.

Corollary 5.1 follows from Theorems 5.1 and 5.2 together with Corollary 5.4.

5.6.3. Far-Field Existence Theorems. In the far-field ($\alpha_2 > 1$), if the hyperbolic structure of CM_r does not influence the dynamics, the existence theorems are unaltered (Theorems 5.3 and 5.4). When the hyperbolic structure of CM_r does influence the dynamics, we can track the invariant manifolds using their linear subspaces.

Proposition 5.15. *Let $\alpha_2 > 1$ and $\delta = 1$. Let R_+ be the amount of rotation from $y_{2,0} < -\sqrt{\alpha_2 + 1}$ along an elliptic path to the hyperbola H. Similarly, let R_- denote the amount of rotation from $y_{2,*} \in (-\sqrt{\alpha_2 - 1}, 0)$ backwards along the path to the hyperbola. Then*

$$\frac{d}{d\alpha_2}(R_+ - R_-) < 0.$$

Proof. By similar arguments as in Proposition 5.12, the amount of rotation along an elliptic path starting at $y_{2,0} < -\sqrt{\alpha_2+1}$ and ending at $y_{2,*} \in (-\sqrt{\alpha_2-1}, 0)$ is

$$F(\alpha_2) := \varepsilon^{1/4}(R_+ - R_-) = \int_{-\sqrt{\alpha_2+1}}^{-\sqrt{\alpha_2-1}} \sqrt{1-(\alpha_2-s^2)^2}\, ds.$$

To prove that $\varepsilon^{1/4}(R_+ - R_-)$ is decreasing, we want to show that

$$F'(\alpha_2) = \frac{d}{d\alpha_2}F(\alpha_2) = \int_{-\sqrt{\alpha_2+1}}^{-\sqrt{\alpha_2-1}} \frac{s^2-\alpha_2}{\sqrt{1-(\alpha_2-s^2)^2}}\, ds < 0.$$

Consider first the following standard integral

$$\int_{\alpha_2-1}^{\alpha_2+1} \frac{u-\alpha_2}{\sqrt{1-(\alpha_2-u)^2}}\, du = 0.$$

Changing variables $s = -\sqrt{u}$, we obtain the relation

$$\int_{-\sqrt{\alpha_2+1}}^{-\sqrt{\alpha_2-1}} \frac{s^2-\alpha_2}{\sqrt{1-(\alpha_2-s^2)^2}}\, ds = \frac{1}{\sqrt{\alpha_2}} \int_{-\sqrt{\alpha_2+1}}^{-\sqrt{\alpha_2-1}} \frac{(s-\sqrt{\alpha_2})(s+\sqrt{\alpha_2})^2}{\sqrt{1-(\alpha_2-s^2)^2}}\, ds.$$

Note that the integrand of the right hand side is negative on the integration interval (except at the endpoints where it diverges to $-\infty$ and at $s=-\sqrt{\alpha_2}$ where it is zero). □

Remark 5.21. Analogues of Proposition 5.15 exist for $\delta = -1$ and for the positive real axis.

Recall that we are interested in solutions of (5.28) that correspond to real solutions of (5.15). For real y_2, the necessary conditions on u_2 and v_2 are:

- $u_2 = \overline{v}_2$ if $\lambda(y_2, \alpha_2, \varepsilon^{1/4}), \nu(y_2, \alpha_2, \varepsilon^{1/4}) \in \mathbb{C}$
- $u_2, v_2 \in \mathbb{R}$ if $\lambda(y_2, \alpha_2, \varepsilon^{1/4}), \nu(y_2, \alpha_2, \varepsilon^{1/4}) \in \mathbb{R}$

Let $u_2(\tau)$ be a solution of (5.23) corresponding to a real solution of (5.15), where $y_2 = y_2(\tau)$ parametrizes an elliptic path with $y_2(0) < -\sqrt{\alpha_2+1}$. Let $u_2^H(\alpha_2) = u_2(\tau_H)$, where τ_H is such that $y_2(\tau_H) \in H$. Similarly, let $u_{2,*}(\tau)$ be the solution of (5.23) corresponding to a real solution of (5.15) with $u_{2,*}(T) \in (-\sqrt{\alpha_2}, 0)$ and let $u_{2,*}^H(\alpha_2) = u_{2,*}(\tau_H)$. We interpret $u_2^H(\alpha_2)$ and $u_{2,*}^H(\alpha_2)$ as vectors in $\mathbb{R}^2$. Let $\theta(\alpha_2)$ be the angle between $u_2^H(\alpha_2)$ and $u_{2,*}^H(\alpha_2)$ and define

$$A_d = \{\alpha_2 : \theta(\alpha_2) \geq d \quad \text{for all} \quad \alpha_2 \in A\},$$

where $A := [\alpha_{2,0}, \alpha_{2,1}]$ with $1 < \alpha_{2,0} < \alpha_{2,1}$. Let A_d^c be the complement of A_d in A. Then, by Proposition 5.4 of [**76**], we have:

Proposition 5.16. *There exists a constant $K > 0$ such that for each $d > 0$ and $0 < \varepsilon \ll 1$, the total length of A_d^c is bounded by Kd.*

For the case of ε-dependent elliptic paths, let A_d^ε and $A_d^{\varepsilon,c}$ denote the analogues of A_d and A_d^c, respectively, where the elliptic path Γ_e^ε is used instead of Γ_e. By Proposition 5.5 of [**76**]:

Proposition 5.17. *There exists a constant $K > 0$ such that for each $d > 0$ and $0 < \varepsilon \ll 1$, the total length of $A_d^{\varepsilon,c}$ is bounded by Kd.*

The implication of Propositions 5.15 and 5.17 is that for most $\alpha_2 \in A$, the vectors $u_2^H(\alpha_2)$ and $u_{2,*}^H(\alpha_2)$ rotate in opposite directions. We have equivalent results for $\delta = -1$ and for the positive real y_2-axis.

Outline of Proof (Theorems 5.5 and 5.6). We deal with Theorem 5.5 for $\delta = 1$ and refer to Theorem 5.1 of [**76**] for details. We take a set of initial conditions in $S_a^{\varepsilon^{1/4}} \cap \Sigma_2$ that is $\mathcal{O}(\varepsilon^{1/4})$ close to CM and evolve it forward along the elliptic path Γ_e^ε up to the hyperbola H. Similarly, we take a set of initial conditions in $S_r^{\varepsilon^{1/4}} \cap \Sigma_*$ that is $\mathcal{O}(\varepsilon^{1/4})$ close to CM and evolve it backward along Γ_e^ε up to H. We can show that these invariant bundles are close (Proposition 5.14) and rotate in opposite directions (Proposition 5.15). Hence they intersect transversally for most α_2. The proof for faux canards is the same.

5.6.4. Estimates of Bifurcation Delay. We now consider how long general solutions stay close to CM before escaping. We first consider trajectories that start close to CM (Theorem 5.7, which is the FSN I analogue of Theorem 5.2 from [**76**]).

Outline of Proof (Theorem 5.7). We treat the near-field case for $\delta = 1$. Consider solutions (u_2, v_2, y_2) of (5.20) that correspond to real solutions of (5.15) with elliptic paths $y_2(\tau)$, $\tau \in [0, T]$ connecting points on the real y_2-axis. Let $U_2(\tau) = (u_2(\tau), v_2(\tau))$ and $U_{2,*}(\tau) = (u_{2,*}(\tau), v_{2,*}(\tau))$ be solutions of (5.20) with initial conditions $U_2(0) = U_0$ with $y_2(0) < -\sqrt{\alpha_2 + 1}$ and $U_{2,*}(T) = U_{0,*}$ with $|y_{2,*}(T)| < \sqrt{\alpha_2}$ subject to the requirement $U_0 = \mathcal{O}(\varepsilon^{1/4})$ and $U_{0,*} = \mathcal{O}(\varepsilon^{1/4})$.

We follow $U_2(\tau)$ forward (in τ) and $U_{2,*}$ backward (in τ) along the elliptic path up to the hyperbola H. Then, by Proposition 5.14 and Remark 5.20, the distance between U_2 and $U_{2,*}$ is $\mathcal{O}(\varepsilon^{1/4})$. We then follow the solutions down H to the point $y_2 = -\sqrt{\alpha_2}$. Exponential contraction in the u_2 coordinate shrinks the distance between the two solutions:

$$|u_2 - u_{2,*}|_{y_2 = -\sqrt{\alpha_2}} = \mathcal{O}\left(\exp\left(\varepsilon^{-1/4} I_\lambda(y_{2,0}, -\sqrt{\alpha_2})\right)\right).$$

Since we are considering real solutions of (5.15), we have $u_2 = \overline{v}_2$ and $u_{2,*} = \overline{v}_{2,*}$ so that the above estimate holds for v_2 and $v_{2,*}$ at $y_2 = -\sqrt{\alpha_2}$. Finally, the maximal expansion along a solution from $y_2 = -\sqrt{\alpha_2}$ to any $y_2 > -\sqrt{\alpha_2}$ is

$$\exp\left(\varepsilon^{-1/4} I_\lambda(-\sqrt{\alpha_2}, y_2)\right).$$

Hence, if $y_2 > -\sqrt{\alpha_2}$ is such that $I_\lambda(y_{2,0}, y_2) < 0$, then the corresponding solution of (5.15) on the interval between $y_{2,0}$ and y_2 must be $\mathcal{O}(\varepsilon^{1/4})$. Similarly for the far-field and $\delta = -1$.

We now estimate the maximal delay before solutions leave CM and move to Σ_3 (Theorem 5.8).

Outline of Proof (Theorem 5.8). We consider the far-field case for $\delta = 1$, which contains all of the essential steps required for the other cases. Suppose $y_{2,B} \in (-\sqrt{\alpha_2}, -\sqrt{\alpha_2 - 1})$ so that CM_r is elliptic. Fix a $K > 0$ and suppose we have a trajectory of (5.28) with

$$|(u_2, v_2)| \geq K\,\varepsilon^{1/4}, \quad \text{for all } \; y_2(\tau) \leq y_{2,B} + d(\varepsilon), \tag{5.32}$$

and (u_2, v_2) is not exponentially close to $S_r^{\varepsilon^{1/4}}$. Then (5.32) implies (x_2, y_2, z_2) is $\mathcal{O}(\varepsilon^{1/4})$ away from CM. Consequently, (x_2, y_2, z_2) follows the layer dynamics and reaches Σ_3 in $\mathcal{O}(-\ln \varepsilon)$ time (see Theorem 3.1 of [**76**]). To prove the result for this subcase, we must show that (5.32) holds for most trajectories.

Suppose then that $p \in J_+$ is such that

$$|(u_2, v_2)| < K\,\varepsilon^{1/4}, \quad \text{for all } \; y_2(\tau) \leq y_{2,B} + d(\varepsilon), \tag{5.33}$$

and consider the trajectory of $\Pi_1(p)$ under the flow of (5.15). Then to leading order, the flow about $\Pi_1(p)$ from Σ_2 up to the section defined by $y_2 = y_{2,B} + d(\varepsilon)$ is an expansion with expansion rate

$$\exp\left(\varepsilon^{-1/4} I_\lambda(y_{2,0}, y_{2,*} + d(\varepsilon))\right). \tag{5.34}$$

We can show (see Lemma 5.4 of [**76**]) that the maximal contraction rate of Π_1 is smaller than the contraction in (5.34) so that the composition of Π_1 and transition by (5.15) exponentially expands the distance between points $p, q \in J_+$. Thus, q can only satisfy (5.33) if it is exponentially close to p.

Suppose now that $y_{2,B} \in (-\sqrt{\alpha_2 - 1}, 0)$ so that CM_r is hyperbolic. Consider a solution $U_2 = (u_2, v_2)$ of (5.20) with initial condition not exponentially close to the weak canard. By Theorem 5.5, $S_a^{\varepsilon^{1/4}}$ and $S_r^{\varepsilon^{1/4}}$ intersect transversally for most $\alpha_2 \in A$. This means the angle between the invariant manifolds is bounded below by some positive constant, which implies that $U_2(\tau_H)$ has a large component in the strongly expanding direction, where $y_2(\tau_H) \in H$. Linearization of (5.20) along CM allows us to measure the evolution of the strongly expanding component. By continuing the solution U_2 down H to the real axis at $y_2 = -\sqrt{\alpha_2}$, the strongly expanding component shrinks by the factor

$$\exp\left(\varepsilon^{-1/4} I_\lambda(y_{2,0}, -\sqrt{\alpha_2})\right).$$

Now, continuing U_2 along the real axis, the component in the strong unstable direction expands to $\mathcal{O}(1)$ when y_2 reaches a neighbourhood of the point $y_{2,*}$.

5.7. Discussion

The canard phenomenon occurs generically in singular perturbation problems with at least two slow variables. Closely related to folded singularities of the reduced flow, canards are solutions that follow a repelling invariant manifold for $\mathcal{O}(1)$ times on the slow timescale and partition the flow. Folded nodes and folded saddles with eigenvalue ratio μ bounded away from zero have been studied extensively. The main gaps in the theory are related to the FSN, of which there are two types: one where the center manifold is tangent to the fold (type I) and another where the center manifold is transverse to the fold (type II). Canard theory has been extended to the FSN II case with $\mu = \mathcal{O}(\varepsilon)$ [**51**], with $\mu = \mathcal{O}(\sqrt{\varepsilon})$ [**76, 119**] and for the transition between these two regimes [**20**]. The FSN I is known (via Melnikov methods on non-compact domains) to possess canard solutions [**139**].

The main contribution of this chapter was the extension of canard theory into the FSN I regime, which complements [**76, 139**]. We combined GSPT (blow-up) and dynamic bifurcation theory (complex time path analysis) to study the FSN I in the $\mu = \mathcal{O}(\varepsilon^k), k \geq 1/4$ regime. Although our results were formulated in terms of the parameter α, we note from Remark 5.1 that the interval $\alpha \geq 0$ is equivalent to $\mu \in \mathbb{R}$. We showed the existence of $\mathcal{O}(\varepsilon^{-1/4})$ canards and faux canards, which rotate around the primary weak canard. Our theorems explain the transition between folded node and folded saddle regimes (i.e. how Figure 2.4(a) is converted to Figure 2.4(b)). In the folded node regime, the secondary canards rotate about the weak canard. As μ decreases through zero (via the FSN I), the primary weak canard becomes the folded saddle faux canard (see Figure 2.2). The folded node secondary canards then become faux canard type solutions that rotate about the folded saddle faux canard. Thus, the rotational behaviour near the folded saddle in Figure 2.4(a) cannot be seen because the numerical method is suited to detecting canards, not faux canards.

In addition to the existence of canards and faux canards near the FSN I limit, we studied their properties. We showed that the canard and faux canard solutions exhibit characteristics of dynamic Hopf bifurcations: namely, growing/decaying amplitude on the attracting/repelling manifold and bifurcation delay. We provided delay estimates by means of way-in/way-out functions, which naturally pop out of the complexification process. For $\delta = 1$, generic solutions in the near-field can follow CM on S_r until they return to S_a. In the far-field, the folded node and folded saddle are too well-separated that most trajectories cannot make it more than halfway along CM_r. For $\delta = -1$, most trajectories in the funnel

can only trace CM_r a finite distance before they must escape. The main differences to the FSN II case are the lack of a full system Hopf bifurcation and the existence of faux canards. These differences allow canards of FSN I type to traverse the entire length of the repelling manifold.

We illustrated our assertions numerically in the forced VdP oscillator and in a hybrid neural excitability model (see Table 5.1). The forced VdP oscillator corresponded to the $\delta = -1$ subcase (center manifold of the FSN I on S_r) with flow directed from folded saddle to folded node. In the Morris-Lecar/FitzHugh-Nagumo excitability model, the flow had the $\delta = 1$ configuration (center manifold on S_a and flow directed from folded node to folded saddle). In both examples, we demonstrated the existence of canards, faux canards and canard-faux canard concatenations in the near-field and far-field. We also showed that the number of rotations about the folded saddle was $\mathcal{O}(\varepsilon^{-1/4})$. Moreover, we showed that there is always at least one solution that traces CM_r all the way. There are numerous examples where the dynamics near the FSN I have only been cursorily glossed over, such as [**39, 123, 136**], and the examples studied here show that the dynamics near the FSN I can be very rich.

There are many details yet to be worked out. In this article, we only provided a partial blow-up analysis of the FSN I, restricting attention to the entry and rescaling charts. That is, we focused on the delayed loss of stability in $\mathcal{O}(\varepsilon^{1/4})$ neighbourhoods of the FSN I. We have also yet to make explicit the connection between our work and the results of [**139**]. Another issue to be resolved is the task of calculating faux canards numerically. In the folded node case, the invariant slow manifolds are computed by reformulating the system as a boundary value problem and using homotopic continuation to generate a family of solutions that form a mesh of the surface (Section 2.7). The folded node canards are then identified as intersections between the surfaces. To the author's knowledge, there is currently no such analogue for computing faux canards and the best prospect for developing such an algortihm is a detailed blow-up analysis of the folded saddle singularity [**89**].

CHAPTER 6

Summary, Discussion & Open Questions

In this thesis, we studied the pseudo-plateau bursting activity produced by hormone-secreting pituitary lactotrophs. A vital feature of the analysis of bursting rhythms is the multiple-timescale structure of the governing system, which typically takes the form

$$\begin{aligned} \varepsilon \dot{x} &= f(x, y, z, \varepsilon, \delta), \\ \dot{y} &= g(x, y, z, \varepsilon, \delta), \\ \dot{z} &= \delta h(x, y, z, \varepsilon, \delta), \end{aligned} \tag{6.1}$$

where $0 < \varepsilon, \delta \ll 1$ are small, independent perturbation parameters, $x \in \mathbb{R}$ is fast, $y \in \mathbb{R}^2$ is intermediate and $z \in \mathbb{R}$ is slow. Such multiscale problems are amenable to singular perturbation methods. One particular singular perturbation technique that has been used with great success is GSPT, which is most naturally suited to 2-timescale problems. The presence of two perturbation parameters means there are various ways in which GSPT can be implemented as illustrated in Figures 1.7 and 4.1, and reproduced in Figure 6.1 for convenience.

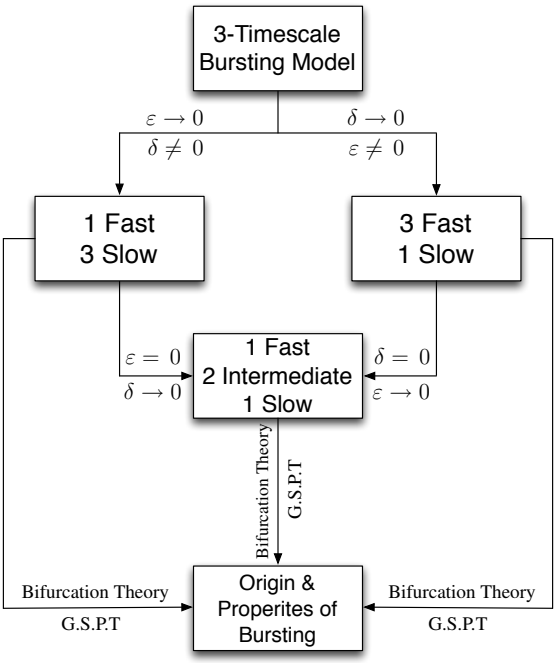

Figure 6.1. Slow/fast decompositions in the 3-timescale context.

In the classic implementation of GSPT in bursting problems [**98**], δ is treated as the principal perturbation parameter and the bursts are classified according to the fast (x, y)-subsystem bifurcations (with respect to z) involved in the initiation/termination of the burst [**65**] (3-fast/1-slow pathway of Figure 6.1). Plateau and pseudo-plateau bursting in particular feature a fast subsystem Hopf bifurcation in the active phase, the criticality of which distinguishes the two bursting types. In the plateau case, the Hopf is supercritical and the large-amplitude active phase spikes are related to stable periodic orbits of the fast subsystem.

In the pseudo-plateau case, the small amplitude spikes are transient oscillations generated by unstable limit cycles emanating from a subcritical Hopf. Plateau bursting and various features of pseudo-plateau bursting such as resetting properties [**116**] and burst termination due to fast subsystem manifolds [**94**] are well understood in this classic approach. Despite this, the standard slow/fast analysis has been demonstrated to be of limited use for understanding the underlying dynamics of pseudo-plateau bursting [**123**].

This thesis broke partially from the traditional approach to bursting by looking at alternative slow/fast analyses where there is more than 1 slow variable. We provided an alternative view of pseudo-plateau bursting by considering a slow/fast decomposition in which ε is the principal perturbation parameter and δ is fixed (1-fast/3-slow pathway of Figure 6.1). This splitting gave us access to canard theory, which in the 1-slow setting was degenerate and exponentially sensitive. The theory of canard-induced MMOs is one of the first areas where this alternative slow/fast decomposition has been introduced with some success. We summarize and discuss the implications of the main contributions of the thesis below.

6.1. Canard-Induced MMOs as a Mechanism for Bursting

The pituitary cell model we studied is unlike other bursting models in that the bursting persists almost unaltered when the calcium concentration c is fixed [**130**]. This is unusual, since the slow variation in the intracellular calcium concentration is typically responsible for clustering impulses into periodic episodes of activity. This suggests an intrinsic bursting mechanism independent of c. To investigate this novel form of bursting, we fixed the calcium ($\delta \to 0$) and employed GSPT to unravel the underlying dynamics. Following the 1-fast/3-slow pathway of Figure 6.1 (with $\delta \to 0$), we showed that the bursting was a canard-induced MMO. MMOs have been described previously for neural models and data [**15**], but this was the first example where they formed pseudo-plateau bursting oscillations [**123, 134**].

Key organizing structures in this slow/fast splitting were the fast x-subsystem equilibria (the critical manifold) and singularities of the slow (y, z)-subsystem. Normally hyperbolic critical manifolds approximate attracting and repelling slow manifolds of (6.1). The extension of these manifolds into nonhyperbolic regions (folded nodes) led to local twisting behaviour. Transverse intersections of these manifolds (canards) form separatrices that partition the phase space and shape the dynamics [**119, 140**]. The theory of canard-induced MMOs [**14**] provided the theoretical basis for understanding properties of the bursting such as the transition from spiking (relaxation oscillations) to bursting (MMOs) and how spike-adding bifurcations occur. The MMOs were the result of the interaction between local and global mechanisms. The local mechanism was the folded node, which caused a local twisting of trajectories. The global mechanism was the global return, which re-injected trajectories into the funnel region, thus resetting the dynamics after completion of the local passage.

We studied the bifurcations of the (folded node type) canard-induced MMOs under variations in the eigenvalue ratio μ of the folded node and the distance d of the global return of trajectories to the strong canard. To do this, a global return map induced by the flow of the equations was constructed and a qualitative analysis given [**135**]. The canards acted as separatrices in the return maps, organizing the dynamics along the Poincaré section. The (approximately) 1D return map covered the essential dynamics, allowing for an explanation of the different MMO patterns observed in the lactotroph model with fixed c.

6.2. Analysis and Prediction Testing On Real Cells

In our pituitary cell model analysis, we demonstrated the genesis of the bursting rhythm [**8**], identified the regions in parameter space where it exists [**123, 134**], and showed how features of the bursting vary in parameter space [**135**]. That is, through the combined power

of GSPT and bifurcation analysis, we made theoretical predictions about the bursting that could be tested experimentally. Here, we briefly discuss one context in which the geometric singular perturbation analysis has informed experimentation and vice versa [**137**].

Authors' Contributions: The analysis in this section [**137**] was performed by TV. The experiments were done by JT and TV. The manuscript was written by TV, and edited by TV, RB, JT, and MW.

6.2.1. Fast-Activating BK Current Promotes Bursting. Pituitary cells express a variety of ion channels and establishing the role of any given channel type is difficult. It has been proposed that large conductance potassium (BK) channels [**80, 106, 118**] primarily determine whether a pituitary cell spikes or bursts [**86, 117**]. In [**122**], a computational/experimental approach was used to study how kinetic properties of BK channels affect bursting. Blocking of the BK channels using paxilline generally resulted in an irreversible conversion from bursting to spiking. Using the dynamic clamp technique [**110**], artificial BK current was injected into the cell, which was observed to reliably return the cell to a bursting state. However, it was also observed that the burst promoting effect of the BK current came with a caveat: BK activation must be sufficiently fast to promote bursting. If the BK activation is too slow, then the BK current inhibits bursting by speeding up repolarization [**122**]. The primary aim of [**137**] was to explain the physiological observations of [**122**], i.e. to understand why BK activation must be fast in order to promote bursting.

6.2.2. Theoretical & Experimental Setup. In [**137**], a pituitary cell model similar to (1.3) was studied, the key difference being that the BK channels were no longer assumed to activate instantaneously. That is, the gating dynamics of the BK channels were included:

$$\tau_{BK}\frac{db}{dt} = b_\infty(V) - b,$$

where τ_{BK} is the time constant of the activation variable b for the BK channels. We refer to [**137**] for details of the model. One of the key observations from [**122**] was that the activation of the BK channels needed to be fast to promote bursting. Otherwise, the BK current has an inhibitory effect and the cell spikes. Using geometric singular perturbation analysis, we showed that the bursting can either be a canard- or a Hopf-induced MMO, depending on parameter values. The question then is whether or not they are observed experimentally.

To test our predictions experimentally, we employed a hybrid experimental/modelling tool called dynamic clamp [**110**]. In the dynamic clamp technique, an electrode is attached to a cell to record its voltage. To investigate I_{BK}, we block I_{BK} by introducing pharmacological agents (such as paxilline), which are known BK channel blockers. Once I_{BK} is blocked, we take our live voltage recordings and send them to a computer, where we compute a model (voltage-dependent) current, I_{BK}^{model}, with parameters that we specify. We then take that model current and inject it into the cell to see how the cell responds. Thus, the computer calculates I_{BK}^{model} using V from the cell and then injects the model current into the cell. In this way, we can use I_{BK}^{model} to simulate I_{BK} and hence investigate (in vitro) how kinetic properties of the BK current enhance/inhibit bursting in pituitary cells.

6.2.3. Experimental Results. A simple test to distinguish between the canard- and Hopf-induced MMOs is to inject artificial BK current (via dynamic clamp) and vary τ_{BK}. Based on the bifurcation and geometric singular perturbation analyses (see [**137**]), we expect the canard-induced MMOs to have weak response to variations in τ_{BK}, whilst the Hopf-induced MMOs have extreme sensitivity to variations in τ_{BK}. To test the sensitivity of the trajectories to variations in τ_{BK}, we blocked the BK channels using paxilline and measured the response of the cell to injection of BK current at different activation rates.

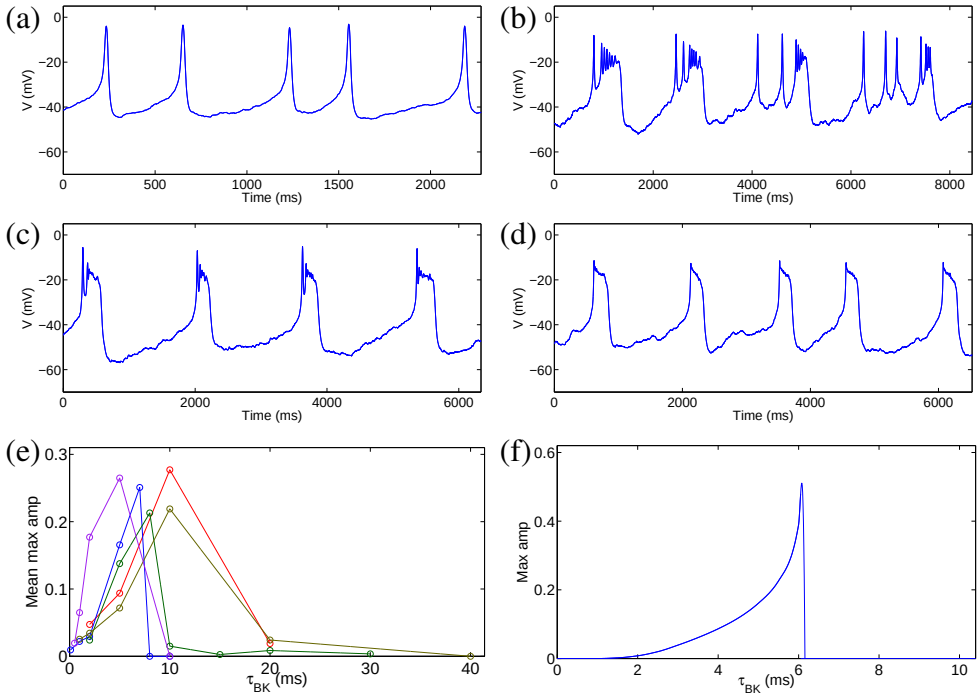

Figure 6.2. Effect of variations of τ_{BK} in dynamic clamp experiments recorded from a GH4C1 lacto-somatotroph cell line. (a) $\tau_{BK} = 10$ ms: spiking. (b) $\tau_{BK} = 7$ ms: mixture of spiking and bursting. (c) $\tau_{BK} = 5$ ms: bursting. (d) $\tau_{BK} = 2$ ms: plateauing. Note the different timescales. (e) Summary of the behaviour of the small oscillation amplitude under τ_{BK} variations in different cells. The g_{BK} values for the red, blue, green, olive and purple curves are $g_{BK} = 0.5, 1.6, 2, 0.5, 1$ nS, respectively. The blue curve ($g_{BK} = 1.6$ nS) corresponds to the cell in panels (a) to (d). (f) Theoretical analogue of (e) calculated for the associated model.

In Figure 6.2, we show evidence for Hopf-induced MMOs in pituitary cells. Panels (a)–(d) show the effect of varying τ_{BK} for fixed g_{BK}. For BK current injected with slow activation time constant (i.e. τ_{BK} large), the cell is spiking (panel (a)). By decreasing τ_{BK}, we eventually cross a threshold and bursting can be observed interspersed with the spiking activity (panel (b)). Further decreasing τ_{BK} reliably converts the electrical activity to bursting and the spiking behaviour is absent (panel (c)). Moreover, the amplitude of the small oscillations decreases with τ_{BK}. For sufficiently fast activation rates, the small oscillations are virtually non-existent and the electrical activity exhibits plateau behaviour (panel (d)). These observations are consistent with the prediction that for Hopf-induced MMOs, decreasing τ_{BK} switches the activity from spiking to bursting to plateauing (see [**137**]).

To quantify how changing τ_{BK} affects the bursting, we measured the amplitude of the largest small-amplitude active phase oscillation in a given burst for a fixed g_{BK} with activation time constant τ_{BK}. We then normalized the amplitude relative to the maximum and minimum voltage values of that burst to obtain the maximal relative amplitude. Averaging over the number of events (where an 'event' refers to a spike, burst or plateau) produced the mean maximal small-oscillation amplitude for a fixed (τ_{BK}, g_{BK}) pair. This was repeated for each (τ_{BK}, g_{BK}) pair used in the dynamic clamp experiments. Figure 6.2(e) provides a graphical summary of the amplitude data from these experiments for 5 cells. Bursting appears for fast activation rates with small oscillations of large amplitude (relative to the size of the pulse). For very fast BK activation, the mean maximal small-oscillation amplitude decreases and eventually disappears, giving way to plateaus. Figure 6.2(f) shows an equivalent diagram for the associated bursting model. The model predicts the trends observed

experimentally. Namely, that fast BK activation generates bursting with small oscillations that decay as τ_{BK} is decreased.

6.2.4. Summary. One of the key observations from [**122**] was that the BK activation rate τ_{BK} played a vital role in the spiking/bursting activity of pituitary cells. GSPT provided the theoretical framework necessary to understand the burst generating mechanisms. One of the hallmarks of the Hopf-induced MMOs is the sensitivity to variations in τ_{BK}. Two easily observable traits that change dramatically with τ_{BK} are the number and amplitude of small oscillations in the burst pattern. To test the model predictions, we blocked BK channels in GH4 cells and injected artificial BK current (via dynamic clamp) at different activation rates. We observed that at the onset of bursting, the amplitude of the small oscillations is large. Injecting more rapidly activated BK current reliably decreased the amplitude of the small oscillations. For injected BK current with sufficiently small τ_{BK}, the small oscillations disappear and the bursting is replaced by plateauing. Thus, the dynamic clamp experiments support the notion that the bursting arises from Hopf-induced MMOs. The canard mechanism completes the theoretical picture, but experimental evidence for canard-induced MMOs is more elusive.

6.3. Bursting as a 3-Timescale Problem

Multiple methods from dynamical systems theory have been used to understand pseudo-plateau bursting. The classic 2-timescale approach (3-fast/1-slow path of Figure 6.1) provides valuable information about how the transition from plateau to pseudo-plateau bursting occurs under parameter variation. It also provides information about complex phase resetting properties and the termination of spikes in a burst. Our more novel 2-timescale approach (1-fast/3-slow path of Figure 6.1) shows that the bursting arises from canard dynamics. This approach explains the origin of the small-amplitude spikes that occur during the active phase of the bursting, the transition between spiking and bursting, and provides information about how the number of spikes per burst varies with parameters. Both methods can be effective analytic tools, but there has been little justification for one approach over the other.

That the two slow/fast analyses yield key insights points to the fact that the system evolves on three timescales. Such 3-timescale systems have received little attention [**67, 74, 75**] and are typically treated as 2-timescale problems, which is the natural setting for GSPT. Comparative analyses of the two slow/fast methods have been performed [**123**], however, there have been few attempts to reconcile these approaches [**125**] in the context of (6.1). In Chapter 4 [**136**], we broadened the scope of GSPT by showing that elementary applications of the theory can be a powerful analytical tool in understanding 3-timescale problems. We showed that the two analysis techniques are different unfoldings of a 3-timescale system (1-fast/2-intermediate/1-slow path of Figure 6.1) and the results from each method can be reconciled in the 3-timescale context. As to the question of which method is most appropriate, we assert that the 3-timescale decomposition provides the best results asymptotically, independent of the model, as it inherits all of the geometric information contained in the 2-timescale methodologies.

6.4. Extending Canard Theory to FSN I Singularities

One of the key results of our model analysis was that the bursting arose from canard dynamics. Canards are special solutions of singularly perturbed problems that partition the flow, helping to organize the dynamics in phase space. They are closely associated with folded singularities of the reduced flow, and in the case of folded nodes, lead to a local twisting of invariant manifolds. Folded node canards and folded saddle canards have been

studied extensively in $\mathbb{R}^3$ [**119, 140**]. The folded saddle-node (FSN) is the codimension-1 bifurcation that gives rise to folded nodes and folded saddles, and there are two types.

The FSN type I corresponds to a true saddle-node bifurcation of folded singularities, i.e. a folded node and a folded saddle coalesce and annihilate each other. The FSN type II corresponds to a transcritical bifurcation of a folded singularity with an ordinary singularity. Both types of FSN are common in applications, often leading to the onset of complex and chaotic dynamics. FSN I singularities arise in the forced van der Pol oscillator, where they lead to the creation of MMOs [**11**]. The FSN I has also been identified in 3-timescale problems as the region of phase space where all three timescales interact [**136**]. The FSN II explains the rapid transition from $\mathcal{O}(\sqrt{\varepsilon})$-amplitude limit cycles to relaxation oscillations via canard explosion in singular perturbation problems [**73**]. Moreover, both types of FSN tend to demarcate the regions in parameter space where bursting behaviour can occur [**123, 135**]. Despite their ubiquity, the dynamics near FSNs are not completely understood.

The existing folded node canard theory has been extended into the FSN II regime for $\mu = \mathcal{O}(\varepsilon)$ [**51**], for $\mu = \mathcal{O}(\sqrt{\varepsilon})$ [**76**] and for the transition between these two settings [**20**]. To the author's knowledge, there are currently no such results for the FSN I. The main mathematical contribution of this thesis then, was the extension of canard theory into the FSN I regime [**138**]. By combining methods from GSPT (blow-up), and the theory of dynamic bifurcations (analytic continuation into the plane of complex time), we proved the existence of canards and faux canards near the FSN I limit. We focused on the delayed loss of stability near the FSN I, showing that canards and faux canards could connect, allowing trajectories that start on an attracting manifold to traverse the entire length of the repelling manifold and return to the attracting side.

6.5. Open Questions

In this thesis, we have demonstrated the potency of combining theory, numerics and experimentation. The theory of canard- and Hopf-induced MMOs provides a theoretical framework in which experimental predictions can be made. The dynamic clamp technique can then be used to confirm or counter these predictions in an experimental setting. In spite of the success of these techniques, there are various limitations, complications and open questions that have yet to be addressed. Broadly speaking, these fall into three distinct categories:

(i) canard phenomena in higher dimensions,
(ii) GSPT in 3-timescale systems,
(iii) GSPT in electrophysiology.

6.5.1. Canard Phenomena in Higher Dimensions. Canards and their bifurcations have been studied extensively in $\mathbb{R}^3$. These results extend to higher dimensional systems [**143**], where the canards persist with enriched dynamics. That is, the folded singularities (and canards) can interact with other dynamical objects and these interactions can have drastic impact on the evolution of a system, such as in [**26, 28**]. Many of these phenomena have not been studied in detail and the field is ripe for the picking.

One pressing example in the bursting context is the interaction between a folded node and a dynamic Hopf bifurcation, such as in the 2-fast/2-slow system presented in [**137**]. The issue is how the switch from canard-induced to Hopf-induced MMOs occurs in the fully perturbed problem $0 < \varepsilon \ll 1$. In the singular limit, the switch can be well understood as a Bogdanov-Takens bifurcation of the layer problem, which alters the jumping mechanism for the singular orbits. How the switch in the oscillation mechanism perturbs (i.e. how the slow and fast subsystems interact away from the singular limit) is much less clear. Studies of how

the BT bifurcation unfolds in systems with one slow variable have been considered [**18, 43**], however, the 2-slow variables case is different since the canard phenomenon is generic.

A related issue is what happens to canard-induced MMOs in these higher dimensional systems. How the bifurcation structure of a system is affected when the canard mechanism interacts with other mechanisms is an interesting problem. We only briefly touched upon this in the context of our pituitary cell model (1.3). More specifically, in Section 3.2, we performed careful one parameter bifurcation analyses of (1.3) with $\delta = 0$ via return maps. Our return map formulation did not cover all of the dynamics and a careful study of canard cycles in pseudo-plateau bursting has yet to be done. We then extended the bifurcation analysis to (1.3) with $\delta \neq 0$ in Section 4.2. However, since the detailed bifurcation structure of (1.3) was not a primary focus of Chapter 4, we only highlighted the salient features, leaving more detailed discussions to future work. Moreover, our singular analysis showed that the switch between dynamic and calcium-conducting MMOs corresponded to a global bifurcation, wherein the geometry of the critical manifold of the 3-fast/1-slow system changed from a bistable regime to a non-bistable regime. How this global singular bifurcation manifests in the fully perturbed problem remains an open question.

6.5.2. GSPT in 3-Timescale Problems. Many natural phenomena evolve on more than two timescales. Currently, GSPT is formulated for 2-timescale problems and there is no rigorous theoretical framework for problems involving three or more timescales. There are several interesting problems that need to be addressed such as understanding the local dynamics near singularities of the 3-timescale problem and working out which timescales are truly important to the evolution.

There are various types of singularities that can arise in the 2-timescale problem. For instance, fast subsystem bifurcations can lead to slow passage effects (such as in the case of the dynamic Hopf bifurcation). Alternatively, singularities of the slow subsystem (folded singularities) can generate canards. In the 2-timescale context, these singularities remain as separate entities. In the 3-timescale scenario however, these singularities can merge and arise from some higher codimension bifurcation in the double singular limit $(\varepsilon, \delta) \to (0, 0)$. The unfolding of such points poses an interesting mathematical problem, an understanding of which would help to clarify the disparity between the various slow/fast decompositions of 3-timescale systems such as (6.1).

Another interesting problem is the question of which timescale dominates the evolution. In the 2-timescale context, either the fast or slow timescale dominates and the fast or slow dynamics closely follow their singular counterparts. In neighbourhoods of the singularities however, the timescale separation is not so clear and the timescales can mix, a well known example being the dynamics near folded nodes where trajectories evolve on $\mathcal{O}(\sqrt{\varepsilon})$ timescales. This problem is only exacerbated in the 3-timescale problem, where there are two perturbation parameters, and singularities of the 2-timescale problem become extra degenerate.

6.5.3. GSPT in Electrophysiology. In Section 6.2, we showed how GSPT combined with electrophysiology can be used to answer biologically inspired questions. That is, observations from dynamic clamp experiments showed that fast-activating BK current tended to promote bursting in pituitary cells. Motivated by this, we used GSPT to predict that the root cause of the observations was a dynamic Hopf mechanism. We then used dynamic clamp to verify our predictions. Thus, we have provided experimental evidence for Hopf-induced MMOs, but experimental evidence for the canard-induced MMOs is currently tenuous and left to future work. The theory (GSPT) and experiments (dynamic clamp) form a symbiotic relationship and their interplay will continue to both deepen our knowledge of the biological

mechanisms that generate bursting in pituitary cells, and drive new and innovative mathematical methods for analyzing such systems.

References

[1] B. ALBERTS, A. JOHNSON, J. LEWIS, M. RAFF, K. ROBERTS AND P. WALTER, "Molecular Biology of the Cell", 5th edition, Garland Science, 2007.

[2] S. BAER, AND T. ERNEUX, *Singular Hopf bifurcation to relaxation oscillations*, SIAM J. Appl. Math., **46** (1986), 721–739.

[3] S. M. BAER, T. ERNEUX AND J. RINZEL, *The slow passage through a Hopf bifurcation: delay, memory effects, and resonance*, SIAM J. Appl. Math., **49** (1989), 55–71.

[4] S. BAER, AND T. ERNEUX, *Singular Hopf bifurcation to relaxation oscillations II*, SIAM J. Appl. Math., **52** (1992), 1651–1664.

[5] E. BENOIT, *Canards et enlacements*, Publ. Inst. Hautes Études Sci., **72** (1990), pp. 63–91.

[6] R. BERTRAM, M. J. BUTTE, T. KIEMEL AND A. SHERMAN, *Topological and phenomenological classification of bursting oscillations*, Bull. Math. Biol., **57** (1995), 413–439.

[7] R. BERTRAM AND A. SHERMAN, *Negative calcium feedback: the road from Chay-Keizer*, in "The Genesis of Rhythm in the Nervous System" (eds. S. Coombes and P. Bressloff), World Scientific, New Jersey (2005), 19–48.

[8] R. BERTRAM, J. TABAK, W. TEKA, T. VO AND M. WECHSELBERGER, *Bursting oscillations in pituitary cells: Z-curves, folded nodes, calcium stores, and mixed-mode oscillations*, Frontiers in Applied Dynamics, in press.

[9] R. BERTRAM, J. TABAK AND N. TOPORIKOVA, *Models of hypothalamus*, Scholarpedia, (2006) **1**(12):1330.

[10] J. BEST, A. BORISYUK, J. RUBIN, D. TERMAN AND M. WECHSELBERGER, *The dynamic range of bursting in a model respiratory pacemaker network*, SIAM J. Appl. Dyn. Syst., **4** (2005), 1107–1139.

[11] K. BOLD, C. EDWARDS, J. GUCKENHEIMER, S. GUHARAY, K. HOFFMAN, J. HUBBARD, R. OLIVA, AND W. WECKESSER, *The forced van der Pol equation II: canards in the reduced system*, SIAM J. Appl. Dyn. Syst., **2** (2003), 570–608.

[12] B. BRAAKSMA, *Singular Hopf bifurcation in systems with fast and slow variables*, J. Nonlinear Sci., **8** (1998), pp. 457–490.

[13] H. W. BROER, T. J. KAPER AND M. KRUPA, *Geometric desingularization of a cusp singularity in slow-fast systems with applications to Zeeman's examples*, J. Dyn. Diff. Equat., **25** (2013), 925–958.

[14] M. BRØNS, M. KRUPA AND M. WECHSELBERGER, *Mixed mode oscillations due to the generalized canard phenomenon*, in "Bifurcation Theory and Spatio-Temporal Pattern Formation", Fields Institute Communications, **49** Amer. Math. Soc., Providence, RI, (2006), 39–63.

[15] M. BRØNS, T. J. KAPER AND H. G. ROTSTEIN, *Introduction to focus issue: Mixed mode oscillations: Experiment, computation, and analysis*, Chaos, **18** (2008), 015101, 4 pp.

[16] R. J. BUTERA, J. RINZEL AND J. C. SMITH, *Models of respiratory rhythm generation in the pre-Bötzinger complex. I. Bursting pacemaker neurons*, J. Neurophysiol., **82** (1999), 382–397.

[17] S. A. CAMPBELL, E. STONE AND T. ERNEUX, *Delay induced canards in a model of high speed machining*, Dynamical Systems, **24** (2009), 373–392.

[18] H. CHIBA, *Periodic orbits and chaos in fast-slow systems with Bogdanov-Takens type fold points*, J. Differential Equations, **250** (2011), 112–160.

[19] S. COOMBES AND P. C. BRESSLOFF, "Bursting: The Genesis of Rhythm in the Nervous System", World Scientific, 2005.

[20] R. CURTU AND J. RUBIN, *Interaction of canard and singular Hopf mechanisms in a neural*

model, SIAM J. Appl. Dyn. Syst., **10** (2011), 1443–1479.

[21] C. A. DEL NEGRO, C. F. HSIAO AND S. H. CHANDLER, *Outward currents influencing bursting dynamics in guinea pig trigeminal motoneurons*, J. Neurophysiol., **81** (1999), 1478–1485.

[22] Z. DENKOWSKA AND R. ROUSSARIE, *A method of desingularization for analytic two-dimensional vector field families*, Bol. Soc. Bras. Mat., **22** (1993), 93–126.

[23] M. DESROCHES, B. KRAUSKOPF, AND H. M. OSINGA, *The geometry of slow manifolds near a folded node*, SIAM J. Appl. Dyn. Syst., **7** (2008), 1131–1162.

[24] M. DESROCHES, B. KRAUSKOPF, AND H. M. OSINGA, *Mixed-mode oscillations and slow manifolds in the self-coupled Fitzhugh-Nagumo system*, Chaos, **18** (2008), 015107, 8 pp.

[25] M. DESROCHES, B. KRAUSKOPF, AND H. M. OSINGA, *Numerical continuation of canard orbits in slow-fast dynamical systems*, Nonlinearity, **23** (2010), 739–765.

[26] M. DESROCHES, J. BURKE, T. J. KAPER AND M. A. KRAMER, *Canards of mixed type in a neural burster*, Physical Review E, **85** (2012), 021920, 6 pp.

[27] M. DESROCHES, J. GUCKENHEIMER, B. KRAUSKOPF, C. KUEHN, H. M. OSINGA AND M. WECHSELBERGER, *Mixed-mode oscillations with multiple time scales*, SIAM Review, **54** (2012), 211–288.

[28] M. DESROCHES, T. J. KAPER AND M. KRUPA, *Mixed-mode bursting oscillations: dynamics created by a slow passage through spike-adding canard explosion in a square-wave burster*, Chaos, **23** (2013), 046106, 13 pp.

[29] F. DIENER AND M. DIENER, *Nonstandard analysis in practice*, Springer-Verlag, Berlin/New York, 1995.

[30] M. DIENER, *The canard unchained or how fast/slow dynamical systems bifurcate*, The Mathematical Intelligencer, **6** (1984), pp. 38–48.

[31] E. J. DOEDEL, *AUTO: A program for the automatic bifurcation analysis of autonomous systems*, Congr. Numer., **30** (1981), 265–284.

[32] E. J. DOEDEL, A. R. CHAMPNEYS, T. F. FAIRGRIEVE, Y. A. KUZNETSOV, K. E. OLDEMAN, R. C. PAFFENROTH, B. SANSTEDE, X. J. WANG AND C. ZHANG, *AUTO-07P: Continuation and bifurcation software for ordinary differential equations*, Available from: http://cmvl.cs.concordia.ca/

[33] J. DROVER, J. RUBIN, J. SU AND B. ERMENTROUT, *Analysis of a canard mechanism by which excitatory synaptic coupling can synchronize neurons at low firing frequencies*, SIAM J. Appl. Math., **65** (2004), 69–92.

[34] F. DUMORTIER, *Local study of planar vector fields: Singularities and their unfoldings*, in "Structures in Dynamics, Finite Dimensional Deterministic Studies" (H. W. Broer *et al.*, Eds.), Stud. Math. Phys., Vol. 2, North-Holland, Amsterdam (1991), pp. 161–241.

[35] F. DUMORTIER, *Techniques in the theory of local bifurcations: Blow-up, normal forms, nilpotent bifurcations, singular perturbations*, in "Bifurcations and Periodic Orbits of Vector Fields" (ed. D. Szlomiuk), Kluwer Academic, Dordrecht (1993), pp. 19–73.

[36] F. DUMORTIER AND R. ROUSSARIE, *Canard cycles and center manifolds*, Mem. Amer. Math. Soc., **577** (1996).

[37] W. ECKHAUS, *Relaxation oscillations including a standard chase on french ducks*, Lecture Notes in Math., **985** (1996) pp. 449–494.

[38] I. ERCHOVA AND D. J. MCGONIGLE, *Rhythms of the brain: An examination of mixed mode oscillation approaches to the analysis of neurophysiological data*, Chaos, **18** (2008), 015115, 14 pp.

[39] B. ERMENTROUT AND M. WECHSELBERGER, *Canards, clusters, and synchronization in a weakly coupled interneuron model*, SIAM J. Appl. Dyn. Syst., **8** (2009), 253–278.

[40] J. J. FEHER, "Quantitative Human Physiology: An Introduction", Academic Press, 2012.

[41] N. FENICHEL, *Geometric singular perturbation theory for ordinary differential equations*, J. Differential Equations, **31** (1979), 53–98.

[42] M. E. FREEMAN, *Neuroendocrine control of the ovarian cycle of the rat*, in "Knobil and Neill's Physiology of Reproduction" (ed. J. D. Neill), Elsevier (2006), 2327–2388.

[43] M. GOLUBITSKY, K. JOSIC AND T. J. KAPER, *An unfolding theory approach to bursting in*

fast-slow systems, in "Global Analysis of Dynamical Systems" (H. W. Broer, B. Krauskopf and G. Vegter, eds.), Institute of Physics Publishing, Bristol (2001), 277–308.

[44] G. N. GORELOV AND V.A. SOBOLEV, *Duck-trajectories in a thermal explosion problem*, Appl. Math. Lett. **5** (1992), 3–6.

[45] G. N. GORELOV, E. A. SHCHEPAKINA AND V.A. SOBOLEV, *Canards and critical behavior in autocatalytic combustion models*, J. Eng. Math. **56** (2006), 143–160.

[46] J. GUCKENHEIMER AND P. HOLMES, "Nonlinear Oscillations, Dynamical Systems, and Bifurcations of Vector Fields", Springer, 1983.

[47] J. GUCKENHEIMER, R. HARRIS-WARRICK, J. PECK AND A. WILLMS, *Bifurcation, bursting and spike frequency adaptation*, J. Comput. Neurosci. **4** (1997), 257–277.

[48] J. GUCKENHEIMER, K. HOFFMAN AND W. WECKESSER, *The forced van der Pol equation I: the slow flow and its bifurcations*, SIAM J. Appl. Dyn. Syst., **2** (2003), 1–35.

[49] J. GUCKENHEIMER AND R. HAIDUC, *Canards at folded nodes*, Mosc. Math. J., **5** (2005), 91–103.

[50] J. GUCKENHEIMER, M. WECHSELBERGER AND L.-S. YOUNG, *Chaotic attractors of relaxation oscillations*, Nonlinearity **19** (2006), 701–720.

[51] J. GUCKENHEIMER, *Singular hopf bifurcation in systems with two slow variables*, SIAM J. Appl. Dyn. Syst., **7** (2008), 1355–1377.

[52] J. GUCKENHEIMER, *Return maps of folded nodes and folded saddle-nodes*, Chaos, **18** (2008), 015108, 9 pp.

[53] J. GUCKENHEIMER AND C. SCHEPER, *A geometric model for mixed-mode oscillations in a chemical system*, SIAM J. Appl. Dyn. Syst., **10** (2011), 92–128.

[54] J. GUCKENHEIMER AND H. M. OSINGA, *The singular limit of a Hopf bifurcation*, Discrete Cont. Dyn. Syst. – A, **8** (2012), 2805–2823.

[55] R. HAIDUC, *Horseshoes in the forced van der Pol system*, Nonlinearity, **22** (2009), 213–237.

[56] J. E. HALL, "Guyton and Hall Textbook of Medical Physiology", 12th edition, Saunders, 2010.

[57] X. HAN AND Q. BI, *Slow passage through canard explosion and mixed-mode oscillations in the forced Van der Pol's equation*, Nonlinear Dyn., **68** (2012), pp. 275–283.

[58] E. HARVEY, V. KIRK, H. OSINGA, J. SNEYD AND M. WECHSELBERGER, *Understanding anomalous delays in a model of intracellular calcium dynamics*, Chaos, **20** (2010), 045104, 19 pp.

[59] E. HARVEY, V. KIRK, M. WECHSELBERGER AND J. SNEYD, *Multiple timescales, mixed mode oscillations and canards in models of intracellular calcium dynamics*, J. Nonlinear Sci., **21** (2011), 639–683.

[60] G. HEK, *Geometric singular perturbation theory in biological practice*, J. Math. Bio., **60** (2010), 347–386.

[61] E. HILLE, *Ordinary Differential Equations in the Complex Domain*, Wiley–Intersci. Ser. Pure Appl. Math., John Wiley & Sons, New York, 1976.

[62] B. HILLE, *Ion Channels of Excitable Membranes*, 3rd edition, Sinauer Associates, Inc., 2001.

[63] M. W. HIRSCH, C. C. PUGH AND M. SHUB, "Invariant manifolds", Springer-Verlag, New York, 1977.

[64] A. L. HODGKIN AND A. F. HUXLEY, *A quantitative description of membrane current and its application to conduction and excitation in nerve*, J. Physiol., **117** (1952), 500–544.

[65] E. M. IZHIKEVICH, *Neural excitability, spiking and bursting*, Internat. J. Bifur. Chaos Appl. Sci. Engrg., **10** (2000), 1171–1266.

[66] E. M. IZHIKEVICH, "Dynamical Systems in Neuroscience", MIT Press, 2007.

[67] J. JALICS, M. KRUPA AND H. G. ROTSTEIN, *Mixed-mode oscillations in a three time-scale system of ODEs motivated by a neuronal model*, Dynamical Systems, **25** (2010), 445–482.

[68] C. K. R. T. JONES, *Geometric singular perturbation theory*, in "Dynamical Systems" (ed. R. Johnson), Lecture Notes in Mathematics, Springer, New York (1995), 44–120.

[69] T. J. KAPER, *An introduction to geometric methods and dynamical systems theory for singular perturbation problems*, in "Analyzing Multiscale Phenomena Using Singular Perturbation Methods, Proceedings of the Symposium on Applied Mathematics" (J. Cronin and R. E. O'Malley Jr.,

eds.), American Mathematical Society, Providence, RI, Vol. **56** (1999), 85–131.
[70] J. KEENER AND J. SNEYD, *Mathematical Physiology*, 2nd edn, Springer, New York, 2008.
[71] M. KRUPA AND P. SZMOLYAN, *Extending geometric singular perturbation theory to nonhyperbolic points–fold and canard points in two dimensions*, SIAM Journal of Mathematical Analysis, **33** (2001), 286–314.
[72] M. KRUPA AND P. SZMOLYAN, *Extending slow manifolds near transcritical and pitchfork singularities*, Nonlinearity, **14** (2001), 1473–1491.
[73] M. KRUPA AND P. SZMOLYAN, *Relaxation oscillation and canard explosion*, J. Differential Equations, **174** (2001), pp. 312–368.
[74] M. KRUPA, N. POPOVIĆ, N. KOPELL AND H. G. ROTSTEIN, *Mixed-mode oscillations in a three time-scale model for the dopaminergic neuron*, Chaos, **18** (2008), 015106, 19 pp.
[75] M. KRUPA, N. POPOVIĆ, AND N. KOPELL, *Mixed-mode oscillations in three time-scale systems: a prototypical example*, SIAM J. Appl. Dyn. Syst., **7** (2008), 361–420.
[76] M. KRUPA AND M. WECHSELBERGER, *Local analysis near a folded saddle-node singularity*, J. Differential Equations, **248** (2010), 2841–2888.
[77] C. KUEHN, *On decomposing mixed-mode oscillations and their return maps*, Chaos, **21** (2011), 033107, 15 pp.
[78] Y. A. KURYSHEV, G. V. CHILDS, A. K. RITCHIE, *Corticotropin-releasing hormone stimulates Ca^{2+} entry through L- and P-type Ca^{2+} channels in rat corticotropes*, Endocrinology, **137** (1996), 2269–2277.
[79] Y. A. KUZNETSOV, "Elements of Applied Bifurcation Theory", 3rd edition, Springer-Verlag, New York, 2004.
[80] R. LATORRE AND S. BRAUCHI, *Large conductance Ca^{2+}-activated K^+ (BK) channel: activation by Ca^{2+} and voltage*, Biological Research, **39** (2006), 385–401.
[81] A. P. LEBEAU, A. B. ROBSON, A. E. MCKINNON AND J. SNEYD, *Analysis of a reduced model of corticotroph action potentials*, Journal of Theoretical Biology, **192** (1998), 319–339.
[82] J. E. LISMAN, *Bursts as a unit of neural information: Making unreliable synapses reliable*, Trends in Neuroscience, **20** (1997), 38–43.
[83] D. A. LOVEJOY, "Neuroendocrinology: An Integrated Approach", Wiley, 2005.
[84] G. MEDVEDEV AND J. CISTERNAS, *Multimodal regimes in a compartmental model of the dopamine neuron*, Physica D, **194** (2004), 333–356.
[85] A. MILIK, P. SZMOLYAN, H. LOEFFELMANN, AND E. GROELLER, *Geometry of mixed-mode oscillations in the 3-d autocatalator*, Int. J. of Bif. and Chaos **8** (1998), 505–519.
[86] P. MIRANDA, P. DE LA PEÑA, D. GÓMEZ-VARELA AND F. BARROS, *Role of BK potassium channels shaping action potentials and the associated Ca_i^{2+} oscillations in GH_3 rat anterior pituitary cells*, Neuroendocrinology **77** (2003), 162-176.
[87] E. F. MISHCHENKO AND N. KH. ROZOV, *Differential equations with small parameters and relaxation oscillations (translated from Russian)*, Plenum Press, New York, 1980.
[88] E. F. MISHCHENKO, YU. S. KOLESOV, A. YU. KOLESOV, AND N. KH. RHOZOV, *Asymptotic Methods in Singularly Perturbed Systems*, Monographs in Contemporary Mathematics, Consultants Bureau, New York, 1994.
[89] J. MITRY AND M. WECHSELBERGER, *Faux canards of folded saddle type*, in preparation.
[90] J. MOEHLIS, *Canards in a surface oxidation reaction*, J. Nonlin. Sci., **12** (2002), pp. 319–345.
[91] A. I. NEISHTADT, *Persistence of stability loss for dynamical bifurcations. I*, Differential Equations, **23** (1987), 1385–1391.
[92] A. I. NEISHTADT, *Persistence of stability loss for dynamical bifurcations. II*, Differential Equations, **24** (1988), 171–176.
[93] A. NEISHTADT, *On stability loss delay for dynamical bifurcations*, Discr. Cont. Dyn. Syst. Ser. S, **2** (2009), pp. 897–909.
[94] J. NOWACKI, S. MAZLAN, H. M. OSINGA, AND K. TSANEVA-ATANASOVA, *The role of large-conductance calcium-activated K^+ (BK) channels in shaping bursting oscillations of a somatotroph cell model*, Physica D, **239** (2010), 485–493.
[95] H. M. OSINGA AND K. TSANEVA-ATANASOVA, *Dynamics of plateau bursting depending on*

the location of its equilibrium, Journal of Neuroendocrinology, **22** (2010), 1301–1314.

[96] C. PERRYMAN AND S. WIECZOREK, *Adapting to a changing environment: non-obvious thresholds in multi-scale systems*, Preprint.

[97] V. PETROV, S. K. SCOTT AND K. SHOWALTER, *Mixed-mode oscillations in chemical systems*, J. Chem. Phys., **97** (1992), pp. 6191–6198.

[98] J. RINZEL, *Bursting oscillations in an excitable membrane model*, In: Lecture Notes in Mathematics, vol. 1151(1985), 304–316.

[99] J. RINZEL, *A formal classification of bursting mechanisms in excitable systems*, in 'Proc. Intl. Cong. Math., Vol. 1, 2' (Berkeley, Calif., 1986) (ed. A. M. Gleason), American Mathematical Society, Providence, RI, (1987), 1578–1593.

[100] H. G. ROTSTEIN, J. OPPERMAN, T. WHITE AND N. KOPELL, *The dynamic structure underlying subthreshold activity and the onset of spikes in a model of medial entorhinal cortex stellate cells*, J. Comput. Neurosci., **21** (2006), 271–292.

[101] H. ROTSTEIN, M. WECHSELBERGER AND N. KOPELL, *Canard induced mixed-mode oscillations in a medial entorhinal cortex layer II stellate cell model*, SIAM J. Appl. Dyn. Syst., **7** (2008), 1582–1611.

[102] R. ROUSSARIE, *Techniques in the theory of local bifurcations: Cyclicity and desingularization*, in "Bifurcations and Periodic Orbits of Vector Fields" (ed. D. Szlomiuk), Kluwer Academic, Dordrecht (1993), pp. 347Ð382.

[103] J. RUBIN AND M. WECHSELBERGER, *Giant squid-hidden canard: the 3D geometry of the Hodgkin-Huxley model*, Biological Cybernetics, **97** (2007), 5–32.

[104] J. RUBIN AND M. WECHSELBERGER, *The selection of mixed-mode oscillations in a Hodgkin-Huxley model with multiple timescales*, Chaos, **18** (2008), 015105, 12 pp.

[105] V. F. SAFIULINA, P. ZACCHI, M. TAGLIALATELA, Y. YAARI AND E. CHERUBINI, *Low expression of Kv7/M channels facilitates intrinsic and network bursting in the developing rat hippocampus*, Journal of Physiology, **586** (2008), 5437–5453.

[106] P. SAH AND E. S. FABER, *Channels underlying neuronal calcium-activated potassium currents*, Progress in Neurobiology, **66** (2002), 345–353.

[107] J. A. SANDERS, F. VERHULST AND J. A. MURDOCK, *Averaging Methods In Nonlinear Dynamical Systems*, 3rd edition, Springer, New York, 2007.

[108] C. SAPER, *Hypothalamus*, Scholarpedia, (2009) **4**(1):2791.

[109] D. SATO, L-H. XIE, T. P. NGUYEN, J. N. WEISS AND Z. QU, *Irregularly appearing early afterdepolarizations in cardiac myocytes: random fluctuations or dynamical chaos?*, Biophys. J., **99** (2010), 765–773.

[110] A. A. SHARP, M. B. O. NEIL, L. F. ABBOTT AND E. MARDER, *Dynamic clamp – computer-generated conductances in real neurons*, Journal of Neurophysiology, **69** (1993), 992–995.

[111] E. SHCHEPAKINA, *Black swans and canards in self-ignition problem*, Nonlin. Anal.: Real World Applic., **4** (2003), 45–50.

[112] A. SHERMAN, J. KEIZER AND J. RINZEL, *Domain model for Ca^{2+}-inactivation of Ca^{2+} channels at low channel density*, Biophysical Journal, **58** (1990), 985–995.

[113] M. SHISHKOVA, *Examination of a system of differential equations with a small parameter in the highest derivatives*, Dokl. Akad. Nauk SSR, **209** (1973), pp. 576–579.

[114] P. R. SHORTEN, A. B. ROBSON, A. E. MCKINNON AND D. J. WALL, *CRH-induced electrical activity and calcium signalling in pituitary corticotrophs*, Journal of Theoretical Biology, **206** (2000), 395–405.

[115] V. A. SOBOLEV AND E. SHCHEPAKINA, *Duck trajectories in a problem of combustion theory*, Differential Equations, **32** (1996), 1177–1186.

[116] J. V. STERN, H. M. OSINGA, A. LEBEAU AND A. SHERMAN, *Resetting behavior in a model of bursting in secretory pituitary cells: distinguishing plateaus from pseudo-plateaus*, Bull. Math. Biol., **70** (2008), 68–88.

[117] S. S. STOJILKOVIC, H. ZEMKOVA AND F. VAN GOOR, *Biophysical basis of pituitary cell type-specific Ca^{2+} signaling-secretion coupling*, Trends in Endocrinology and Metabolism, **16** (2005), 152–159.

[118] S. S. STOJILKOVIC, J. TABAK AND R. BERTRAM, *Ion channels and signaling in the pituitary gland*, Endocrine Reviews, **31** (2010), 845–915.

[119] P. SZMOLYAN AND M. WECHSELBERGER, *Canards in* $\mathbb{R}^3$, J. Differential Equations, **177** (2001), 419–453.

[120] P. SZMOLYAN AND M. WECHSELBERGER, *Relaxation oscillations in* $\mathbb{R}^3$, J. Differential Equations, **200** (2004), 69–104.

[121] J. TABAK, N. TOPORIKOVA, M. E. FREEMAN AND R. BERTRAM, *Low dose of dopamine may stimulate prolactin secretion by increasing fast potassium currents*, J. Comput. Neurosci., **22** (2011), 211–222.

[122] J. TABAK, M. TOMAIUOLO, A. E. GONZALEZ-IGLESIAS, L. S. MILESCU, R. BERTRAM, *Fast-activating voltage- and calcium-dependent potassium (BK) conductance promotes bursting in pituitary cells: A dynamic clamp study*, Journal of Neuroscience, **31** (2011), 16855–16863.

[123] W. TEKA, J. TABAK, T. VO, M. WECHSELBERGER AND R. BERTRAM, *The dynamics underlying pseudo-plateau bursting in a pituitary cell model*, Journal of Mathematical Neuroscience, **1** (2011), 12.

[124] W. TEKA, K. TSANEVA-ATANASOVA, R. BERTRAM AND J. TABAK, *From plateau to pseudo-plateau bursting: Making the transition*, Bull. Math. Biol., **73** (2011), 1292–1311.

[125] W. TEKA, J. TABAK AND R. BERTRAM, *The relationship between two fast/slow analysis techniques for bursting oscillations*, Chaos, **22** (2012), 043117, 10 pp.

[126] D. TERMAN, *Chaotic spikes arising from a model of bursting in excitable membranes*, SIAM J. Appl. Math., **51** (1991), 1418–1450.

[127] D. X. TRAN, D. SATO, A. YOCHELIS, J. N. WEISS, A. GARFINKEL AND Z. QU, *Bifurcation and chaos in a model of cardiac early afterdepolarizations*, Phys. Rev. Lett., **102** (2009), 258103, 4 pp.

[128] K. TSANEVA-ATANASOVA, A. SHERMAN, F. VAN GOOR AND S. S. STOJILKOVIC, *Mechanism of spontaneous and receptor-controlled electrical activity in pituitary somatotrophs: Experiments and theory*, J. Neurophysiol., **98** (2007), 131–144.

[129] K. TSANEVA-ATANASOVA, H. M. OSINGA, T. RIEB AND A. SHERMAN, *Full system bifurcation analysis of endocrine bursting models*, Journal of Theoretical Biology, **264** (2010), 1133–1146.

[130] N. TOPORIKOVA, J. TABAK, M. E. FREEMAN AND R. BERTRAM, *A-type* K^+ *current can act as a trigger for bursting in the absence of a slow variable*, Neural Computation, **20** (2008), 436–451.

[131] S. A. VAN GILS, M. KRUPA AND P. SZMOLYAN, *Asymptotic expansions using blow-up*, Zeitschrift für angewandte Mathematik und Physik, **56** (2005), 369–397.

[132] F. VAN GOOR, Y. X. LI AND S. S. STOJILKOVIC, *Paradoxical role of large-conductance calcium-activated* K^+ *(BK) channels in controlling action potential-driven* Ca^{2+} *entry in anterior pituitary cells*, Journal of Neuroscience, **21** (2001), 5902–5915.

[133] F. VAN GOOR, D. ZIVADINOVIC, A. J. MARTINEZ-FUENTES AND S. S. STOJILKOVIC, *Dependence of pituitary hormone secretion on the pattern of spontaneous voltage-gated calcium influx: cell type-specific action potential secretion coupling*, Journal of Biological Chemistry, **276** (2001), 33840–33846.

[134] T. VO, R. BERTRAM, J. TABAK AND M. WECHSELBERGER, *Mixed mode oscillations as a mechanism for pseudo-plateau bursting*, J. Comput. Neurosci., **28** (2010), 443–458.

[135] T. VO, R. BERTRAM, AND M. WECHSELBERGER, *Bifurcations of canard-induced mixed mode oscillations in a pituitary lactotroph model*, Discrete Cont. Dyn. Syst. – A, **32** (2012), 2879–2912.

[136] T. VO, R. BERTRAM, AND M. WECHSELBERGER, *Multiple geometric viewpoints of mixed mode dynamics associated with pseudo-plateau bursting*, SIAM J. Appl. Dyn. Syst., **12** (2013), 789–830.

[137] T. VO, J. TABAK, R. BERTRAM, AND M. WECHSELBERGER, *A geometric understanding of how fast activating potassium channels promote bursting in pituitary cells*, J. Comput. Neurosci., **36** (2014), 259–278

[138] T. VO AND M. WECHSELBERGER, *Canards of folded saddle-node type*, preprint.
[139] M. WECHSELBERGER, *Extending Melnikov theory to invariant manifolds on non-compact domains*, Dynamical Systems, **17** (2002), pp. 215–233.
[140] M. WECHSELBERGER, *Existence and bifurcation of canards in* $\mathbb{R}^3$ *in the case of a folded node*, SIAM J. Appl. Dyn. Syst., **4** (2005), 101–139.
[141] M. WECHSELBERGER AND W. WECKESSER, *Bifurcations of mixed-mode oscillations in a stellate cell model*, Physica D, **238** (2009), 1598–1614.
[142] M. WECHSELBERGER AND W. WECKESSER, *Homoclinic clusters and chaos associated with a folded node in a stellate cell model*, Discrete Cont. Dyn. Syst. – S, **2** (2009), 829–850.
[143] M. WECHSELBERGER, *À propos de canards (apropos canards)*, Transactions of the American Mathematical Society, **364** (2012), 3289–3309.
[144] M. WECHSELBERGER, J. MITRY AND J. RINZEL, *Canard theory and excitability*, in "Nonautonomous Dynamical Systems in the Life Sciences", Lecture Notes in Mathematics, Vol. 2102 (Mathematical Biosciences Subseries), 2014.
[145] S. WIGGINS, "Normally hyperbolic invariant manifolds in dynamical systems", Springer-Verlag, New York, 1994.
[146] M. ZHANG, P. GOFORTH, R. BERTRAM, A. SHERMAN AND L. SATIN, *The* Ca^{2+} *dynamics of isolated mouse* β*-cells and islets: Implications for mathematical models*, Biophysical Journal, **84** (2003), 2852–2870.